Transactions of the ASME

Coefficients of Float-Type Variable-Area Flowmeters

By V. P. HEAD,[1] HATBORO, PA.

A uniform method of correlating flow data for all float-type variable-area meters is presented. Curves correlating the results of 73 calibrations of rotameters in $1/2$-in. to 2-in. sizes and suitable for general flow calculation purposes are presented. Installation influences are discussed. A theoretical equation combining energy and momentum considerations is presented and compared with available data for incompressible flow.

NOMENCLATURE

The following nomenclature is used in the paper for general correlation and calculation procedures; any consistent units may be employed:

C = simplified flow parameter
D_f = float diameter at largest section or reading edge
D_t = tube diameter corresponding to a particular scale reading
D_b = diameter of weight-giving float body below float head
D_g = diameter of bore of float guide bushings, if employed
e = gas elasticity = kP
E = compressibility parameter
f_b = flow factor for deviation of D_b from correlation value
f_g = flow factor for deviations of D_g from zero
F = restoring force tending to zero the float
g = local acceleration of gravity
k = ratio of specific heats of gas
K = over-all flow coefficient in theoretical equation for turbulent flow
M_f = mass of float
N = viscosity parameter for meter application
P = absolute static pressure
q = volume flow rate
$\mathbf{R}$ = viscosity parameter for meter design, a Reynolds number
w = mass-flow rate
α = ratio of tube diameter to float diameter = D_t/D_f
μ = dynamic viscosity
π = ratio of circle circumference to diameter = 3.1416
ρ = fluid density, mass per unit volume
ρ_f = float density

The following additional nomenclature is used in this paper for the development of theoretical principles only: see Fig. 6 for clarification of area definitions:

a_0 = approach area well upstream from float in an assumed cylindrical tube
a_1 = approach area immediately upstream from float head and approach area (on one side of the line of symmetry) of a two-dimensional orifice

a_2 = aperture area
a_j = jet area at point where jet streamlines are presumed parallel
a_3 = area of full flow well downstream from the stagnant wake above the float
a_f = float-head area = $a_0 - a_2$
C_c = contraction coefficient = a_j/a_2
K' = coefficient in Colburn-Schoenborn equation
V_0, V_1, V_j = velocities in regions of parallel streamlines; subscripts same as area subscripts
ΔP_s = difference between static pressures, $P_0 - P_f$
ΔP_t = difference between jet total and jet static pressures = jet velocity pressure
P_0, P_j, P_3 = static pressures; subscripts same as area subscripts
θ = float-head angle at aperture approach, Fig. 6
β = conventional orifice diameter ratio
ϵ = velocity ratio, V_1/V_f
$x, y, z, A_n, B_n, \theta_n$ = mathematical tools employed in contraction coefficient calculation (Appendix)

INTRODUCTION

Widespread application of "rotameters" for measurement of rate of fluid flow has aroused the interest of the ASME Special Research Committee on Fluid Meters in the fundamental principles and in such coefficient correlations as may be available. The device has been on record in the United States since 1868, when U. S. Patent Number 84,476 was issued to Edmund Chameroy of Paris. Many years passed before the use of tapered glass tubes, the development of precise glass and metal tube-forming techniques, and friction-free magnetic and electrical transmitters led to general employment of this principle in the chemical-process industries, oil industries, aircraft-test work, and many other flow-measurement and control applications.

A tapered tube with axis vertical and smaller end at the bottom conveys the flowing fluid in an upward direction. The float, an obstruction which is only slightly smaller than the lower end of the tube, closes off the flow passage and rests on a stop at the bottom when there is no flow. At any particular flow rate, drag decreases as the float rises until the drag is just balanced by the net weight of the buoyed float. Flow rate then is indicated by the position of the float's "reading edge" against a scale on the tube.

Fig. 1 shows a modern test-type rotameter employing a sharp square-edged float disk with weight-giving portions contained within the limits of a 30-deg half-angle cone above the disk and a cylindrical portion not exceeding about 0.66 times the float head diameter extending below the float head or disk.

Fig. 2 shows the flow pattern revealed by "two-dimensional" flow around a model of the cross section of an industrial rotameter using the same float shape. Note particularly the high-velocity jet next to the walls, where the air bubbles admitted to the water move too fast to be visible, and the virtually stagnant wake inside the annular jet.

Early rotameters in the United States and Europe employed an unguided "plumb-bob" float shape, with notches in the periphery to impart rotation (hence the name rotameter) to stabilize and center the float. Sensitivity to viscosity prompted
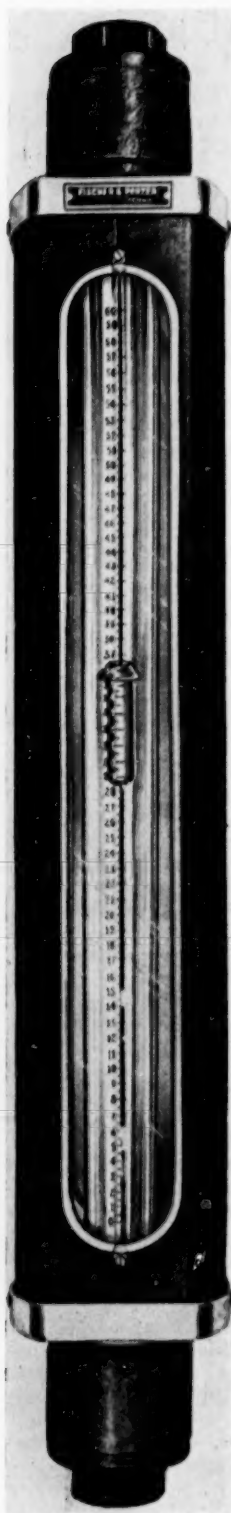
the study of other float shapes (1).[2] The modern test meter, having generally lower variations in coefficient than a sharp-edged orifice with changes in viscosity, makes no provision for float rotation. In fact, accidental visible rotation serves as a warning of undesirable installation effects upon the approach flow pattern, but the name rotameter has been employed widely by manufacturers and users. The "cone and disk" type of "area meter" described in ASME literature (2) is one of many types of rotameter.

The term "variable-area" is roughly descriptive of many devices which experience deflection of a solid body as a result of fluid drag. The correlating parameters of the "orifice and plug," the "cone and disk," the "cylinder and plunger," and the "vane meter" (2) are identical dimensionless quantities except in the choice of purely geometric ratios. On the other hand, the adjustable gate with external head measurement belongs with the fixed-area orifice, nozzle, venturi, and so forth, in so far as fluid mechanics is concerned, and is excluded from this discussion of variable-area devices. The drag force in any variable-geometry meter may be balanced by any type of external force. The term "float-type" is used here to describe those variable geometry devices in which the external force is provided wholly by gravity and so is equal to the net buoyed weight of the drag body or float whose position provides the flow-rate indication. Such devices generally permit the use of pressure drops from a few hundredths of an inch of water to 1 or 2 in. of mercury, with accurate indication at a very small percentage of maximum flow. One variable-area meter handles a flow range covered by three fixed-area meters of comparable scale length. In laboratory and test work, the high readability of the single sharp float edge position and the visible evidence of freedom from contamination and swirl count heavily in the unusual accuracy achievable with tapered glass tube types.

[2] Numbers in parentheses refer to the Bibliography at the end of the paper.

FIG. 1 (left)   A 600-MM TEST RO-
TAMETER WITH SQUARE-EDGED FLOAT

FIG. 2   FLOW PATTERN REVEALED BY INJECTING AIR INTO WATER
FLOWING THROUGH A SECTION MODEL

WORKING EQUATIONS

The equations of this section involve no theory and may be derived by dimensional analysis.

Flow rate normally is calculated by means of one of the equations

$$
\left.
\begin{aligned}
w &= C\,D_f\,\sqrt{F\rho} \\
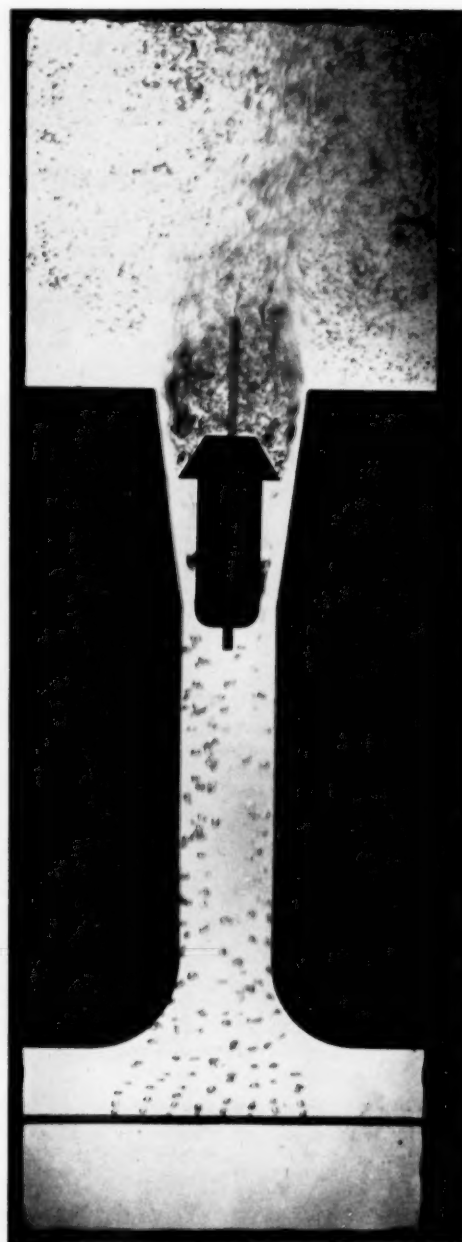q &= C\,D_f\,\sqrt{F/\rho}
\end{aligned}
\right\} \quad\dots\dots\dots\dots\dots\quad [1]
$$

in which the right-hand members are constant for any one instrument and fluid, except for the value of the flow parameter, C. This parameter varies primarily with float elevation in the tube. A curve of C versus diameter ratio α is the generalized equivalent of a curve of flow rate versus scale reading. Such a curve derived from a precise calibration may be applied to the calibrated meter or to other meters with any other fluid as long as dynamic similarity between the test and the service situations exists. Dynamic similarity means, first of all, geometric similarity in every respect. Geometric variation requires additional test work until freedom from or correlation of the effects of particular geometric variations is demonstrated.

When measuring the flow of incompressible true fluids, the only additional parameter which must be held constant to assure dynamic similarity is the viscosity parameter N, defined by the equation

$$N = \frac{\sqrt{F\rho}}{\mu} \qquad \qquad [2]$$

Complete working data for a family of variable-area flowmeters for incompressible true fluid flow will consist of a family of curves of C versus N, each curve representing a particular value of scale reading or diameter ratio α, and a correlation of the influences of geometric variation or a statement of limitation upon such variation within which effects are known to be negligible at all values of α and N under consideration.

Fig. 3 shows such a correlation for square-edged floats in low-taper tubes with float-body to head-diameter ratio, D_b/D_f, of 0.640. Fig. 4 shows the geometric variations found in the instruments from whose calibrations the curves were organized.

The form of the viscosity parameter N is such that, with a given instrument and fluid density and viscosity, N is a constant at all flow rates. Thus a cross plot of C values picked from a vertical line on Fig. 3 yields the complete calibration with no trial and error. However, when designing a float, the value of F is unknown, and the use of N would incur a trial-and-error design procedure. A design viscosity parameter R is obtained by multiplying C and N to introduce the known design value of flow rate w and to eliminate the unknown F

$$R = \frac{4}{\pi} \; CN = \frac{4w}{\pi D_f \mu} \qquad \qquad [3]$$

The factor $4/\pi$ is introduced only to make the numerical values of R equal to a sort of Reynolds number. The Reynolds numbers calculated from Equation [3] are identical to pipe Reynolds numbers for pipes having diameter equal to float diameter, D_f. Other forms of Reynolds number may be obtained by combining R, Equation [3], with any of several functions of α, but these are of academic interest and quite unsuitable for design calculations. Lines showing certain values of R have been superimposed on Fig. 3. Their location is completely independent of the test correlations, and graph paper with such lines permanently located may be used for any type of variable-geometry flowmeter. On a log-log plot, these lines will have a slope of minus 1 and intercepts of $C = 0.7854$ where $R = N$. No other form of Reynolds number permits such simple and general application.

When measuring the flow of gases, compressibility demands an additional criterion for dynamic similarity

$$E = \frac{F}{D_f e} \qquad \qquad [4]$$

Here e is the adiabatic elasticity of the gas, the product of the absolute pressure at whatever point is chosen for absolute pressure measurement and the ratio of specific heats of the gas. For any arbitrarily chosen absolute pressure-tap location, values of an expansion factor Y will depend on α, N, and E, or should be stated with tolerances as a function of E only. However, values of Y for the float shape of Fig. 4 may be held within a fraction of a per cent of unity when the absolute pressure tap is located somewhere above the outlet of the tapered tube. The exact construction of the pressure tap is determined by trial and error, when extreme accuracy of gas measurement is desired. Calibrations of the test meter with gasoline and atmospheric air at identical values of N are repeated with several pressure taps until the values of C from both fluids are identical within the required
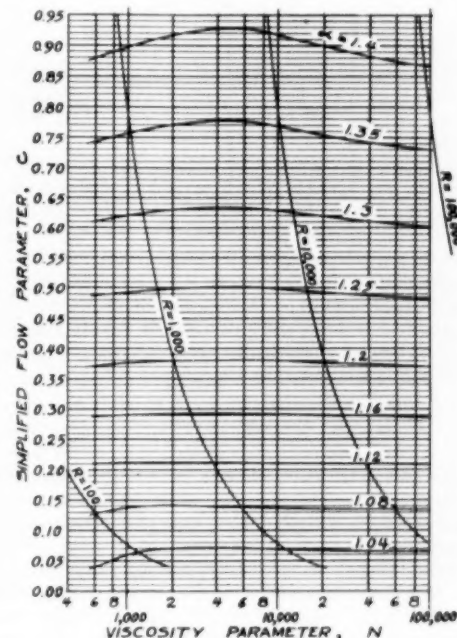

FIG. 3 COMPOSITE CORRELATIONS OF THE FLOW PARAMETER FOR $\frac{1}{2}$ TO 2-IN. ROTAMETERS WITH SQUARE-EDGED FLOATS HAVING 0.64 BODY RATIO
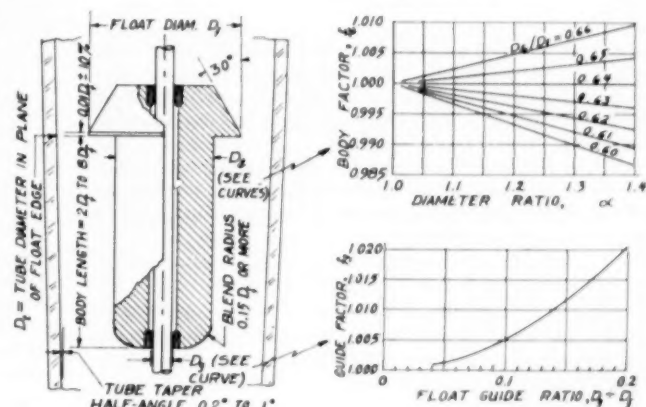

FIG. 4 GEOMETRY RESTRICTIONS AND KNOWN EFFECTS FOR THE SQUARE-EDGED ROTAMETER FLOAT

accuracy when based on ρ at one of the taps tried. The accumulation of such results will permit more detailed recommendations in the future. Any outlet tap for absolute pressure is satisfactory for most industrial gas measurement.

When measuring the flow of non-Newtonian fluids, an additional parameter is required. A straight line of the shear stress versus shear rate curve of such materials approximating "plastics" may be used to define the material numerically, the slope of the line defining a value of μ suitable for use in Equation [2] or [3], and the intercept obtained by extrapolating the straight line of the shear diagram to zero shear rate defining an additional fluid property, the apparent yield stress s. An appropriate criterion for dynamic similarity in such applications is the shear parameter S defined by

$$S = \frac{s D_f^2}{F} \qquad [5]$$

Data correlating the performance of large variable-area instruments in measuring the flow of "fluids" having significant yield stress such as paper and pulp-stock suspensions have been presented elsewhere (3).

The equations and correlation technique given thus far are applicable to any variable-area or variable-geometry meter, regardless of the nature of the external restoring force provided to urge the moving element toward zero. The term "float-type" is proposed for any variable-geometry meter employing gravity for the restoring force. In this case, the influence of fluid density in buoying the float must be considered, and for vane meters, orifice and plug meters, cylinder and piston meters, and the like, as well as for rotameters, all of which are float-type variable-area meters, the value of F is determined by the equation

$$F = g M_f \frac{\rho_f - \rho}{\rho_f} \qquad [6]$$

For other than rotameters, D_f may be replaced by any linear measurement characterizing the size of the moving element, and α by any appropriate dimensionless expression for the geometric deflection.

The working equations specifically applicable to those float-type variable-area flowmeters employing float shapes within the limits of Fig. 4 are then

$$\left. \begin{aligned} w &= C f_b f_g D_f \sqrt{g M_f \frac{\rho_f - \rho}{\rho_f} \rho} \\ q &= C f_b f_g D_f \sqrt{g M_f \frac{\rho_f - \rho}{\rho_f \rho}} \end{aligned} \right\} \qquad [7]$$

where C is the flow parameter shown by Fig. 3 for 0.64 body ratio and zero center-guide ratio, and f_b and f_g are given in Fig. 4 for body ratios differing significantly from 0.64, and for center guides, if employed. The body and guide factors are derived in the sections entitled Theory and Tests.

Alternate equations based on turbulent incompressible-flow theory, to be given, offer the advantage of better curve readability. These equations are obtained by replacing C in Equations [1] and [7] with the following

$$C = K(\alpha^2 - 1)\alpha\sqrt{\pi/2} \qquad [8]$$

Values of K corresponding to the values of C given in Fig. 3 are given in Fig. 5, and the use of these curves and the somewhat more complex calculation required by Equation [8] is recommended for precise measurement when calibration data is not available.

TOLERANCES

Tests with inspected tubes and floats with lapped lower sur-

faces indicate preliminary tolerances or twice the standard deviation (4) on over-all flow-measurement accuracy of ± 0.6 per cent when N is greater than 2000 and α is between 1.06 and 1.4. When α is less than 1.06, dimensional determinations are unreliable, viscosity effects are significant, and the coefficients are affected by both microscopic roundness of float edge and the width of the cylindrical portion of the float head. Above $\alpha = 1.4$, disturbances due to installation piping and variations in meter inlet-fitting design produce detectable deviations in coefficient. Within the stated limits, unusual piping such as a sudden expansion from very small pipe at the meter inlet, or a valve within two or three pipe diameters of the meter inlet may produce swirl causing significant increase in coefficients at high α ratios, but the swirl is accompanied by visible steady float rotation which serves as adequate warning. If the fluid is clean, cylinders of wire screen inserted in the inlet, or minor piping revision, may help.

Below $N = 2000$ a tolerance approaching ± 2 per cent is required unless much more rigid limitations on float geometry are imposed.

When unlapped floats are used in uninspected tubes, calculations based on nominal values of α require tolerances which increase rapidly as α decreases and may be stated best in industrial parlance as about ± 1 per cent of maximum flow rather than as a percentage of the measured rate.

Calibrated instruments have shown agreement within ± 0.25 per cent of the measured rate after years of service, and the use of ratios of C or K to correct calibration data from one viscosity to another yields results in the order of ± 0.5 per cent, so it remains to be seen whether or not the costs of lapping and precision inspection can compete with the costs of calibration in the $1/_8$-in. to 2-in. meter sizes. The scope of the problem is indicated by Equation [8]. Evaluation of the tube diameters and the float diameter to a tolerance of ± 0.02 per cent leads to a tolerance of $\sqrt{0.02^2 + 0.02^2} = \pm 0.028$ per cent for α, and the resulting tolerances on $(\alpha^2 - 1)\alpha$ are ± 0.15 per cent at $\alpha = 1.4$ but increase to ± 0.78 per cent at $\alpha = 1.04$.

Geometric effects associated with absolute size are believed extremely small owing to the smoothness of glass tubing and the ease with which float head lower surfaces may be lapped, but further studies in this direction are required.

THEORY

The only theoretical equation in common use up to the present has been the "Colburn-Schoenborn" equation (5). This equation is developed by assuming the ratio F/a_f to be the jet velocity pressure and substituting it in the conventional orifice equation

$$q = K' a_2 \sqrt{2 \Delta P_t / \rho}$$

$$\Delta P_t = F / a_f,$$

or

$$\left. \begin{aligned} q &= K' a_2 \sqrt{2 F / a_f \rho} \\ w &= K' a_2 \sqrt{2 F \rho / a_f} \end{aligned} \right\} \qquad [9]$$

Any and all theoretical flow equations for variable-geometry meters which recognize only density as a fluid property must be reducible to a combination of Equation [1] and a function of geometry. Thus Equation [9] is converted readily to the form

$$w = K'(\alpha^2 - 1)\sqrt{\pi/2} \ D_f \sqrt{F \rho} \qquad [10]$$

Correlation of this coefficient K' with Reynolds number failed to yield valid results. The various Reynolds numbers obtained by varying the rate of flow of a particular fluid could not be ex-

pected to yield coefficients which would remain constant when the same values of Reynolds number were obtained with another fluid of different viscosity, because, under such conditions, like values of **R** must fall at different values of α, and the conditions of dynamic similarity which include geometric similarity could not be satisfied.

The apparent changes in coefficient with Reynolds number reported (5) were the result of the form of Equation [9] and were actually variations due largely to changes in α, not to changes in **R**. Nevertheless, once correlations on separate lines for each value of α were employed, valid and useful results were obtained.

The correlation of test data never demands a theoretical equation. The simplest equations for correlation and application of data are those resulting from dimensional analysis, mere statements of the dimensional equivalence, in the mass-length-time system or other fundamental system, of the variables when combined with the proper exponents. The laws of nature are the correlations of experimental coefficients in such simple forms as those of Equations [1] through [5], and the general statement, with numerical evaluation by experiment, that

$$C \text{ depends on } \alpha, N, E, S, \text{ geometry} \ldots \ldots \ldots [11]$$

constitutes the complete equation of the variable-geometry meter, provided that some additional variable has not been overlooked (as, for example, the mean free path (MFP) of gas molecules in high-vacuum gas measurement which would demand an additional parameter, such as $\text{MFP} \div D_f$).

The objectives of a theoretical derivation are not to replace experiment. They are (a) to provide an equation whose coefficients have a reduced numerical spread to improve curve or table readability (Fig. 5 versus Fig. 3); (b), to permit at least rough numerical estimates when experimental data are wanting; (c), to satisfy man's desire to understand "why."

Equation [9] contributed to the first of these objectives. It also gave numerical results in lieu of experiment, which were roughly correct at low-diameter ratio. As α decreases so as to approach unity as a limit, the validity of expressing pressure drop as F/a_f improves. At high values of α, the academic problem of whether F/a_f should represent the jet velocity pressure or only the static pressure drop requiring a velocity of approach correction remained the subject of debate which experiment could not

FIG. 5 COMPOSITE CORRELATIONS OF THE FLOW COEFFICIENT K FOR $^{1}/_{2}$ TO 2-IN. ROTAMETERS WITH SQUARE-EDGED FLOATS HAVING 0.64 BODY RATIO

answer. Data with floats having hollow heads somewhat resembling the sketch, $\theta = 180$ deg, Fig. 6, supported the velocity-pressure theory, while data for floats having $\theta = 90$ deg or slightly less, supported the static-pressure theory.
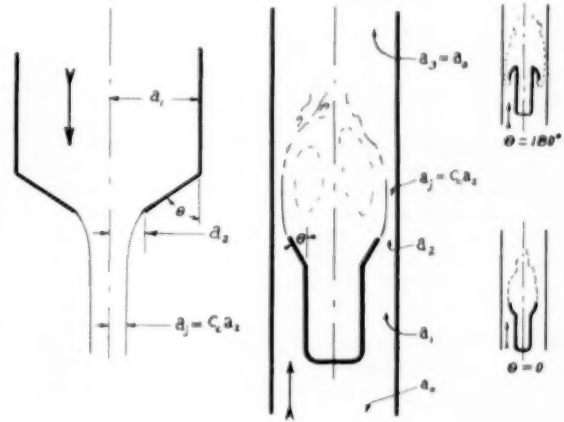
FIG. 6 VON MISES TWO-DIMENSIONAL ORIFICE AND EQUIVALENT ROTAMETER SHAPES

When θ was close to zero, as in many of the early plumb-bob rotameters, results indicated that even the static-pressure drop could exceed F/a_f by many per cent when α is high. The author's file contains coefficient data obtained in 1946 for a 4-in. meter with $\theta = 0$ deg, in which the values of K', Equation [9], were found to equal 1.8 or more at excessive diameter ratios and dropped to approach unity as diameter ratio, α, decreased. A supposed velocity of approach correction could account for only a 1.25 value of K', and the results were charged to some freak inlet condition at the time. A comparison of Equations [8] and [10] reveals the absence of an α in Equation [10] which would largely account for the discrepancy. Repeated evidence of the need of an extra α to modify the Colburn-Schoenborn equation to make sense at high α ratios was largely responsible for the theoretical approach given in this paper.

Referring to Fig. 6, two separate theoretical problems must be posed: (a) What is the actual relationship between float force F, and the pressure drop accelerating the fluid from section a_0 to section a_j; and (b) what values of contraction coefficient may be expected?

A clue to problem (a) is suggested in the use of float force set equal to the difference in momentum flux at these sections for an orifice-and-plug meter in reference (2). However, consideration of this situation reveals that these forces act in the same direction and must be added (together with the indeterminate drag on the orifice fixed to the frame in the case cited) and not set equal to each other. The correct force-balance equation for the rotameter, neglecting elevation which would cancel later, and neglecting taper angle, is obtained for all material contained within the tube between section a_0 and section a_j by equating the upward force due to static pressure drop and acting on the full area a_0 to the sum of the two downward forces F due to gravity or other external force provided to zero the float, and the jet reaction or difference in momentum flux between sections, $w(V_j - V_0)$

$$\text{Force balance:} \quad (P_0 - P_j)a_0 = F + w(V_j - V_0) \ldots [12]$$

The Bernoulli equation for kinetic and potential-energy balance may be written between the same sections, again omitting elevation
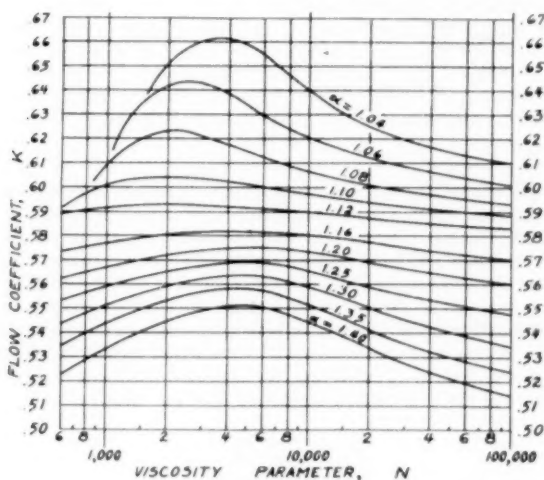
Energy balance: $P_0 - P_j = \dfrac{\rho}{2}(V_j{}^2 - V_0{}^2)$ .... [13]

For incompressible or constant density flow, we have

Continuity: $w = \rho V_0 a_0 = \rho V_j A_j$

or

$$V_0 = \frac{w}{\rho a_0}, \quad V_j = \frac{w}{\rho a_j} \dots \dots \dots \dots [14]$$

Once the applicability of these three equations is recognized, it is a simple matter to replace the velocities of Equations [12] and [13] with their equivalents in Equation [14] and combine the results to eliminate the common term $P_0 - P_j$, and solve for w to obtain

$$w = \frac{a_j}{a_0 - a_j}\sqrt{2a_0 F\rho} \dots \dots \dots \dots [15]$$

This is the basic equation of the rotameter which, if contraction coefficients can be estimated to relate a_j to a_2, will permit numerical prediction of approximate performance when viscous effects are negligible.

To form a practical working equation, the effects of differences between a_2 and a_j and all effects associated with the viscosity parameter N, the compressibility parameter E, and so forth, are lumped into the experimental coefficient K, yielding

$$w = K\frac{a_2}{a_0 - a_2}\sqrt{2a_0 F\rho}$$

or, since

$$\alpha = \sqrt{a_0/(a_0 - a_2)} = D_t/D_f$$

we have

$$w = K(\alpha^2 - 1)\alpha \sqrt{\pi/2}\, D_f \sqrt{F\rho} \dots \dots [16]$$

which may be compared with Equation [1] to demonstrate the validity of Equation [8], and which defines the flow coefficient K used in this paper and proposed for general variable-area meter work. Equation [16] fulfills the first objective of theoretical investigation permitting the use of experimental values of K which have a small numerical spread for high curve readability and easy interpolation, as in Fig. 5. It still fails, however, to permit theoretical numerical estimates in the absence of test data unless θ is close to zero and C_e close to unity, in which case K will be close to unity also. If now we replace a_j in Equation [15] with $C_e a_2$ and make the substitution $\alpha = D_t/D_f$, we obtain

$$w = \frac{C_e a_2}{a_0 - C_e a_2}\sqrt{2a_0 F\rho}$$

or

$$w = \frac{C_e(\alpha^2 - 1)\alpha \sqrt{\pi/2}}{\alpha^2 - C_e(\alpha^2 - 1)}\, D_f \sqrt{F\rho} \Bigg\} \dots \dots [17]$$

Numerical estimates of K then may be made by substituting estimated contraction coefficients after combining Equations [16] and [17] to obtain

$$\text{Theoretical } K = \frac{C_e}{\alpha^2 - C_e(\alpha^2 - 1)} \dots \dots [18]$$

or, if we prefer, we may regard C_e as a value calculable from experimental values of K, after solving Equation [18] for C_e.

$$C_e = \frac{K\alpha^2}{1 + K(\alpha^2 - 1)} \dots \dots \dots \dots [19]$$

The experimental values of C_e given in Fig. 7 were calculated using Equation [19].

The derivations thus far have made no assumptions regarding float shape. Prediction of approximate contraction coefficients can be made for a limited range of float shapes represented in Fig. 6, by noting the resemblance of the annular flow passage bounded by the float body and float head and the tube wall to the flow passage on one side of the line of symmetry in the two-dimensional orifice shown on the left of Fig. 5. This two-dimensional orifice, with various values of θ and approach area ratio a_2/a_1, was studied in detail by von Mises some years ago (6), using the mathematics of potential and stream functions. The author has attempted to give in the Appendix of this paper the detailed steps by which theoretical values of C_e may be computed, following the equations derived by von Mises. The values of C_e marked "theory" in Fig. 7 were so calculated.
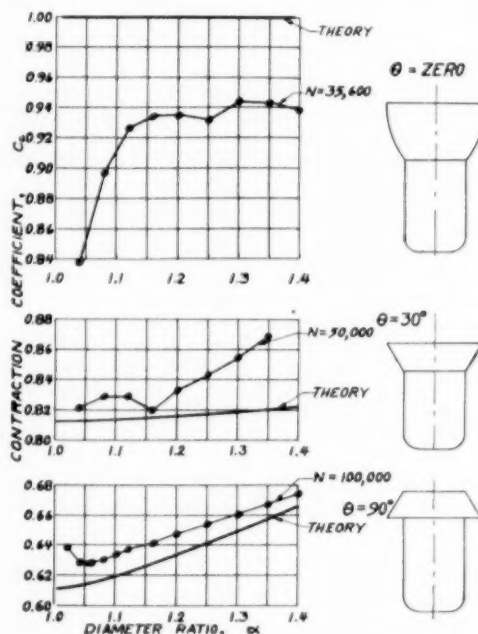
FIG. 7 THEORETICAL AND EXPERIMENTAL CONTRACTION CO-
EFFICIENTS

The values of a_1, a_2, a_j may be interpreted as either linear section dimensions (widths) or as areas in the two-dimensional flow diagram. The author has used an area interpretation throughout, simply because this assumption gives closer agreement between two-dimensional theory and experimental results for both the annular-flow passages of the rotameter and the circular-flow passage of concentric orifices. The reader may satisfy himself on this score after noting that the experimental contraction coefficient for an orifice at various β ratios may be calculated from experimental values of the over-all flow coefficient K of the orifice, using

$$C_e = \frac{K\ (\text{orifice})}{\sqrt{1 + K^2\beta^4}} \dots \dots \dots \dots [20]$$

A still more impressive argument for interpretation of a_1, a_2, and a_j as areas results from a comparison of the jet velocity pres-

sures and the value of F/a_f. The Colburn-Schoenborn Equation [10], in which K' should be close to C_c only if F/a_f should actually equal ΔP_t, may be combined with our universal "momentum theory" Equation [17] and the result solved for C_c to obtain

$$C_c = \frac{\alpha}{\alpha + 1} \dots \dots \dots \dots \dots [21]$$

as the condition required to make F/a_f precisely equal to ΔP_t in frictionless flow. Thus, for example, as α approaches unity, the contraction coefficient must approach 0.500; if $\alpha = 1.4$, C_c must be 0.5833, and so forth, if the velocity pressure assumption in the Colburn-Schoenborn equation is to apply. If now we compare Equation [21] with von Mises results, assuming them applicable on an area basis, for the case $\theta = 180$ deg and $a_1 = a_2 + a_f$ (or no float body), so that the float resembles a vertical tube closed at the upper end, identical numerical values of the contraction coefficient are obtained at every value of α. Whether this observation will permit a theoretical development of an equation for the mechanism of the impact tube, which the author has been unable to find in the literature, and perhaps throw more light on desirable impact-tube-tip shapes, remains to be seen. The point of immediate importance is that an area interpretation of a_1, a_2, a_f permits identical numerical results from both the two-dimensional hydrodynamics and three-dimensional momentum theory for the one case where hydraulic experience suggests that F/a_f should equal the jet velocity pressure. Attempts to interpret a_1, a_2, a_f as linear section dimensions in this three-dimensional case fail.

Similar studies demonstrate special cases where particular combinations of C_c (a little greater than 0.6) and α would make F/a_f precisely equal to ΔP_3 instead of ΔP_t. This explains the diversity of experimental results and the long controversy on the subject. The momentum theory makes both possible as special cases and permits many other relationships as well. The general expression for theoretical jet velocity pressure is found to be

$$\Delta P_t = \left[\frac{\alpha}{\alpha^2 - C_c(\alpha^2 - 1)} \right]^2 \frac{F}{a_f} \dots \dots \dots [22]$$

which has been verified experimentally by measuring the difference between jet impact pressure and the pressure in the stagnant wake of a 2-in. instrument with a thin movable probe extending downward from the top of a rotameter. The principal usefulness of this equation is to assist in estimating the minimum pressure in a meter installation handling liquids near the vapor pressure such as liquid chlorine.

A theoretical equation for the permanent head loss caused by the float as a percentage of the jet velocity pressure is found to be identical to that for an orifice or nozzle. Since, however, the value of ΔP_t is rarely of concern in the use of variable-area flowmeters, a much simpler equation yielding identical results is suggested, based also on the assumption of a virtually cylindrical tube, Fig. 6. The area a_3 is presumed to describe the region where full parallel flow again exists, identical to that at a_0. The velocity pressures at sections 0 and 3 then are equal, as are the momentum flux values. The complete force balance for all material between a_0 and a_3 (neglecting the boundary shear which is small in turbulent flow over short distances) is

$$F = a_0(P_0 - P_3) \dots \dots \dots \dots \dots [23]$$

or

$$\Delta P_{\text{loss}} = \frac{1}{\alpha^2} \frac{F}{a_f}$$

which is equal to F/a_f at low α and decreases as α increases. Ad-

ditional allowance, of course, must be made for inlet and outlet fitting losses.

The influence of center-guide diameter shown in Fig. 4 is based on the Colburn-Schoenborn Equation [9]. The center-guide bushings reduce the float area a_f by their own area, so that

$$f_g = \sqrt{\frac{D_f^2}{D_f^2 - D_g^2}} \dots \dots \dots \dots \dots [24]$$

If the results of the momentum theory are studied, it is found that a more exact correction will be

$$f_g = \frac{\alpha^2 - C_c(\alpha^2 - 1)}{\alpha^2 - C_c(\alpha^2 - 1) - (D_g/D_f)^2} \sqrt{\frac{\alpha^2 - (D_g/D_f)^2}{\alpha^2}} \dots \dots [25]$$

but for α less than 1.4, D_g/D_f less than 0.2, and C_c less than 0.7, the errors in the use of Equation [24] do not exceed about 0.1 per cent, and the use of f_g as a function of C_c and α is not justified. For very precise work when C_c is greater than 0.7, the use of Equation [25] is justified, Equation [24] yielding errors of about 1 per cent when $\alpha = 1.4$, $D_g/D_f = 0.2$, and $C_c = 1$.

The theoretical effects of body-diameter change included in Fig. 8 are based on evaluations of C_c for each combination of α with the body ratios 0.60, 0.64, and 0.655 from von Mises results for $\theta = 90$ deg, conversion of each C_c to the theoretical value of K by means of Equation [18], and calculating body factors as the ratio of theoretical K for either the 0.600 body or the 0.655 body to theoretical K for the 0.64 body ratio. The experimental values were obtained by ratio of individual test values of K, corrected for center-guide effect, to the corresponding values of K read from Fig. 5.

Tests

The curves in Figs. 3 and 5 were first prepared to determine the effects of viscosity for use in correcting data when an instrument calibration at one viscosity is available. Seventy-three tests were selected from the production files for fifty-four 600-mm scale-length instruments of the type commonly employed in measuring aircraft-engine fuel consumption in mass-rate units in ground test. The floats were of the "density-compensating" type, that is, constructed of a combination of metal and plastic to have a density of 1.54 grams per cc, so that the effect of fuel-density variations will tend to decrease the value of F through increased buoyancy as the value of ρ increases, leaving $\sqrt{F\rho}$ and hence the mass-rate of flow at any one viscosity constant within ± 0.25 per cent for any fuel density from 0.70 to 0.84. The values of α and of ρ_f were nominal and not based on individual inspection, since the original object of the calibrations was to provide flow-rate data for the scale of each instrument and not coefficient data. Values of flow rate were picked from curves through the original calibration data (about 25 test points on each calibration, showing point scatter of about 0.25 per cent) at the nominal location of each diameter ratio. Consequently, the errors in the values of C are small, but the errors in the values of α, and hence of K, may be quite large but presumably random. Hoping to keep average results as accurate as possible, corrections were made for the center-guide effect, but not for body diameter. Corrections also were made for the influence of calibrating fluid temperature on the float density. No correction for float head and tube expansion was made, as these floats were made with float heads of a 39 per cent nickel-iron alloy matching the expansion of the tapered glass tubes so that α is unaffected by temperature and the value of D_f and hence of flow, Equation [1], changed by only 0.018 per cent per 100 F.

The float edges were machined and inspected for freedom from visible roundness and burrs, but the analysis shows this to be in-

adequate, small instruments yielding, in general, somewhat higher coefficients than large as well as greater variations from float to float. The curves were not drawn to provide a minimum rms deviation for all data but rather to favor observed concentrations of data in the 1 to 2-in. sizes and then to follow downward to lower-size data at the lower values of N parallel to rather than through the $^{3}/_{4}$ and $^{1}/_{2}$-in. trends. It was believed that this procedure more nearly would represent the effects of viscosity and also would yield absolute coefficients which could be approached in the future as improvements in edge sharpness in smaller sizes were incorporated into the production procedures.

The data for these instruments at nominal diameter ratios from 1.08 to 1.35 are available from Fischer & Porter Company, Hatboro, Pa. (reference 7).

The 1.04-diam-ratio line was based on the average of calibrations of some 200 production instruments of 5-in. scale length industrial flowmeter design. Again, the absence of inspection dimensions gave rise to point scatter of over ±10 per cent, or approximately "±0.7 per cent of scale length," but when arranged in order of N, averaged in groups of 30, and plotted against N values determined by taking the reciprocal of the average of the individual reciprocals of N, these average points scattered only about ±1 per cent about the 1.04 line as drawn. Since these float edges were of excellently controlled sharpness, lapped, and then air-flow checked for uniformity at $\alpha = 1.03$, it is believed that the 1.04 line is valid. The 1.06, 1.10, and 1.4 lines were determined by cross-plotting K against α at each of 11 values of N.

It is through a study of these data that a conservative statement of tolerance of about ±1 per cent of maximum flow for unlapped float heads and nominal float and tube dimensions is arrived at.

To determine the effects of float-body diameter, a 1-in. meter with all-metal float, employing a single lapped float head with each of two float bodies at body ratios of 0.600 and 0.655, was tested in June, 1953. Every precaution was taken to determine tube and float dimensions precisely. Absolute values of K were calculated from the average of two liquid mass and time determinations for each test point, and corrected for center-guide effect and for thermal expansion. The test points for body factor, Fig. 8, were obtained as the ratio of each experimental value of K to the corresponding value in Fig. 5. The tolerance estimate of ±0.6 per cent for uncalibrated meters with lapped floats and adequate mechanical inspection was based on these tests.

Fluid mass-rate determinations were made by means of vertical standpipes ranging from 3 to 30 in. diam with pressure taps at the bottom connected to well-type mercury manometers with tungsten contacts extending through the tube wall and bent downward at the center to make contact with the rising mercury meniscus at a point where the meniscus is not distorted by local glass deformation at the contact seals. This equipment is standard at the author's laboratory and comparisons with laboratory calibrations of rotameters at aircraft companies and at the National Bureau of Standards lead to the belief that mass values are accurate within 0.05 per cent. Time is determined through electronic relays between the mercury contacts and the clutches of electric clocks. Clock motors are operated by crystal-controlled-frequency power sources checked periodically against WWV time signals. Over-all point scatter including routine overlap tests between different contact intervals and different standpipes at the same indicated flow rarely exceeds ±0.25 per cent.

The experimental values of contraction coefficient shown in Fig. 7 were obtained as follows: For $\theta = 90$ deg, values of K were picked from Fig. 5 at $N = 100,000$. For $\theta = 30$ deg, values of K were obtained from the data in the "Variable Area Meter Handbook," published by the author's company for industrial metering

purposes. For $\theta = 0$ deg, a special 2-in. aluminum float was constructed and calibrated with water in May, 1953. Values of K were picked from a point-to-point curve through these data. These values of K were converted to C_c by means of Equation [19]. It is believed that these comparisons, Fig. 7, demonstrate the validity of the theoretical equations derived herein and the applicability of two-dimensional coefficients to the annular-flow passages of rotameters using tubes of circular section to arrive at estimates of the limits to be approached as N increases indefinitely.

CONCLUSIONS AND RECOMMENDATIONS

The float-type variable-area flowmeter fills a definite need in the measurement of flow in 2-in. pipes and smaller and at low Reynolds numbers in larger pipe sizes as well. Its cost may be prohibitive in pipe sizes above 4 in. unless accurate measurement over a high-range ratio is required or unless normal piping layouts fail to provide the long runs of installation piping required for otherwise less costly primary elements such as concentric orifices.

An adequate theory for estimating performance of a wide variety of float shapes has been made available, and correlations which show promise of eliminating the need for costly calibrations in test work are available. These correlations are already in use in the general application of industrial instruments, but further test work with controlled float-edge sharpness and careful mechanical inspection, preferably by independent laboratories, is required before a tolerance for the uncalibrated test-type instrument can be stated with confidence. Whether this tolerance and the inspection costs necessary to achieve it can compare favorably with the tolerance and cost of individual calibration of test-type instruments remains to be seen.

Experimental work with other float shapes should continue. It is expected that an angle θ somewhere between 30 and 90 deg may yield coefficients which are independent of N at medium and high N values.

Considerable theoretical and experimental information in the viscous flow region also is available. Spherical floats in tapered tubes and cylindrical floats extending upward through a sudden enlargement in cylindrical tubes have shown the most promise of standardization and this study should continue and be made available for general application.

* THEORETICAL
* .655 BODY RATIO, N = 40,200
▲ .655 BODY RATIO, N = 2,950
× .600 BODY RATIO, N = 40,500
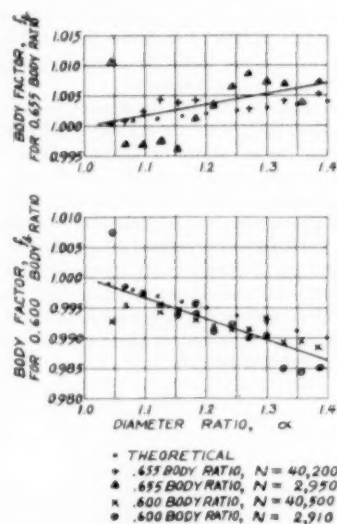● .600 BODY RATIO, N = 2,910

FIG. 8   EFFECTS OF FLOAT-BODY RATIO

As indicated in the text, further work on gas-flow measurement to establish expansion factors for various absolute pressure taps is required and is under way.

ACKNOWLEDGMENT

The author is indebted to the ASME Research Committee on Fluid Meters, whose interest made this presentation possible. Thanks are due to the Fischer & Porter Company for making laboratory facilities and personnel available for many of the special projects described. The guidance of Prof. A. L. Jorissen of Cornell University, in the choice of terminology and nomenclature, and of Mr. Daniel Evans of Fischer & Porter Company, for assistance in interpreting the mathematics of von Mises' equations, is also gratefully acknowledged.

BIBLIOGRAPHY

1 "Elimination of Viscosity as a Factor in Determining Rotameter Calibration," by K. Fischer, S. Blechman, and E. Lipstein, Trans. AIChE, vol. 36, 1940, pp. 857–869.
2 "Fluid Meters—Their Theory and Application," ASME Research Publication, fourth edition, 1937, pp. 71–74, 82.
3 "A Shear Criterion for Hydraulic Behavior of Paper Stocks in Pumps, Pipes, Valves, and Flowmeters," by V. P. Head, *Tappi*, vol. 35, 1952, pp. 260–266.
4 "On the Evaluation of the Accuracy of the Coefficient of Discharge in the Basic Flow Measurement Equation," by A. L. Jorissen, Trans. ASME, vol. 75, 1953, pp. 1323–1326.
5 "The Flow Mechanism and Performance of the Rotameter," by E. M. Schoenborn, Jr., and A. P. Colburn, Trans. AIChE, vol. 35, 1939, pp. 359–381.
6 "Berechnung von Ausfluss- und Überfallzahlen," by R. von Mises, *Zeitschrift des Vereines deutscher Ingenieure*, vol. 61, 1917, pp. 447–452, 469–474, and 493–498.
7 "Square-Edged Float Data," Fischer & Porter Research Report FX1-116, January, 1954.

Appendix

TWO-DIMENSIONAL CONTRACTION COEFFICIENTS

Von Mises' procedure for evaluating the contraction coefficients may be reduced to the following steps in which jet-velocity ratio and restricted values of the angle θ are assumed, and the contraction coefficient C_c and approach area ratio a_2/a_1 are calculated:

Step 1: Assume any value of velocity ratio ϵ between zero and unity

$$\epsilon = \frac{V_1}{V_j}$$

Step 2: Assume any angle θ, Fig. 6, which lies between 0 and 180 deg such that it is a rational fraction, y/x, of 90 deg, and such that the numerator y is odd and as small as possible

$$\theta = \frac{y}{x}\,(90\ \mathrm{deg})$$

Step 3: Calculate z

$$z = \text{the } y\text{th root of } \epsilon$$

Step 4: Evaluate θ_n, A_n, B_n for each successive value of n from $n = 1$ to $n = x$

$$\theta_n = \frac{2n-1}{y}\,\theta$$

$$A_n = 2\log_e(1 - \cos\theta_n) - \left(\epsilon + \frac{1}{\epsilon}\right)\log_e(1 - 2z\cos\theta_n + z^2)$$

$$B_n = 2\left(\frac{1}{\epsilon} - \epsilon\right)\arctan\frac{z\sin\theta_n}{1 - z\cos\theta_n}$$

NOTE: Arc tan is here expressed in radians.
Step 5: Calculate the contraction coefficient, C_c

$$C_c = \frac{1}{1 + \dfrac{\sin\theta}{\pi}\sum_{n=1}^{n=x}[A_n\cos(y\theta_n) + B_n\sin(y\theta_n)]}$$

Step 6: Calculate the corresponding area ratio, a_2/a_1, Fig. 6

$$\frac{a_2}{a_1} = \frac{\epsilon}{C_c}$$

Thus direct solution of C_c for arbitrarily specified values of θ and a_2/a_1 is impossible, but by investigating a sufficient number of jet-velocity ratios ϵ, for any one angle θ, curves may be prepared from which C_c may be read for any a_2/a_1 from 0 to 1.

Discussion

A. L. JORISSEN.[3] The contribution to the problem of flow measurement made by the author is both useful and timely. It has been felt for some time that the work done on float-type variable-area meters had now reached such stature that they should be recognized as suitable instruments for the measurement of discharge both in the case of low Reynolds numbers and in the case of pipe lines of small sizes.

The author should be congratulated for the excellence of his work in analyzing a wealth of experimental information and in formulating the rules which will lead to the establishment of an adequate theory for the instrument.

The following discussion is submitted to clarify some of the points raised in the paper:

The writer fails to see the relative significance of the parameter **R** (Equation [3]), defined as "identical to pipe Reynolds number for pipes having diameter equal to float diameter, D_f." This may be a useful "working parameter" but the Reynolds number for the flow through the annulus between tube and float

$$\text{Reynolds number} = \frac{4}{\pi}\,\frac{C}{\alpha + 1}\,N$$

should be of greater physical significance in the evaluation of the balance between inertia and viscous forces in the critical section and, therefore, in the appraisal of the characteristics of the flow.

More specific information is needed on the magnitude of the expansion factor Y and its dependency on α, N, and E (Equation [4] of the paper).

The attempt to compute the meter coefficient K (or C) from a value of the coefficient of contraction C_c as derived from a comparison with a two-dimensional orifice (slot) seems futile to the writer for the following reasons:

(a) In writing Bernoulli's Equation [13] neither potential heads, nor pressure losses, nor kinetic-energy correction factors were taken into consideration.

(b) More important, the three-dimensional problem cannot be solved by comparison with the simpler two-dimensional case. Despite the favorable condition of axial symmetry, it appears that the three-dimensional case would be difficult to solve by an analytical method.

[3] Professor of Civil Engineering, Head, Department of Hydraulics and Hydraulic Engineering, Cornell University, Ithaca, N. Y.   Mem. ASME.

A more practical approach would be the experimental determination of the coefficient of drag for a float-shaped body in a tapered conduit. The writer strongly recommends that a research program be undertaken in which direct measurements of drag would be made and correlated with the flow characteristics.

The writer has had the opportunity to test a number of float-type variable-area flowmeters in the Hydraulic Laboratory at Cornell University. The floats used in these meters were not geometrically similar to that represented in Fig. 4 of the paper, the body length being only 1.5 times the float diameter D_f. In a first series of experiments, five meters manufactured by the Fischer and Porter Company and of the type used in their aviation test flowrator meter were calibrated. The main dimensions of these tubes are given in Table 1 of this discussion.

TABLE 1   DIMENSIONS OF TUBES TESTED

Tube number[a]	Serial number	Pipe nominal diam, in.	D_f, in.
4-35-600	T12-1510₁	¹/₂	0.4944
5-35-600	T12-1510₂	³/₄	0.7862
6-35-600	T12-1510₃	³/₄	0.9749
8-35-600	T12-1510₄	1¹/₄	1.4613
9-35-600	V2-1162₁	1¹/₂	1.9616

[a] The first figure gives the meter size, the second number indicates the tube taper (from $\alpha = 1.04$ to $\alpha = 1.39$) and the last number the scale length in millimeters.

These meters were installed in a water line supplied by a small constant-head tank under a head of 16 ft. A straight length of approach pipe 8 ft long was maintained upstream of the meter. The rate of discharge was measured by weighing.

Discharge coefficients C computed by Equation [1] of the paper were compared with data supplied by the manufacturer. It is believed that these data are substantially identical to those used in Fig. 3. A typical comparison is indicated in Fig. 9, herewith.

FIG. 9   COMPARISON BETWEEN EXPERIMENTAL COEFFICIENT AND MANUFACTURER'S DATA FOR VARIABLE-AREA FLOWMETERS—SERIES 35-600
(Fischer and Porter meter No. T12—1510/2, size 5.)

The correction for center guide diameter f_g was applied but that for body ratio f_b was not available at the time the meters were tested (body ratio = 0.62). Application of this correction would reduce the deviations at large values of α.

For one meter (T12—1510/3, size 6) the deviations were unusually large at small values of α (Fig. 10 of the discussion). The same trend was observed later for two meters of size 8

(V3—1302/1 and V3—1302/2) (Fig. 11).

Observation of the float surface and comparison with results

FIG. 10   COMPARISON BETWEEN EXPERIMENTAL COEFFICIENT AND MANUFACTURER'S DATA FOR VARIABLE-AREA FLOWMETERS—SERIES 35-600
(Fischer and Porter meter No. T12—1510/3, size 6.)

FIG. 11   COMPARISON BETWEEN EXPERIMENTAL COEFFICIENT AND MANUFACTURER'S DATA FOR VARIABLE-AREA FLOWMETERS—SERIES 35-600
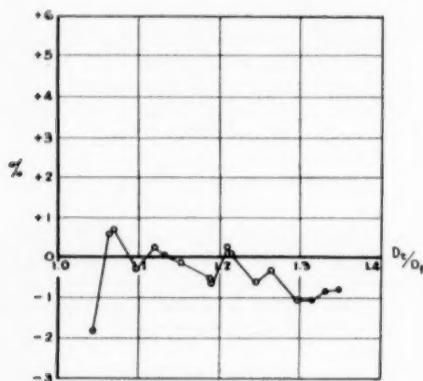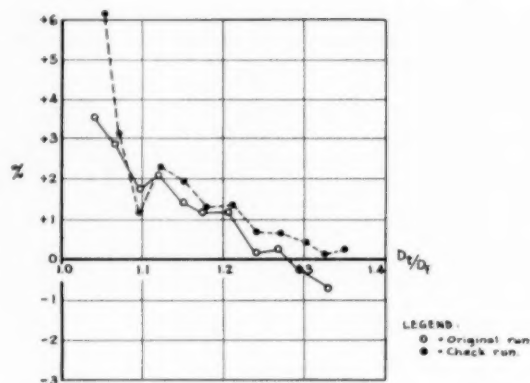(Fischer and Porter meters Nos. T12—1510/4; V3—1302/1; V3—1302/2, size 8.)
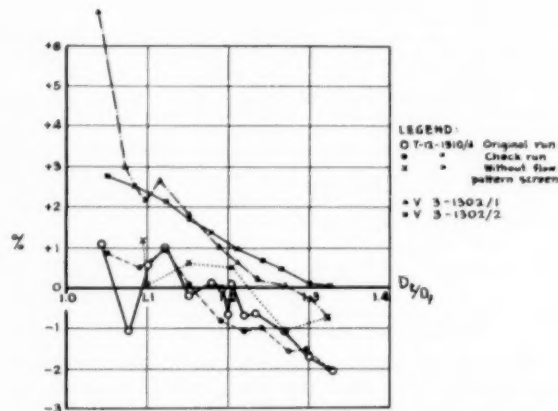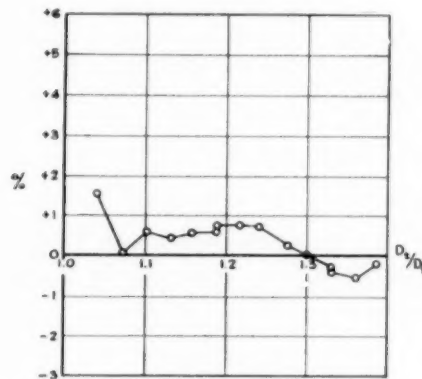

FIG. 12   COMPARISON BETWEEN EXPERIMENTAL COEFFICIENT AND MANUFACTURER'S DATA FOR VARIABLE-AREA FLOWMETERS—SERIES 35-600
(Fischer and Porter meter No. T12—1510/2, size 5, with float SVP 559.)

obtained elsewhere led to the belief that the large deviations might be due to a lack of flatness of the upstream surface of the float head. A new series of floats, one per tube size, having body ratios equal to 0.640 and lapped heads, was then tested in the same tubes with definitely better results. The experimental results were compared with the data from Fig. 5 of the paper. Typical results are shown in Fig. 12, herewith. Computed tolerances, however, are all larger than the figure of 0.6 per cent given in the paper. A conservative value would be 1.5 per cent (for $1.06 < \alpha < 1.4$). It remains for subsequent experiments to show whether or not this larger tolerance is required because of the difference in body length.

In the course of the first series of tests some experiments were made to study the effect of upstream conditions. The results, summarized in Table 2, indicate that, when extreme accuracy is not required, the float-type variable-area flowmeter is remarkably insensitive to upstream disturbances.

TABLE 2 EFFECT OF UPSTREAM CONDITIONS
Meter 8-35-600 No. T12—1510/4

	D_t/D_f	N	C experimental	C from T-1889	Difference %	Observations
Upstream pipe straight	1.381	27460	0.8310	–	–	Flow pattern-screen removed.
	1.323	27940	0.6724	0.6776	– 0.77	" " " "
	1.269	27940	0.5365	0.5424	– 1.09	" " " "
	1.205	27940	0.3881	0.3863	+ 0.46	" " " "
	1.151	27940	0.2719	0.2703	+ 0.59	" " " "
	1.102	28960	0.1748	0.1748	0	" " " "
	1.092	27940	0.1583	0.1563	+ 1.15	" " " "
	1.373	29460	0.8020	–	–	Flow pattern screen in place. Valve open.
	1.368	28960	0.7874	–	–	" " " "
Upstream pipe with 2 elbows and a valve	1.327	29460	0.6756	0.6877	– 1.76( )	" " " "
	1.277	29460	0.5504	0.5582	– 1.40	" " " "
	1.203	29460	0.3793	0.3812	–00.50	" " " "
	1.135	29460	0.2392	0.2379	+ 0.55	" " " "
	1.074	29460	0.1250	0.1242	+ 0.64	" " " "
	1.366	28960	0.7815	–	–	Valve 3/4 open.
	1.355	28960	0.7522	–	–	" " ½ "
	1.224	28960	0.4062	0.4070	– 0.20	" " ¼ "
Upstream pipe with 2 elbows	1.350	29460	0.7432	0.7493	– 0.81	Flow pattern screen removed. Valve open.
	1.348	29460	0.7384	0.7441	– 0.77	" " Valve 3/4 open.
	1.335	29460	0.7073	0.7091	– 0.25	" " " " ½
	1.332	29460	0.6975	0.7011	– 0.51	" " " "
	1.189	29960	0.3556	0.3504	+ 1.48	" " " " ¼
	1.172	29460	0.3179	0.3139	+ 1.27	" " " "
	1.098	29960	0.1690	0.1674	+ 0.96	" " " " 1/6

AUTHOR'S CLOSURE

Dr. Howard Bean's verbal discussion of his experience showing the long life of rotameter calibrations is appreciated. In the author's experience, errors of a fraction of a per cent in secondary mass and time standards have frequently been tracked down through apparent failure of a rotameter to repeat.

Professor Jorissen's questions are interesting and his laboratory findings have advanced this project immeasurably.' First, we will try to answer the questions raised. Certain combinations of the parameters of Equation [11] may be found convenient for specific purposes but we cannot reduce the number of parameters thereby. The similarity between **R** and pipe Reynolds number was intended as a useful observation rather than a definition. The annulus Reynolds number is of academic interest in comparing the performance of floats of given shape with other devices which are similar. For example, it was found that

the "contraction coefficients" of long-radius nozzles published by Ohio State University, calculated by means of Equation [20], were almost identical to those of the float having $\theta = 0$, Fig. 6, when nozzle throat Reynolds number was equal to the annulus Reynolds number $R/(\alpha + 1)$, for like ratios of approach to throat area. It is not necessary to burden routine calculations with such parameters, however. Interest in the expansion factor Y has led to a program of theoretical and experimental research and results will be available soon.

If potential heads are included in Equation [13] it will be necessary to include the weight of liquid between sections 0 and j in Equation [12]. When combined to eliminate $P_0 - P_j$, these effects cancel and Equation [15] will stand. Pressure losses and kinetic-energy corrections associated with various velocity distributions are both functions of N and are, therefore, covered by the functional statement, Equation [11]. The author has made a study of friction losses to be expected between float body and tube at various values of the tube half-angle φ and the results have provided a fifth-power equation in L/D_f and φ for any named droop in flow coefficient at specified α and N. As a result, the maximum body length, given as $8 D_f$ in Fig. 4, is better expressed as in Equation [26] below.

Perhaps some day mathematicians can set up three-dimensional equations and electronic-computer time can be spared to solve them. In the meantime von Mises has provided results which appear excellent as a first approximation, as shown in Fig. 7. Annular-flow passages are inherently more similar to two-dimensional than are circular passages. As α approaches unity, this similarity approaches identity. Such similarity is not approached at either extreme of β in concentric apertures.

The coefficient of drag may be readily evaluated from any flow coefficient data. It will be simply $1/C^2$ times a function of α which will depend on the defining velocity. It is not likely that any other experimental evaluation of drag can compare in accuracy with the measurement of float weight on a good laboratory balance.

The Cornell University tests under Professor Jorissen's supervision have rendered Fig. 5 and all tolerance statements associated with it obsolete. The necessity for flatness of the lower surface of the float head is undeniable. A series of 48 additional full-scale experimental calibrations have been conducted at Hatboro between October, 1953, and March, 1954. Six body lengths ranging from zero to 6 D_f were tested at eight viscosities, covering a span from $N = 300$ to $N = 200,000$ and from $\alpha = 1.04$ to $\alpha = 1.39$. It was necessary to eliminate tests at N less than 3000, and tests of the longest body, because of the effects of viscosity between body and tube. Tests with zero-body length were also eliminated, giving much lower coefficients as predicted by von Mises' results.

The remaining results, including 32 values of N and 416 individual mass and time determinations, were retained for correlation. The seven tests of the second Cornell series were also recalculated with thermal corrections, corrections for atmospheric buoyancy on the weighed water, and using revaluated float diameters by the optical method for the three smaller sizes, providing seven additional values of N and 98 individual mass and time determinations. These 514 test points have been appended in reference (7) for distribution to the ASME Fluid Meters Research Committee. They are correlated by the solid lines of Fig. 13. The tolerance calculated as twice the standard deviation of these test points has been found to be ±0.94 per cent for α greater than 1.06. In some of the tests the radius at the bottom of the body was increased from 0.15 D_f to $L/8$ with definite reduction in scatter at high values of α. Recommended body lengths, L, are as follows, for tube taper half-angle, φ, expressed in degrees and ranging from zero to 1.2 degrees
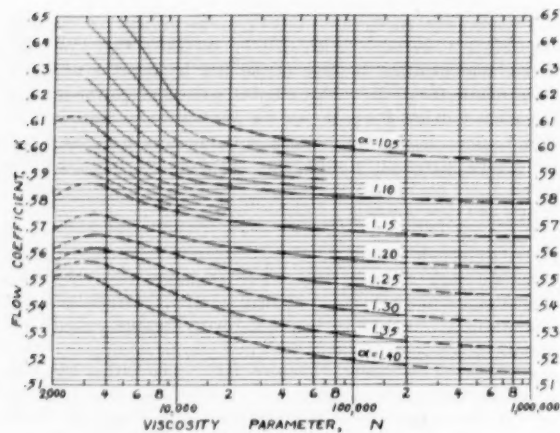
Fig. 13   Flow Coefficients for $1/2$ to 2 in. Rotameters With Square-Edged Floats Lapped and Optically Measured, Having 0.64 Body Ratio and Body Length Per Equation [26]

$$0.75 < L/D_f < (10 - 6\sqrt{\varphi}) \dotfill [26]$$

All float body diameters were 0.64 D_f.

The dashed lines from $N = 200,000$ to $N = 1,000,000$ were extrapolated by plotting K versus $1/\sqrt{N}$, which gave straight lines from $N = 9000$ up. Plots of K versus $1/N$ gave equally good straight lines above $N = 20,000$ and gave extrapolated results at 1,000,000 about 0.1 per cent lower than shown. Above 1,000,000, these alternate abscissas gave diverging results, with over one per cent difference at $N = $ infinity, so extrapolation beyond 1,000,000 is hardly justified.

Professor Jorissen's findings concerning installation effects are particularly encouraging. However, if it should prove that installation influences become more critical as Reynolds number at the approach increases, as seems to be the case for concentric fixed-area devices, some precautions may be required relative to upstream installation before this extrapolated region can be verified.

The contribution by Professor Jorissen and the Cornell Hydraulics Laboratory has been invaluable, and should certainly serve to high light the importance of independent work in several laboratories before confidence in results can be established.

Small Nozzles and Low Values of Diameter Ratio

By H. S. BEAN,[1] R. M. JOHNSON,[2] AND T. R. BLAKESLEE[3]

In 1943 the National Bureau of Standards calibrated ten sets of nozzles for the Heat Exchange Institute, using adapters originally intended for open-inlet or discharge conditions, in a modified arrangement for in-line measurements. These calibrations were made with air. Since then, new adapters have been prepared to facilitate using them in the "in-line" manner. Two sets of the nozzles have been recalibrated using these new adapters and a weighed-water procedure. The results of these new calibrations are presented and a comparison made with the earlier results. For most of the nozzles, the agreement between the original air calibrations and the recent water calibrations is well within the range of experimental uncertainties.

INTRODUCTION

THE commercial use of small flow nozzles for the measurement of fluid flow has been associated closely with the steam-jet ejector and related industries. In 1943 the Heat Exchange Institute (HEI) developed designs and established a system of manufacture for a set of ten nozzles ranging from $1/16$ to 1 in. diam. Twenty-four complete sets of these nozzles were produced by a skilled instrument maker. Ten sets were calibrated on air by the National Bureau of Standards (1, 2).[4]

Although these calibrations were made primarily to establish discharge coefficients for air at critical-flow conditions, a considerable proportion of the test work was arranged to cover a wide range of Reynolds numbers. The coefficients obtained were appreciably higher than expected, based on previous work with larger nozzles and there was an unusual degree of uniformity among nozzles of the same size. This experience demonstrated that the small flow nozzle, when properly manufactured and applied, could be a reliable instrument for measuring the flow of fluids.

Recognizing a growing interest in this flow-nozzle development, HEI, in 1951, sponsored additional testing, using weighed-water measurements, to confirm the original work and to extend the usefulness of the small nozzle by a better design and location of pressure taps than were used originally.

The original calibrations were made using adapter fittings, designed for testing ejectors by the critical-flow method, which are

not generally suitable where gas flow is to be measured in a closed system. Due to these adapters the downstream pressure-tap location was slightly different from that recommended by the ASME (3, 4). For the new series of tests, this situation was corrected by the design of adapters suitable for pipe-flange mounting which included both positions for the downstream pressure taps.

The results of the 1951–1952 tests with weighed water, covering twenty-two nozzles, are presented in this paper. Comparisons are made with other available data and the pressure-tap situation is resolved. The instrumentation and test procedure have been described in considerable detail in anticipation of probable routine calibration requirements where small nozzles are used in code tests.

DESCRIPTION OF NOZZLES AND PRESSURE TAPS

The HEI nozzles were designed to conform, as closely as possible, with the shape and proportions proposed by the ASME Fluid Meters Research Committee (4, 5). The throat contour is the familiar ellipse, commonly referred to as the long-radius flow nozzle. The dimensions for the throat were computed from data published in the Power Test Codes, Supplement on Instruments and Apparatus.[5]

However, there are some features of the nozzle design, as a whole, which unavoidably deviate from the geometry of an ideal nozzle. The exterior contour of a small nozzle cannot conform exactly to the proportions just referred to because of the practical requirements for metal thickness. When nozzles are used for critical-flow metering, the stresses become a factor of importance and metal thickness must be substantial to avoid distortion. The
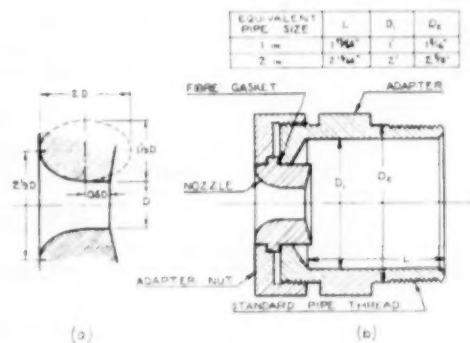

FIG. 1 HEI NOZZLE AND CRITICAL-FLOW ADAPTER
[(a) Proportions of the nozzles; (b) adapter for critical flow with atmospheric inlet.]

thick, sturdy design used for the HEI nozzles meets this requirement. It is illustrated by the sectional view in Fig. 1.

As stated previously, a complete set contains ten nozzles rang-

[5] I & A, part 5, chapter 4 (1949).

TABLE 1 HEI NOZZLES; DIAMETERS AS DETERMINED ON OPTICAL COMPARATOR

Nom. diam, in.	Mean of go and no-go gages	"Actual" diameter, in.		
		Set 3	Set 15	Set 16
1.000	1.0003	1.0007	1.0007	1.0011
0.750	0.7502	0.7499	0.7505	0.7504
0.500	0.5003	0.5005	0.5003	0.4998
0.375	0.3752	0.3752	0.3748	0.3750
0.313	0.3132	0.3134	0.3136	0.3131
0.250	0.2502	0.2503	0.2499	0.2498
0.188	0.1881	0.1882	0.1879	0.1879
0.125	0.1251	0.1253	0.1249	0.1249
0.094	0.0941	0.0942	0.0941	0.0941
0.063	0.0631	0.0633	0.0650	0.0631

ing in size from $^1/_{16}$ to 1 in. diam. It should be remembered that these nozzles originally were intended for use in ejector testing and the sizes were selected to provide capacity adjustment, with critical flow, of about 5 lb per hr when metering atmospheric air. The sequence of individual nozzle capacity is not of the 5-lb increment but when used in combinations, the nozzles provide this adjustment throughout the range of ejector capacity.

All the nozzles are made of stainless steel except for the $^3/_4$ and 1-in. sizes which are Tobin bronze. Nozzles of the same nominal diameter are duplicated accurately in respect to dimension, contour, and surface finish (1) (see Table 1 for dimensions). The excellent surface finish is believed to have contributed to the high values of discharge coefficients obtained.

The original adapter fittings were not well-suited for use with subcritical flow as they did not provide for downstream pressure taps. For the new tests, three adapters were designed for pipe-flange mounting. These adapters accommodate the ten nozzles in meter runs of standard weight pipe with a maximum diameter ratio of 0.25. The nominal pipe sizes for the meter runs are 1, 2, and 4 in.

Detail dimensions of the three meter runs, the arrangement of the adapters, and the location of the pressure taps are shown in Figs. 3, 4, and 5. Two systems were followed in locating the pressure taps. First, to conform with a widely used ASME practice, pressure-measuring stations were located one pipe diameter upstream and one-half pipe diameter downstream. Both positions are measured from the upstream face of the nozzle. A second downstream station was located to duplicate the positions used by the National Bureau of Standards for the tests made in 1943, on nozzle set No. 3. This provision was made in order to correlate the earlier tests on air with the new tests on weighed water. For convenience, the two systems of pressure taps are referred to herein as ASME and HEI, respectively.

All pressure-measuring stations were provided with duplicate taps in the same plane spaced 90 deg circumferentially. In this manner, two independent readings of differential pressure could be obtained for each of the pressure-tap systems mentioned.

Special care was observed in making the pressure-tap holes (6). For the 4-in. and 2-in. pipes, the holes were finished with a $^1/_8$-in. drill. A No. 46 drill (0.081 in.) was used for the pressure holes on the 1-in. pipe. Internal burrs were removed carefully and the holes checked for location. Connections to holes in pipe walls were made by using $^1/_c$-in. pipe couplings welded to the pipe before drilling.

The pipes used for the meter runs were smooth and straight in the region of the pressure taps. The pipe lengths exceeded the minimum requirements[5] and the measured dimensions appear in Figs. 3, 4, and 5. Straightening vanes were used as indicated in the 1 and 2-in. pipes but inadvertently were omitted from the 4-in. pipe. Care was taken to maintain a fixed gasket thickness and the inside edges of the gaskets were ground flush with the pipe wall. The 1 and 2-in. meter runs being made of brass had to be bored with a light finishing cut to match the adapter fittings which had been made to handbook dimensions.
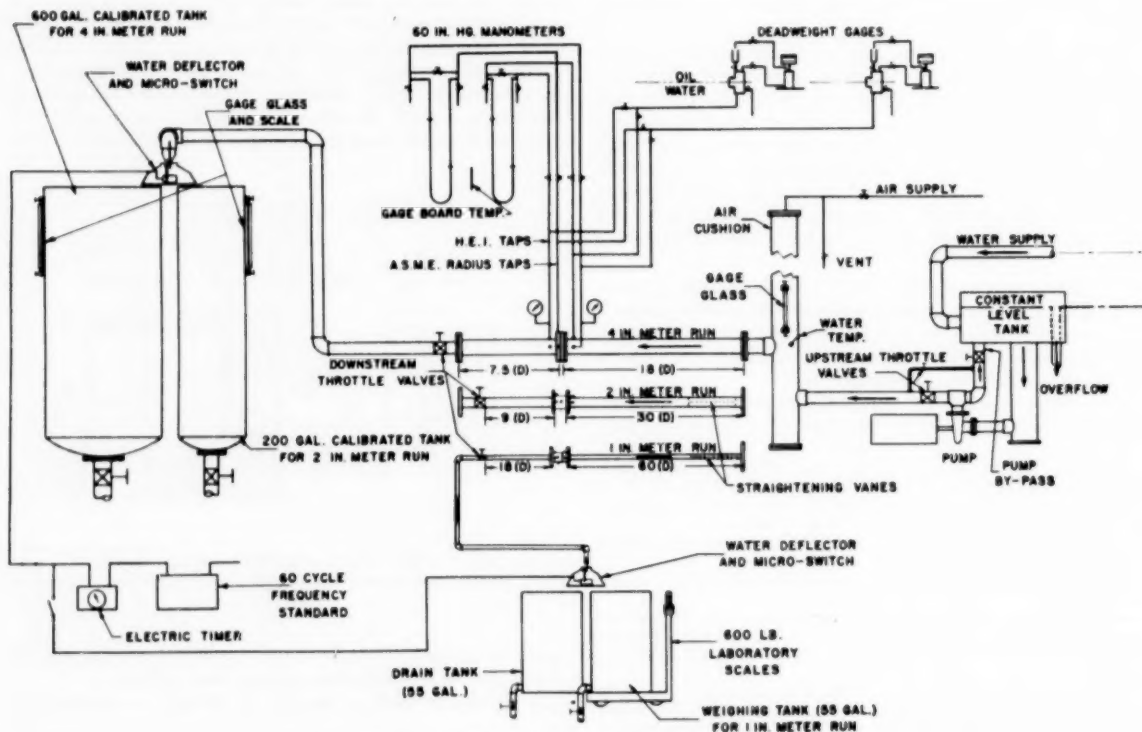

FIG. 2 SCHEMATIC DIAGRAM OF NOZZLE CALIBRATION APPARATUS

APPARATUS AND TEST ARRANGEMENT

The general arrangement of the test apparatus is indicated in the schematic diagram, Fig. 2. The water was supplied from the plant spray-pond cooling system and was reasonably clean. A steady pressure was maintained in the metering system by a single-stage centrifugal pump supplied from a constant-level tank. The piping system contains throttle valves for control of flow and pressure and an arrangement for by-passing part of the pump capacity when necessary. An air chamber, made from a length of 8-in. pipe, is provided between the pump and the meter run.

Three tank systems, of graduated capacity, were used for measuring the quantity of water discharged with the selection depending on the range of flow rates expected. For the 1-in. meter run, an open-ended, 55-gal drum was used on a laboratory scale of 600 lb capacity equipped with agate bearings. These scales were calibrated with standard test weights and could be read to the $1/4$ oz. The 2-in. and 4-in. meter runs discharged into adjacent volumetric tanks of 200 and 600 gal capacity, respectively. Near the top of each tank a 30-in. gage glass and scale were mounted. The brass scales on these tanks were graduated at 0.05-in. intervals and readings were estimated to 0.01 in. The tanks were calibrated with water weighed on the 600-lb scales. The volumetric tank readings were converted to weight units by using the specific weight of water and the existing water temperature.

Each of the three measuring systems was equipped with a flipper spout arranged so that the water flow could be diverted from the drain into the tank without disturbing the flow rate. The flipper spout was connected mechanically to a microswitch which controlled the timing circuit.

Time intervals were measured with an electric stop clock (Type S-6, Standard Electric Time Company). Electric power for the timing circuit was provided by a 60-cycle, crystal-operated frequency standard. This oscillator was checked for accuracy against time signals broadcast by the National Bureau of Standards. Time intervals could be read directly to the 0.001 min and estimated to the fourth decimal.

The differential pressure across the nozzle was determined by one of two methods selected according to the pressure range. For flow rates such that the differential pressure did not exceed 60 in. of mercury under water, a mercury U-tube manometer of $5/8$-in-OD glass tubing was used. This manometer was equipped with a brass scale accurately graduated to 0.05 in. When the differential pressure exceeded the range of the manometers, two dead-weight gages were used.

Fig. 2 shows the tubing connections used for both methods of pressure measurement. The pressure system for the dead-weight gages included an oil reservoir equipped with a sight glass for observance of the oil-water separation. These dead-weight gages could be read to the nearest 0.1 psi.

In selecting the instruments, an effort was made to maintain an over-all accuracy of 0.2 per cent. Except for the effects of pulsation, it is believed that this accuracy was achieved.

The problems of pulsation control and its probable effect on the over-all accuracy of the discharge coefficients are discussed later.

TEST PROCEDURE

Before installing a nozzle in the meter run, it was carefully cleaned with a soft cloth. No abrasive cleaners were used. Oil and greases were removed with a solvent. The cleaning operation was repeated at frequent intervals during the test. The gaskets were inspected for proper fit and thickness and were not permitted to protrude into the flow stream. After the nozzle was in place with instruments connected and flow established, the gage lines were purged of air. The purging operation was repeated at frequent intervals throughout the test.
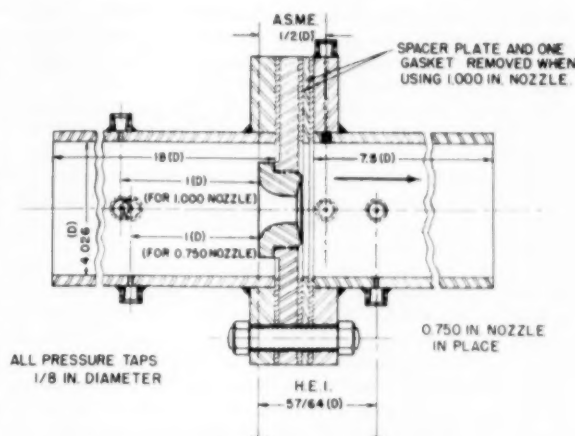
FIG. 3   FOUR-INCH METER RUN WITH NOZZLE HOLDER AND PRESSURE-TAP LOCATIONS
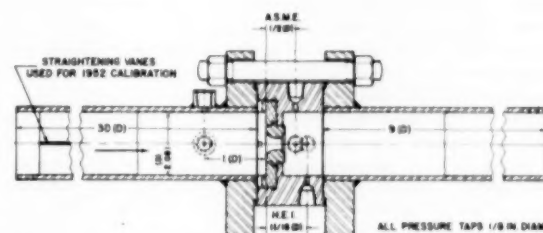
FIG. 4   TWO-INCH METER RUN WITH NOZZLE HOLDER AND PRESSURE-TAP LOCATIONS
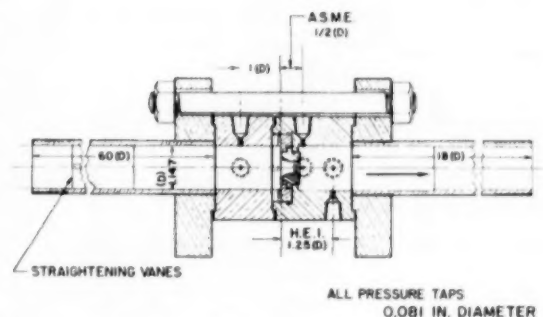
FIG. 5   ONE-INCH METER RUN WITH NOZZLE HOLDER AND PRESSURE TAP LOCATIONS

The throat diameters of the nozzles used were checked on an optical comparator. This instrument has a magnification of 30 diam and can be read easily to 0.0001 in. The average value of four readings on each of two diameters at 90 deg was used as the correct value. The measured values of nozzle diameter are listed and compared with the mean plug gage values in Table 1. All nozzles were round within 0.2 per cent except for three which deviated by 0.3 per cent.

Early in the test program several investigations were made which have a bearing on the test procedure adopted and on the final results.

Duplicate pressure taps were provided at each of the pressure-

measuring stations for the purpose of avoiding possible false readings. The pair of taps at each of the stations was investigated with a manometer connected across the taps and filled with alkazene. This liquid has a specific gravity of approximately 1.75 and shows a clean meniscus under water. This investigation was made for all three meter runs and the maximum differential between taps in the same plane was approximately 0.021 psi with a nozzle differential of 90 psi. This indicated a reliable duplication of all pressure taps and, indirectly, gave additional assurance of good flow conditions. It was not considered necessary to use more than one tap at each pressure station.

Although the magnitude of the pulsation noted in the differential manometers, as such, was normal, it was of sufficient magnitude to affect the accuracy of the work. Consequently, a careful investigation was made to locate and eliminate, where possible, the causes of pulsation. After much experimenting with the air cushion in the standpipe, it was evident that the centrifugal pump was not a factor in this matter. High-frequency vibrations produced by throttle valves located at various places in the system caused definite and pronounced effects on the amplitudes noted in the manometers. Best results were finally obtained by doing the major part of the throttling on the downstream side of the nozzle. In general, gate valves were very unsatisfactory. Plug valves proved to be the most reliable. In spite of the best efforts to prevent it, there was considerable oscillation at certain of the test points. In many cases the amplitude was reduced by merely resetting the point at a very slightly different flow rate.

After it was discovered that the 1-in. nozzles showed coefficients of discharge greater than unity at high values of Reynolds number, an investigation was made of downstream pressure-tap location. For this study, pressure taps were located at approximately $1/2$-inch intervals in the 4-in. meter run. Detailed dimensions of the tap locations are shown in Fig. 6. The results of this investigation are discussed in later paragraphs.
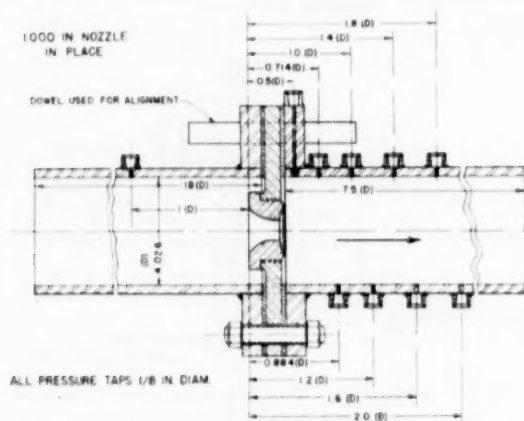

FIG. 6 FOUR-INCH METER RUN WITH DOWNSTREAM TAP LOCATIONS FOR STUDY OF EFFECT OF TAP LOCATION ON COEFFICIENT OF DISCHARGE

The essential observations recorded for each of the test points included the duration of the run, quantity of water, pressure differential, and water temperature. The minimum time interval, which occurred at the largest flow rates in the 4-in. meter run, was approximately 2.3 min. It was the general practice to set a point and record the observed values of pressures and temperatures at regular intervals during the time necessary to fill the measuring tank. When this procedure revealed any shift in the flow rate, the point was repeated.

The test work was performed by two investigators who worked independently at different periods. Check runs were used to eliminate the personal factor where nozzles of the same size did not check one another and where there was a question of the accuracy of the result.

Tests were made for twenty-two individual nozzles which comprised two complete sets with two additional nozzles from a third set. One of the complete sets tested, set No. 3, was calibrated on air by the National Bureau of Standards during the 1943 tests.

The Reynolds number was carried to the limit of available pressure at existing water temperatures and, in general, duplicated the range used in the Bureau of Standards tests. The nozzle-throat velocity varied between 10 and 115 fps with water temperatures ranging from 44 F to 87 F.

COMPUTATIONS

The following nomenclature is used in the equations of this section:

a = nozzle-throat area, sq in.
C = coefficient of discharge, dimensionless
D = internal diameter of pipe upstream of nozzle, in.
d = nozzle-throat diameter, in.
E = area multiplier for thermal expansion of the primary element (see reference 3)
K = flow coefficient, dimensionless
p = static pressure differential, psi
R_d = Reynolds number based on nozzle-throat diameter, dimensionless
V_2 = average velocity at nozzle throat, fps
w = flow rate, lb per sec
β = diameter ratio, d/D, dimensionless
γ = specific weight, pcf
μ = absolute viscosity, lb per ft sec

In determining the coefficient of discharge, the calculations were based on Equation [1][3]

$$w = 0.668 a \, KE \sqrt{\gamma \Delta p}, \text{ lb per sec} \dots \dots \dots [1]$$

Converting this equation to nozzle-throat diameter d, and discharge coefficient C, yields

$$w = 0.525 \frac{C d^2 E \sqrt{\gamma \Delta p}}{\sqrt{1 - \beta^4}}, \text{ lb per sec} \dots \dots \dots [2]$$

The water temperatures obtained during the calibration tests were such that it was impossible to note any value of the thermal-expansion multiplier E other than unity. With this value of E, Equation [2] may be solved for the coefficient of discharge as

$$C = \frac{w \sqrt{1 - \beta^4}}{0.525 d^2 \sqrt{\gamma \Delta p}} \dots \dots \dots \dots [3]$$

This is the equation which was used to calculate the coefficient of discharge from the observed data.

In order to calculate the Reynolds number, the classic form of the expression was altered by using the continuity equation so that Reynolds number could be determined more conveniently. Thus

$$R_d = \frac{\gamma V_2 d}{12 \mu} \dots \dots \dots \dots \dots [4]$$

and

$$w = \gamma a V_2 = \frac{\gamma \pi d^2 V_2}{576}, \text{ lb per sec} \dots \dots \dots [5]$$

TABLE 2   SAMPLE OF TEST DATA AND RESULTS

Set 3, nominal diameter = 0.313 in.
(Measured diameter = 0.3132 in., β = 0.1505)

R_d	HEI taps			ASME radius taps		Temp, deg F	Average throat velocity, V_t, fps
	C	Δp, psi		C	Δp, psi		
204280	0.9891	90.20		0.9886	90.39	47.7	114.482
182680	0.9881	71.80		0.9867	72.00	47.8	102.033
160860	0.9861	55.90		0.9853	56.00	47.8	89.847
138730	0.9836	41.70		0.9836	41.70	47.9	77.399
112610	0.9829	27.34		0.9824	27.37	48.1	62.633
98310	0.9812	20.86		0.9810	20.87	48.2	54.615
82450	0.9797	14.62		0.9791	14.64	48.4	45.662
64340	0.9759	8.72		0.9754	8.73	49.3	35.120
50810	0.9730	5.18		0.9710	5.20	51.0	26.971
35570	0.9666	2.64		0.9653	2.65	49.9	19.158

combine to give

$$R_d = \frac{48w}{\pi\mu d} \quad \dots \dots \dots \dots \dots \dots [6]$$

the expression used to determine the Reynolds number at the nozzle throat.

Values of the specific weight of water, absolute viscosity of water, and the multiplying factor used to convert manometer readings, water over mercury, to psi were obtained from data given in the Smithsonian Physical Tables, 7th Revised Edition.

CALIBRATION OF HEI NOZZLES WITH ASME RADIUS TAPS

The observed data and computed quantities recorded in the 1951–1952 tests were: Nozzle diameter, diameter ratio, the water temperature, the differential pressure for each set of pressure taps, the discharge coefficient for each set of pressure taps, Reynolds number at the nozzle throat, and the water velocity at the nozzle throat. Table 2 is a sample of these data and results for one nozzle.

The coefficients of discharge for the ten nozzles of set 16 are plotted as a function of Reynolds number in Fig. 7 on semilog co-ordinates. Smooth curves have been drawn through the test points with an average deviation of not more than ±0.001 for values of the coefficient. The curves are typical, size for size, of all the HEI nozzles.

Fig. 8 shows the agreement of the results obtained by two different observers on one of the nozzles. Unfortunately, the agreement was not as good as this with all of the nozzles, especially those of the smaller sizes. Also, for the ¹/₂-in. nozzles, the results by the two observers showed a noticeably different shape of curve.

An average curve of coefficient of discharge for the HEI nozzles is shown in Fig. 9. This average curve includes tests made on twenty-two different nozzles installed in 1, 2, and 4-in. pipes with diameter ratios ranging from 0.250 down to 0.055. It will be noted that there is a point spread of ±1.0 per cent from the average curve. This is the type of spread experienced in the Fluid Meters Research Program and is neither better nor worse than might be expected (4). It illustrates the pitfall of the usual handbook average coefficient which attempts to include too many variables.

In Fig. 10 the average (new) HEI curve is compared with data obtained from the Nozzle Research Program of the Fluid Meters Committee (4). These latter data are the correlated results for nozzles in 2 to 10-in. pipes at a diameter ratio of 0.20. This comparison seems to support the contention that has been expressed by others interested in this subject, namely, that pipe diameter as an independent variable is of little importance. The most striking feature of this comparison is in the high Reynolds number region where the HEI curve does not show a tendency to "flatten" off as does the ASME. No satisfactory explanation for this failure to flatten off has been found.

As further evidence that the discharge coefficient is nearly independent of pipe diameter, new average curves were drawn for
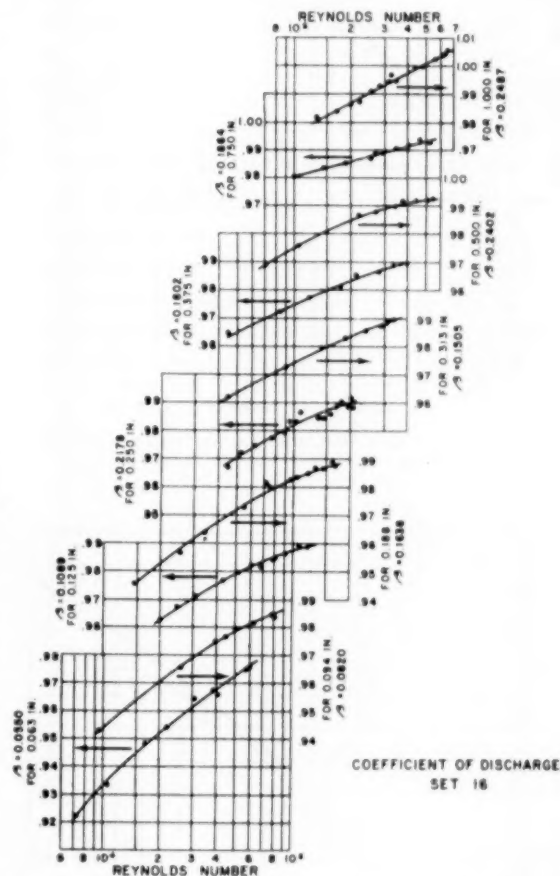
FIG. 7   COEFFICIENTS OF DISCHARGE FOR NOZZLES OF SET 16
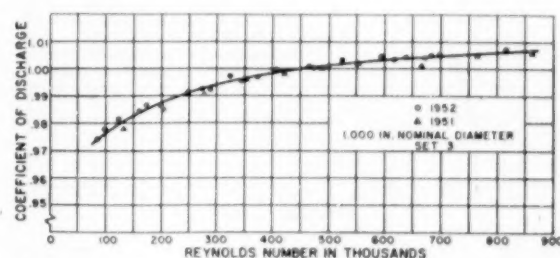
FIG. 8   COEFFICIENT OF DISCHARGE FOR 1-IN. NOZZLE, SET 3, SHOWING AGREEMENT OF 1951 AND 1952 TESTS
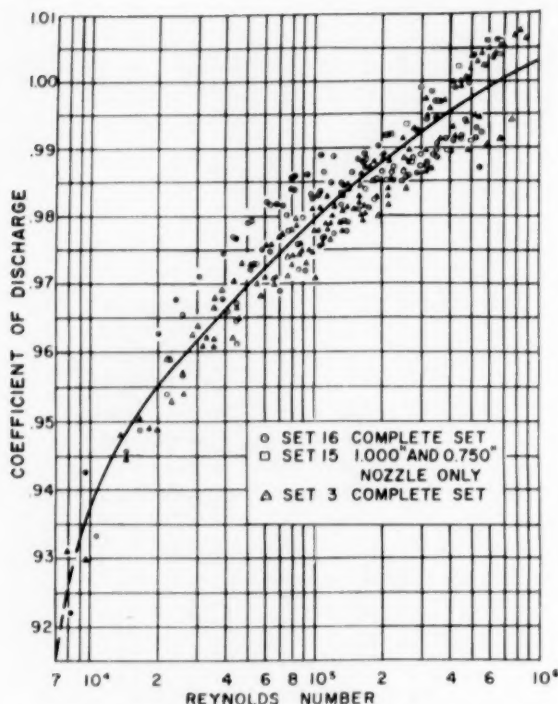
FIG. 9   AVERAGE COEFFICIENT OF DISCHARGE AND TEST POINTS FOR TWENTY-TWO HEI NOZZLES TESTED

FIG. 11   COMPARISON OF AVERAGE COEFFICIENTS OF HEI NOZZLES IN 2 AND 4-IN. PIPE WITH THAT OF ASME FLUID METERS RESEARCH COMMITTEE FOR NOZZLES IN 2-IN. TO 10-IN. PIPE AT A DIAMETER RATIO OF 0.02

FIG. 10   COMPARISON OF AVERAGE COEFFICIENT OF DISCHARGE OF HEI NOZZLES TESTED WITH THAT OF ASME FLUID METERS RESEARCH COMMITTEE FOR NOZZLES IN 2-IN. TO 10-IN. PIPE AT A DIAMETER RATIO OF 0.2

the tests on HEI nozzles separating the 4-in. and 2-in. pipe tests. The resultant curves are compared with the Fluid Meters data in Fig. 11. In the case of the 4-in. pipe at Reynolds numbers below 200,000 the curves are practically identical whereas at higher Reynolds numbers the coefficients of HEI nozzles are considerably above the ASME curves. For the 2-in. pipe, substantially the same situation prevails.

The nozzles of set 3 were among those calibrated with air by the National Bureau of Standards in 1943. Curves of the 1943 air tests are compared with those of the 1951 water tests for eight of the nozzles as shown in Fig. 12. The agreement is good or fair for all except the $1/_2$-in. and 1-in. nozzles.

It will be noted in Figs. 7 and 9 that the discharge coefficients exceed unity for the 1-in. nozzles in the region of Reynolds number of 600,000. This result was obtained on three 1-in. nozzles in a 4-in. pipe and was verified by some further investigations discussed in later paragraphs.

In connection with coefficients greater than unity just discussed, it is of interest to note that the curves of Fig. 11 in both the 2-in. and 4-in. meter runs continue to rise.

No reason has been advanced, as yet (except that mentioned in a later section) for the high values of the coefficient of discharge obtained with the HEI nozzles at high Reynolds numbers and values of the diameter ratio approaching 0.25. All physical measurements have been checked as to method and accuracy and no errors have been discovered. Speculation has even in-

FIG. 12   COMPARISON OF 1943 AND 1951 CALIBRATION TESTS ON
SET 3

FIG. 13   COMPARISON OF COEFFICIENTS OF DISCHARGE OBTAINED
FROM ASME AND HEI PRESSURE TAPS ON A TYPICAL NOZZLE
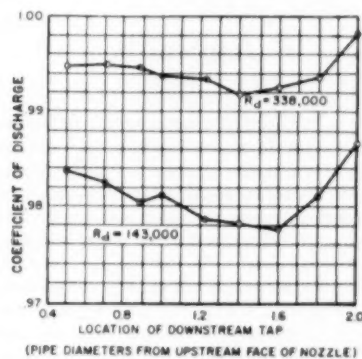
FIG. 14   EFFECT OF DOWNSTREAM TAP LOCATION ON COEFFICIENT
OF DISCHARGE FOR 1-IN. NOZZLE IN 4-IN-METER RUN

cluded consideration of the excellent surface finish of the nozzles.

These tests demonstrate some of the risks involved where average curve values of the discharge coefficient are used for commercial metering. If accuracy better than 1 per cent is desired, the nozzle and meter run must be calibrated as a complete assembly.

COMPARISON OF PRESSURE TAPS

One of the secondary objectives of this work was to evaluate the pressure-tap locations used by the National Bureau of Standards in 1943, for the tests with air. These taps were compared with the radius taps by simultaneous readings on all of the nozzles for set 3. Plots of the discharge coefficients produced uniform and parallel curves. The values for the radius taps (one pipe diameter upstream and one-half pipe diameter downstream) were consistently about 0.2 per cent lower for all of the nozzles. A typical comparison is shown for one nozzle in Fig. 13.

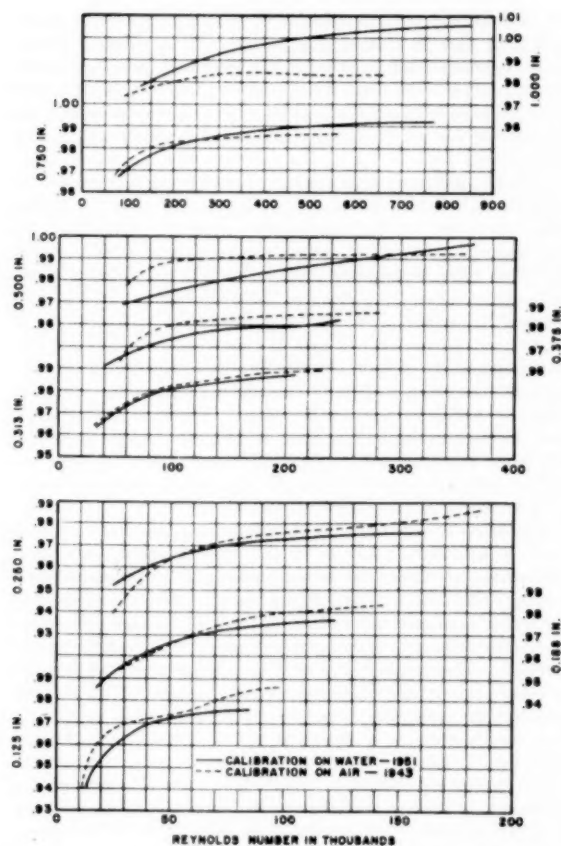On the basis of these results, the new adapters and radius taps can be used in conjunction with 1943 calibration curves for the HEI nozzles without introducing an uncertainty in excess of 0.2 per cent.

INVESTIGATION OF TAP POSITION IN THE 4-IN. METER RUN

Suspicion of the high values of discharge coefficient obtained on the 1-in. nozzle in the 4-in. meter run led to an investigation of the effects of changing the downstream pressure-tap position.

Taps were added to the meter run in approximately $1/2$-in. intervals as shown in Fig. 6.

Differential pressures were observed for each of these taps as two flow rates and the values of the discharge coefficient obtained are plotted against tap positions in Fig. 14.

This plot shows that the maximum differential pressure, and therefore the minimum coefficient, would be obtained with the outlet pressure tap located between 1.4 and 1.6 pipe diam downstream from the nozzle-inlet face. These curves, based on a small number of tests, seem to disagree with the general result represented by Fig. 13. However, it should be noted that Fig. 13 is representative of the average result of many tests on 10 nozzles. Also, there was more fluctuation in the tests of Fig. 14 than in the other tests reported. This emphasizes the need of further experimental work.

CONCLUSIONS

With accurately made and well-polished nozzles having throat diameters from $1/16$ to 1 in. it has been possible to obtain reproducible calibrations that agree within a few tenths of 1 per cent.

While there is a small difference between the coefficients for pressure taps at the locations designated as HEI and ASME, the difference is not of a sufficient magnitude to justify changing the general coefficient curves now used with the HEI nozzles.

When the throat Reynolds number (R_d) is between 50,000 and 200,000, a coefficient value could be selected from the average curve published by the Fluid Meters Committee, provided the over-all accuracy requirements for the measurement was not too restrictive, as, for example, not less than 1 per cent.

BIBLIOGRAPHY

1 "Standard Nozzles Mean Better Fluid Flow Measurements," by H. S. Bean, W. H. Reynolds, and R. M. Johnson, *Power*, vol. 89, 1945, p. 10.

2 "Research on Flow Nozzles by the ASME Special Research Committee on Fluid Meters," by S. R. Beitler and H. S. Bean, Ohio State University, Engineering Experiment Station Bulletin 131, May, 1948.

3 ASME Power Test Codes, Supplement on Instruments and Apparatus, part 5, chapter 4, Flow Measurement, 1949.

4 "Discharge Coefficients of Long-Radius Flow Nozzles When Used With Pipe-Wall Taps," by H. S. Bean, S. R. Beitler, and R. E. Sprenkle, Trans. ASME, vol. 63, 1941, pp. 439-442.

5 "Some Results From Research in Flow Nozzles," by H. S. Bean and S. R. Beitler, Trans. ASME, vol. 61, 1938, pp. 235-244.

6 "Piezometer Investigations," by C. M. Allen and L. J. Hooper, Trans. ASME, vol. 54, paper HYD-54-1, 1932, pp. 1-11.

7 "Determination of ASME Nozzle Coefficients for Variable Nozzle External Dimensions," by R. G. Folsom, Trans. ASME, vol. 72, 1950, pp. 651-654.

8 "Piping Arrangements for Acceptable Flowmeter Accuracy," by R. E. Sprenkle, Trans. ASME, vol. 67, 1945, pp. 345-357.

Appendix

General Problems of Metering With Small Nozzles

Experience with the HEI nozzles seems to indicate that the most common error in measuring flow rate is related to the measurement of the nozzle diameter. It is normal practice to measure nozzle diameters to the nearest thousandth of an inch and if they are slightly out of round to use an average diameter. This practice, quite adequate for the larger nozzles, is unsatisfactory for the small nozzle. To illustrate, an error of 0.001 in. in diameter will introduce an error in the flow calculation of 0.02 per cent for a 12-in. nozzle, 0.20 per cent for a 1-in. nozzle, and 3.11 per cent for a $1/_{16}$-in. nozzle. Thus it becomes imperative to measure the diameter of small nozzles to a degree of accuracy appropriate to the size of the nozzles.

A poor surface finish in the throat of a flow nozzle has the effect of reducing diameter. Acceptable surface finish for a 12-in. nozzle might well produce an error of several per cent for the $1/_{16}$-in. nozzle. A highly polished surface has proved necessary to facilitate accurate measurement of the diameter, and to reveal surface irregularities which might affect the flow pattern adversely.

Because of the importance of size, the nozzles should be cleaned with a clean, soft cloth. Under no circumstances should abrasive material be used. Oil and grease should be removed with a noncorrosive solvent. Every effort must be made to maintain the dimensions, contour, and finish built into the nozzle.

When flow nozzles are used in 1 and 2-in. pipe the pressure taps must be proportionately small. Great care is necessary to insure smoothness of the internal surfaces in the region of the pressure taps. If gaskets are used they must fit smoothly within the internal bore.

When accuracies better than 1 per cent are required the nozzle and the pipe assembly should be calibrated as a unit. Pipe lengths shorter than the prescribed minimums should be avoided. Throttling devices should be placed downstream of the nozzle. If the manometer indicates pulsation of appreciable magnitude the cause should be sought and eliminated if possible.

Discussion

H. V. BECK.[3] The authors are to be complimented on the care which they exercised in an effort to insure uniformity of

---

[3] Chief Engineer, American Meter Company, Inc., Erie, Pa. Mem. ASME.

dimensions and surface finish of the component test elements, and their care in cleansing these elements to remove foreign material before conducting tests. It might not have been necessary to follow these precautions; however, failure to have done so would have left a cloud of suspicion over the results—especially in view of certain observed characteristics which are, as yet, unexplained.

It might be appropriate to enlarge somewhat on a general reference made by the authors concerning the necessity for having relatively equal surface finishes on various components of the test elements. If tests are to be conducted on small-size apparatus, then extreme accuracy must be exercised in machining the test elements, and the surfaces must be highly polished if a reasonable degree of dimensional similarity is expected. If these requirements are not met, the data automatically fall into the classification of individual calibrations of certain particular elements, and the ability to extrapolate those data with any degree of confidence has been sacrificed. The continuation of the tests through to line sizes as great as 4-in. pipe is also commendable since the existence of data on these relatively large line sizes is additional substantiation to the right to extrapolate the data to similar elements in large-size lines.

A possible avenue of future investigation in the work reported on by the authors, might be to determine whether a divergent section downstream of the nozzle throat might be necessary when testing with an expansible fluid, such as air. Tests conducted by the writer's company have indicated the need for such a divergent section in their critical flow-prover orifices (which are essentially nozzles). These orifices are used as field-proving standards for proving large-capacity-displacement gas meters. With a divergent section, smoothly faired to the throat of the nozzle, the flow results were more consistent and their calibration became substantially constant over a wide range of operating pressures.

The primary function of critical-flow orifices, when used as field-proving devices for positive-displacement meters is to establish a constant volume rate of flow (measured at conditions upstream of the orifice). With these devices it is a basic consideration that pressure variations downstream of the orifice (nozzle) have no effect on the rate of flow—as long as conditions of upstream and downstream pressure exist which correspond to critical flow. This would indicate that conventional methods of obtaining differential pressure would not be applicable under conditions of critical flow. Neglect of this fact would result in an increase in coefficient with decrease in downstream pressure—below the maximum downstream pressure corresponding to critical flow. This, in part, might account for coefficients obtained by the authors which were in excess of unity.

AUTHORS' CLOSURE

After the tests described in the paper had been completed at the plant of Ingersoll-Rand Company, nozzle set No. 3 was sent to the National Bureau of Standards, where, during the fall of 1953, some additional tests with water were made on the 1 and $3/_4$-in. nozzles.

For these tests the piece of 4-in. pipe used as the inlet section in the 1943 tests was at hand and used in the same position again. There was at hand also, the same nozzle-mounting plate. However, it was necessary to prepare a new outlet section of pipe. In addition to the inlet section of pipe mentioned, additional 4-in. pipe was added to provide about 53 PD of straight pipe on the inlet side of the nozzle. Straightening vanes were installed 37 PD from the nozzle. Preceding the 4-in. pipe, there was a short section of 2-in. pipe containing a gate-type regulating valve, and this in turn was connected through reducers to an 8-in. supply line. On the outlet side of the nozzle there were 10 PD of 4-in.
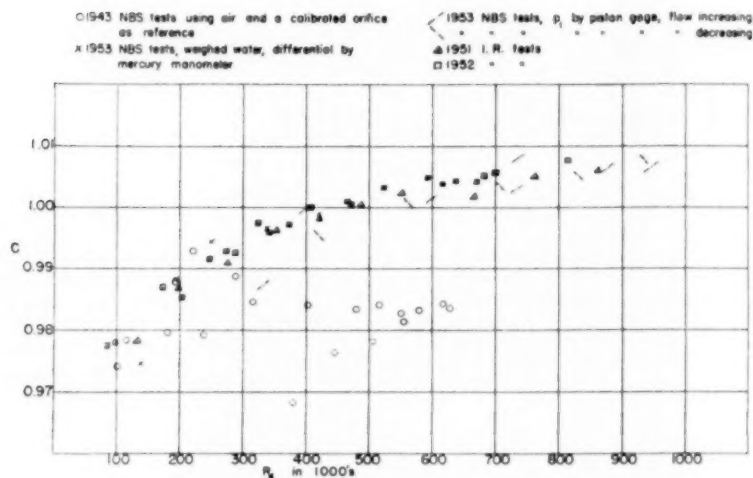
O 1943 NBS tests using air and a calibrated orifice as reference
x 1953 NBS tests, weighed water, differential by mercury manometer
⟨ 1953 NBS tests, p₁ by piston gage, flow increasing
" " " " " " decreasing
▲ 1951 I.R. tests
□ 1952 " "

FIG. 15   TESTS OF 1-IN. HEI NOZZLE, SET NO. 3

o 1943 NBS Tests with air
x 1953 NBS Tests weighed water, and mercury manometer
⟨ " " " " " flow increasing
" " " " " flow decreasing
▲ 1951 I.R. Tests
□ 1952 " "
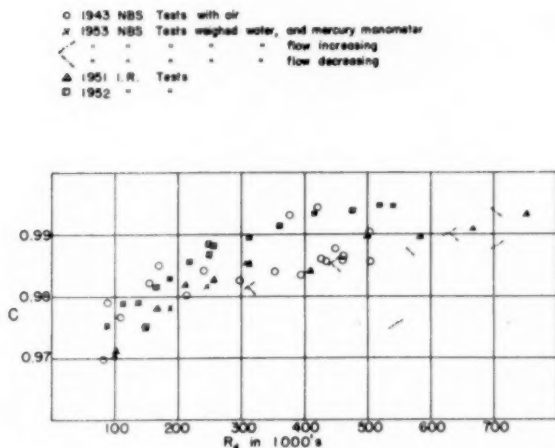
FIG. 16   TESTS OF 3/4-IN. HEI NOZZLE, SET NO. 3

pipe followed by a tee (elbow) to the discharge riser in which there was the outlet control valve.

The pressure taps were located 4 in. preceding and 2 in. following the inlet face of the nozzle, thus corresponding with the locations used at Ingersoll-Rand. The inlet pressure was measured with a piston gage for which there are 0.1-lb weights. The outlet pressure, which was maintained nearly constant, was measured with a mercury manometer.

The water was weighed in a tank mounted on 1500-lb platform scales. A diverter directed the water into the tank or to the sump channel as desired. The motion of the diverter actuated one pen of a chronograph. The time pen of this chronograph was actuated by a ship chronometer through a relay system.

The results of these tests are shown in Figs. 15 and 16 of this closure. In the case of the 1-in. nozzle, the Bureau's recent tests agree very well with both the 1951 and 1952 Ingersoll-Rand tests. All of these tests were made by the weighed-water method. The 1943 tests, which agree with the recent tests only at the lower rates, were made with air, and a calibrated orifice meter was used

as the reference. It may be added that this reference orifice meter had been calibrated by weighed-water tests. Hence, without the aid of further experimental studies, no explanation can be offered for the difference between the 1943 tests and the recent tests.

It was gratifying to find the recent Bureau tests and the 1951 I-R tests agreeing very well with most of the 1943 tests on the 3/4-in. nozzle. Moreover, the divergence between these and the 1952 I-R test and 2 points of the 1943 tests is not excessive (about 0.1 per cent) for tests of this kind.

Mr. Beck has mentioned the desirability of further work on nozzles having a slightly divergent (expanding) throat section. In this, the authors concur.

Not long ago the Bureau had occasion to test several small nozzles which had short and slightly expanding throat sections. The first attempt at calibration by weighed-water procedure gave rather surprising results, as shown by the solid lines 1 and 2 in Fig. 17 of this closure. A second calibration was then made with air, using a calibrated orifice meter on the inlet side of the nozzle. The nozzle under test was mounted between two sections of 2-in. pipe, the outlet or downstream section being about 2 ft long and open to the air at the exit end. The results of these tests are shown by the dotted lines 3 and 4 in Fig. 17.

o 3/16" nozzle in horizontal pipe, back pressure about 2 psig
△ " " free discharge downward, water freed of air
/ " " " " " " air in water
x 1/2" nozzle in horizontal pipe, back pressure about 2 psig

FIG. 17   WEIGHED-WATER TESTS OF A 3/16-IN. AND 1/2-IN. NOZZLE

Boiler and Furnace Designed for Spreader-Stoker Firing

By L. H. COYKENDALL[1] and P. R. LOUGHIN,[2] NEW YORK, N. Y.

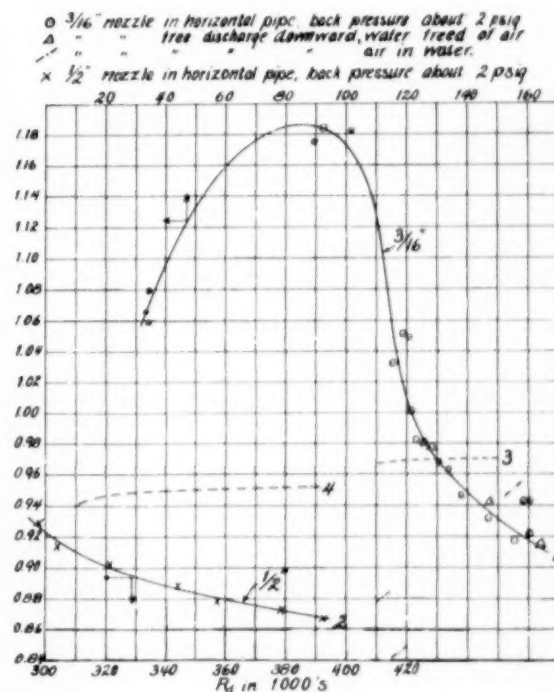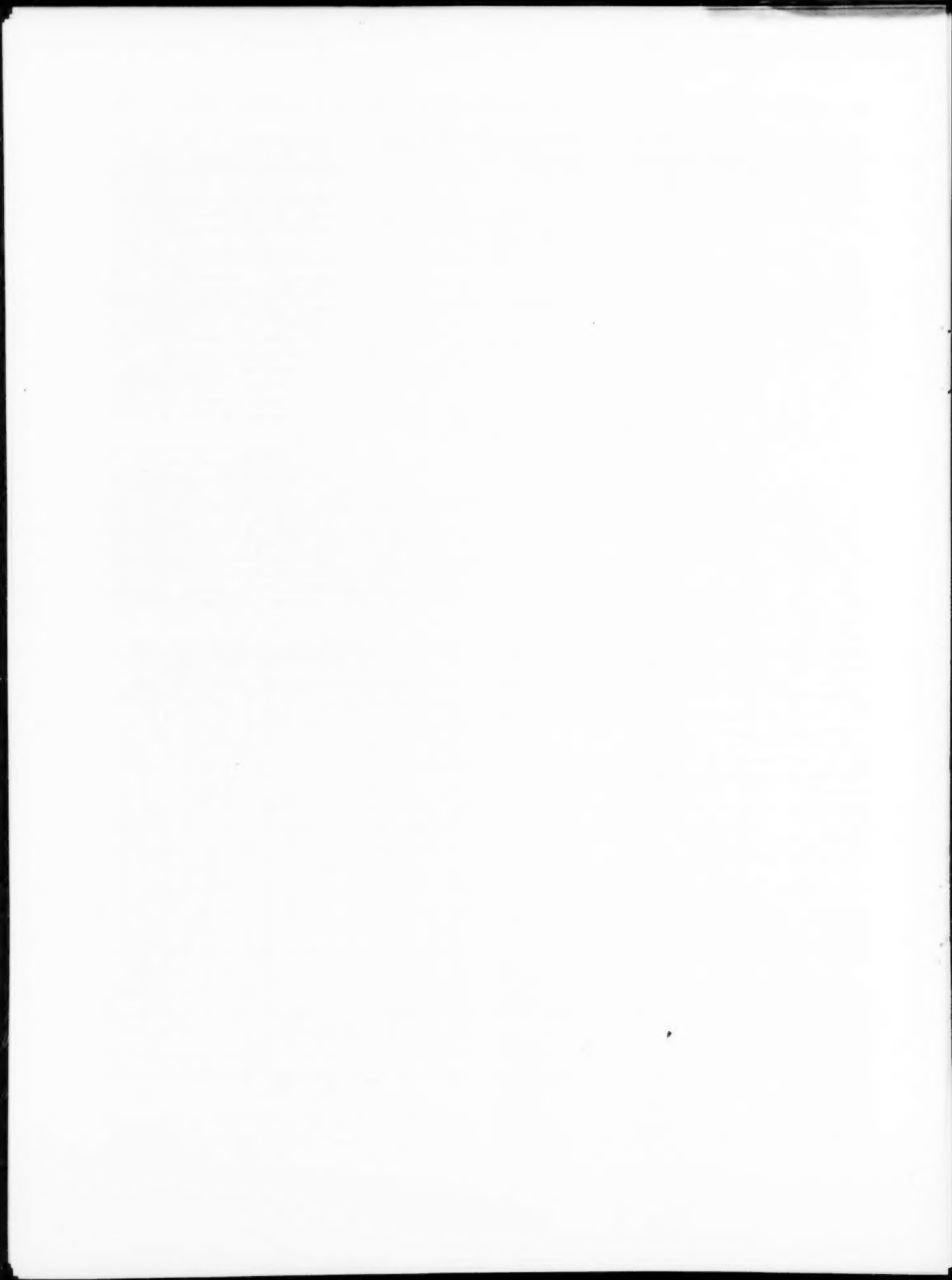This paper includes a brief review of the history of spreader-stoker firing, and describes the development of a furnace and boiler design particularly adapted to the spreader stoker. Test results present coal analysis, ash balance, and flue-dust loading, distribution, combustible content, and size consist, as well as gas temperatures and draft differentials throughout the unit.

Introduction

WHEN man first began to stoke furnaces for steam production, he did it by hand, spreading the coal on the grates with a shovel. According to Best,[3] in 1857 some ingenious individual devised a means of spreading the coal mechanically and thus simulated hand-firing. Through the years this method was gradually improved, but it was not generally recognized or accepted as a good method of stoking coal until the later thirties or early forties. This slow growth and general reluctance to accept spreader-stoker firing was due to the inherent tendency to emit from the stack a considerable portion of the coal fired and to smoke excessively at reduced firing rates.

Many of the early applications were made on existing boilers with low setting heights, some with portions of the boiler bank tubes located only 3 or 4 ft above the grate. According to Wagner[4] some installations were successful even though the setting heights were only 5 ft 4 in. above the grate level. In the early forties most applications were on multi-gas pass boilers equipped with refractory gas baffles. The inherent characteristics of heavy fly ash and combustible carryover, accentuated in the cases of low setting heights, resulted in erosion of pressure parts, which became a serious problem on numerous installations. During the period of development from about 1940 to 1948, firing rates were increased from around 450,000 Btu per sq ft of grate area to over 900,000 Btu per sq ft[4] in an effort to reduce smoking at low loads, resulting in further aggravation of the erosion problem.

During this same period the practice of reinjecting cinders was adopted in order to reduce the unburned carbon losses, and this greatly increased the dust loading of the gases passing through the boiler and heat traps. Kaiser[5] reports nearly three times the dust loading leaving the furnace with reinjection as compared with no reinjection. At these high burning rates and high dust loadings, even the highest set multiple gas pass units, such as that shown by Fig. 1, suffered serious tube erosion at the baffle turns. This unit is typical of several in which erosion of pressure parts
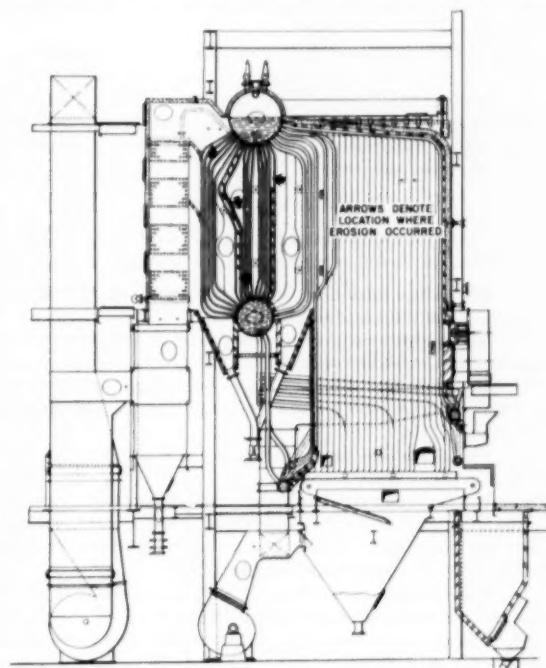
Fig. 1 Serious Tube Erosion Shown at Baffle Turns in Multiple Gas-Pass Boiler

was experienced in the general locations indicated by the arrows. In one case, tube failures occurred in less than 1 year of operation at rated full load.

The ability of the spreader stoker to handle fluctuating load conditions satisfactorily when supplied with a wide variety of available coal of suitable sizing, increased the popularity of this method of firing during the middle forties. Recognizing the rapidly increasing popularity of the spreader stoker and the need for a boiler unit designed to accommodate its characteristics, a committee was established in the authors' company in 1947, to consider the problem. Statistics on the operation and maintenance problems of existing units were studied and several spreader-stoker manufacturers were consulted. As a result of this survey, several pertinent conclusions were reached:

[1] Engineering Co-Ordinator, The Babcock & Wilcox Company. Mem. ASME.

[2] Executive Assistant, The Babcock & Wilcox Company. Mem. ASME.

[3] "What the Mechanical Type Dust Collector Industry Is Doing to Meet the Various Problems Presented by Spreader Stoker Fired Water Tube Boilers," by P. F. Best, Chief Mechanical Engineer, The Thermix Corporation.

[4] "Light-Load Design Features for Spreader Stokers," by Herbert L. Wagner, *Mechanical Engineering*, vol. 74, 1952, pp. 458–460.

"Spreader Stokers and Fly-Ash Reinjection," by H. L. Wagner, Vice-President in Charge of Engineering, Detroit Stoker Company. Presented at the Wisconsin Power Conference and Exposition, June, 1952.

[5] "Dust Emission From Coal-Fired Boiler Furnaces," by E. R. Kaiser, Assistant Director of Research, Bituminous Coal Research, Inc., presented at the Midwest Power Conference, April, 1951.

CORRECTIVE ACTION RECOMMENDED

1 The furnace walls should be water-cooled but the degree of wall cooling should not be more than that required to prevent excessive maintenance and troublesome slagging so that the combustion process would be aided with a furnace temperature as high as possible.

2 The arrangement of the furnace should be such as to promote maximum turbulence and to provide for the proper flow of furnace gases so that the most desirable furnace absorption would be obtained irrespective of coal sizing.

3 The distance from the grate to the lowermost point of the furnace outlet should be in the order of 12 ft or more. The purpose of this is twofold—to reduce the amount of cinders carried out of the furnace and increase the time of passage through the furnace for burning of carbon in the flue dust.

4 Gas turns and gas baffles that concentrate the flue dust should be eliminated from the boiler bank to avoid erosion of pressure parts.

5 In order to reduce dust loading and collect for reinjection the most abrasive large particles high in carbon, the boiler should be fitted with large hoppers. These should be so designed that the maximum amount of cinders would be collected as soon as practical after their exit from the furnace, and thus assist in eliminating erosion of pressure parts.

DESIGN SPECIFICATIONS

The combination of past experience and commercial considerations resulted in the following design specifications:

(a) The design should permit the installation of oil and gas burners to allow the use of alternate fuels.

(b) The size increments of the standard design should cover a capacity range extending to 250,000 lb of steam per hr.

(c) The units should be capable of delivering steam at pressures up to about 1050 psi and at temperatures ranging from saturation to 950 F.

(d) The maximum rate of furnace heat release should be 35,000 Btu per cu ft per hr.

(e) The heat released per square foot of flat projected furnace surface per hour should not exceed 100,000 Btu for coal having an ash-fusing temperature (oxidizing basis) below 2300 F and 115,000 Btu for ash-fusing temperatures above 2300 F.

(f) The maximum rate of heat release per square foot of gross grate area per hour should not exceed 650,000 Btu.

(g) The gas velocity through the superheater and boiler bank should not exceed 60 fps.

Over 100 different designs were studied by the committee. The performance characteristics of many designs were developed for a common base to permit comparison, and estimates were made of the costs. The design selected as the best was a single-pass two-drum boiler with swaged tubes, a water-cooled furnace, an arch under the superheater to promote gas turbulence and optimum furnace heat absorption, and a completely enclosed superheater pass to assure required steam temperatures under the varying firing conditions peculiar to spreader-stoker firing.

In order to increase the gas-mass flow through the single-pass boiler bank and obtain the high absorption rates required for desired efficiency, it was necessary to reduce the lateral tube spacing below that required for an economical drum ligament. Reasonably efficient performance, and other considerations, dictated a clear space between the 2½-in-OD tubes of about 1 in.; but such spacing would have required unreasonably thick and expensive drums for the proper drum efficiency. Therefore tubes swaged from 2½ in. to 2 in. OD at the drums were desirable and new shop facilities were installed to make this swaging operation economical.

Field surveys also had indicated that excessive maintenance and slagging of the rear furnace wall was experienced unless closely spaced tubes were used, so this feature was adopted for the new unit. Trouble was being experienced with excessive maintenance and slag on furnace side and front walls with a tube spacing greater than twice the tube diameter. Therefore a tube-and-tile wall with 3-in-OD tubes on 6-in. spacing was specified for these walls. In several installations, stress cracks, commonly known as fire cracks, had occurred in the lower side-wall headers exposed to the furnace. Protection for these headers was provided by the use of two horizontal chill tubes 3 in. diam. Sufficient water velocity in these tubes was provided by using the chill tubes as supply tubes for the front waterwall.

A STANDARDIZED DESIGN

At the conclusion of 2 years of investigation, study, and planning, the design was standardized in accordance with the previously mentioned design specifications. The first of these standardized two-drum boilers was sold in September, 1949. Since then many of them have been sold and placed in service and the results have been very gratifying. The standardized design is shown in Fig. 2.

The rear wall is of closely spaced tube construction carried up to form a water-cooled arch to promote turbulence and direct the hot gas toward the front wall for maximum absorption and furnace efficiency. The tube-and-tile side and front walls, with 3-in. tubes on 6-in. centers, result in a high furnace temperature promoting more complete combustion and yet provide sufficient
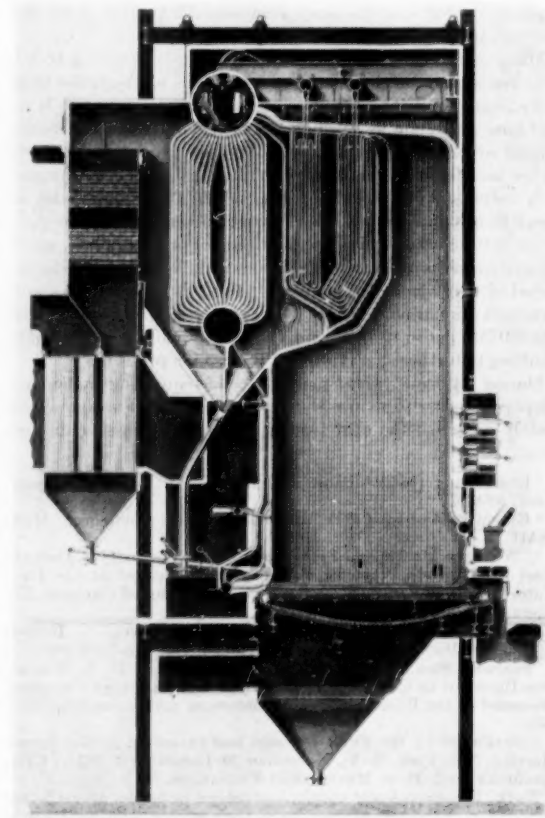
FIG. 2 STANDARDIZED BOILER DESIGN

cooling to prevent excessive brickwork maintenance and troublesome slag. Auxiliary or alternate firing by oil or gas is permitted by suitable burners located in the front wall over the coal feeders. A large, double, cinder-collection hopper extends under the boiler the full depth of the boiler bank, with the boiler tubes themselves acting as retarders to increase the collection efficiency of each section of the hopper. Note that a single outlet serves the front and rear section and gas is prevented from by-passing the boiler bank through the hopper by virtue of the low boiler-draft loss and the suction generated by the cinder injectors. The single-pass boiler bank without baffles, is formed of $2\frac{1}{2}$-in-OD tubes on $3\frac{9}{16}$-in. side spacing with the tubes swaged to 2 in. at the drums, thus reducing the possibility of erosion, but maintaining efficient heat-transfer surface and permitting an economical drum thickness.

TEST INSTALLATION

An installation on which a complete series of tests were obtained, including dust-loading data, is shown in Fig. 3. This unit is fired by a Detroit Rotograte spreader stoker and was designed for a capacity of 160,000 lb per hr continuous and 177,000 lb per hr 4-hr peak.

Full-load test data and other pertinent information on this unit are given in the table of Performance Data. The relatively low gas temperature at the furnace exit was obtained by means of a 60-point high-velocity thermocouple traverse, while gas temperature at the boiler, economizer, and air-heater exit were obtained by two 30-point and a 24-point bare thermocouple traverses, respectively. An accurate determination of rate of coal feed was not obtainable, and therefore, the efficiency of the unit, 85.4 per cent, was determined by taking the difference between 100 per cent and the total losses, including an assumed radiation and unaccounted loss.
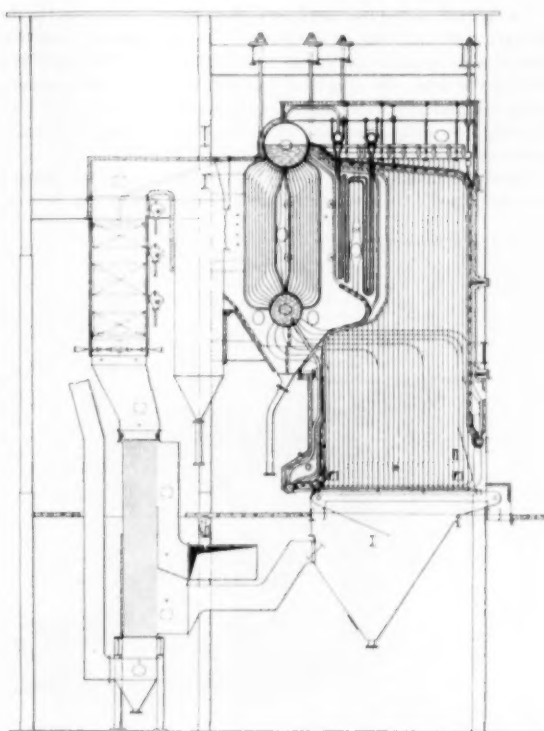
FIG. 3   COMPLETE TESTS CONDUCTED ON THIS TYPE INSTALLATION

PERFORMANCE DATA

STEAM FLOW	M LB PER HR	182
STEAM PRESSURE AT S.H. OUT	PSI	604
STEAM TEMPERATURE	DEG. F	706
EXCESS AIR AT BOILER OUTLET	%	38
FEEDWATER TEMPERATURE		
ECONOMIZER INLET	DEG. F	333
ECONOMIZER OUTLET	DEG. F	394
AIR TEMPERATURE		
F. D. FAN INLET	DEG. F	88
AIR HEATER OUTLET	DEG. F	257
GAS TEMPERATURE		
BOILER SCREEN (HVT)	DEG. F	1780
BOILER OUTLET	DEG. F	630
ECONOMIZER OUTLET	DEG. F	430
AIR HEATER OUTLET	DEG. F	321
AIR PRESSURE		
F. D. FAN OUTLET	IN H₂O	3.6
AIR HEATER OUTLET	IN H₂O	1.8
STOKER WINDBOX	IN H₂O	1.7
DRAFT		
FURNACE	IN H₂O	−0.14
BOILER OUTLET	IN H₂O	−0.5
ECONOMIZER OUTLET	IN H₂O	−3.2
AIR HEATER OUTLET	IN H₂O	−5.2
I. D. FAN INLET	IN H₂O	−8.8
HEAT RELEASE RATES		
PER FT² GRATE AREA PER HR.	M. BTU	595
PER FT³ FURNACE VOL. PER HR.	M. BTU	25.7
PER FT² PROJ. FURN. SURF. PER HR.	M. BTU	93.7
HEAT BALANCE		
DRY GAS LOSS	%	5.8
MOISTURE AND HYDROGEN LOSS	%	3.9
UNBURNED COMBUSTIBLE LOSS	%	2.9
RADIATION LOSS (ASSUMED)	%	0.5
UNACCOUNTED LOSS (ASSUMED)	%	1.5
TOTAL LOSSES	%	14.6
UNIT EFFICIENCY (DIFFERENCE)	%	85.4

On the unit tested the flue dust collected in the boiler and in the primary collector hoppers is reinjected into the furnace, and that from the air heater and secondary collector hoppers is discarded. During the tests, the weight of flue dust collected by the several boiler hoppers was determined by timing the collection rates accurately over short intervals. The flue-dust loading at the boiler outlet was obtained by a 30-point aspirated sample traverse.

From the data collected and flue-dust analyses, an ash balance was developed. It is shown schematically in Fig. 4. It is of in-

FIG. 4   ASH BALANCE

terest to note that of the ash entering the system in the raw coal, 64 per cent leaves the system via the grate and ashpit and 36 per cent carries through the primary collector. It is also of interest to note that almost as much ash as that in the raw coal, or about 92 per cent, enters the furnace with the reinjected flue dust. This is made up of 34 per cent collected in the boiler hoppers and 58 per cent collected in the primary collector and results in 128 per cent passing out of the furnace in the flue dust, which amounts to 1640 lb of ash per hr circulated.

FLUE—DUST DISTRIBUTION

From the viewpoint of dust loading, erosion, and material handling it is pertinent to consider the distribution of flue dust (ash plus carbon) through the system. This is shown schematically in Fig. 5. In this case the expected efficiency of the primary flue-dust collector was used in determining the quantity of flue dust returned to the furnace. The weight of flue dust leaving the furnace is 4230 lb per hr, which is equivalent to 27 per cent of the weight of coal fired. On many installations this percentage will range from 35 to 50 per cent when all of the flue dust is reinjected. Assigning 100 per cent to the 4230 lb per hr leaving the furnace, as shown in Fig. 5, over 29 per cent of this amount is collected in the boiler hoppers and 51 per cent in the primary col-

FIG. 5   FLUE-DUST DISTRIBUTION

lector hoppers making a total of 3430 lb per hr or 81 per cent reinjected into the furnace. The calculated dust loading in pounds of dust per thousand pounds of gas, corrected to 50 per cent excess air, is 16.4 lb per thousand pounds leaving the furnace, 11.3 lb per thousand pounds leaving the boiler, and 3.1 lb per thousand pounds leaving the primary collector. The dust loadings at the boiler and primary collector outlets show that either two-stage collectors or a highly efficient (93 per cent in this case) single dust collector is necessary on spreader-stoker-fired units in order to meet the requirements of the ASME recommended code on stack emission.

Samples of the raw coal and of the flue dust collected at the several locations were sent to the laboratory for analysis and sizing. The laboratory determinations are plotted in Fig. 6. The high combustible content of the material collected in the boiler and primary collector hoppers, coupled with the large quantity collected as shown in Fig. 5, makes the refiring of this material desirable if excessive carbon loss is to be prevented. On the other hand, in most cases, the fine sizing and lower combustible content of the secondary collector refuse coupled with the low collection rate, justifies the discard of this material.

RESULTS IN SERVICE

Operation and field service reports on a number of these standardized units have confirmed that the design specifications set forth previously are sound and that they have been attained or exceeded. These include the following:

1   The use of tube-to-tube construction in the rear wall and arch is very desirable, as indicated by its ability to shed dry-ash deposits as they accumulate.

FIG. 6   RAW COAL AND FLUE-DUST SIZING AND ANALYSIS

2   No troublesome slagging or brickwork maintenance on the tube-and-tile side and front walls has been reported, indicating that the objective of maintaining a high temperature in the lower part of the furnace to promote more complete combustion has not resulted in trouble from these sources.

3   The ability of the furnace arch to promote turbulence and good furnace absorption is confirmed by the relatively low average temperature of the furnace-exit gas.

4   The horizontal slag-chill tubes at each side of the grate have functioned as intended.   There has been no failure or other sign of distress in them, indicating that circulation, as designed, is entirely adequate.

5   Some of these units have been in service for over 2 years at high load and no pressure-part erosion can be detected in the superheater and boiler banks.

6   The collection efficiency of the boiler cinder hoppers ranges from 27 per cent to 35 per cent, depending upon the raw-coal sizing.   Observation has confirmed that there is no gas by-passing of the boiler bank through these double hoppers.

7   Predicted steam temperature has been obtained on practically all of these installations which justifies the design provisions incorporated for this purpose.

8   The absorption in the boiler bank has been found to be somewhat better than expected and our design factors accordingly have been changed to take advantage of this increase in efficiency.

Discussion

JOHN CALLAN.[6]   Our first experience with spreader-stoker-fired boilers was acquired in an industrial plant located near the northeast border of Tennessee.   The original installation, which

[6] Superintendent, Power and Services Division, Tennessee Eastman Company, Division of Eastman Company, Kingsport, Tenn.   Mem. ASME.

went into service in 1948, consisted of three 150,000-lb-per-hr 4-drum boilers equipped with conventional baffles.   All fly ash collected by the various boiler hoppers and the high-efficiency dust collectors located ahead of the induced-draft fans was returned to the furnace.

Less than a year after starting up, fly-ash erosion caused a generating-tube failure in one of the boilers.   An inspection of the three boilers revealed that cutting was general.   It had progressed to such an extent that many tubes were condemned and had to be replaced.   Many more required build-up by welding to permit continued service.   Cutting in all cases was located just after those places where the baffles caused a change in direction of the flue-gas stream.

The boiler manufacturer, when called on for assistance, recommended the removal of the refractory baffles and their replacement with filter baffles.   These filter baffles consist of 6 in. × 10-gage steel strips attached directly to the generating tubes by means of Nelson studs and clamp washers.   The strips were installed horizontally across the tubes with $^3/_8$-in. openings in the first baffle and 1-in. in the second.

The filter baffles, together with some other changes of a more or less minor nature, seem to have eliminated fly-ash cutting in these units.   Operating conditions and operator morale improved to the extent that when, in 1949, we needed additional steam-generating capacity two spreader-stoker-fired boilers of 150,000 lb per hr were purchased.   The spreader stokers selected were sized for a heat release of 550,000 Btu per sq ft per hr compared to 700,000 Btu in the original units.   Fig. 3 in the paper shows a cross section of the new units.   The first was placed in service on April 30, 1951, and the other on July 14, 1953.

Generally speaking, the new units have been very satisfactory. They steam well, respond readily to load changes, and have ample reserve capacity.   However, the close spacing of the tubes has not been too effective in eliminating the formation of troublesome slag on the rear walls.   Lancing ports located in each side wall,

about 8 ft above the grates and just forward of the rear walls would, we believe, provide an acceptable means of controlling this slag growth.

Availability of the new units has met our expectations, being better than 93 per cent for the first unit, after 30 months of operation. This includes scheduled as well as unscheduled outages. The second unit has operated without interruption since it went on the line in July of this year.

Operating and economic data collected independently by our own test engineers substantiate closely the performance data which appear at the end of the paper.

While the smoking characteristics of our spreader-stoker-fired units are not quite as good as those for boilers equipped with underfeed stokers, recent tests of the flue gas enroute to the chimneys show dust loadings to be substantially less than the maximum permitted by ASME recommendations and the local air-pollution ordinance. The high efficiency of our secondary dust collectors is an important factor in making this possible.

We are of the opinion that the unit shown in Fig. 3 of the paper is a good example of what can be done in the way of balanced design.

F. G. FEELEY, JR.[7] The authors have done a workmanlike job of presenting their company's concept of spreader-stoker-fired boiler-design problems and the steps taken to overcome them. The resulting boiler they describe would appear to be a satisfactory solution to most of the recognized problems of spreader-stoker firing.

However, certain problems with large spreader-stoker-fired units in plants of the writer's company would not appear to have been recognized or solved by the boiler design under discussion.

We have found that the presence of refractory in lower furnace side walls causes slag build-up to a point where the outer surface drips molten particles onto the edge of the grate, tending to cause trouble at this critical point of the fuel bed. The tube arrangement on the job where this trouble has been particularly severe is $3^{1}/_{4}$-in. tubes on 6-in. centers—leaving a smaller gap than that in the B&W standard boiler. Correction has been achieved by the use of welded stud plates leaving only a $1/_{2}$-in. nonmetallic gap. In a new spreader-stoker-fired boiler we would insist upon tangent tubes or extended metallic surface for a distance of at least 8 ft above the fuel bed.

Having recently experienced the complete destruction of lower side waterwall headers on three boilers in a single plant by "fire cracks," in approximately 2 years of operation, we question the ability of horizontal water-cooling tubes to eliminate completely the cause of the difficulty. Henceforth we will insist that side-wall headers be removed completely from the furnace atmosphere.

The provision of gas and oil burners in the front wall of a spreader-stoker-fired unit seriously complicates the design of coal bunkers and access and operating platforms for the oil and gas burners. A preferable arrangement would appear to be oil and gas burners located in the side walls with extended controls, permitting operation from a common level with the stoker.

In the boiler whose test results have been reported upon, it is stated that a 93 per cent efficiency dust collector would be required to permit the reinjection of all dusts while still meeting the ASME recommended Code on stack emission. Tests on boilers of the writer's company and the J. I. Case Company have been reported to this Society in recent years, indicating that the code can be met with collectors having substantially lower efficiencies. In our estimation more attention needs to be given by designers to the number and orientation of reinjection points. We are quite certain of one thing, and that is,

[7] Mechanical Engineer, Carbide & Carbon Chemicals Company, Union Carbide & Carbon Corp., New York, N. Y. Mem. ASME.

the more reinjection points, i.e., the less dust return to any one point, the better are the chances for success.

The authors have established a desirable gas velocity not in excess of 60 fpm through the superheater and boiler bank. This might be acceptable in a single-pass boiler, but velocities of this magnitude in a baffled boiler most assuredly would cause pressure-part erosion. Our experience would indicate that with gas velocities in the order of 40 fpm, very high dust loadings can be tolerated without erosion—leading us to the conclusion that erosion is mainly a function of gas velocity and not of dust loading.

The boiler whose tests are reported upon is one reinjecting only part of collected dusts. While this practice is recommended by many, the presence of $42^{1}/_{2}$ per cent combustible in rejected dust is a factor which should encourage further attempts to achieve universally successful 100 per cent reinjection of all dusts. Such efforts by manufacturers and users alike will result in lower first and operating costs by the elimination of fly-ash-removal facilities and disposal problems.

This co-ordinated effort by the authors' company to produce a boiler to achieve good results with spreader-stoker firing is a commendable one. We believe a comparable effort on the part of stoker manufacturers could improve their product greatly, as all spreader stokers currently available appear incapable of carrying maximum loads continuously for the 6-month to 12-month periods required in process-type industrial plants. Particular reference is made to the coal-feed mechanisms which mechanically are too complicated to run trouble-free for such extended periods.

W. C. HOLTON.[8] Any contribution to the technical literature on spreader stokers which presents test data is of interest, and these authors are particularly to be congratulated for the interesting way in which their data are offered. However, the casual reader of this paper might not realize all of the benefits which can be obtained from reinjection of fly ash and might be discouraged by the amount of fly ash shown to be in circulation through the boiler furnace.

Some tests in which we participated and which have been reported[9] offer some data giving interesting comparisons with those presented by the authors. The boiler used for these tests (which is rated at 100,000 lb per hr) had a projected waterwall area of 271 sq ft. The heat-release rates, expressed in terms of Btu per sq ft per hr, were more than four times as high as those recommended by the authors. In spite of this more radical design, it is our understanding that no erosion has been observed in boilers of this type which have been fired for more than 8 years. This emphasizes the authors' point that boiler design is critical if fly ash is to be reinjected.

Because this paper does not contain test data it is difficult to compare results directly with our tests. However, certain data can be obtained which confirm those of the authors. For example, the Racine tests referenced earlier showed that 57 per cent of the ash leaves the system via the grate. In the Racine tests, however, a larger amount was reinjected (114 per cent, as compared to 92 per cent). The material collected by the primary dust collector represented about three fourths of that reinjected, and the remainder was divided between that caught in the boiler hoppers and in the economizer hoppers.

When the amount of flue dust (ash plus carbon) is considered, the Racine tests showed a maximum of 15.3 per cent of the weight

[8] Assistant Chief, Fuels and Air Pollution Division, Battelle Memorial Institute, Columbus, Ohio. Assoc. Mem. ASME.
[9] "Investigation of Gravity Reinjection of Fly Ash on a Spreader-Stoker-Fired Boiler Unit," by C. H. Morrow, W. C. Holton, and H. L. Wagner, Trans. ASME, vol. 75, 1953, pp. 1363–1372.

of coal fired appeared as fly ash. This is certainly on the low side of the authors' figure of 27 per cent; the reason for the difference is not apparent. Slightly more than one half of the flue dust is collected in the primary collector, and the rest is divided about equally between the other two hoppers.

The maximum dust loading reported for the Racine tests was 0.30 lb dust per 1000 lb gas, adjusted to 50 per cent excess air. This was obtained by a stack traverse taken during a test when all of the collected fly ash was returned to the furnace. The efficiency of the dust collector used was 95 per cent. Consequently, it is possible to operate a modern spreader stoker in a furnace equipped with an adequate dust-recovery system without exceeding the recommended limit of 0.85 lb dust per 1000 lb of gas and still gain the benefits of cinder reinjection.

It should be noted that cinder reinjection not only decreases carbon loss, but also solves a waste-disposal problem. In some areas this factor is important in plant design. The fine fly ash from a high-efficiency dust collector is difficult to handle without creating an additional dust nuisance. The plant that can design for the disposal of all its fly ash in the furnace has thus simplified its over-all maintenance problem.

E. R. KAISER.[10] The authors deserve high praise for the design and heat-absorption performance of the steam generator described in the paper. Freedom from ash deposits in the furnace and in the convection passes will make for high availability and reliability.

The writer has made a few calculations based on the data given in the paper. The calculations indicate that approximately 340 lb of combustible is picked up by the flue gases from the 15,800 lb of coal fired per hr. This is indeed a small amount and is probably much less than is actually the case.

The data indicate a high percentage of dust recirculation through the furnace. It should be possible, as has been demonstrated in other cases, to burn two thirds of the combustible reinjected per hour. Also, approximately one sixth of the ash reinjected should be redeposited on the grate. As no information was given about the reinjection-nozzle design and arrangement, or regarding the overfire-air jets, it is impossible to make a suggestion how the combustion might have been improved.

Previous tests at Elyria, Ohio, and at Racine; Wis., have shown the difficulty of measuring the dust accurately at various points in the circuit. Weighing over fairly long intervals would be required, rather than the methods used in the present instance. The dust flow fluctuates considerably from hour to hour, possibly as a result of snowdrifting. Likewise, the size analysis of the coal will vary because of segregation in the pile or bunker.

The coal used had an excellent size consist for a $1\frac{1}{2} \times 0$-in. coal. In fact, there was more coarse coal present than normally would be the case. It is the writer's observation that the minus-20-mesh coal is the one which contributes most to the flue dust, because the particles are carried upward by the gases issuing from the fuel bed at normal operating rates.

W. S. MAJOR.[11] This paper is quite timely because of the continuing activity in spreader-stoker firing. It clearly presents features of boiler and furnace design that are conducive to best operation, reliability, and low maintenance.

However, it is interesting to compare the test data and calculated dust loadings with results from other sources. While the combustible contents of the dusts compare quite favorably, the dust loading of 16.4 lb per 1000 lb of gases reported in this

[10] Associate Director of Research, Bituminous Coal Research, Inc., Columbus, Ohio. Mem. ASME.

[11] Project Engineer, Power Department, Dravo Corporation, Pittsburgh, Pa.

paper is much higher than loadings from other research studies. For instance, Table 1 of this discussion shows findings from two Midwestern furnaces when operated at substantially the same heat-release rates of grate and furnace.

TABLE 1   DUST IN GASES LEAVING FURNACE

Plant	Test	Burning rate, Btu/sq ft per hr	Dust* in gases leaving furnace, lb per 1000 lb gas adj. to 50% exc. air	Heat release in furnace, btu/cu ft per hr
A	1	595000	7.7	26200
A	2	591000	7.5	26100
A	3	631000	4.6	27800
A	4	619000	7.4	27300
B	5	596000	9.9	30080
B	6	596000	10.9	30080
B	7	594000	12.3	30000
B	8	624000	10.6	31550
B	9	596000	8.6	30150
B	10	589000	4.7	29750

* Based upon reinjection of cinder and dust collected in boiler, economizer, and dust-collector hoppers.

Coal Burned

Tests 1, 2—Washed, Island Creek, 2×0, 25% minus $\frac{1}{4}$
Tests 3, 4—Illinois, Knox County, 1-in. screenings, 31% minus $\frac{1}{4}$
Tests 5, 6, 7, 9—Ohio Pittsb No. 8, washed, $\frac{3}{4} \times 0$, 65% minus $\frac{1}{4}$
Test 8—Island Creek, $\frac{1}{4} \times 0$, 95% minus $\frac{1}{4}$
Test 10—Ohio No. 8, Pine Fork, $1\frac{1}{4} \times \frac{1}{2}$; 13% minus $\frac{1}{4}$

This table is the result of co-operative research sponsored by Bituminous Coal Research, Inc., a group of spreader-stoker manufacturers, and two Midwestern industrial concerns under the supervision of Battelle Memorial Institute engineers.

From a careful study of Table 1 and the supporting data, it is the writer's opinion that a dust loading of about 16 lb is abnormally high. It should not be interpreted as representative or typical of the quantity of dust leaving the furnace proper of a spreader-stoker-fired unit.

On the other hand, dust emission from spreader-stoker-fired units must be recognized and high-efficiency collectors employed for high burning rates where low stack dust is essential.

EDMUND McCARTHY.[12] The authors have presented an excellent paper covering the practical approach in eliminating trouble spots in design of spreader-stoker-fired boiler units with the objective of developing a combination of boiler, furnace, and grate conditions so interrelated that the process of heat release and heat absorption can be carried on with minimum heat loss and without excessive erosion or objectionable stack discharge.

From the viewpoint of the combustion engineer, a mechanical spreader stoker constitutes a most effective means of utilizing efficiently a very wide range of coals, mainly because the radiant heat evolved from the entire floor of the furnace stabilizes ignition, while the high resistance grates provide well-balanced air distribution, so that favorable conditions for oxidation exist throughout the lower part of the furnace. As a consequence, the ash-fusion temperature and the coking characteristics have very little influence on the process of heat release regardless of the type coal consumed. The principal advantage of continuous ash discharge is the ability to maintain continuity of steam output with economical coals of average quality, regardless of reasonable variation in ash content and size consist.

A high degree of operating flexibility is obtainable because a relatively thin fuel bed can be maintained throughout a normal range of load conditions. Restricting the grate area to the extent that the fuel bed is intensely active at maximum firing rate makes it possible to attain complete combustion in the shortest possible time after the coal is projected into the furnace. This minimizes the possibility of the fuel bed suddenly becoming too

[12] Consulting Engineer, The Pittston Company, New York, N. Y. Mem. ASME.

lazy for smokeless combustion when carrying a fluctuating load.

In picking up steam load with an active fuel bed, both the firing rate and the rate of heat release from fixed carbon and volatile can be increased quickly with the result that particles of coal, smaller than about 200 mesh, are burned in suspension. Since the efficiency of a water-cooled furnace will increase with the rate of furnace heat release, it will become apparent that ample furnace height is necessary to afford plenty of time for complete combustion and to provide adequate surface for heat absorption to reduce both the temperature and velocity of gases leaving the furnace.

The kicker arch is located high enough above the grate to preclude the possibility of flame impingement on cold surface. The purpose of the arch is to break up stratification and to induce turbulence in the upper part of the furnace so that combustion can be carried out to an economical degree of completeness before the gases travel beyond the boiler-screen tubes.

The single-pass boiler with closely spaced tubes is productive of equalized gas flow and low gas velocities which minimize erosion and improve boiler heat absorption.

E. C. MILLER.[13]   The authors are to be commended for the fine work they have done with the preparation and presentation of this paper. This contribution is greatly appreciated.

The paper stresses the problem of tube erosion in baffled boilers and points out briefly some of the causes of this erosion. The emphasis on erosion in baffled boilers is so great as to create the impression that baffles cannot be used in spreader-stoker-fired units. Such is not the case. Many baffled boilers have failed, and, as the authors state, certain designs failed within 6 months, but many baffled boilers have been trouble-free. The failures have taken a definite pattern as have the trouble-free units. Certainly not all spreader-stoker-fired boilers need be of the single-pass design.

It is noted with interest that total reinjection is given as a cause of boiler-tube erosion in baffled boilers but that total reinjection is not used with this design of single-pass boilers. Total reinjection of fly ash for this particular case would appear to be an advantage in reducing the high carbon loss, 2.9 per cent, and in eliminating a potential disposal problem. A comment from the authors on this would be appreciated. Did the furnace design prevent total reinjection? Was the high dust loading the result of furnace design or did the designs of the grate, the overfire air, or the reinjection contribute to high dust loading?

The design specifications for furnace heat release is higher than used by and published by this discusser's company.[14] It is presumed that the grate heat release is not adhered to rigidly.

The use of an arch under the superheater "to promote gas turbulence and optimum furnace heat absorption" does not seem justified in the light of the data. This arch, one of the "commercial considerations," is common in single-pass boilers but available data indicate this design of furnace does not produce better furnace heat absorption[15] or reduce dust loading,[15,16] when compared to open furnaces. The arch, to be effective in turbulence, would have to be very close to the grate. This high arch

[13] Research Engineer, Riley Stoker Corporation, Worcester, Mass. Mem. ASME.

[14] "Some Engineering Considerations in the Application of Spreader Stokers," by E. C. Miller, *Industry and Power*, vol. 64, March, 1953, pp. 107–110.

[15] "Furnace Heat Absorption in a Spreader-Stoker-Fired Steam Generator," Part 1, by J. W. Myers and R. C. Corey, Trans. ASME, vol. 75, 1953, pp. 909–923; Part 2, by F. G. Feeley, Jr., and E. C. Miller, pp. 925–942.

[16] "An Investigation of Gravity Reinjection of Fly Ash on a Spreader-Stoker-Fired Boiler Unit," by C. H. Morrow, W. C. Holton, and H. L. Wagner, Trans. ASME, vol. 75, 1953, pp. 1363–1372.

is a necessary part of this design but should not be used when not needed to provide superheater space.

A. S. TYSON[17] AND H. NASH.[18]   A B&W 80,000-lb, two-drum, sterling-type boiler equipped with a Detroit rotograte stoker was placed in operation June, 1950. The unit is generating 85,000 lb per hr at 615 psig and 760 F superheat. We are using Indiana coal sized $1^1/_4$ in. × 10 mesh. This coal has a Btu value of 11,400 and the fusion temperature is 2580 F. We ran tests on coals with a Btu content of 11,500 and a fusion temperature of 2200. These coals caused serious slagging on the side tube walls in the firebox and on the tubes of the backwall. This slagging discontinued when we returned to our present coal.

The rear-wall arch drops the slag formations before they become large enough to close off the gas passages.

We find the flue dust of the primary collector to be granular and a combustible content of 25 per cent. The secondary collector has a tendency to build up in quantity while the combustible per cent decreases as the volume of reinjection increases; this would indicate a recycle of a portion of this material. We are discharging from this stream to eliminate overloading of this reinjection equipment and to eliminate some piling of fly ash on grate surface.

We have examined the tube surfaces for erosion and find no serious condition in the boiler area. There is some erosion at the sides of the economizer in the top section. We shielded these tubes to protect them from further damage.

We have examined the swaged tubes internally and find no visible scale build-up in the enlarged portion of the tube and no erosion in the 2 in. portion tube. The external surfaces of these tubes were polished bright with no indications of metal having been removed from the surface.

The smoke emitted from the stack is equivalent to the No 1 Ringelmann chart during normal operation, and at no time is the fly ash which is discharged from the stack a nuisance in the area.

This boiler is inspected and cleaned once each year. The firebox and other gas passages are inspected and cleaned if necessary.

We have had an average load of 86,000 lb per hr for a period of 24 hr with peak loads of 92,000 lb.

This boiler has achieved a performance better than the calculated figures and is operating at a high efficiency.

AUTHORS' CLOSURE

The authors are pleased at the interest aroused by the paper as evidenced by the number of discussions and the interesting and pertinent observations made by the discussers. We wish to thank them and to express the hope that this will promote the development of reinjection methods and stoker improvements which will reduce the amount of flue dust carried from the furnace.

Mr. Callan's discussion confirms essential data given in the paper. We have made arrangements for the installation of lance doors in the side walls of the unit for control of slag growth on the rear wall as he suggests. However, we understand that there have been only one or two occasions during the several years operation of the unit where the slag growth on the rear wall has reached troublesome proportions.

Mr. Feeley describes a troublesome slagging condition and its correction on tube and tile side walls of a unit operated by his company. We are of the opinion that this condition is the result of operation at ratings in excess of the limits given in the

[17] Plant Engineer, Central Soya Company, Inc., Decatur, Ind.
[18] Plant Superintendent, Central Soya Company, Inc.

paper for heat release per square foot of projected furnace surface, per square foot of grate area, or both. We have not experienced this trouble on any of a number of our standard units operated within these limits.

Our experience indicates that the heat input to exposed lower side-wall headers with spreader firing is not sufficient to cause stress cracks in headers $^5/_8$ in. or less thick, if the headers are maintained clean internally. However, we have provided in the design for the top of the square headers to be flush with the grate in the hot position. The horizontal chill tubes are placed on top of the header in front of the side-wall tubes to provide a slag chill surface. Thus in this design, the headers are removed completely from exposure as suggested by Mr. Feeley, and we recommend this construction where feasible, regardless of header thickness.

We considered locating the oil and gas burners in the side walls but the resulting unbalance in gas temperatures from side to side entering the superheater makes this arrangement impractical. Actually, we have a number of successful installations with the burners located in the front wall without any undue complication of coal-bunker design or operating convenience.

We agree in general with Mr. Feeley's conclusions regarding the relation of velocity and pressure-part erosion, however, we are sure that dust loading and the nature of the dust play an important part and should not be disregarded. It is obvious that the reinjection of all of the flue dust is desirable in the interest of higher efficiency. It is hoped that these discussions will encourage the developments of methods of doing this with decreased gas dust loading so that uneconomical boiler designs are not required to prevent erosion and excessive maintenance.

We are indebted to Messrs. W. C. Holten and W. S. Major for the comparison with the tests at Racine and gratified by the close agreement in several respects. We believe that the difference in the amount of flue dust reported is due to a difference in the quality and sizing of the coal fired during the respective tests, rather than errors in testing as suggested by Mr. E. R. Kaiser. It has been our experience that when firing the more friable eastern coals, the dust loading is considerably higher than experienced with the harder lower grindability midwestern coals.

Recently, comparable tests have been obtained on the second unit installed in the plant where the tests reported in the paper were obtained. The stoker for the second unit incorporates the latest improvements, consisting of seals and a coking section at the rear of the grate. Apparently, these improvements have resulted in lower dust loading since the dust loading leaving the furnace under the same operating conditions was 14.5 lb versus 16.4 lb per thousand pounds of gas for the test reported in the paper. The dust loading at the boiler outlet was 8.4 lb as against 11.6 lb for the test reported.

We are grateful for Mr. McCarthy's favorable remarks about the design and his description of combustion conditions on spreader stokers which justify his opinions. Messrs. A. S. Tyson and H. Nash have covered the operating experience on another successful application of this design. Their tests of low fusion-ash coal at ratings in excess of design, and the resulting slagging troubles, indicate what happens when the limits set in the paper are exceeded and are reminiscent of the troubles described by Mr. Feeley. We particularly appreciate their contribution.

We believe the foregoing discussion answers the questions raised by Mr. E. C. Miller. There is no doubt that the single-pass boiler design already has been accepted as the superior design for spreader-stoker firing and will permit higher dust loadings, with higher gas velocity, than can be tolerated with baffled boilers. A comparison of the tests cited by Mr. Miller with the series of tests, one of which is discussed in the paper, shows that the heat-absorption characteristics of the furnace surfaces over the heat-release range is much more uniform for the arch design than for the open-furnace design. This is beneficial in setting superheater heating surface and accurately predicting superheated steam temperature. Thus the arch plays an integral part in the successful design of the unit rather than just a "commercial consideration."

Again, we would like to express our appreciation to the discussers for their interest in preparing these discussions.

Mechanical Analog-Computing Elements and Their Applications to Automatic Control

By ALVIN PIATT,[1] GLENDALE, CALIF.

In this paper some representative mechanical computing elements are described. The manner in which these computing elements can be utilized in computing systems applicable to the automatic control of industrial processes also is discussed. As examples of the way in which these mechanical computing elements can be used in computers, a computing flowmeter and a multi-element controller for a heat-transfer process are described.

INTRODUCTION

AS industrial processes become more complex, and better performance is expected, simple control systems may become inadequate. Information may be required about variables which it is not practical to measure directly, but which must be computed from other quantities more easily measured. It is because of such trends in the requirements for automatic control that computing instruments and controllers are becoming increasingly important. The computations may be performed in a number of ways. The computers may utilize mechanical, electromechanical,[2] or electrical computing elements. This paper will be limited to the consideration of mechanical computing elements which employ rotations or displacements as inputs and outputs. There will be some examples of how these computing elements may be used in computers applicable to the control of industrial processes.

GENERAL CONSIDERATIONS

Applications of computing devices to the automatic control of industrial processes can be grouped into two broad classifications; i.e., open-loop systems, and closed-loop systems.

In open-loop computing systems the inputs to the computer result in one or more outputs which have no influence on the inputs. The output information may be in a more useful form than the measured variables, or the output information may be required in addition to the measured variables. Computing and integrating flowmeters and ratio computers are examples of open-loop computers which may be used in industrial control. It is apparent that the accuracy of the output for this type of computer depends entirely on the accuracy of the input information and the accuracy of the computation.

In a closed-loop computing system one or more of the outputs is employed to adjust certain control agents in the controlled process. The inputs to the computer are responsive to changes in the variables of the process which in turn is influenced by the outputs of the computer system. Thus, as seen in Fig. 1, the system including the process and the computer is a closed loop which is influenced by changes in the uncontrolled variables of the proc-
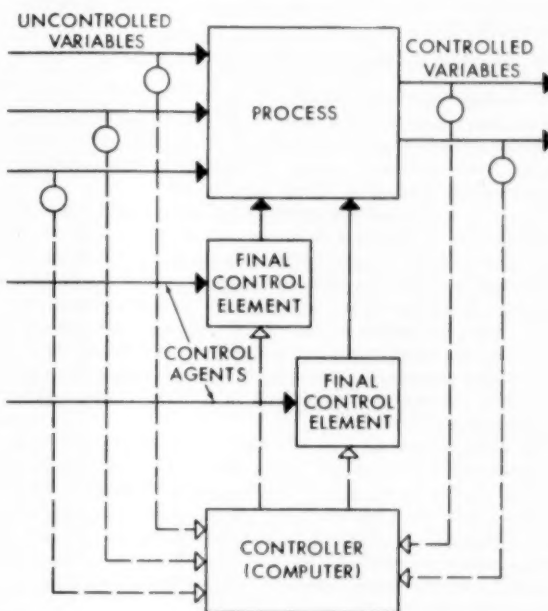
FIG. 1   BLOCK DIAGRAM OF A MULTI-ELEMENT CONTROL SYSTEM

ess. When there is more than one measured variable and possibly more than one control agent, the system is called a multi-element-control system and the controller generally will perform certain computations.

In multi-element control the variables of the process are measured and their effects on the process simulated in the computer so that a change in any of the variables of the process will result in controlling action which tends to maintain the controlled variable at the desired value. Multi-element control reduces lags in the process, reduces the effect of changes in uncontrolled variables, and permits closer control of the controlled variable without instability in the system.[3,4] The number of inputs employed and the accuracy of the computer depend on the quality of control desired. For many systems a very simple system using an approximate computer may be employed. In other systems the requirements may justify the use of more inputs to the computer and a computer which closely simulates the controlled process. In a closed-loop system the accuracy of the computation may be poor as compared to the precision of control of the controlled variable. The accuracy of all the inputs, except for the controlled variables, also may be of a low order.

There are cases where computers classed as open-loop computers may be used in closed-loop systems. An example of this would be the control of the flow of a gas. Differential pressure,

[3] "The ABC's of Multi-Element Control," by C. H. Barnard, Instruments, vol. 22, February, 1949, p. 179.

[4] "Operating Experiences With Multi-Element Control," by H. L. Andersen, Instruments, vol. 25, January, 1952, p. 101

absolute pressure, and temperature would be used to compute the flow of gas. The computed gas flow is then an input to a controller, which could be a multi-element system. In such a case the inputs to the flow computer and the flow computation would be required to have accuracies consistent with the desired accuracy of the flow indication and control. On the other hand, any computations performed in the controller can be of a much lower-order accuracy, as the accuracy of the controlled flow is basically determined by the accuracy of the computed flow and the sensitivity of the controller.

Computing Elements

An analog-computing element simulates a corresponding mathematical operation. In some cases an analog-computing element simulates a complete problem or a part of a problem rather than a single mathematical operation. Mechanical analog-computing elements have mechanical inputs and outputs.

Since the mechanical computing components considered here receive inputs as rotations or displacements, manual inputs to such computers can be accomplished conveniently by knobs or hand cranks with the functions displayed on dials or mechanical counters. Electrical inputs to mechanical computers require the use of servomechanisms to convert the electrical quantities to mechanical rotations or displacements. Quantities in a mechanical analog computer are transmitted between computing components by means of shafts and gears for rotations, and by means of links for displacements.

The outputs from mechanical computers in some cases can be used directly. The outputs can position dials and counters directly. If electrical outputs are required, transducers such as potentiometers can be driven directly by the mechanical computing components. If considerable power is required from the outputs, servomechanisms or other power-amplification means are required since the power output of the computing components, being moderately small in size, is limited.

In the following paragraphs some mechanical analog-computing elements are described which are particularly applicable for use in computing systems used in the control of industrial processes.

Addition or subtraction is accomplished with mechanical gear differentials when the quantities are available as shaft rotations. When the addition or subtraction is to be performed with displacements rather than rotations, an additive or subtractive link may be used.

Fig. 2 shows such a linkage. The bar to which the input and output links are connected is the additive or subtractive link. The two outer links are the inputs, and the link in between is the output which represents the sum or difference of the two input quantities. When the distances between the connection point of the output link and the connection points of each of the input links are the same, the output link will move one half the distance that one input link is displaced when the other input is fixed. By making the two arms of the additive link unequal, the two inputs, in effect, can be multiplied by different constants.

It is seen that by means of linkages such as the additive or subtractive linkage, displacements can be multiplied by constants. For a quantity which is in the form of a shaft rotation, gear ratios are used to multiply the quantity by a constant. If two variables are to be multiplied, a multiplying mechanism is used for mechanical analog multiplication. A linkage-multiplying mechanism is shown in Fig. 3. In this multiplying mechanism the inputs and the output are displacements. The two inputs are displaced proportionally to the two quantities to be multiplied. The displacement of the output link is then proportional to the product of the two inputs. The inputs and the output, in effect, can be multiplied by constants by the placement of the pivot points for the
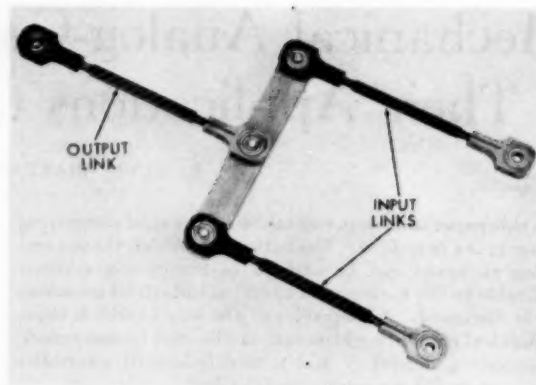

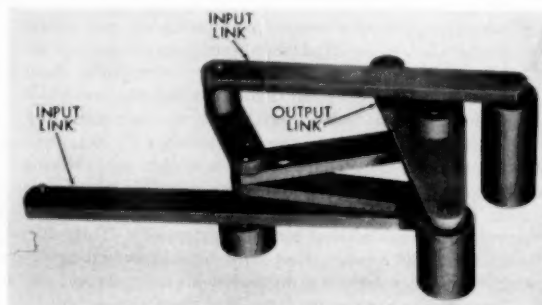Fig. 2   Additive or Subtractive Linkage

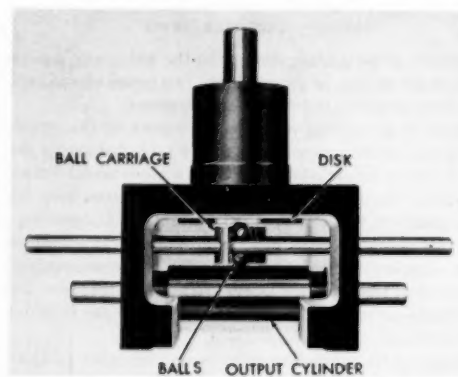Fig. 3   Linkage-Multiplying Mechanism

Fig. 4   Cutaway View of Ball-and-Disk Integrator

input and output links. Alignment holes are provided in the mechanism to facilitate setting the zero positions of the inputs and the output.

When it is desired to perform integration rather than multiplication, or to multiply a shaft rotational speed by a variable, a ball-and-disk integrator may be used. Fig. 4 is a cutaway view of a ball-and-disk integrator. The disk is rotated by one input. In integrating ydx, the disk is rotated such that increments of disk rotation are proportional to increments of dx. The ball carriage is displaced proportionally to y. The cylinder is the output of the integrator and the cylinder rotation is then proportional to the integral of y with respect to x. The ball carriage contains a sleeve in which there are two steel balls. The two balls separate

the cylinder and the disk which are forced toward each other by a spring in the disk-bearing assembly. At the zero position of the ball carriage, the balls are over the center of the disk, and rotation of the disk causes no rotation of the cylinder. The use of two balls in this type of integrator permits positioning the ball carriage without the balls slipping on either the disk or cylinder, even though there is no rotation of the disk. It is seen that when the ball carriage is moved, the two balls will rotate in opposite directions and will roll against the cylinder and the disk and against each other. For maximum resistance to wear, the disk surface is of carboloy, which is lapped to a mirror finish.

In addition to the mathematical operations mentioned, it is often required to generate functions of one variable. Typical of such functions are exponential, logarithmic, square, square-root, and trigonometric functions. Function generators may be designed for empirical relations or intricate mathematical functions. A common type of mechanical function generator is a cam with a cam follower.
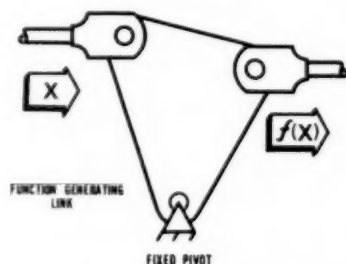
Fig. 5   Linkage-Type Function Generator

Fig. 5 shows an example of a simple linkage-type function generator. Function generators of this type can be made to approximate quite closely the mathematical functions mentioned. Linkage-type function generators usually require some time to design, but are simple to manufacture.

Mechanical computing elements like those described will have accuracies of the order of 0.1 per cent.

Computing and Integrating Flowmeter

The use of mechanical computing elements in a computer can be best understood by means of examples. Let us consider the problem of a computing and integrating flowmeter. This is a computer of the open-loop type so that the accuracy of computation must be consistent with the accuracy required of the flow.

The equation for the rate of discharge of a gas through an orifice meter when the differential pressure is small compared with the absolute pressure of the gas is

$$W = K \sqrt{\frac{w_0 P_1}{T_1} \Delta P} \quad \ldots \ldots \ldots \ldots \ldots [1]$$

where

$$K = C_d A_1 \sqrt{\frac{2g T_0}{P_0 \left[\left(\frac{D_1}{D_2} \right)^4 - 1 \right]}}$$

W = discharge rate, lb per sec
C_d = discharge coefficient of orifice
A_1 = area in square feet of pipe on high-pressure side
g = 32.17 fps per sec
T_0 = standard absolute temperature at which density w_0 of gas is measured

P_0 = standard absolute pressure at which density w_0 of gas is measured
D_1 = diameter of pipe on high-pressure side of orifice
D_2 = diameter of orifice, measured in same units as D_1
w_0 = density in pounds per cubic foot of gas measured at standard temperature T_0, standard pressure P_0
P_1 = absolute pressure on high-pressure side of orifice, measured in same units as P_0
T_1 = absolute temperature of gas on high-pressure side of orifice, measured in same units as T_0
ΔP = differential pressure between high and low-pressure sides of orifice, psf

If the volume of flow measured at standard temperature and pressure had been desired, the equation would be

$$V_0 = K \sqrt{\frac{P_1}{w_0 T_1} \Delta P}$$

Fig. 6 is a schematic diagram of a computing and integrating flowmeter which computes the rate of flow by Equation [1] and also determines the integral of the rate of discharge with respect to time. Because it is desirable to operate near zero rates of flow, it is impossible to drive the computing mechanism by the ΔP differential-pressure element because the mechanical advantage

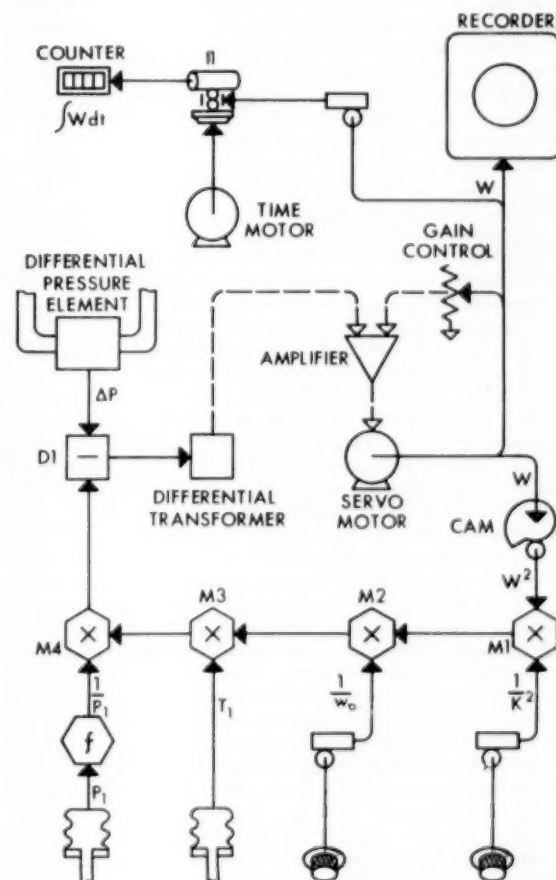Fig. 6   Schematic Diagram of Computing and Integrating Flowmeter

goes to zero at zero flow rate. For these reasons Equation [1] is rearranged for mechanization as follows

$$\frac{W^2 T_1}{K^2 w_0 P_1} = \Delta P \dots\dots\dots\dots\dots [2]$$

As seen in Fig. 6, the left-hand side of the equation is compared by a subtractive link D1, with the differential pressure ΔP. If both sides of the equation are not equal, there is a difference between the two quantities which displaces the differential transformer from zero. The error signal from the differential transformer, amplified by an amplifier, causes the servomotor to run in a direction depending on which side of the equation is greater. The rotational displacement of the servomotor is proportional to the rate of flow W. The servomotor positions the rate-of-flow recorder, the ball carriage of integrator I1, and the square-function cam which provides the square of W for the determination of the left-hand side of Equation [2]. If the left-hand side of Equation [2] should be smaller than ΔP, the difference will result in W being increased so that the equation will be in balance. In practice, a gain control probably will be required to reduce the gain of the amplifier at larger values of W.

The rotational displacement of the gear train which positions the square-function cam is proportional to the quantity W. A linkage-function generator also might have been used to generate the square of W. The linear displacement of the cam follower is one input to the linkage multiplier M1. The other input to M1 is derived from a manual input knob and dial. The dial and knob are shown as positioning a rack and pinion which in turn position the input to M1. The dial can have nonlinear graduations so that when the dial is set to the value of K, the reciprocal of the square of K will be introduced into the multiplier.

The output of M1 is an input to M2. The other input is shown as a manual input knob and dial to introduce w_0 into the computation. Like the K input, the dial for w_0 is graduated nonlinearly so that when the dial is set to w_0 the reciprocal of w_0 is entered into M2. The w_0 input is shown as a manual input. However, w_0 could be introduced automatically from a densitometer. This would probably require a servomechanism.

The output of M2 is one input to linkage multiplier M3. The other input is shown as the displacement of a bellows which receives a pressure proportional to temperature. This pressure could be obtained from a pneumatic temperature transmitter. With an input direct from a bellows, care must be taken that the area of the bellows is sufficient so that the load due to the linkage does not introduce an appreciable error. This simple bellows input is particularly applicable where the input is used for a relatively small correction in the equation.

The output of M3 is one input to M4. The other input to M4 is a displacement proportional to the reciprocal of pressure P_1. This is obtained from a function generator which has an input proportional to pressure. The output of M4 is one input to D1 which is used to equate both sides of Equation [2].

Integrator I1 integrates the rate of discharge, thus computing the total discharge. The disk of I1 is driven by a time motor which normally can be a synchronous motor operated from the power lines. The ball carriage is positioned proportional to W by a rack and pinion or by a cam positioned by the servogear train. The cylinder of the integrator derives a mechanical counter. The counter then will indicate the total discharge, since the counter has been set to zero.

The accuracy required of a computing flowmeter probably would be of the order of 0.5 per cent of the maximum rate of discharge. However, the accuracy of a computer will vary with the flow. At maximum flow rates, the accuracy of the computation may approach 0.1 per cent. Owing to the square-root function in

Equation [1] the error may be of the order of 1 per cent for flows about 5 per cent of maximum.

CONTROL OF A HEAT-TRANSFER PROCESS

Consider a heat-transfer process as shown in Fig. 7. The liquid leaving the heat exchanger is at temperature T_2. Assume that it is desired to maintain this temperature constant at the set point T_2'. The liquid enters the heat exchanger at temperature T_1 which is an uncontrolled variable subject to change due to con-
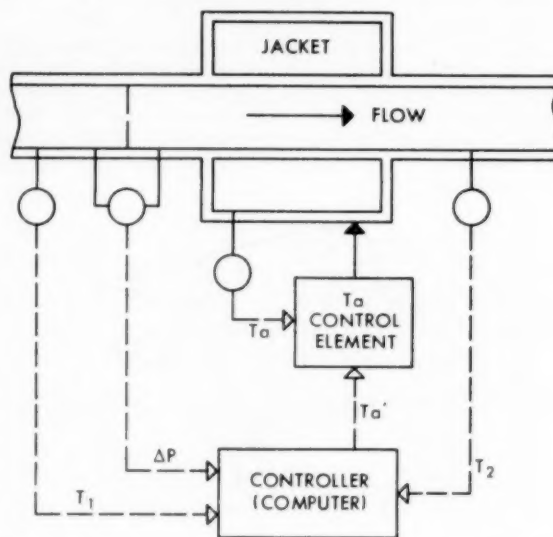

FIG. 7 , BLOCK DIAGRAM OF CONTROL SYSTEM FOR HEAT-TRANSFER PROCESS

ditions external to the process. The mass rate of flow W is also an uncontrolled variable and can change through a range of flows from near zero to maximum. The temperature of the jacket Ta is controlled by a separate controller which has the set point introduced by the output of the main controller Ta'. An equation can be written for Ta' in terms of T_1, T_2', W, and the constants of the system

$$Ta' = \frac{T_2' - T_1 e^{-k/W}}{1 - e^{-k/W}} \dots\dots\dots\dots [3]$$

where

$k = \pi D U L/c$
$D =$ inside diameter of heat-exchanger tube
$U =$ coefficient of heat transfer between jacket and liquid whose temperature is being controlled
$L =$ length of tube
$c =$ specific heat of liquid whose temperature is being controlled

The mass rate of flow W and the inlet temperature T_1 can be measured and introduced to a computer which computes the required jacket temperature to maintain the outlet temperature T_2 at the set-point temperature T_2'. If the constants of the process were known with sufficient accuracy, the variables were measured with sufficient accuracy, and the computation could be performed with sufficient accuracy, T_2 could be controlled without measuring T_2. While it might be possible ideally to do this, it is undoubtedly more advisable to measure T_2 also and to use this to monitor the action of the controller. By using T_2 it is not neces-

sary that the constants of the process be as accurately known, that the measurements of the variables (except T_2) be as accurate, or that the computation need be as accurate.

Since it is desired that the process be controlled primarily as a result of changes in T_1 and W, generally there should be little supplementary correction of T_2 required, and such correction should occur only after there has been time for the controller to have acted as a result of changes in T_1 and W. In order to accomplish such a result, even though T_1 and W may be continually changing, I1 (Fig. 8) is employed. This integrator is driven by a constant-speed motor, and its effect is to add a correction to the set point T_2'' so that a variable set point T_2'' is used in the computations of Ta'. The correction added to T_2'' is proportional to the integral of the difference between T_2 and T_2' with respect to time. The correction is such that T_2 will be brought closer to T_2'. The

Fig. 8 Schematic Diagram of Computer Used in Control of Heat-Transfer Process of Fig. 7

correction is larger the greater the error in T_2, and becomes larger the longer the error persists.

To facilitate mechanization of the equation, it is rearranged as follows

$$Ta'\,(1 - e^{-k/W}) = T_2'' - T_1 e^{-k/W} \ldots \ldots \ldots [4]$$

In the schematic, Fig. 8, W is shown as being obtained in a manner similar to that employed in the computing flowmeter, Fig. 6, except that no corrections are included for temperature and pressure since the fluid is considered to be a liquid. W is one of the inputs to the linkage multiplier, M1. The other input is the reciprocal of k which is introduced by a dial graduated nonlinearly. For any particular installation, D and L would be constants. However, U and c would vary with changes in the properties of the liquid.

If the quantity U divided by c can be expressed as a function of some easily measured property of the liquid, then the dial could be graduated in terms of this property of the liquid. The reciprocal of k also might be introduced automatically if indicated by the requirements of the control system. The ratio W divided by k is the input to the linkage function generator which generates the function $e^{-k/W}$. This function is an input to M2. The other input to M2 is T_1. The output of M2 is one input to D2 which subtracts $T_1 e^{-k/W}$ from T_2''. The output of D2 is one input to D3 which compares the right and left-hand sides of Equation [4]. The other input to D3 is the output of M3 which multiplies Ta' and the quantity $1 - e^{-k/W}$.

In a mechanical analog computer a constant can be added to a function without the use of additional computing elements. This is accomplished by providing means so that when the output of one element is at zero, the input to the other element will differ from zero by an amount corresponding to the constant. Also in a mechanical analog computer the algebraic signs of quantities can be changed simply by ascertaining that the linkages are so connected and the gearing between shafts so arranged that the directions of the displacements from zero of all the input and output devices and all the computing elements result in the correct algebraic sign for all quantities in the equation. By such means the output of the function generator, $e^{-k/W}$, is converted to the quantity $1 - e^{-k/W}$ which is one input to M3.

The output of D3 represents the difference between the right and the left-hand sides of Equation [4]. This difference is zero when the equation is solved correctly. A differential transformer, amplifier, and servomotor could have been used to balance the equation as in the case of the solution for flow. However, since forces of reasonable magnitude are available, and time constants of the order of a second or two probably would be acceptable in the solution, the method shown in the schematic can be used. The output displacement of D3 positions the ball carriage of I2. When the output of D3 is at zero, there is no rotation of the cylinder of I2 which positions the input to M3 and the output device of the computer proportional to Ta'. When the output of D3 is zero, Ta' has the correct value corresponding to the inputs to the computer. If the output of D3 is not zero, there will be rotation of the cylinder of I2 which will change the value of Ta' so as to tend to make both sides of Equation [4] equal.

Equation [3] used in this example is for steady-state conditions and will not give perfect control for transient conditions. Furthermore, the equation solves for the jacket temperature and it is not possible instantaneously to change the jacket temperature. Some of these shortcomings are inherent in the process rather than the controller. For example, if a steady-state condition existed and either W or T_1 changed instantaneously, there is no jacket temperature Ta, which if applied instantaneously to a heat exchanger of finite length would not result in a transient change in T_2. However, if a reservoir was provided on the output of the heat exchanger, it then would be possible to provide a controller which would tend to maintain the integral of $T_2' - T_2$ with respect to time equal to zero. Thus a reservoir of sufficient capacity in which mixing occurs could be maintained within close limits of the set point. Such a system is more complex than the simple heat exchanger used in this example.
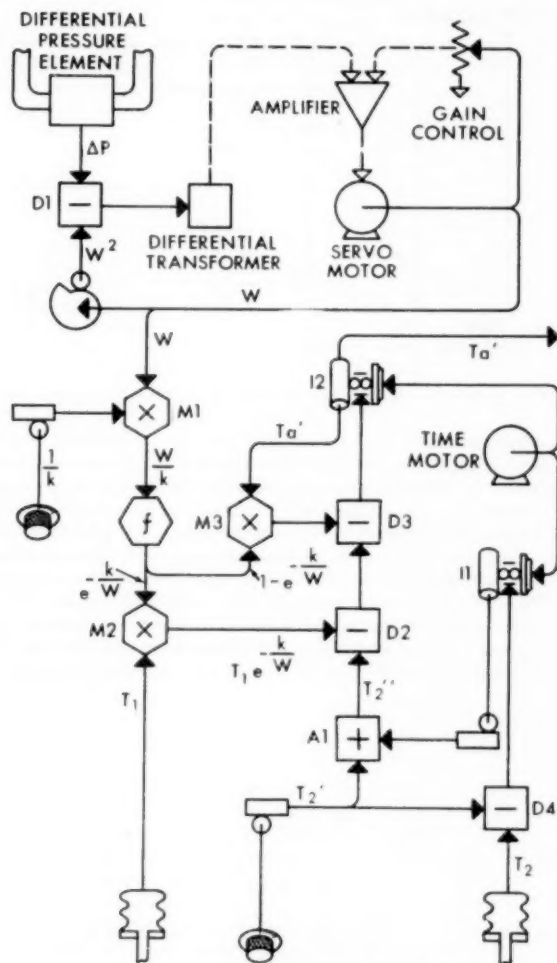
In cases where the flow is subject to rapid increases and decreases due to fluctuations in demand, it may be preferable to average or smooth the flow input in some manner. Fig. 9(a) shows a schematic representation of a simple smoothing circuit consisting of an integrator and a differential with appropriate interconnections. If there is an input u to this system, the equation relating the output v to u is

$$\frac{dv}{dt} = \frac{1}{k}(u - v)$$

where k is the time constant of the system. This system operates in the same fashion as the equivalent electrical circuit shown in Fig. 9(b). In the electrical circuit, the time constant is the product RC, E_1 corresponds to u, and E_2 corresponds to v. These circuits perform first-derivative smoothing. The response of such a system to a step input of u is

$$v = u(1 - e^{-t/k})$$

which is shown graphically in Fig. 9(c). Additional derivatives can be used in more complex systems to obtain better smoothing. Smoothing techniques may be indicated where the flow of material is subject to considerable fluctuations. An example might be in the control of the temperature of a furnace where there are considerable fluctuations in the rate of flow of material owing to variations in demand.

The system shown in Fig. 9(a) also can be used to determine rates or derivatives. If u changes at a constant rate, the displacement of the ball carriage of the integrator will be proportional to the rate of change of u with respect to time after equilibrium has been reached. In many cases an adequate solution can be obtained in a fraction of a second. If the disk of the integrator had been driven by some other function rather than time, the rate of change of u would have been determined with respect to this function.

CONCLUSIONS

This paper has discussed in a limited way the application of mechanical analog-computing elements to computers for use in the automatic control of industrial processes. The application of these devices to automatic control certainly has not been exhausted.

No attempt has been made to compare mechanical computing systems with corresponding electrical, electromechanical, or digital systems. The form in which inputs are available and the
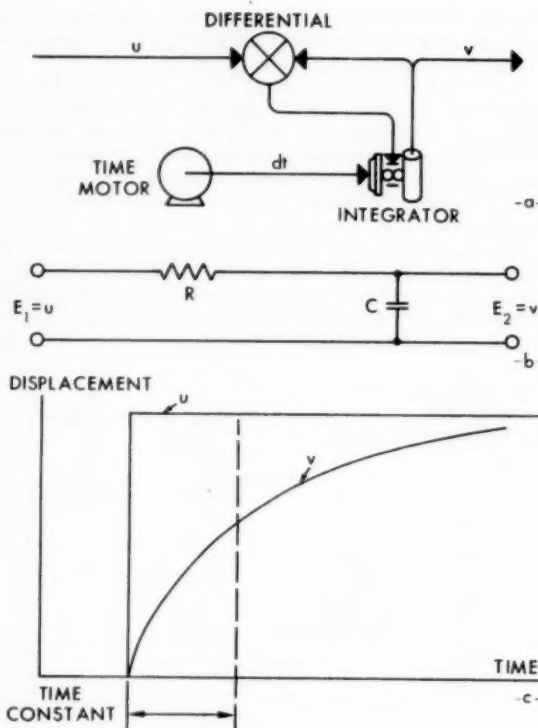
FIG. 9   SCHEMATIC DIAGRAM OF SYSTEM FOR SMOOTHING INFORMATION

form required for the outputs is probably the most important factor in selecting the type of computation. The speed of computation of mechanical or electromechanical systems is probably adequate for most industrial processes.

Little in the way of general statements can be made regarding the preference of one method of computation over another. Each problem should be considered individually to determine which method is most advantageous. It can be expected that the various types of computing devices available will continue to find increased application in the control of industrial processes.

Proportional Control of Rate-Type Servomotors

By J. L. SHEARER,[1] CAMBRIDGE, MASS.

Optimum proportional control of various kinds of rate-type servomotors having second-order lag effects has been determined by means of an electronic-analog study. The results of this study, presented in the form of non-dimensional graphs, establish the conditions for obtaining the fastest closed-loop response with no overshoot and closed-loop response with 20 per cent overshoot. Information relating to the speed of response associated with optimum control also is given graphically. It is shown that the results of this work may be applied likewise to the floating control of second-order processes.

Nomenclature

The following nomenclature is used in the paper:

B = measured variable

C = controlled variable

D = derivative with respect to time, $\dfrac{d}{dt}$

E = error

K_l = loop gain

M = manipulated variable

N = controller output

R = reference input

T_1 = time at first crossover, transient response with 20 per cent overshoot

T_2 = time at first peak, transient response with 20 per cent overshoot

T_3 = time to reach final value, fastest transient response with no overshoot

T_b' = time to reach final value, fastest transient response with no oscillation

X = servomotor input

a_1 = servomotor constant

a_2 = servomotor constant

k = steady-state gain

k_f = measuring-means gain

k_s = servomotor gain

t = time

ζ = damping ratio

τ_1 = larger time constant of servomotor

τ_2 = smaller time constant of servomotor

ω_n = undamped natural frequency

s = uncontrolled servomotor (subscript)

ss = steady state (subscript)

l_1 = length of upper part of summation lever

l_2 = length of lower part of summation lever

Introduction

When rate-type servomotors are put under proportional control, the resulting closed-loop systems may become unstable when the amount of proportional control is increased indiscriminately. A rate-type servomotor is defined here as a servomotor with a rate of change of output proportional to the input during steady-state operation. It is usually advantageous to introduce as much proportional control as possible in order to obtain the fastest speed of response. More elaborate means of control may be employed to improve speed of response without sacrificing system stability, but it is important to know first what performance may be attained with simple proportional control. Recent work by the author on hydraulic control systems revealed the need of understanding thoroughly the performance of rate-type servomotors having second-order lag effects when under proportional control. A high-speed electronic-analog computer proved to be a satisfactory means of gaining this understanding for various types of second-order lag effects.

Characteristics of Rate-Type Servomotors

The power required to manipulate the input to a process under automatic control, such as that shown schematically in Fig. 1, often makes necessary the use of a means of power amplification which is capable of manipulating a variable M so that it is proportional to controller output N.
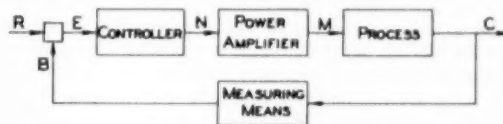

FIG. 1 TYPICAL AUTOMATIC CONTROL SYSTEM

Instantaneous response of M to changes in N would be highly desirable, but such a response, if truly instantaneous, would require the expenditure of large amounts of power for rapidly changing values of N. The need for fast response in each instance must be reconciled with the availability of power for the amplification to be attained.

The power level required in many mechanical systems is attainable only by using a rate-type servomotor with a *rate of change* of output proportional in the steady state to its input. In other words, the servomotor steady-state output is proportional to the integral of its input. The valve-controlled fluid motor and the resistance-controlled electric motor, shown schematically in Fig. 2, are examples of rate-type servomotors when motor-shaft *position* is the output. Unless such a steady-state integration is required specifically in the automatic control system, some means must be employed to convert this steady-state integrating action into the desired steady-state proportional action.

In addition to the steady-state integration inherent in these devices, time-lag effects between output *rate* and input are often significant during transient operation, depending on the design of the servomotor and the type of load it must drive. When only one time-lag effect between output rate and input is significant,
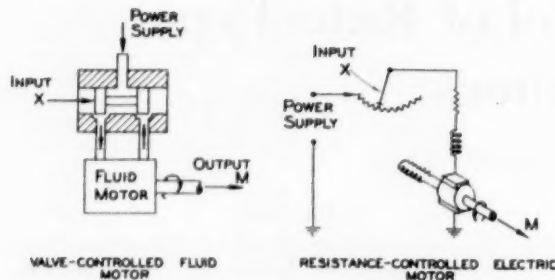
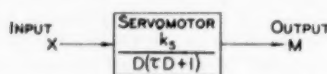FIG. 2   EXAMPLES OF RATE-TYPE SERVOMOTORS

FIG. 3   BLOCK-DIAGRAM REPRESENTATION OF RATE-TYPE SERVO-MOTOR HAVING SINGLE TIME LAG BETWEEN OUTPUT RATE AND INPUT
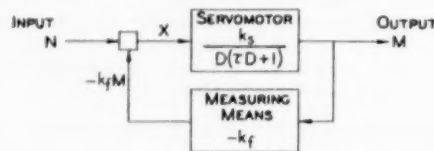

FIG. 4   PROPORTIONAL CONTROL OF RATE-TYPE SERVOMOTOR HAVING SINGLE TIME-LAG EFFECT

the servomotor may be represented symbolically by a functional block diagram, as shown in Fig. 3. A servomotor of this type may be employed in a system such as that shown symbolically in Fig. 4 in order to obtain an output M which is proportional, in the steady state, to an input N. This is basically a closed-loop control system in which the servomotor output is measured and fed back in such a way that it is compared with the input N. If the measuring means is sufficiently fast (negligible time lags), the relationship between the output M and the input N may be expressed by the following second-order differential equation

$$(\tau D^2 + D + k_s k_f)M = k_s N \dots\dots\dots\dots\dots [1]$$

and in the steady state

$$M_{ss} = \left(\frac{1}{k_f}\right) N_{ss} \dots\dots\dots\dots\dots\dots [2]$$

The dynamic characteristics of such a system are ascertained readily from the coefficients of Equation [1], and its transient and frequency-response characteristics are discussed thoroughly elsewhere.[2,3,4,5] It is worthwhile noting here that the undamped natural frequency ω_n and the damping ratio ζ of this system are determined as

[2] "Principles of Servomechanisms," by G. S. Brown and D. P. Campbell, John Wiley and Sons, Inc., New York, N. Y., 1950, pp. 48-56.

[3] "Automatic Feedback Control," by W. R. Ahrendt and J. F. Taplin, McGraw-Hill Book Company, Inc., New York, N. Y., 1951, pp. 53-63.

[4] "Servomechanisms and Regulating System Design," by H. Chestnut and R. W. Mayer, John Wiley and Sons, Inc., New York, N. Y., 1951, pp. 59-63.

[5] "Methods for Associating Mathematical Solutions With Common Forms," by C. S. Draper, S. Lees, and W. McKay, *Instrument Engineering*, vol. 2, McGraw-Hill Book Company, Inc., New York, N. Y., 1953, chapter 19, pp. 184-357.

$$\omega_n = \sqrt{\frac{K_l}{\tau}} \dots\dots\dots\dots\dots [3]$$

$$\zeta = \frac{1}{2\sqrt{K_l \tau}} \dots\dots\dots\dots\dots [4]$$

where

$$K_l = k_s k_f$$

Thus, increasing the loop gain K_l increases the speed of response and decreases the degree of stability of this system. Fortunately, many servomotors have only one significant time-lag effect when driving certain types of loads, and their performance under various operating conditions can be surveyed readily with Equations [3] and [4]. In instances when τ is negligible, the system is stable for all values of K_l.

SERVOMOTORS WITH SECOND-ORDER LAG EFFECTS

Experience has shown that a second-order lag effect is significant in some servomotors. When this condition exists, the servomotor may be represented symbolically as shown in Fig. 5
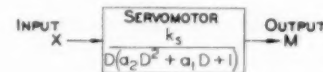

FIG. 5   BLOCK-DIAGRAM REPRESENTATION OF RATE-TYPE SERVO-MOTOR HAVING SECOND-ORDER LAG EFFECT BETWEEN OUTPUT RATE AND INPUT

The relationship between output rate DM and X is expressed mathematically as

$$DM = \frac{k_s X}{a_2 D^2 + a_1 D + 1} \dots\dots\dots\dots [5]$$

If this system is *overdamped*, the denominator of Equation [5] may be expressed as

$$a_2 D^2 + a_1 D + 1 = (\tau_1 D + 1)(\tau_2 D + 1) \dots\dots [6]$$

where

$$\tau_1, \tau_2 = \frac{a_1}{2}\left(1 \pm \sqrt{1 - \frac{4a_2}{a_1^2}}\right) \dots\dots\dots [7]$$

The time constants, τ_1 and τ_2, which are positive real numbers, denote two distinct time lags. If this system is *underdamped*, the denominator of Equation [5] may be written as

$$a_2 D^2 + a_1 D + 1 = \left(\frac{1}{\omega_{ns}}\right)^2 D^2 + \left(\frac{2\zeta_s}{\omega_{ns}}\right) D + 1 \dots [8]$$

where

$$\omega_{ns} = \sqrt{\frac{1}{a_2}} \dots\dots\dots\dots\dots [9]$$

$$\zeta_s = \frac{a_1}{2\sqrt{a_2}}, \dots\dots\dots\dots\dots [10]$$

and the subscript s refers to the uncontrolled servomotor.

When a servomotor with a second-order lag effect is put under proportional control as shown in Fig. 6, the relationship between output M and input N may be expressed by the third-order differential equation

$$(a_2 D^3 + a_1 D^2 + D + k_s k_f)M = k_s N \dots\dots [11]$$

and in the steady state

$$M_{ss} = \frac{1}{k_f} N_{ss} \quad \dots \dots \dots \dots \dots \quad [12]$$

The dynamic characteristics of this system cannot be revealed by a simple analytical treatment similar to that employed for a
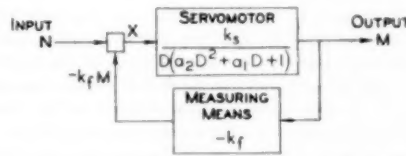

FIG. 6 PROPORTIONAL CONTROL OF RATE-TYPE SERVOMOTOR HAVING SECOND-ORDER LAG EFFECT

system with a second-order differential equation. It is possible to find the roots of the characteristic equation

$$a_2 D^3 + a_1 D^2 + D + k_s k_f = 0 \quad \dots \dots \dots \quad [13]$$

But this process usually proves cumbersome if a comprehensive survey of all system parameters is to be made in order to achieve an optimum system design.

ELECTRONIC-ANALOG STUDY

An electronic-analog computer was found to be very useful in gaining a thorough understanding of the dynamic performance of this type of third-order system under all possible conditions of operation. A dimensional analysis may be employed[6] to show that the loop gain $K_l = k_s k_f$ of the system in Fig. 6 is related to the second-order lag effect, as shown in the following equations

$$K_l \tau_1 = f_1 \left(\frac{\tau_1}{\tau_2}\right) \text{ (overdamped servomotor)} \dots \dots \quad [14]$$

$$\frac{K_l}{\omega_{ns}} = f_2(\zeta_s) \text{ (underdamped servomotor)} \dots \dots \quad [15]$$

if a given type of response of M is to be obtained when a step change in N is made.

The types of response of most interest are (a) the fastest response with no overshoot and (b) the response with 20 per cent overshoot. Figs. 7(a) and 7(b) show the actual transient-response curves that were obtained during an electronic-analog study. When this study was made, unity feedback was employed and the effects of k_f and k_s were combined into K_l as shown in the upper parts of Fig. 8 in order to simplify presentation of the results. It is interesting to note that the rate of decay of the 20 per cent overshoot response becomes small and that the fastest response with no overshoot is still oscillatory when the uncontrolled servomotor is well underdamped. This shows clearly that care must be taken in specifying the transient-response performance of such systems. In cases where this effect occurred, the fastest nonoscillatory response also was found. Fig. 8 shows graphically the functional relationships of Equations [14] and [15] plotted from the data given in Fig. 7.

Furthermore, it can be shown by dimensional analysis that the response times T_1, T_2, and T_3, as defined in Fig. 9, are related to the second-order lag characteristics as follows

$$\frac{T}{\tau_1} = f_3 \left(\frac{\tau_1}{\tau_2}\right) \dots \dots \dots \dots \dots \quad [16]$$

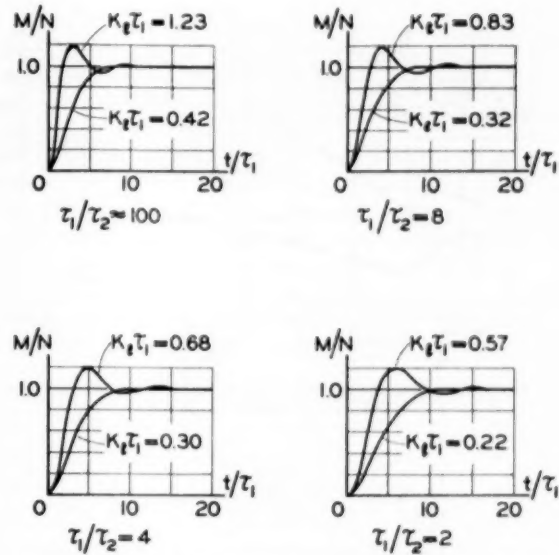[6] See Appendix for sample dimensional analysis.

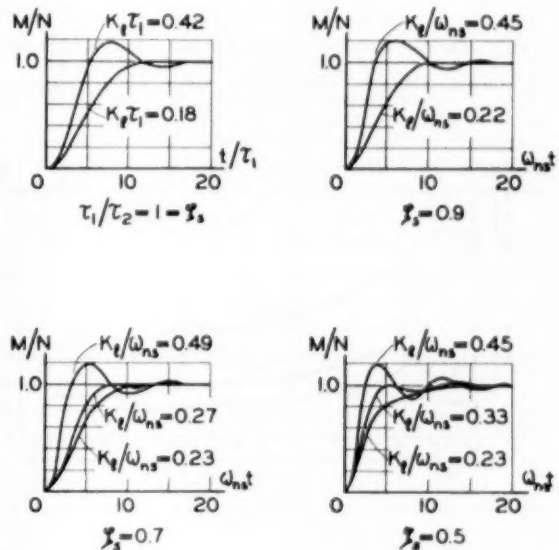FIG. 7(a) TRANSIENT-RESPONSE CURVES OBTAINED FROM ELECTRONIC-ANALOG STUDY—SERVOMOTOR OVERDAMPED

FIG. 7(b) TRANSIENT-RESPONSE CURVES OBTAINED FROM ELECTRONIC-ANALOG STUDY—SERVOMOTOR UNDERDAMPED

$$\omega_{ns} T = f_4(\zeta_s) \dots \dots \dots \dots \dots \quad [17]$$

These functional relationships of Equations [16] and [17] are shown in Fig. 10.

This paper has been limited to the treatment of proportional control of rate-type servomotors because this is the simplest way to eliminate the steady-state integration inherent in a rate-type servomotor, and it was believed that it would be useful to survey comprehensively the capabilities of this type of control before investigating more elaborate means of control.
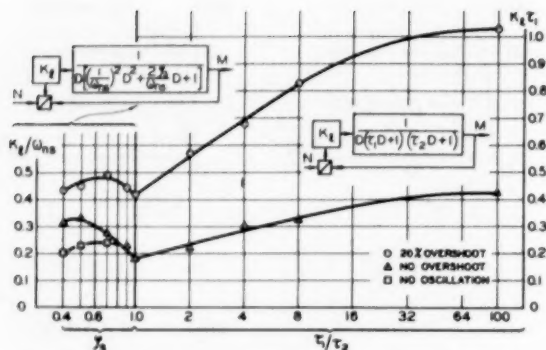
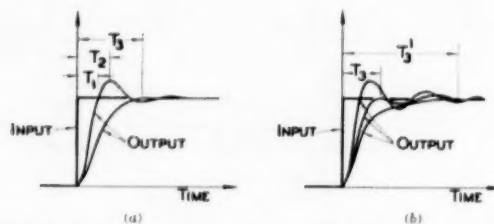FIG. 8 DIMENSIONLESS LOOP GAIN VERSUS ζ_s AND τ_1/τ_2 FOR TYPICAL TRANSIENT RESPONSES

FIG. 9 TYPICAL TRANSIENT RESPONSES SHOWING CHARACTERISTIC RESPONSE TIMES

(a, Proportional control of *overdamped* rate-type servomotor; b, proportional control for *underdamped* rate-type servomotor.)
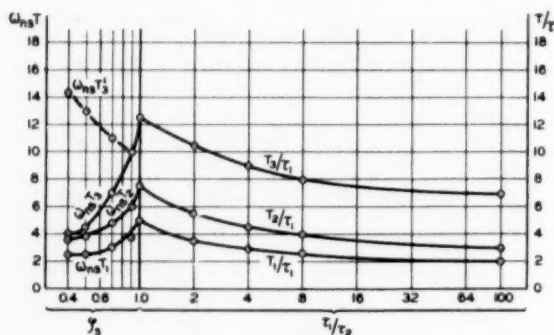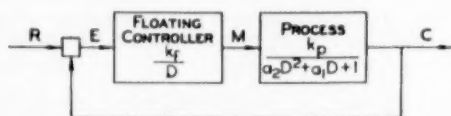

FIG. 10 DIMENSIONLESS RESPONSE TIMES VERSUS ζ_s AND τ_1/τ_2

FIG. 11 FLOATING CONTROL OF SECOND-ORDER PROCESS

The application of this work to a typical problem is demonstrated in the Appendix.

The results of this investigation also are applicable to the reset control (with no proportioning action) of second-order processes, as shown in Fig. 11, because this is dynamically the same type of problem.

CONCLUSIONS

The results of this work show clearly that a rate-type servomotor with second-order lag effects may be controlled satisfactorily by simple proportional feedback if its damping ratio without control is greater than 0.7. The ratio of the loop gain K_l to the servomotor natural frequency ω_{ns} required to produce a given type of response does not vary appreciably with servomotor damping ratio ζ_s if the servomotor is underdamped. Expressing the second-order lag effect of an overdamped rate-type servomotor in terms of its real time constants τ_1 and τ_2 where τ_1 is the larger time constant, it may be seen that the value of $K_l \tau_1$ required to produce a given type of response is roughly doubled as the value of τ_1/τ_2 varies from 1 to 10. As the value of τ_1/τ_2 increases above 10, little variation of $K_l \tau_1$ occurs, indicating that the effect of τ_2 is negligible when it is less than $\tau_1/10$.

It may be seen that the characteristic response times of underdamped and overdamped servomotors are affected most strongly by the values of ω_{ns} and τ_1, respectively, and they never vary by more than a factor of 2 as the degree of damping in the uncontrolled servomotor is changed.

ACKNOWLEDGMENT

The author is indebted to Profs. J. A. Hrones, J. B. Reswick, and Gerhard Reethof of the Massachusetts Institute of Technology, for the advice and counsel given by them during the preparation of this paper.

Appendix

DIMENSIONAL ANALYSIS

Consider the case when the servomotor is overdamped. Let M_{max} be the maximum value that M attains on the first overshoot and M_{ss} be the final steady-state value of M after a step change in N. In general, M_{max} will be a function of all of the other variables and we may write

$$M_{max} = f_a(M_{ss}, K_l, \tau_1, \tau_2)$$

where M_{max} and M_{ss} have the same dimensions, K_l has the dimension $(1/t)$ and τ_1 and τ_2 have the dimension (t). Forming dimensionless π's we find

$$\frac{M_{max}}{M_{ss}} = \pi_1$$

$$K_l \tau_1 = \pi_2$$

$$\frac{\tau_1}{\tau_2} = \pi_3$$

Then we may write

$$\pi_2 = f_b(\pi_1, \pi_3)$$

or

$$K_l \tau_1 = f\left(\frac{\tau_1}{\tau_2}\right) \text{ for a given value of } \pi_1$$

SOLUTION OF A TYPICAL CONTROL PROBLEM

The results of this paper may be employed in the solution of a typical control problem in order to illustrate how they may be used in engineering practice.

Consider the problem of controlling the position of a moving member of a machine. In order to meet requirements such as maximum velocity, acceleration, load forces, and speed of response, a rate-type hydraulic servomotor is employed as shown schematically in Fig. 12. The load consists of the member to be

positioned and effects associated with its motion. The input to this system is the position X of the servomotor-stroking mechanism and the output is the position M of the load. In order to determine how M is related to X, the dynamic characteristics of the
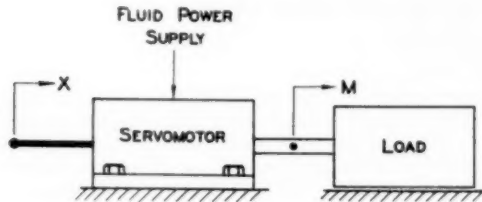

FIG. 12 RATE-TYPE HYDRAULIC SERVOMOTOR AND LOAD

servomotor and its load must be ascertained. In reality, the load must be considered as part of the servomotor system, and henceforth the term servomotor system shall mean the servomotor and its load.

Suppose that a dynamic analysis of the servomotor system yields the following relationship between M and X

$$(3 \times 10^{-4}D^2 + 10^{-2}D + 1)DM = 100X \quad \text{[18]}$$

where the damping ratio of the servomotor system is found to be

$$\zeta_s = \frac{10^{-2}}{2\sqrt{3 \times 10^{-4}}} = \frac{1}{2\sqrt{3}} = 0.285 \quad \text{[19]}$$

Since the analog study indicates that proportional control is not very satisfactory with a rate-type servomotor system having a damping ratio less than 0.7, it is necessary first to improve the servomotor-system characteristics. Suppose that this can be done and that the system now yields the following relationship between M and X

$$(4 \times 10^{-4}D^2 + 5 \times 10^{-2}D + 1)DM = 100X \quad \text{[20]}$$

Now the damping ratio is

$$\zeta_s = \frac{5 \times 10^{-2}}{2\sqrt{4 \times 10^{-4}}} = \frac{5}{4} = 1.25 \quad \text{[21]}$$

and the time constants τ_1 and τ_2 are found to be

$$\tau_1, \tau_2 = \frac{5 \times 10^{-2}}{2}\left(1 \pm \sqrt{1 - \frac{16 \times 10^{-4}}{25 \times 10^{-4}}}\right)$$

$$= 2.5 (1 \pm 0.6) \times 10^{-2} \text{ sec} \quad \text{[22]}$$

or

$$\tau_1 = 0.04 \text{ sec} \quad \text{[23]}$$

and

$$\tau_2 = 0.01 \text{ sec} \quad \text{[24]}$$

In order to establish control of the output *position M*, a simple feedback linkage and summation lever may be employed as shown in Fig. 13. An analysis of small motions of this linkage yields the following equation

$$X = \left(\frac{l_1 + l_2}{l_2}\right)N - \left(\frac{l_1}{l_2}\right)M \quad \text{[25]}$$

The complete system now may be represented by the functional block diagram shown in Fig. 14. The loop gain is given by
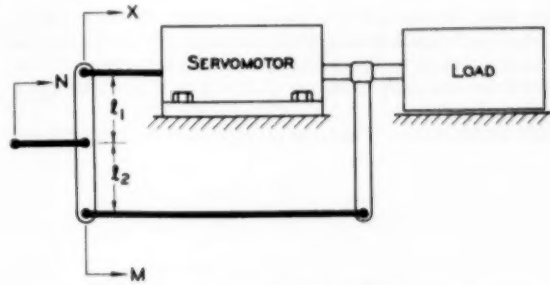

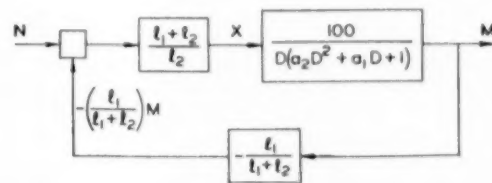FIG. 13 PROPORTIONAL CONTROL WITH MECHANICAL FEEDBACK

FIG. 14 BLOCK-DIAGRAM REPRESENTATION OF COMPLETE SYSTEM

$$K_l = 100 \frac{l_1}{l_2} \quad \text{[26]}$$

and using the value of τ_1 found in Equation [23]

$$K_l\tau_1 = 4 \frac{l_1}{l_2} \quad \text{[27]}$$

In order to attain highest speed of response, a transient response with 20 per cent overshoot is considered to be acceptable and, from Fig. 8, it is seen that when the value of $K_l\tau_1$ is equal to 0.69 this system will respond with 20 per cent overshoot when a step change in N occurs.

Substituting this value of $K_l\tau_1$ in Equation [27] and solving for l_1/l_2 we find

$$\frac{l_1}{l_2} = \frac{0.69}{4} = 0.17 \quad \text{[28]}$$

Employing Equation [12], the steady-state relationship between M and N is found to be

$$M_{ss} = \frac{N_{ss}}{k_f} = \left(\frac{l_1 + l_2}{l_1}\right)N_{ss} = 6.9N_{ss} \quad \text{[29]}$$

From Fig. 10 is seen that a period of

$$T_2 = 4.6\tau_1 = 0.18 \text{ sec} \quad \text{[30]}$$

must elapse before the value of M can reach its first peak.

Discussion

P. S. CREAGER.[7] The author has presented an interesting study of an important and, at the same time, a basic class of servomotors.

The consistent use of nondimensionalized quantities is to be especially commended. The data and curves should be directly usable in a wide variety of problems.

Oral discussion clarified a point of nomenclature and, at the

same time, emphasized the difficult problem of achieving a standard set of symbols that would be reasonably satisfactory to the many diverse groups working with feedback control. The writer refers especially to the use of $D = d/dt$, rather than p or s (Laplace transform).

The author states, "The types of response of most interest are (*a*) the fastest response with no overshoot and (*b*) the response with 20 per cent overshoot." As far as the writer knows, (*a*) applies in all fields of feedback control. However, considerable process control and servomechanism literature uses 25 per cent overshoot for case (*b*). The writer suggests that some discussion of the choice involved would be helpful.

Dynamic Characteristics of Valve-Controlled Hydraulic Servomotors

By J. L. SHEARER,[1] CAMBRIDGE, MASS.

A servomotor consisting of a valve-controlled ram connected to a mass plus viscous-friction load is analyzed on the basis of its response to small changes of valve position and external load force. The approach is sufficiently general to enable one to deal effectively with systems in which fluid compressibility is an important factor. At the same time, this approach is helpful in working with simpler systems. A functional block diagram is employed to delineate symbolically the significance of each system characteristic. A sample design problem is worked out to demonstrate how the material in this paper may be applied to a practical problem.

NOMENCLATURE

The following nomenclature is used in the paper:

A = ram area, sq in.
A_1 = area of orifice No. 1, sq in.
A_2 = area of orifice No. 2, sq in.
A_3 = area of orifice No. 3, sq in.
A_4 = area of orifice No. 4, sq in.
b = load damping coefficient, lb-sec/in.
C_1 = valve characteristic—partial derivative of flow with respect to pressure, in^3/lb-sec
C_2 = laminar leakage flow coefficient, in^5/lb-sec
C_d = orifice discharge coefficient
D = differential operator denoting derivative with respect to time d/dt, 1/sec
i = subscript denoting initial value
k_1 = valve characteristic—partial derivative of flow with respect to valve position, in^2/sec
k_2 = $C_1 + C_2$, in^5/lb-sec
k_3 = $\dfrac{1}{2}\left(k_e + \dfrac{\mathcal{V}_i}{\beta}\right)$, in^5/lb
k_e = coefficient of elasticity of each fluid line connecting ram to valve, in^5/lb
L = external load force, lb
m = load mass, lb-sec^2/in.
P_a = fluid pressure on left side of ram, psi
P_b = fluid pressure on right side of ram, psi
P_e = exhaust pressure, psi
P_m = difference in pressure across ram ($P_m = P_a - P_b$), psi
P_s = supply pressure, psi
Q_a = volume rate of flow of fluid into chamber on left side of ram, in^3/sec
Q_b = volume rate of flow of fluid into chamber on right side of ram, in^3/sec
Q_l = volume rate of leakage flow past ram, in^3/sec
Q_q = quiescent supply flow to valve, in^3/sec

Q_{max} = maximum no-load motor flow of open-center 4-way valve, in^3/sec
Q_1 = rate of flow through orifice No. 1, in^3/sec
Q_2 = rate of flow through orifice No. 2, in^3/sec
Q_3 = rate of flow through orifice No. 3, in^3/sec
Q_4 = rate of flow through orifice No. 4, in^3/sec
t = time, sec
U = valve underlap, in.
$\mathcal{V}_a$ = volume of fluid between left side of ram and valve, in.^{3}
$\mathcal{V}_b$ = volume of fluid between right side of ram and valve, in.^{3}
$\mathcal{V}_i$ = initial value of $\mathcal{V}_a$ and $\mathcal{V}_b$, in.^{3}
w = valve port width, in.
X = displacement of valve from center position, in.
Y = position of ram from arbitrary datum, in.
β = bulk modulus of elasticity of fluid, psi
Δ = prefix indicating a small change
ζ_s = servomotor damping ratio
π_a = dimensionless parameter
π_b = dimensionless parameter
ρ = mass density of fluid, lb-sec^2/in.^{4}
τ_1 = larger time constant of overdamped servomotor, sec
τ_2 = smaller time constant of overdamped servomotor, sec
ω_{ns} = undamped natural frequency of servomotor, 1/sec

INTRODUCTION

Experience has shown that when the mass on the output shaft of a valve-controlled servomotor is sufficiently large, the effect of fluid compressibility and elasticity of fluid lines plays an important role in system performance. As industrial and military requirements have created a demand for faster, stable systems capable of driving massive loads, the problems associated with the compliant nature of the coupling between valve and motor have grown. Recent work in the Dynamic Analysis and Control Laboratory and in the Department of Mechanical Engineering at the Massachusetts Institute of Technology with flow-valve characteristics and the simulation of dynamic systems has led to a better understanding of the dynamic behavior of systems employing valve-controlled servomotors. Experience has shown that it is important to understand thoroughly the characteristics of the servomotor and its load in order to incorporate the servomotor successfully into more complex systems. A 4-way valve and a ram-type motor have been chosen as the hydraulic components to be analyzed here. The fundamental concepts developed are common to servomotors employing either 3-way or 4-way valves and either linear or rotary motors.

MAJOR ASSUMPTIONS

A typical valve-controlled hydraulic servomotor with mass and viscous friction on its output shaft is shown schematically in Fig. 1. A number of simplifying assumptions are necessary in order to maintain simplicity in the analysis which is to follow. Radial clearance between the valve spool and valve body is taken to be zero, and the metering edges are assumed to be perfectly sharp and perfectly oriented. The flow through each orifice is assumed to be simple orifice-type flow with negligible viscous effects, and the flow rate is assumed to change instantaneously with change in either pressure drop across the orifice or with change in orifice
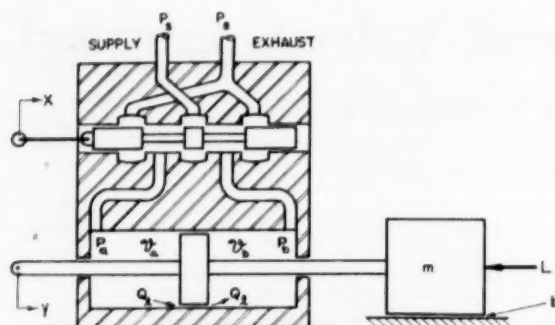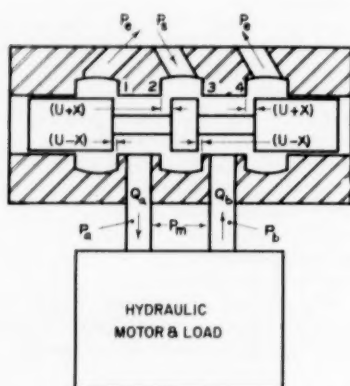
Fig. 1   Valve-Controlled Hydraulic Servomotor With Load

Fig. 2   Typical 4-Way Valve; U = Valve Underlap

area. All of the connecting passages are short enough and large enough to eliminate the effects of fluid mass on the flows through them. Friction losses in the lines and passages are neglected, and leakage flow past the ram is assumed to be laminar. Supply pressure is kept constant and the bulk modulus of the fluid is taken to be constant within the range of pressures employed (i.e., the fluid is a pure liquid). The valve is a 4-way control valve as shown in detail in Fig. 2. Exhaust pressure P_e is zero.

ANALYSIS

When the motion of the ram is restricted to small displacements from its center position, then $\mho_a \approx \mho_b$, and it can be shown[2] that the following relationship exists between ram velocity dY/dt, valve position X, leakage flow Q_l, and pressure across the ram P_m

$$A\Delta(DY) = k_1\Delta X - C_1\Delta P_m - \Delta Q_l - \frac{1}{2}\left(k_e + \frac{\mho_i}{\beta}\right)D\Delta P_m \ldots [1]$$

where Δ indicates the small change of each variable that has taken place from an initially steady value and D denotes derivative with respect to time d/dt. The coefficients are defined as follows:

A = ram area

$$k_1 = \left.\frac{\partial Q_m}{\partial X}\right|_{P_m} = \text{const}$$

$$C_1 = \left.\frac{\partial Q_m}{\partial P_m}\right|_X = \text{const}$$

[2] See Appendix 1 for detailed analysis.

k_e = coefficient of elasticity of each line connecting ram to valve

$\mho_i$ = volume of fluid between one side of ram and valve when ram is centered

β = bulk modulus of elasticity of fluid

It is significant that the flow rate Q_a is always equal to the flow rate Q_b when $\mho_a \approx \mho_b$ so that it is possible to speak of a single motor flow $Q_m = Q_a = Q_b$.

Fig. 3 shows the pressure-flow curves which were obtained experimentally from a 4-way valve for both open-center and closed-center operation. These curves were obtained only for the quadrants in which fluid power was being delivered to the motor because of the experimental difficulties involved in performing tests in which fluid power is taken from the motor. These experimental curves show good qualitative agreement with those derived analytically by Blackburn.[3] They reveal imperfections in the valve which may be impossible to predict or analyze.

Graphical interpretations of k_1 and C_1 for small changes of Q_m, P_m, and X are also given in Fig. 3. The coefficient k_1 is a measure of the amount by which the steady-state load flow Q_m varies when only a change of X occurs, and C_1 is a measure of the amount by which Q_m changes when only a change in P_m occurs. It is significant that the pressure-flow characteristics of an open-center 4-way valve yield nearly constant values of k_1 and C_1 for widely different initial conditions. This means that the analysis given in Appendix 1 may be expected to hold for fairly large variations of Q_m, X, and P_m when using an open-center valve. It is interesting to note that C_1 is zero when operating about the origin of the pressure-flow characteristics of a closed-center 4-way valve, and that both k_1 and C_1 vary more from point to point than with an open-center valve.

It should be emphasized that the use of the 4-way-valve steady-state pressure-flow curves can be justified rigorously only when $\mho_a \approx \mho_b$ (i.e., when the ram is near its center position). When the ram is near one end of the cylinder, the analysis is complicated by the lack of symmetry in the system and it is no longer possible to deal with a single-motor flow rate Q_m, since the flow rate Q_a is equal to the flow rate Q_b only in the steady state. When $\mho_a \neq \mho_b$, it is necessary to consider each end of the ram to be controlled by a 3-way valve, each 3-way valve consisting of two of the four orifices of the 4-way valve. This paper will deal only with the case when $\mho_a \approx \mho_b$.

For laminar leakage flow past the ram

$$\Delta Q_l = C_2\Delta P_m \ldots [2]$$

where C_2 = laminar flow coefficient for the leakage path.

Now coefficients k_2 and k_3 which are defined

$$k_2 = C_1 + C_2 \ldots [3]$$

$$k_3 = \frac{1}{2}\left(k_e + \frac{\mho_i}{\beta}\right) \ldots [4]$$

may be used to rewrite Equation [1] obtaining

$$A\Delta(DY) = k_1\Delta X - k_2\Delta P_m - k_3 D\Delta P_m \ldots [5]$$

Equation [5] is the fundamental equation which may be used to describe the behavior of the fluid part of the servomotor when it undergoes small changes.

Turning now to the mechanical part of the system consisting of the ram and mass plus viscous-damping load, an analysis of the

[3] "Contributions to Hydraulic Control, 3 Pressure-Flow Relationships for 4-Way Valves," by J. F. Blackburn, Trans. ASME, vol. 75, 1953, pp. 1163–1170.
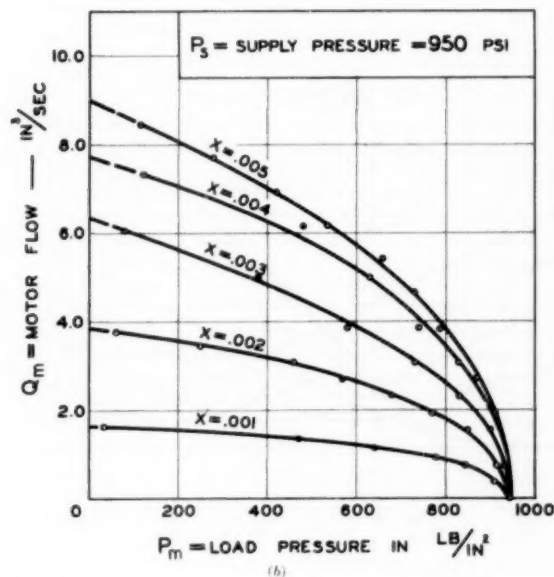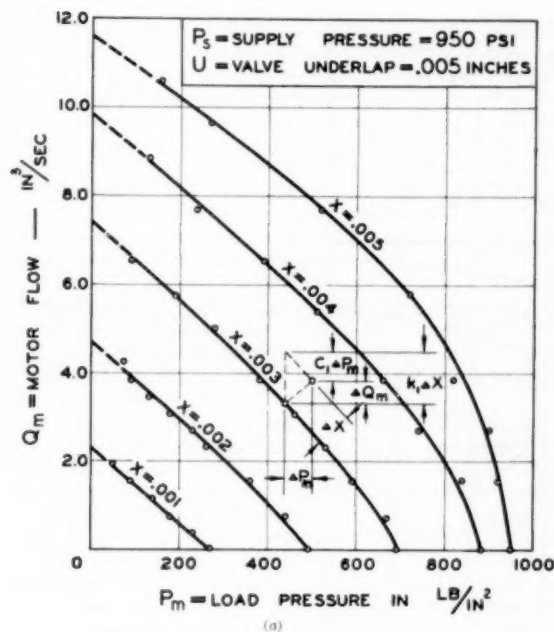
FIG. 3   MEASURED PRESSURE-FLOW CHARACTERISTICS OF TYPICAL 4-WAY CONTROL VALVE; PORT WIDTH $w \approx 1$ IN.

(a, Open-center operation; b, Closed-center operation; Valve underlap = 0.)

forces acting on this part of the system yields the following equation

$$\Delta P_m A = m D\Delta(DY) + b\Delta(DY) + \Delta L \dots\dots [6]$$

The relationship between ΔY, ΔX, and ΔL may be obtained by combining Equations [5] and [6] and noting that $\Delta(DY) = D\Delta Y$

$$AD\Delta Y = k_1\Delta X - (k_2 + k_3 D)\left(\frac{mD^2\Delta Y + bD\Delta Y + \Delta L}{A}\right)$$

or

$$\left[\left(\frac{k_3 m}{k_2 b + A^2}\right)D^2 + \frac{k_2 m + k_3 b}{k_2 b + A^2}D + 1\right]D\Delta Y =$$
$$\frac{k_1 A\Delta X - (k_2 + k_3 D)\Delta L}{k_2 b + A^3} \dots\dots [7]$$

which is a second-order differential equation.

The damping ratio ζ_s and the undamped natural frequency ω_{ns} of this system are given by the following equations

$$\zeta_s = \frac{k_2 m + k_3 b}{2\sqrt{k_1 m(k_2 b + A^2)}} \dots\dots\dots [8]$$

and

$$\omega_{ns} = \sqrt{\frac{k_2 b + A^2}{k_3 m}} \dots\dots\dots [9]$$

Fig. 4 illustrates the nature of the transient response of $D\Delta Y$ to a unit step change in ΔX for various values of ζ_s, when $\Delta L = 0$. The values of ζ_s and ω_{ns} completely describe the dynamic characteristics of this system, and they are usually used to describe the system when it is an underdamped system ($\zeta_s < 1$).   Thus the expression

$$\left[\left(\frac{k_3 m}{k_2 b + A^2}\right)D^2 + \left(\frac{k_2 m + k_3 b}{k_2 b + A^2}\right)D + 1\right]D\Delta Y$$

may be written

$$\left[\left(\frac{1}{\omega_{ns}}\right)^2 D^2 + \frac{2\zeta_s}{\omega_{ns}}D + 1\right]D\Delta Y$$

When the system is overdamped ($\zeta_s > 1$), it is usually more convenient to describe the system in terms of its real time constants τ_1 and τ_2, which are given by the following equation

$$\tau_1, \tau_2 = \frac{k_2 m + k_3 b}{2(k_2 b + A^2)}\left[1 \pm \sqrt{1 - \frac{4k_3 m(k_2 b + A^2)}{(k_2 m + k_3 b)^2}}\right] \dots [10]$$

and which satisfy the following identity

$$\left(\frac{k_3 m}{k_2 b + A_2}\right)D^2 + \left(\frac{k_2 m + k_3 b}{k_2 b + A^2}\right)D + 1 \equiv (\tau_1 D + 1)(\tau_2 D + 1)$$

Fig. 5 shows graphically how ζ_s is related to the dimensionless parameters π_a and π_b where

$$\pi_a = \frac{k_2}{A}\sqrt{\frac{m}{k_3}} \dots\dots\dots [11]$$

and

$$\pi_b = \frac{b}{A}\sqrt{\frac{k_3}{m}} \dots\dots\dots [12]$$

In addition to providing a means of rapidly determining ζ_s, this figure demonstrates clearly how to alter k_2 and/or b to change the damping ratio ζ_s if it is not initially satisfactory.

For the purposes of making an analog study, this system may be represented by the functional block diagram shown in Fig. 6.   This block diagram also shows clearly the complementary roles played by k_2 and m and by k_3 and m in determining over-all system performance.   Analog studies made during initial stages of design have proved to be a very useful means of arriving at optimum design parameters for systems of this kind.

CONCLUSIONS

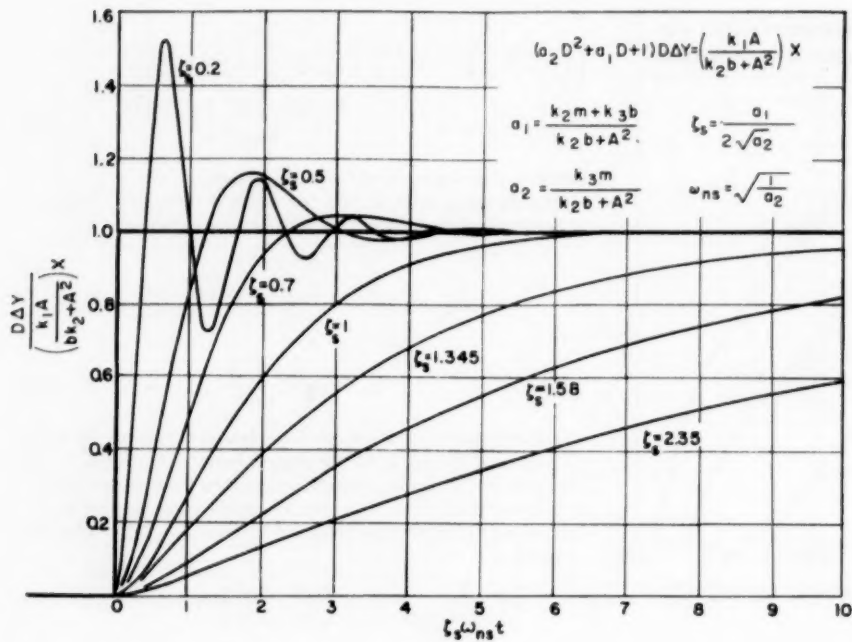*Speed of Response.*   The most significant information relating

$$(a_2 D^2 + a_1 D + 1) D\Delta Y = \left(\frac{k_1 A}{k_2 b + A^2}\right) X$$

$$a_1 = \frac{k_2 m + k_3 b}{k_2 b + A^2} \qquad \zeta_s = \frac{a_1}{2\sqrt{a_2}}$$

$$a_2 = \frac{k_3 m}{k_2 b + A^2} \qquad \omega_{ns} = \sqrt{\frac{1}{a_2}}$$

$\zeta_s = 0.2$

$\zeta_s = 0.5$

$\zeta_s = 0.7$

$\zeta_s = 1$

$\zeta_s = 1.345$

$\zeta_s = 1.58$

$\zeta_s = 2.35$

vertical axis: $\dfrac{D\Delta Y}{\left(\dfrac{k_1 A}{b k_2 + A^2}\right) X}$

horizontal axis: $\zeta_s \omega_{ns} t$

Fig. 4 Transient-Response Characteristics of a Hydraulic Servomotor

$$\zeta_s = \frac{T_a + T_b}{2\sqrt{T_a T_b + 1}}$$

$$\pi_a = \frac{k_2}{A}\sqrt{\frac{m}{k_3}}$$

$$\pi_b = \frac{b}{A}\sqrt{\frac{k_3}{m}}$$

$\pi_a = 10^4$, $\pi_a = 10^3$, $\pi_a = 10^4$, $\pi_a = 10$, $\pi_a = 1.0$, $\pi_a = 10^{-1}$

$\pi_a = 0$, $\pi_a = 10^{-3}$, $\pi_a = 10^{-2}$, $\pi_a = 10^{-1}$, $\pi_a = 1.0$, $\pi_a = 10$, $\pi_a = 10^2$, $\pi_a = 10^3$, $\pi_a = 10^4$

vertical axis: ζ_s horizontal axis: π_b

Fig. 5 Damping Ratio Versus π_a and π_b for Valve-Controlled Hydraulic Servomotor

VALVE POSITION $-A$ RAM VELOCITY

ΔX k_1 Σ $\dfrac{1}{k_3}$ $\dfrac{1}{D}$ ΔP_m A Σ $-\Delta L$ $\dfrac{1}{m}$ $\dfrac{1}{D}$ $D\Delta Y$

$-k_2$ $-b$
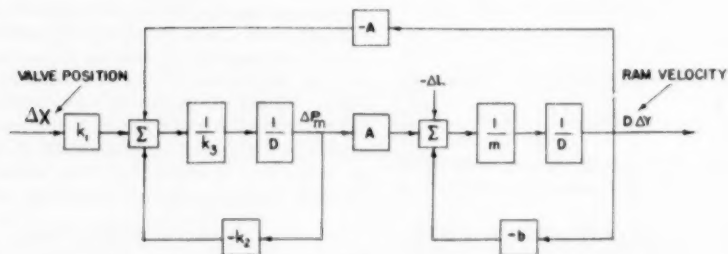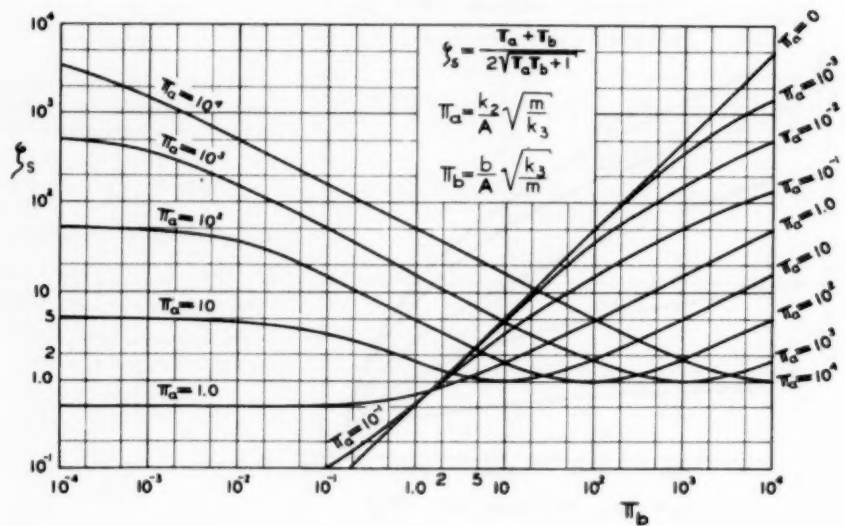
Fig. 6 Block Diagram Representation of Valve-Controlled Hydraulic Servomotor

to speed of response is contained in the expression for ω_{ns} if the servomotor is underdamped or in τ_1 if the servomotor is overdamped. In order to obtain a high undamped natural frequency in the case of an underdamped system, it is seen from Equation [9] that k_3m must be kept small in relation to $(k_2b + A^2)$. In order to attain a small value of τ_1 in an overdamped system, it is seen from Equation [10] that $(k_3m + k_2b)$ must be kept small in relation to $k_2b + A^2$. Thus the smallest attainable values of k_3 and m will yield the fastest servomotor, in either case. The value of m is usually set by other considerations, but the designer has a high degree of latitude in varying k_3. The value of k_3 can be minimized by using rigid fluid lines (to reduce k_e) and using the shortest possible ram cylinder and fluid lines (to reduce $\mathcal{U}_t$). In addition to the direct effect of ram area shown in Equations [9] and [10], the volume of fluid $\mathcal{U}_t$ is related to A, and if the volume of fluid in the lines is negligible, then $\mathcal{U}_t$ is proportional to A for a given ram stroke.

Although increasing A may give a system with higher ω_{ns} or lower τ_1 in some cases, the effect of varying A is usually weak and space limitations may prohibit the larger ram, the larger valve, the larger fluid lines, and the larger fluid power supply required to meet the same ram velocity specifications with increased ram area.

Degree of Damping. From Equation [8] it is seen that the servomotor damping ratio ζ_s is a function of all of the system constants, except k_1, namely, k_2, k_3, A, m, and b. The values of k_3 and m are usually set by considerations such as those discussed in the foregoing section. The ram area often is determined by such practical considerations as maximum load and/or acceleration requirements to be met with a given supply pressure or range of supply pressures.

Once k_3, m, and A have been determined, it is necessary to investigate how a sufficient degree of damping may be attained. If k_2 and b are both zero, ζ_s is zero, and the system will be unsatisfactory for most uses. An exception would be the case when an oscillatory motion at a fixed frequency is desired; here it would be desirable to keep k_2 and b small and select values of k_3, m, and A to produce the desired ω_{ns}.

For many applications the value of ζ_s must be greater than 0.7. The graph shown in Fig. 5 illustrates clearly the effects of varying k_2 and b when k_3, m, and A are held constant. It is significant that appreciable values of k_3 and/or b may be required to obtain a value of ζ_s greater than 0.7. When k_2 is obtained by the use of an open-center valve,[4] the stand-by power dissipation may be excessive if the servomotor is being used to control the position of the mass. If a closed-center valve is used, then C_1 is small and k_2 may be obtained by using a sufficiently large value of laminar leakage coefficient C_2. In this case, power dissipation occurs whenever an appreciable pressure appears across the ram. In some instances a combination of valve underlap and leakage across the ram may produce the desired results. In either case, appreciable displacement of the valve from its center position may be required to hold a steady ram load.

The value of b associated with the bearings on the output shaft may be sufficient in itself to produce the required value of ζ_s. In some instances it may be desirable to add a viscous damper to the output shaft. Power dissipation due to b occurs when the output shaft is moving at high velocity, and the transfer of an appreciable amount of heat from the viscous damper may become necessary.

A number of nonlinear effects which exist in many real systems have not been considered here and the conclusions reached in this paper may not be quantitatively applicable to such systems. On the other hand, the material covered in this paper has been useful

4 See Appendix 2 for discussion of factors which affect the value of k_2.

in gaining a qualitative insight into the behavior of systems containing some nonlinearities. For instance, it is possible to determine the dynamic characteristics for small variations in several regions of the valve characteristics and gain an understanding of how the system performance can be expected to vary from one set of operating conditions to another. The block diagram and analog techniques become essential to a thorough study of many nonlinear systems. The study of problems associated with the performance of hydraulic servomotors with various types of nonlinearities could be the basis of further work in this field.

Appendix 3 discusses a typical servomotor design and shows how the material in this paper may be applied to a practical problem.

BIBLIOGRAPHY

1 "Analysis of Some Hydraulic Components Used in Regulators and Servomechanisms," by S. Z. Dushkes and S. L. Cahn, Trans. ASME, vol. 74, 1952, pp. 595–601.
2 "An Analysis of the Dynamics of Hydraulic Servomotors Under Inertia Loads and the Application to Design," by H. Gold, E. W. Otto, and V. L. Ransom, Trans. ASME, vol. 75, 1953, pp. 1383–1394.
3 "Hydraulic Servos," by R. Hadekel, Conference on Hydraulic Servo-Mechanisms, published by The Institution of Mechanical Engineers, London, England, Feb. 13, 1953.
4 "Some Design Considerations of Hydraulic Servos of Jack Type," by N. F. Harpur, Conference on Hydraulic Servo-Mechanisms, published by The Institution of Mechanical Engineers, London, England, Feb. 13, 1953.
5 "Dynamic Operation of a Force-Compensated Hydraulic Throttling Valve," by J. L. Bower and F. B. Tuteur, Trans. ASME, vol. 75, 1953, pp. 1395–1406.

Appendix 1

DETAILED ANALYSIS OF VALVE-CONTROLLED RAM WITH MASS PLUS VISCOUS-DAMPING LOAD

Because of the nonlinear characteristics of flow through the orifices, the analysis will be limited at first to small changes of all variables. The volume rate of flow through each orifice of the valve is given by an equation of the form

$$Q_1 = C_d A_1 \sqrt{\frac{2(P_{up} - P_{down})}{\rho}} \quad \ldots\ldots\ldots\ldots [13]$$

where

$\quad Q_1$ = volume rate of flow, L^3/T
$\quad C_d$ = discharge coefficient, dimensionless
$\quad A_1$ = orifice area, L^2
$\quad P_{up}$ = upstream pressure, F/L^2
P_{down} = downstream pressure, F/L^2
$\quad \rho$ = fluid density, FT^2/L^4

When only small changes are to be considered, Equation [13] may be reworked by taking its logarithm and differentiating as follows

$$\ln Q_1 = \ln C_d + \ln A_1 + \frac{1}{2} \ln (P_{up} - P_{down}) - \frac{1}{2} \ln \frac{2}{\rho} \quad \ldots\ldots [14]$$

$$\frac{dQ_1}{Q_1} = 0 + \frac{dA_1}{A_1} + \frac{1}{2} \frac{d(P_{up} - P_{down})}{(P_{up} - P_{down})} - 0 \quad \ldots\ldots [15]$$

and for small finite changes of Q_1, A, P_{up}, and P_{down} we may write

$$\frac{\Delta Q_1}{Q_{1i}} = \frac{\Delta A_1}{A_{1i}} + \frac{1}{2}\frac{\Delta(P_{up} - P_{down})}{(P_{up} - P_{down})_i} \dots \dots [16]$$

where the subscript i indicates the initial value of each variable before the small change occurred.

Applying this equation to the flow through each orifice of the valve, the following four equations are obtained

$$\frac{\Delta Q_1}{Q_{1i}} = \frac{\Delta A_1}{A_{1i}} + \frac{1}{2}\frac{\Delta P_a}{P_{ai}} \dots \dots \dots [17]$$

$$\frac{\Delta Q_2}{Q_{2i}} = \frac{\Delta A_2}{A_{2i}} - \frac{1}{2}\frac{\Delta P_a}{(P_s - P_a)_i} \dots \dots [18]$$

$$\frac{\Delta Q_3}{Q_{3i}} = \frac{\Delta A_3}{A_{3i}} - \frac{1}{2}\frac{\Delta P_b}{(P_s - P_b)_i} \dots \dots [19]$$

$$\frac{\Delta Q_4}{Q_{4i}} = \frac{\Delta A_4}{A_{4i}} + \frac{1}{2}\frac{\Delta P_b}{P_{bi}} \dots \dots \dots [20]$$

From the geometry of the valve

$$\frac{\Delta A_1}{A_{1i}} = \frac{-\Delta X}{U - X_i} \dots \dots \dots [21]$$

$$\frac{\Delta A_2}{A_{2i}} = \frac{+\Delta X}{U + X_i} \dots \dots \dots [22]$$

$$\frac{\Delta A_3}{A_{3i}} = \frac{-\Delta X}{U - X_i} \dots \dots \dots [23]$$

$$\frac{\Delta A_4}{A_{4i}} = \frac{+\Delta X}{U + X_i} \dots \dots \dots [24]$$

or

$$\frac{\Delta A_2}{A_{2i}} = \frac{\Delta A_4}{A_{4i}} = \frac{\Delta X}{U + X_i} \dots \dots \dots [25]$$

and

$$\frac{\Delta A_1}{A_{1i}} = \frac{\Delta A_3}{A_{3i}} = \frac{-\Delta X}{U - X_i} \dots \dots \dots [26]$$

By continuity

$$\Delta Q_a = \Delta Q_2 - \Delta Q_1 \dots \dots \dots \dots [27]$$

$$\Delta Q_b = \Delta Q_4 - \Delta Q_3 \dots \dots \dots \dots [28]$$

Letting $\mathcal{V}_a$ and $\mathcal{V}_b$ be, respectively, the volumes of fluid between the left and right sides of the ram and the valve, the continuity equations for control volumes which enclose $\mathcal{V}_a$ and $\mathcal{V}_b$ are as follows

$$\rho Q_a = \frac{d}{dt}(\rho \mathcal{V}_a) + \rho Q_l \dots \dots \dots [29]$$

$$\rho Q_b = -\frac{d}{dt}(\rho \mathcal{V}_b) + \rho Q_l \dots \dots \dots [30]$$

$$\rho Q_a = \rho \frac{d\mathcal{V}_a}{dt} + \mathcal{V}_{ai}\frac{d\rho_a}{dt} + \rho Q_l \dots \dots \dots [31]$$

$$\rho Q_b = -\left(\frac{\rho d\mathcal{V}_b}{dt} + \mathcal{V}_{bi}\frac{d\rho_b}{dt}\right) + \rho Q_l \dots \dots [32]$$

Note that although the change in absolute value of fluid density may be neglected, the *rate of change* of fluid density may not be neglected. Expressions

$$\frac{d}{dt}\mathcal{V}_a \text{ and } \frac{d}{dt}\mathcal{V}_b$$

are given by

$$\frac{d}{dt}\mathcal{V}_a = k_e\frac{dP_a}{dt} + A\frac{dY}{dt} \dots \dots \dots [33]$$

$$\frac{d}{dt}\mathcal{V}_b = k_e\frac{dP_b}{dt} - A\frac{dY}{dt} \dots \dots \dots [34]$$

where k_e represents the elasticity of the lines connecting the valve to the ram, and A is the effective area of the ram.

The equation of state for the fluid under constant temperature conditions is as follows

$$\frac{d\rho}{dt} = \frac{\rho}{\beta}\frac{dP}{dt} \dots \dots \dots [35]$$

where β is the bulk modulus of the fluid.

Substituting Equations [33] and [34] in Equations [31] and [32], and employing Equation [35]

$$\rho Q_a = \rho\left(k_e\frac{dP_a}{dt} + A\frac{dY}{dt}\right) + \mathcal{V}_{ai}\frac{\rho}{\beta}\frac{dP_a}{dt} + \rho Q_l \dots [36]$$

$$\rho Q_b = -\rho\left(k_e\frac{dP_b}{dt} - A\frac{dY}{dt}\right) - \mathcal{V}_{bi}\frac{\rho}{\beta}\frac{dP_b}{dt} + \rho Q_l \dots [37]$$

and collecting terms

$$Q_a = \left(k_e + \frac{\mathcal{V}_{ai}}{\beta}\right)\frac{dP_a}{dt} + A\frac{dY}{dt} + Q_l \dots \dots [38]$$

$$Q_b = -\left(k_e + \frac{\mathcal{V}_{bi}}{\beta}\right)\frac{dP_b}{dt} + A\frac{dY}{dt} + Q_l \dots \dots [39]$$

When the ram is initially being driven at constant velocity

$$\frac{d}{dt}\Delta P_a = \frac{d}{dt}\Delta P_b = 0$$

and

$$Q_{ai} = Q_{bi} = A\left(\frac{dY}{dt}\right)_i + Q_{li} \dots \dots \dots [40]$$

It is convenient to use the foregoing condition as the condition of the unperturbed system. When this is done, it is seen that because of symmetry of the system

$$Q_{3i} = Q_{1i} \dots \dots \dots \dots [41]$$

$$Q_{4i} = Q_{2i} \dots \dots \dots \dots [42]$$

and

$$P_s - P_{ai} = P_{bi} \dots \dots \dots [43]$$

$$P_s - P_{bi} = P_{ai} \dots \dots \dots [44]$$

Equations [17], [18], [19], and [20] may now be rewritten as follows, using Equations [25], [26], [41], [42], [43], and [44]

$$\frac{\Delta Q_1}{Q_{1i}} = \frac{-\Delta X}{U - X_i} + \frac{1}{2}\frac{\Delta P_a}{P_{ai}} \dots \dots \dots [45]$$

$$\frac{\Delta Q_2}{Q_{2i}} = \frac{\Delta X}{U + X_i} - \frac{1}{2}\frac{\Delta P_a}{P_{bi}} \dots \dots \dots [46]$$

$$\frac{\Delta Q_3}{Q_{3i}} = \frac{-\Delta X}{U - X_i} - \frac{1}{2}\frac{\Delta P_b}{P_{ai}} \dots \dots \dots [47]$$

$$\frac{\Delta Q_4}{Q_{2i}} = \frac{\Delta X}{U + X_i} + \frac{1}{2}\frac{\Delta P_b}{P_{bi}} \quad \dots \dots \dots \dots [48]$$

Solving for ΔQ_a and ΔQ_b

$$\Delta Q_a = \Delta Q_2 - \Delta Q_1 = \left(\frac{Q_{2i}}{U + X_i} + \frac{Q_{1i}}{U - X_i}\right)\Delta X$$
$$- \frac{1}{2}\left(\frac{Q_{2i}}{P_{bi}} + \frac{Q_{1i}}{P_{ai}}\right)\Delta P_a \quad \dots [49]$$

$$\Delta Q_b = \Delta Q_4 - \Delta Q_3 = \left(\frac{Q_{1i}}{U - X_i} + \frac{Q_{2i}}{U + X_i}\right)\Delta X$$
$$+ \frac{1}{2}\left(\frac{Q_{1i}}{P_{ai}} + \frac{Q_{2i}}{P_{bi}}\right)\Delta P_b \quad \dots \dots [50]$$

Now, using only small changes in Equations [38] and [39] and combining with Equations [49] and [50]

$$\left(\frac{Q_{2i}}{U + X_i} + \frac{Q_{1i}}{U - X_i}\right)\Delta X - \frac{1}{2}\left(\frac{Q_{2i}}{P_{bi}} + \frac{Q_{1i}}{P_{ai}}\right)\Delta P_a$$
$$= \left(k_e + \frac{\mathcal{V}_{ai}}{\beta}\right)\frac{d}{dt}\Delta P_a + A\Delta\frac{dY}{dt} + \Delta Q_l \quad \dots [51]$$

$$\left(\frac{Q_{2i}}{U + X_i} + \frac{Q_{1i}}{U - X_i}\right)\Delta X + \frac{1}{2}\left(\frac{Q_{2i}}{P_{bi}} + \frac{Q_{1i}}{P_{ai}}\right)\Delta P_b$$
$$= -\left(k_e + \frac{\mathcal{V}_{bi}}{\beta}\right)\frac{d}{dt}\Delta P_b + A\Delta\frac{dY}{dt} + \Delta Q_l \quad \dots [52]$$

and adding

$$2\left(\frac{Q_{2i}}{U + X_i} + \frac{Q_{1i}}{U - X_i}\right)\Delta X - 2A\Delta DY$$
$$= \Delta P_a\left[\left(k_e - \frac{\mathcal{V}_{ai}}{\beta}\right)D + \frac{1}{2}\left(\frac{Q_{2i}}{P_{bi}} + \frac{Q_{1i}}{P_{ai}}\right)\right]$$
$$- \Delta P_b\left[\left(k_e + \frac{\mathcal{V}_{bi}}{\beta}\right)D + \frac{1}{2}\left(\frac{Q_{2i}}{P_{bi}} + \frac{Q_{1i}}{P_{ai}}\right)\right] + 2\Delta Q_l \quad \dots [53]$$

where D denotes derivative with respect to time d/dt.

Note that if $\mathcal{V}_{ai} = \mathcal{V}_{bi} = \mathcal{V}_i$ (and this condition holds in many cases), Equation [53] may be written as follows

$$A\Delta DY = \left(\frac{Q_{2i}}{U + X_i} + \frac{Q_{1i}}{U - X_i}\right)\Delta X - \left(\frac{\Delta P_a - \Delta P_b}{2}\right)$$
$$\left[\left(k_e + \frac{\mathcal{V}_i}{\beta}\right)D + \frac{1}{2}\left(\frac{Q_{2i}}{P_{bi}} + \frac{Q_{1i}}{P_{ai}}\right)\right] - \Delta Q_l \quad \dots [54]$$

and when $d/dt(\Delta P_a - \Delta P_b) = 0$ (i.e., after a new steady state has been attained)

$$\Delta Q_{m(ss)} = A(D\Delta Y)_{(ss)} + \Delta Q_{l(ss)} = k_1\Delta X_{(ss)}$$
$$- C_1(\Delta P_a - \Delta P_b)_{(ss)} = k_1\Delta X_{(ss)} - C_1\Delta P_{m(ss)} \dots [55]$$

where

$$k_1 = \left(\frac{Q_{2i}}{U + X_i} + \frac{Q_{1i}}{U - X_i}\right) = \frac{\partial Q_m}{\partial X}\bigg|_{P_m = \text{const}} \quad \dots [56]$$

$$C_1 = \frac{1}{4}\left(\frac{Q_{2i}}{P_{bi}} + \frac{Q_{1i}}{P_{ai}}\right) = \frac{\partial Q_m}{\partial P_m}\bigg|_{X = \text{const}} \quad \dots [57]$$

Appendix 2

FACTORS WHICH AFFECT VALUES OF k_2 AND k_1

From Equation [3], it is seen that $k_2 = C_1 + C_2$. C_1 is a valve characteristic, and C_2 is a measure of the leakage across the ram per unit pressure drop across the ram. From Appendix 1 it is seen that

$$C_1 = \frac{1}{4}\left(\frac{Q_{2i}}{P_{bi}} + \frac{Q_{1i}}{P_{ai}}\right) \quad \dots \dots \dots \dots [57]$$

When the valve is an open-center valve operating well within the underlap region ($X < U$), C_1 does not vary appreciably from the value it has when $Q_m = 0$ and $P_m = 0$ (i.e., when $Q_{2i} = Q_{1i} = C_d U w\sqrt{P_s/\rho}$ and $P_{ai} = P_{bi} = P_s/2$).
Therefore we may write

$$C_1 \approx C_d U w\sqrt{\frac{1}{P_s\rho}} \quad \dots \dots \dots \dots [58]$$

and it is seen that C_1 varies linearly with valve underlap U and valve port width w and inversely with the square root of supply pressure P_s.

In a similar way it can be shown that

$$k_1 \approx 2C_d w\sqrt{\frac{P_s}{\rho}} \quad \dots \dots \dots \dots [59]$$

Inspection of the 4-way-valve pressure-flow curves also reveals that C_1 becomes larger and k_1 becomes smaller at points remote from the origin.

The laminar leakage coefficient C_2 may be adjusted by providing clearance between the ram and its cylinder or by connecting capillary tubing of proper diameter and length across the ram.

Appendix 3

A TYPICAL SERVOMOTOR DESIGN

Consider the problem of driving a mass weighing 50 lb within a maximum stroke of 6 in. The specifications require a maximum load acceleration of 1000 in/sec² at zero velocity when an external load force of 300 lb is acting to oppose motion of the load; and a maximum steady velocity of 5 ips must be possible when the 300-lb force is acting in opposition. A fluid supply pressure of 1000 psi is to be used and the stand-by power loss (when load is motionless and external-load force is zero) must not exceed $\frac{1}{8}$ hp. The servomotor must have a damping ratio of at least 0.7 for small motions of the ram about its center position with zero external-load force.

First, the ram area may be calculated on the basis of the acceleration and external-load requirements. If the valve is given sufficient displacement from its neutral position, full supply pressure is available to move the ram. Summing the forces acting and applying Newton's second law to the ram and load, we have

$$P_s A = m\frac{d^2Y}{dt^2} + b\frac{dY}{dt}^{\,0} + L$$

$$A = \frac{m\dfrac{d^2Y}{dt^2} + L}{P_s}$$

where

$$m = 50/386 = 0.13 \text{ lb-sec}^2/\text{in.}$$

$$d^2Y/dt^2 = 1000 \text{ in/sec}^2$$

$$L = 300 \text{ lb}$$

so that

$$A = \frac{(0.13)(1000) + 300}{1000} = \frac{430}{1000} = 0.430 \text{ sq in.}$$

A commercially available ram having an effective area of 0.5 sq in. and 6-in. stroke is selected and, if possible, its friction characteristics are measured. Let its measured or estimated viscous-damping coefficient be 0.5 lb-sec/in. and let its static friction be negligible. The load-damping coefficient is measured and found to be 5.4 lb-sec/in. The total viscous-damping coefficient b is 5.9 lb-sec/in.

Now it is possible to determine the pressure across the ram P_m required to meet the maximum steady-state velocity and opposing load force condition. Equating forces, we have

$$P_m A = b \frac{dY}{dt} + L$$

$$P_m = \frac{b \frac{dY}{dt} + L}{A}$$

where

$$b = 5.9 \text{ lb-sec/in.}$$

$$dY/dt = 5 \text{ in/sec}$$

$$L = 300 \text{ lb}$$

so that

$$P_m = \frac{(5.9)(5.0) + 300}{0.50} = 660 \text{ psi}$$

In order to keep k_3 to a minimum, the valve is mounted as close as possible to the ram so that the volume $\mathcal{V}_i$ is nearly 1.5 cu in. and the elastic coefficient k_s is negligible. The value of k_3 is then found to be

$$k_3 = \frac{\mathcal{V}_i}{2\beta} = \frac{1.5}{6 \times 10^5} = 2.5 \times 10^{-6}$$

The value of π_b may now be determined from Equations [11] and [12]

$$\pi_b = \frac{b}{A} \sqrt{\frac{k_3}{m}} = \frac{5.9}{0.5} \sqrt{\frac{2.5 \times 10^{-6}}{0.13}}$$

$$\pi_b = 11.8 \sqrt{19.3 \times 10^{-6}} = (11.8)(0.0044) = 5.19 \times 10^{-2}$$

From Fig. 5 the value of π_a required to produce a ζ_s of 0.7 is found to be approximately 1.5. Now k_2 may be found

$$k_2 = \pi_a A \sqrt{\frac{k_3}{m}} = (1.5)(0.5) \sqrt{19.3 \times 10^{-6}}$$

$$k_2 = (1.5)(0.5)(4.4 \times 10^{-3}) = 3.3 \times 10^{-3}$$

For the time being let the leakage past the ram be zero so that $C_2 = 0$. Then

$$k_2 = C_1 = 3.3 \times 10^{-3}$$

and from Appendix 2 for an open-center valve

$$C_1 \approx C_d U w \sqrt{\frac{1}{P_s \rho}} \quad \dots \dots \dots \dots \dots \dots \quad [58]$$

where

C_d = orifice discharge coefficient = 0.625
U = valve underlap
w = valve port width
P_s = supply pressure = 1000 psi
ρ = mass density of fluid $\approx 0.8 \times 10^{-4}$ for hydraulic oil

and solving for Uw

$$Uw \approx \frac{C_1}{C_d} \sqrt{P_s \rho} = \frac{3.3 \times 10^{-3}}{0.625} \sqrt{(1000)(0.8 \times 10^{-4})}$$

$$Uw \approx \frac{(3.3 \times 10^{-4}) \sqrt{8.0}}{0.625} = 1.49 \times 10^{-3} \text{ sq in.}$$

This means that the area of each orifice of the valve is 1.49 $\times 10^{-3}$ sq in. when the valve is centered. The stand-by power loss may now be calculated

$$\frac{Q_q P_s}{6600} = \frac{1}{6.6} Q_q \text{ hp}$$

where Q_q = quiescent flow to the valve. When the load is motionless and the external load force is zero, $P_a = P_b = P_s/2$ and $Q_1 = Q_2 = Q_3 = Q_4 = C_d U w \sqrt{P_s/\rho}$. Then

$$Q_q = Q_2 + Q_3 = Q_1 + Q_4 = 2 C_d U w \sqrt{P_s/\rho}$$

Therefore the stand-by power loss is

$$\frac{Q_q P_s}{6600} = \frac{(1.25)(1.49 \times 10^{-3})}{6.6} \sqrt{\frac{10^7}{0.8}}$$

$$= \frac{(1.25)(1.49) 10}{(6.6) \sqrt{8.0}} = 1.0 \text{ hp}$$

Since this is 3 times what it should be, it is necessary to reduce Uw by a factor of 3 so that $Uw = 5.0 \times 10^{-4}$ sq in. and then provide leakage across the ram. Reducing Uw to 5.0×10^{-4} sq in. decreases C_1 from 3.3×10^{-3} to 1.1×10^{-3} and makes necessary a value of $C_2 = 2.2 \times 10^{-3}$ in^5/lb-sec.

A capillary-tubing by-pass across the ram is considerably easier to control and adjust than leakage between the ram and cylinder walls. A by-pass of satisfactory diameter and length may be determined from the Hagen-Poiseuille equation for capillary flow.

The leakage past the ram when driving the load at maximum velocity with maximum opposing external load force is found to be

$$Q_l = C_2 P_m = 2.2 \times 10^{-3} \times 660$$

$$Q_l = 1.4 \text{ in}^3/\text{sec}$$

which is a power loss of

$$\frac{Q_l P_m}{6600} = \frac{(1.4)(660)}{6600} = 0.14 \text{ hp}$$

and the maximum power delivered to the external load is

$$\frac{A \frac{dY}{dt} P_m}{6600} = \frac{(0.5)(5.0)(660)}{6600} = 0.25 \text{ hp}$$

The maximum total steady flow to the ram and by-pass is

$$Q_t + A\frac{dY}{dt} = 1.4 + 2.5 = 3.9 \text{ in}^3/\text{sec}$$

and this flow must be obtained when $P_m = 0.66P_s$. The maximum no-load motor flow from an open-center valve (when $X = U$) is the same as the quiescent flow

$$Q_{max} = 2C_d U w\sqrt{\frac{P_s}{\rho}} = \frac{(1.25)(5.0)}{\sqrt{8.0}} = 2.21 \text{ in}^3/\text{sec}$$

This means that the valve must be opened beyond the underlap region to provide maximum motor flow (i.e., two orifices are completely closed and it is operating as a closed-center valve). When P_m is 660 psi, the pressure drop across each open orifice is $(1000-660)/2$ or 170 psi. The maximum valve orifice area is then found to be

$$(U + X)w = \frac{Q_t + A\dfrac{dY}{dt}}{C_d}\sqrt{\frac{\rho}{P_s - P_m}}$$

$$= \frac{3.9}{0.625}\sqrt{\frac{8 \times 10^{-5}}{340}} = \frac{(3.9)}{(6.25)}\sqrt{\frac{80 \times 10^{-6}}{3.4}}$$

$$(U + X)w = \frac{(3.9)\left(\sqrt{20.3}\right)}{(6.25)10^2} = 2.82 \times 10^{-2} \text{ sq in.}$$

The undamped natural frequency ω_{ns} of the servomotor is

$$\omega_{ns} = \sqrt{\frac{k_2 b + A^2}{k_1 m}} = \sqrt{\frac{(3.3)(5.9) \times 10^{-3} + 0.25}{(2.5)(0.13)10^{-6}}}$$

$$\omega_{ns} = \sqrt{\frac{0.269}{(3.25)10^{-7}}} = \sqrt{\frac{(269)10^4}{3.25}}$$

$$\omega_{ns} = 912 \text{ radians/sec or } 145 \text{ cps}$$

Discussion

P. S. CREAGER.[5] Professor Shearer has given a basic analysis of an important group of hydraulic servomotors and has carried the work far enough to show the effect of various design parameters.

It is interesting to the writer to note that the basic differential Equation [7] is of the same form as that commonly given for stroke-controlled rotary pump and motor hydraulic servos. In Fig. 5 the author shows a range of damping ratio ζ_s from 0.1 to $10^2 (+)$. All data that the writer has seen for the rotary servos give ζ_s considerably less than 0.1.

This very noticeable difference is difficult for the writer to understand. The writer interprets the discussion of "Degree of Damping" to mean essentially that the only variables where the designer has some freedom will be the damping (viscous?) of the load, and leakage (valve and ram?).

When considered in the light of the illustrative design problem of Appendix 3, where the author introduced artificial leakage to raise ζ to 0.7, the writer cannot visualize loads with such enormous

damping and motors with sufficient leakage to obtain values of, say, from 10.0 up.

The writer would ask Professor Shearer to comment on this matter of damping ratio, especially as he suspects that any case where ζ is considerably greater than unity would necessarily exhibit slow response.

AUTHOR'S CLOSURE

Professor Creager's comments which relate to the similarity of pump stroke-controlled servomotors to valve-controlled servomotors are well made. Although there are many pump stroke-controlled servomotors in operation having damping ratios of the order of 0.1 or less, their use in the control of the output position is limited to systems having either (1) a relatively slow over-all response or (2) extensive feedback compensation in addition to proportional control of position in order to provide sufficient system stability with related fast response. The difficulty involved in obtaining sufficient system damping in many cases does not mean that this difficulty is encountered in all systems. The author has encountered systems with relatively high values of the damping ratio ζ_s, and the range of ζ_s shown in Fig. 5 resulted from a brief survey of all possible practical combinations of system parameters that might exist for a system of this kind. Examples of systems with large values of ζ_s are systems with very small mass loads or very little fluid compliance. The author does believe, however, that a majority of system design problems arise when the damping ratio lies between 0.1 and 1.0 and that the curves in this region of Fig. 5 could be enlarged and shown in greater detail.

Within the limited scope of this paper, viscous damping and leakage are the only means of improving the damping of a system having a ram of given area and given stroke driving a given mass load. It may be seen from the fundamental equations and from Fig. 5 that the ram area, ram stroke, and load mass are significant system parameters, and the designer must exercise judgment in selecting all of the parameters of the system if he is to arrive at a good design.

The problem of providing adequate system damping without dissipating excessive amounts of power is an important one, particularly in larger systems. The author, in an M.I.T. doctoral thesis,[6] discusses analytical and experimental work which has been done with transient leakage flow stabilization of a system of this kind operating with compressed air. This scheme, which involves connecting a flow resistance and tank to each end of the ram, dissipates energy only during transient operation of the system and may be effectively employed to provide adequate damping in pneumatic and hydraulic systems.

Most of the difficult design problems that the author has encountered have been due to the necessity of providing sufficient damping in systems that are inherently underdamped. Since damping is so difficult to provide in these cases, there is seldom any justification for trying to make ζ_s larger than 1.0. In systems with very small mass load or very small fluid compliance, and therefore possibly large values of ζ_s, the speed of response of the servomotor is usually so fast compared to that of the other components it is being used with that it is important only to know what the speed of response and damping ratio of the servomotor are without trying to decrease its damping ratio ζ_s and improve its speed of response.
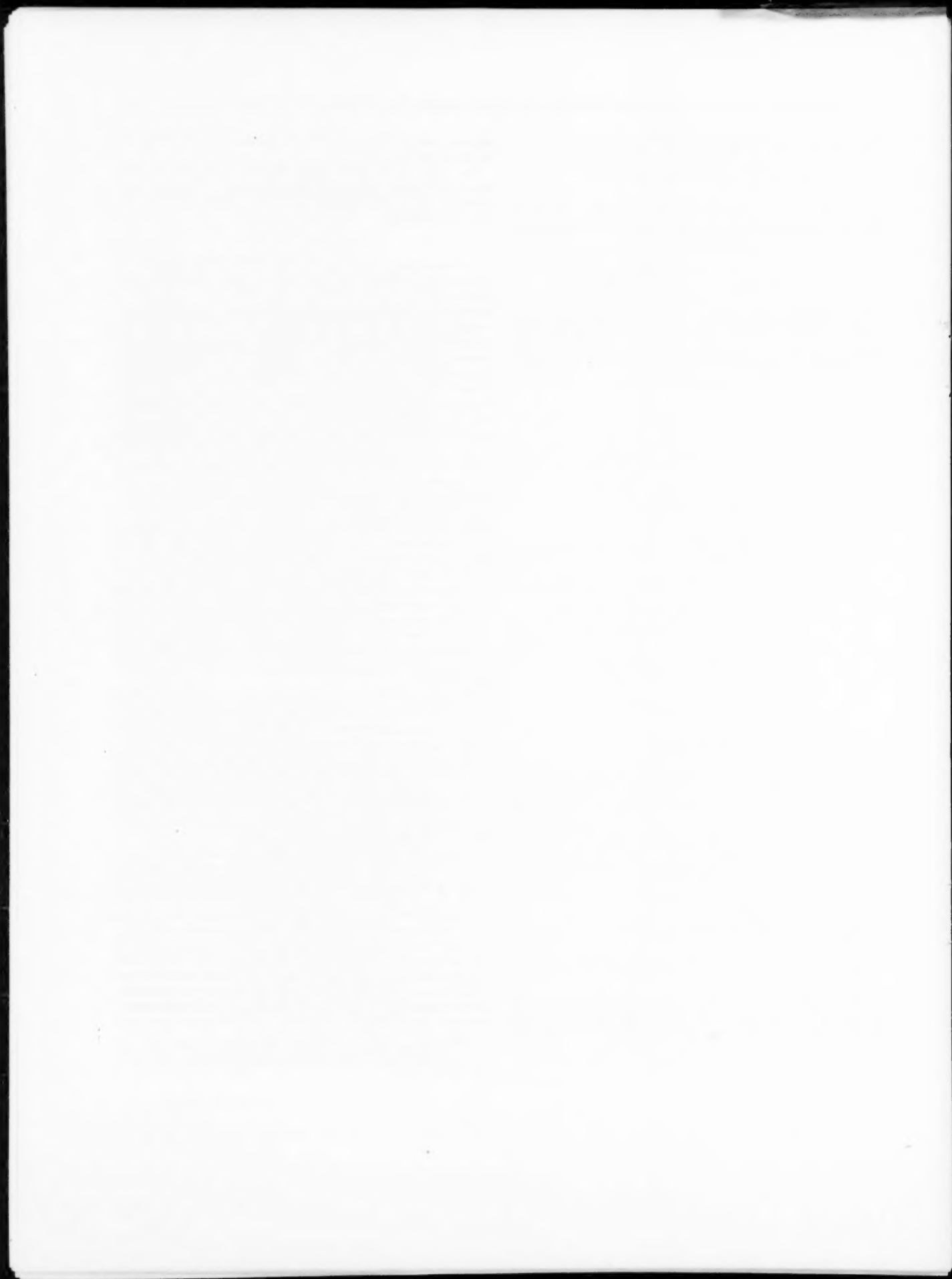
Contributions to Hydraulic Control—6

New Valve Configurations for High-Performance Hydraulic and Pneumatic Systems

By SHIH-YING LEE,[1] CAMBRIDGE, MASS.

In high-performance hydraulic and pneumatic systems, three-way or four-way valves of very high precision are required. Conventional spool-type valves used for this purpose have been found to be difficult and expensive to manufacture. This paper describes a new type of metering orifice and several valve designs utilizing this metering orifice. These valves have proved to be considerably easier to make and more trouble-free than the piston-type design with the same performance. Flow-force-reduction methods for this type also are described. The work to be reported here was carried out at the Dynamic Analysis and Control Laboratory and was supported by the U. S. Navy Bureau of Ordnance Contract NOrd 9661 with the Division of Industrial Cooperation of the Massachusetts Institute of Technology.

INTRODUCTION

THE most common type of valve used in the hydraulic and pneumatic control fields has been the piston or spool type,[2] shown in Fig. 1. This type is simple, compact, requires relatively low operating forces, and, in general, has been quite satisfactory. Few attempts have been made, therefore, to develop other basic designs.

high-performance systems, however, has made necessary a radical reduction in these tolerances, and this has greatly increased the difficulty and cost of manufacturing the valves. It is now of interest to consider other valve configurations in an effort to decrease manufacturing costs without affecting performance adversely. This paper will describe certain valves that have reached this goal successfully.

DESIGN OF VALVES FOR HIGH-PERFORMANCE SYSTEMS

In the absence of a definition of a "high-performance" system, or even of a generally applicable criterion of performance, this section must be qualitative rather than quantitative in nature, but at least it can outline the general philosophy of designing valves for such systems. For the purpose of this paper, a high-performance system is one with a very fast and accurate response, such as the types now being designed for controlling fast airplanes and missiles or for high-speed, high-precision machine tools. Such systems must be made up of components with characteristics that were unheard of a few years ago.

Practically all high-performance systems use negative feedback and obtain their high performance by using large values of loop gain. These large gains can be obtained without making the system unstable only if each element of the system is nearly
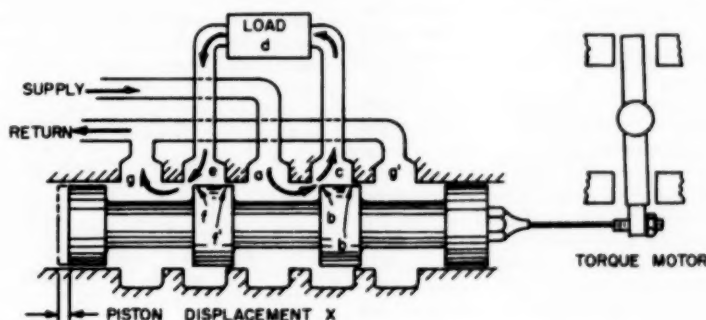
FIG. 1 CONVENTIONAL FOUR-WAY CONTROL VALVE

The spool valve is not hard to make, either in the experimental shop or in production, so long as the required tolerances are those of normal manufacturing practice, say, ± 0.001 in. for the essential dimensions. The recent great demand for really

linear; or if nonlinear, its nonlinearity must be compensated in some fashion. In so far as the valve is concerned, the linearity requirement applies to the relationship between flow rate and valve displacement; i.e., for a given pressure drop across the valve, equal increments of displacement should produce equal increments of flow. This requirement in turn demands that the valve ports be of constant effective width; with the spool valve, it is required that they be rectangular.

Even with accurately rectangular ports, the gain of the valve falls off considerably near the origin if the cutoff is not sharp. This unsharpness, shown in Fig. 2, may arise from several causes, particularly from excessive clearance or underlap, or from rounding or bellmouthing of the port or land edges. These effects are roughly independent of the size of the valve; for example, the
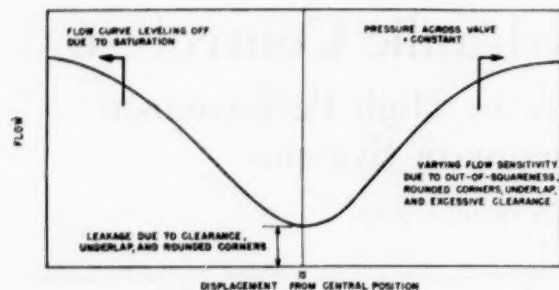
FIG. 2   FLOW-TRAVEL RELATIONSHIP OF TYPICAL CLOSED-CENTER
CONTROL VALVE WITH NO OVERLAP

minimum practicable clearance seems to be approximately 1 micron (40μ in.), and at least for servovalves up to some tens of horsepower, the clearance should not exceed approximately 5 microns. Similarly, in practice it seems to be very difficult to maintain a land corner perfectly sharp; there is always some erosion and rounding, but this decreases to a negligible amount (if the oil is well filtered) after the radius has increased to a few ten-thousandths of an inch.

Since these effects are appreciable only close to the origin, their importance can be lessened by using a long operating stroke. Unfortunately, this is impracticable for many applications. Hydraulic servos usually are chosen in preference to other types because of their very high speed of response, and the use of a long valve stroke in such cases would increase greatly the task of designing the valve actuator, a task which is already sufficiently difficult.

The force required to actuate a valve consists of three principal components, i.e., friction, inertia, and flow forces. For valves of the same power output, supply pressure, and duty cycle, the input power required is proportional to the total stroke for the flow-force component and to the square of the stroke for the other two. Thus the power gain of the valve itself decreases rapidly with increasing stroke.

Not only does the power required to operate the valve increase rapidly with the maximum valve stroke, but also the over-all size and weight of the valve actuator increase at an even faster rate with the maximum valve motion. Size and weight considerations are important factors in designing control valves for air-borne applications. Both the power limitation and the actuator design tend to limit the total stroke to a few thousandths of an inch in practice. This limited stroke means very close control of valve dimensions if the low-gain central portion of the flow curve is to be small in comparison with the total operating region.

Another important parameter of a control valve is the amount of underlap or overlap.[3] A large amount of overlap produces an inactive band which is undesirable for most control systems; a large amount of underlap usually produces the adverse effects of increased error of the controlled quantity, due to load, and excessive leakage. In a feedback system, the load error can be reduced by increasing the feedback gain of the system. Usually, this can be achieved only at the expense of reduction of over-all power gain and stability of the system. Thus, from considerations of leakage and accuracy of control, valves with a very small amount of underlap or overlap are necessary. This again requires highly accurate matching between the metering edges of the valve body and those of the valve piston.

[3] "Contributions to Hydraulic Control—3 Pressure-Flow Relationships for 4-Way Valves," by J. F. Blackburn, Trans. ASME, vol. 75, 1953, pp. 1163–1170.

DIFFICULTIES OF MANUFACTURING SPOOL-TYPE VALVES

The principal difficulty in making spool-type valves arises basically from the fact that it is hard to perform accurate machining operations on the inside of a deep, small-diameter hole. The requirement of constancy of gain demands that the ports in the sleeve be rectangular, with the result that they cannot be drilled from the outside. Although there are certain constructions which permit the use of single-piece sleeves with the ports milled or broached, nearly all spool valves of the highest quality use sleeves comprising five or six parts for a four-way valve. This multiplicity of parts, each with several tight tolerances, makes the valves very expensive.

Even with great care in making and assembling the individual parts of the sleeve, it is still necessary to leave the piston lands excessively long and to grind the land faces as a final operation. The amount to be ground off each face is determined from experimental curves of flow versus displacement, since it is a practical impossibility to determine the effective axial locations of the port faces with sufficient accuracy by mechanical gaging.

It often occurs that even with great care in making the sleeve parts and assembling them in the valve block the flow curves show bellmouthed or staggered ports, bore-diameter variations, or various other defects that are difficult or impossible to discover by conventional methods of inspection and gaging. Some of these are reparable, at a considerable expense, but others require scrapping the whole sleeve assembly. This also makes the valves much more expensive than they should be and demands a new approach to the problem.

HOLE-AND-PLUG CONSTRUCTION

Much of the difficulty of making a high-precision valve arises from the difficulty of machining the inside of a small hole and would disappear if the hole were unwrapped somehow so that its inside surface became accessible. A valve configuration has been developed at the Dynamic Analysis and Control Laboratory of the Massachusetts Institute of Technology, which, in effect, does just this. It is shown schematically in Fig. 3 and several applications of this principle will be described.
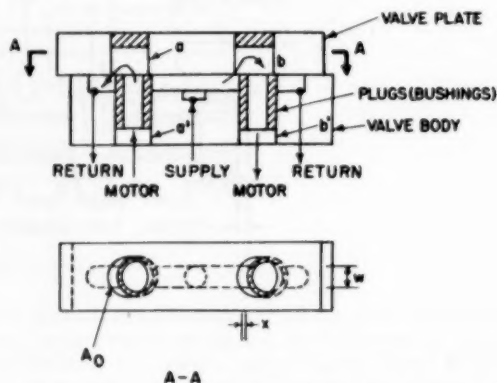

FIG. 3   SCHEMATIC DRAWING OF FOUR-WAY VALVE USING HOLE-
AND-PLUG-TYPE METERING ORIFICES

In Fig. 3 the two parts, the movable valve plate and the fixed valve body, initially are clamped together and the holes a, a' and b, b' are drilled, bored, and finish-lapped through both parts at the same time. This insures that the two pairs of holes will be accurately aligned. A groove of width w is milled in the body, and then bushings are pressed into the lower holes a' and b' and finished off flush with the upper surface of the body.

The edges of these bushings which are exposed by the longitudinal groove, together with the corresponding portions of the upper holes, form the four metering orifices of a four-way valve. Because the holes and bushings are matched accurately as to diameter and alignment, the valve has essentially zero underlap and overlap. Actually, there is normally a very slight overlap since the bushings are sufficiently larger than the holes to give a light press fit, but this geometrical overlap approximately compensates for the opposite effect of the necessary working clearance between plate and body.

When the valve plate is displaced longitudinally as shown in Fig. 3, two orifices are opened. Each of these orifices is bounded by two equal circular arcs and by two parallel straight lines, as shown in Fig. 4, so that they form curved parallelograms. The
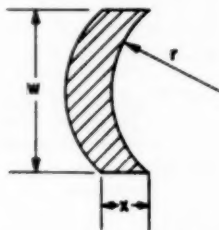
FIG. 4 AREA OF OPENING OF HOLE-AND-PLUG-TYPE ORIFICE

areas of the two are equal and independent of the diameter of the holes a, b so long as this diameter is greater than w. Also, if w is constant, the areas of these orifices are proportional to the displacement x, just as with rectangular ports. As already stated, this is very desirable for high-performance systems.

The drawing in Fig. 3 is merely schematic; obviously, means must be provided to permit the valve plate to move only in the desired direction and to maintain the necessary small clearance between plate and body. These restraints have been applied successfully to two general types of construction; in one, reed-type suspension supports the plate against the unbalanced pressure force and permits longitudinal motion only, and in the other, a symmetrical construction balances out the pressure force, and other constraints assure occurrence of only the desired motion.

SUSPENSION VALVE

The unbalanced pressure force acting on the valve plate in Fig. 3 can be opposed by various types of mechanical supports. One successful type, which is fairly easy to make, is a pair of reeds, preferably made integral with the valve plate, as shown in Fig. 5. The vertical arms of the U-shaped upper assembly act as columns in compression with their upper ends fixed. Thinned portions, c, d, e, f, serve as hinges and permit the valve
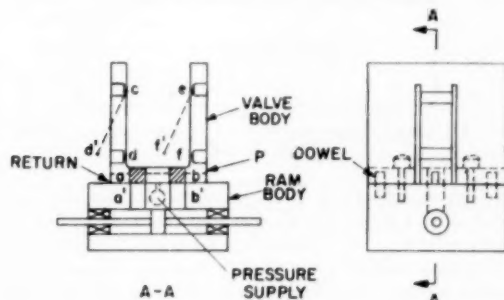

FIG. 5 SUSPENSION VALVE

plate to move parallel with the slot which is milled in its lower surface. They are made sufficiently rigid so that the maximum upward movement permitted to the valve plate under working pressure will be within reasonable limits. The vertical separation of the hinges determines the stiffness of the system to lateral deflections and also the amount of lifting at the end of the stroke. The latter is usually too small to be of any importance; for example, for a hinge separation of 1 in. and a lateral deflection of 0.010 in., the lift is only 0.00005 in.

The metering holes a and b in the valve plate P are drilled and lapped after P is assembled and doweled to the ram body. After the holes are finished, P is removed and solid plugs are pressed into a and b, as shown in Fig. 3. The lower surface of P is finish-ground to insure flatness, and any desired clearance may be established at this time.

One of the important properties of this construction is that there is never a metal-to-metal contact between plate and body, with the result that much of the rather unpredictable friction associated with most valves is eliminated. This low and fairly constant friction, together with the ease of manufacturing the valve in very small sizes, makes this construction ideal for pilot-valve service, where the input power is small, and also for pneumatic systems where lubrication is a serious problem. The cost of manufacture is much less than for a spool-type valve of comparable characteristics.

ROTARY-PLATE VALVE

The construction used for the suspension valve is not well adapted to large valves where the pressure force on the large-area valve plate would be excessive. For such applications it is preferable to use a balanced construction such that the pressure force on one side of the plate is counteracted by a similar force on the other side. A valve of this type is shown schematically in Fig. 6. The valve body is made up of two blocks and two
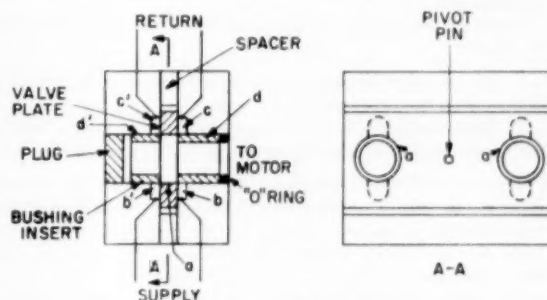

FIG. 6 ROTARY-PLATE VALVE

spacers which are doweled and screwed together. The moving member is a flat plate which rotates about a fixed pivot pin near its center. The metering holes and the pivot-pin hole are drilled and finished as before, in a single setup before the final grinding of the interior surfaces. The pressure cavities b, b' and the return cavities c, c' are milled out normal to the line of centers of the metering holes. Theoretically, they should be segments of circular grooves centered on the pivot pin, but for small angular motions the more convenient straight groove introduces only a very small deviation from linearity.

Hollow sleeves or bushings a, a are lightly pressed into the four holes in the two blocks. These sleeves are bored out to permit the oil to pass through into the motor lines, and it is usually advisable to flare the inner ends of the bores, as shown in Fig. 13, in order to cut down flow resistance at this point. Since there are now two metering orifices in parallel, one above and

one below the valve plate, the effective port width for this valve is twice the width of the milled grooves. The valve is statically pressure-balanced and has practically zero overlap or underlap.

Fig. 7 shows the flow path for the valve when the plate is displaced to one side, and Fig. 8 shows a flow-versus-displacement curve for a typical rotary-plate valve for a supply pressure of 1500 psi. Fig. 9 shows an early high-pressure gas valve of this type.
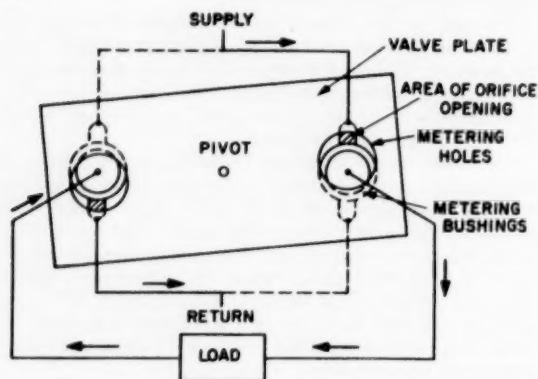

FIG. 7 SCHEMATIC DRAWING OF ROTARY-PLATE VALVE IN DIS-PLACED POSITION

FRICTIONAL FORCES AND FRICTIONAL-FORCE REDUCTION

The basic problems of friction between the moving and fixed members of plate-type valves are essentially the same as those of other valves, but the more accessible construction makes practical several antifriction devices that are difficult to apply to other configurations.

There are apparently two principal causes for excessive friction in valves:[4]

1 Dirt or other foreign material accumulating at the metering orifices or in the clearance spaces.

2 Unsymmetrical pressure distribution, which may result in very high unbalanced lateral forces on the moving member.

The dirt problems of the plate valve are essentially the same as those of any other close-clearance device that operates under the same conditions, and may be solved in the same way. The problems of unbalanced pressure distribution, however, may be somewhat more serious for the plate valve than for the spool valve, since it is more difficult to insure perfect symmetry. This maldistribution of pressure can be improved considerably by providing small holes through the valve plate, which function in exactly the same manner as the grooves usually provided on hydraulic pistons and valve spools. The provision of a few such holes in the proper locations permits a reasonable amount of dissymmetry in the milled cavities or other manufacturing imperfections that otherwise would increase the friction greatly. Experience has shown that this scheme, plus reasonable but not excessive care in manufacturing, results in plate-type valves that have friction levels as low as those of comparable spool valves when used on oil.

When the valves must have exceedingly low friction or when they are used on air or some other nonlubricating medium, it becomes necessary to use a more effective means of centering the valve plate. One simple and practical scheme which originally

[4] "Contributions to Hydraulic Control—5 Lateral Forces on Hydraulic Pistons," by J. F. Blackburn, Trans. ASME, vol. 75, 1953, pp. 1175–1180.
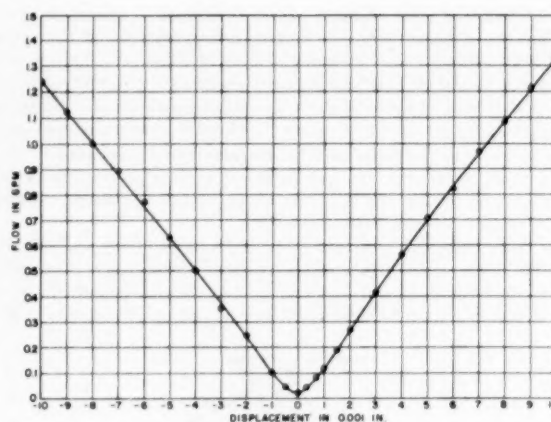
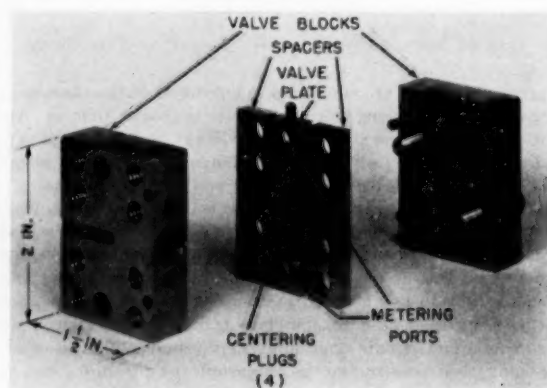FIG. 8 FLOW-TRAVEL RELATIONSHIP OF TYPICAL ROTARY-PLATE VALVE
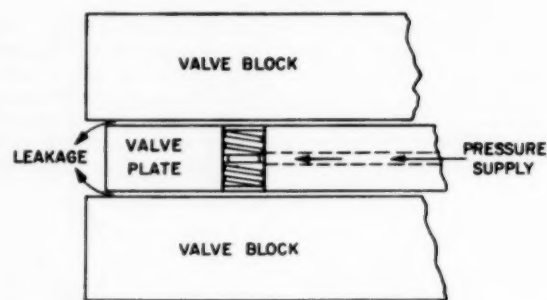

FIG. 9 PHOTOGRAPH OF ROTARY-PLATE VALVE

FIG. 10 SELF-CENTERING DEVICE EMPLOYED IN PNEUMATIC ROTARY-PLATE VALVE

was suggested by Dr. J. F. Blackburn of the Dynamic Analysis and Control Laboratory, Massachusetts Institute of Technology, is shown in Fig. 10. Small plugs are pressed into holes in the valve plate, and the centers of these holes are connected with the pressure supply. The plugs are provided with small grooves which have flow resistances roughly equal to those of the leakage paths outward through the clearance spaces. If the valve plate moves

upward, for example, the average pressure above the plate increases and that below it decreases, thus producing an unbalanced force which recenters the plate effectively. The depth and width of the grooves in the pins will be approximately 0.003 to 0.005 in. Spiral grooves of fine pitch are preferable because they are longer and, therefore, may be larger in diameter for the same resistance and consequently are less likely to be blocked by dirt. In most cases, as additional insurance against blocking, it is advisable to provide small filters in the supply duct. This scheme has proved to be very effective in a number of valves used on both air and oil.

FLOW FORCES AND FORCE COMPENSATION

The hydrodynamic force caused by the flow of fluid through the metering orifices is essentially the same for a plate valve as for a spool valve. It is always in a direction tending to close the valve and is usually considerably larger than either friction or inertial forces. If uncompensated, it is often large enough to prevent single-stage operation from a low-powered actuator such as an electromagnetic torque motor.

For a spool-type valve an effective method has been developed at the Dynamic Analysis and Control Laboratory, Massachusetts Institute of Technology.[2] A somewhat similar arrangement adapted to the hole-and-plug configuration of the plate valve is shown in Fig. 11. This diagram shows schematically a sliding-
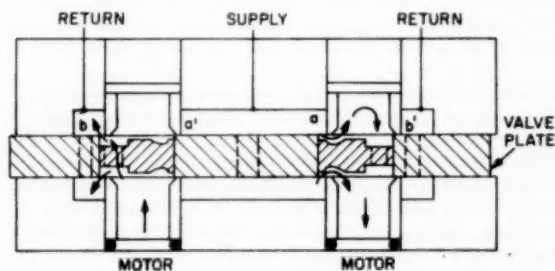

FIG. 11   FLOW-FORCE COMPENSATION, SCHEME 1

plate valve similar to that of Fig. 3 but double-faced and provided with two stream deflectors in the metering holes of the valve plate. The deflectors are shaped somewhat like turbine buckets, in such a way as to produce a net *opening* force which will balance out the *closing* force of the uncompensated downstream orifice. In a closed-center four-way valve, only two orifices are operating in series at any one time, so that this compensation is possible for all flow conditions. The inevitable manufacturing imperfections, however, make this compensation ineffective at very small valve openings, as shown in Fig. 12; hence it is best adapted to comparatively long stroke valves. In addition, at least for small valves, the contoured plugs are rather difficult to make.

A somewhat similar scheme which is easy to make and is particularly well adapted to the rotary-plate valve was designed by Mr. J. L. Coakley of the Dynamic Analysis and Control Laboratory and is shown in Fig. 13. Here the stream deflectors are two simple bushings with chamfered ends, pressed into the metering holes in the valve plate. Instead of being deflected back out of the plate as in the previous scheme, however, the momentum of the incoming jet is absorbed by baffle plates supported from the valve body. In both cases this momentum is transferred to the body rather than to the movable plate, and therefore does not produce a *closing* force on the latter. This momentum is acquired partly from the plate during the entry of the stream. This shows up as an *opening* force which can be used to compen-
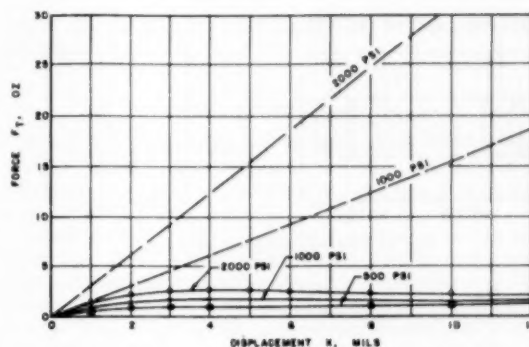

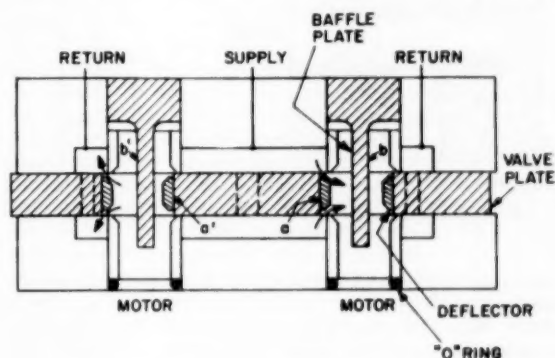FIG. 12   FLOW-FORCE CHARACTERISTICS OF COMPENSATED VALVE

FIG. 13   FLOW-FORCE COMPENSATION, SCHEME 2

sate the closing force of the outgoing stream through the other orifice, just as in the previous case. This second scheme is preferable to the previous one because the angle of deflection of the jet is less, with the result that it works better at small openings, because the parts are much easier to make and because it is possible to adjust the compensation over a small range by slight changes in the position of the baffle plate. This second force-compensation scheme has been applied to a number of rotary-plate valves and works very well.

OTHER RELATED VALVE CONFIGURATIONS

Obviously, the suspension valve and the rotary-plate valve just described are not the only valve configurations for which the basic hole-and-plug geometry is advantageous. Two others are suggested in Figs. 14 and 15. The first is a sliding-cylinder design analogous to the sliding-plate design of Figs. 11 or 13, and the second is a rotating-cylinder type. The cylinders must be constrained, from rotating in the first case and from axial movement in the second. Self-centering devices and flow-force compensation can be applied to these designs also, as well as to the many other possible variants of the basic construction.
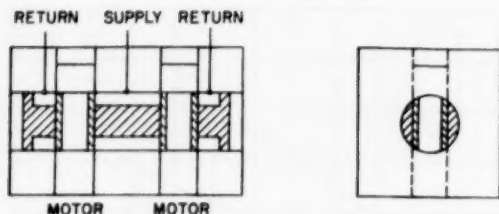
ACKNOWLEDGMENT
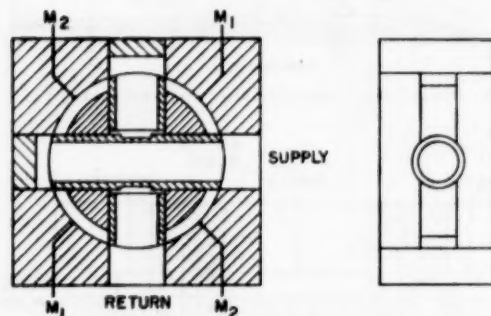
FIG. 14 SLIDING-CYLINDER DESIGN

FIG. 15 ROTARY-CYLINDER VALVE USING HOLE-AND-PLUG-TYPE METERING ORIFICE

struction and testing work of the valves mentioned in this paper was conducted by Mr. C. W. Gould to whom the author is very grateful. Many other members have contributed in the development work, particularly the following: Drs. J. F. Blackburn and T. C. Searle, Messrs. J. L. Coakley, T. E. Hoffman, and J. F. Dunn.

The author is especially grateful to Dr. J. F. Blackburn and Miss C. D. Boyd for their editorial assistance.

Discussion

M. R. HANNAH.[5] The author's work on the rotary-plate valve represents a significant contribution to the field of fluid-power control for high-performance servomechanisms. Although the writer has had no experience with the rotary-plate configuration, nevertheless it does appear to offer obvious advantages in terms of the simplicity with which near-zero overlaps can be achieved.

In fairness to the conventional spool-type valve, it should be pointed out that some of its disadvantages in cost of precision parts and assembly have been reduced considerably in quantity manufacture through the use of well-engineered machine tools and gaging equipment. The author's disparagement of spool-valve manufacture without resorting to trial-and-error tailoring of the axial dimensions merits some rebuttal because there are manufacturers who, during the past few years, have demonstrated their ability to make high-performance valves in large quantities using little or no hand machining and relying strictly upon electromechanical, pneumatic, and optical gaging techniques. Such procedures appear feasible, for example, in control valves having nominal overlaps of the order of 0.0015 in. and wherein overlap tolerances of, say, 0.0008 in. can be accepted. However, in the event that zero overlap, say less than 0.0002 in., is required then it is obvious that the rotary-plate construction can provide such close dimensional control with ease whereas in the

[5] Sperry Gyroscope Company, Great Neck, N. Y.

spool-type valve it would be quite difficult to achieve even with hand-tailoring.

Moreover, it does appear that another important deficiency of the conventional multi-insert sleeve configuration, namely, the geometric instability of the assembled parts due to metal "growth" or aging, might be significantly less serious in the rotary-plate construction because of the relatively greater restraint of those parts whose growth could interfere with the normal motion of the valve plate. These critical parts are considered to be the four "plugs" or inserts occupying the aligned bores in the two halves of the valve body as seen in the author's Fig. 13. It is also significant that the residual stresses in these inserts are radial rather than axial whereas in the insert-sleeve construction they act in the direction in which metal growth would cause valve sticking.

Regarding the valve-body inserts themselves, some comment in the author's closure is invited concerning the nature of the chamfer which he shows on these parts in Fig. 13. It is assumed that the degree of sharpness normally desired is not such that the erosion of the metering edge would be aggravated or that machining would be made more difficult. It has been interesting to note the ease with which the author has been able to apply to the rotary-plate configuration the flow-force compensation techniques which he had developed previously for the spool-type valve.

Widespread use of control valves of the rotary-plate configuration can be expected in guided missiles and similar applications wherein performance requirements are particularly severe.

AVREL MASON.[6] This paper represents another significant contribution to equipment technology originating from the Dynamic Analysis and Control Laboratory at M.I.T.

This latest paper of the series contributes two new ideas to valve technology; the "hole-and-plug" construction as a means for simplifying valve manufacture, and the elimination of coulomb friction by the suspension-type design. The several configurations shown appear to be simple and practical and, within certain limitations as noted by the author, seem eminently suited to high-performance servosystems.

The plug-and-hole type construction seems best suited for intermediate production rates, where its use should cost considerably less than the familiar "grind-after-flow-testing" lap-setting procedure conventionally used for spool valves. The limitations of the hole-and-plug design lie largely in the lack of interchangeability of parts between the valves. It is first necessary to assemble the valve "sandwich," then, after performing the doweling, boring, and lapping, to disassemble for the subsequent surface grinding and bushing-fitting operations. When these operations are complete, this same set of parts must then be reassembled, the key parts of each valve not being interchangeable with those of other valves. To achieve true interchangeability, the same close tolerances would have to be held as are now required in conventional designs.

For high production rates, say over ten per day, this procedure appears to be somewhat cumbersome and one looks to other configurations for low-cost manufacturing. The open-center valve, either flapper or spool type, circumvents some of the manufacturing difficulties inherent in the closed-center type. Manufacturing tolerances on either the flapper orifice width or spool underlap distance can be from 5 to 10 times as large as on the closed-center valve, yet the linearity around the null condition is superior. For use as a pilot stage in two-stage valves, where the power stage usually appears as a light load to the pilot stage, it is hard

[6] Supervisory Engineer, Bendix Aviation Corporation, Research Laboratories, Detroit, Mich.

to beat the open-center configuration for good performance and inexpensive mass production.

The elimination of friction by means of the suspension-type construction or by the hydraulic self-centering feature of the rotary-plate valve is certainly desirable. Reduction of coulomb-friction levels reduces the amount of dither required and results in a more linear system, making linear network compensation considerably more effective in improving the loop response characteristics. Our experience has shown that the friction reduction that can be achieved by these means is so significant that all high-performance single-stage servovalve designs should include them. The self-centering scheme for the rotor plate shown in Fig. 10 of the paper is a variation of the common pressurized-fluid-type bearing. This technique can also be applied readily to spool-type valves.

The scheme for flow-force compensation, shown in Fig. 13, is an extremely neat answer to the manufacturing problems inherent in turbine-type compensation. Although the flow-compensated valve permits handling large fluid power with small power inputs, there are times when use of turbine-type compensation is undesirable, because of the changing compensation effectiveness with valve deflection, as shown in Fig. 12, which results in a nonlinear flow/actuator input current characteristic. System studies at the Bendix Research Laboratories have shown that this effective gain change can, under certain conditions, cause dynamic stability problems. It would be interesting to see a curve corresponding to Fig. 12, for the baffle-type compensation. In considering two-stage valves for handling 10 or more horsepower, there is little to be gained by flow compensation.

Our own experience with the plate-type hole-and-plug valve is not yet adequate to form final conclusions as to its merits. We do know that it takes us considerably less time to construct than a spool type. It would be of interest if the author could furnish a table showing a comparison of manufacturing and checkout test costs between the two new valves and a comparable performance unit of the spool type. Certainly the author is to be commended for such practical steps forward in valve design,

which should promote more general use of high-performance equipment

AUTHOR'S CLOSURE

The author wishes to express his appreciation to Mr. Hannah and Mr. Mason for their discussions and trusts that the following information will supply the answers to their questions regarding manufacturing costs.

In designing fast-response single-stage servovalves, the maximum valve stroke should be kept very small to minimize the power required to operate the valve. Consequently, very close tolerances are required for all dimensions, say, $\pm$ 0.0001 in. For this kind of application, valves with metering orifices of the hole-and-plug type can be manufactured at a fraction of the cost of a conventional spool-type valve. It should be pointed out, however, that production with the aim of attaining interchangeability of parts is not practical for either case. On the other hand, for longer stroke valves (e.g., valves driven from a high-power source), the tolerance requirements are not as severe, that is, $\pm$ 0.001 in. or more. All the critical dimensions of a spool-type valve can be obtained by accurate gaging techniques, thus making all valve parts interchangeable. However, for the longer stroke valve, the hole-and-plug type of metering orifice can be produced with interchangeable parts, perhaps at a cost considerably lower than that for the spool-type valve. At the D.A.C.L. this has been accomplished by drilling and reaming the metering holes on the valve parts with correctly designed drilling jigs. A tolerance of the order of $\pm$ 0.0003 in. was found practical.

It is quite true, as Mr. Mason pointed out, that open-center valves can be made at much less cost than closed-center valves, but the use of an open-center valve is limited to applications in which the leakage flow and output stiffness (load sensitivity) are not important considerations.

The chamfers on the sleeves shown in Fig. 13 are for force-compensation purposes only. The degree of shearness is not at all critical.
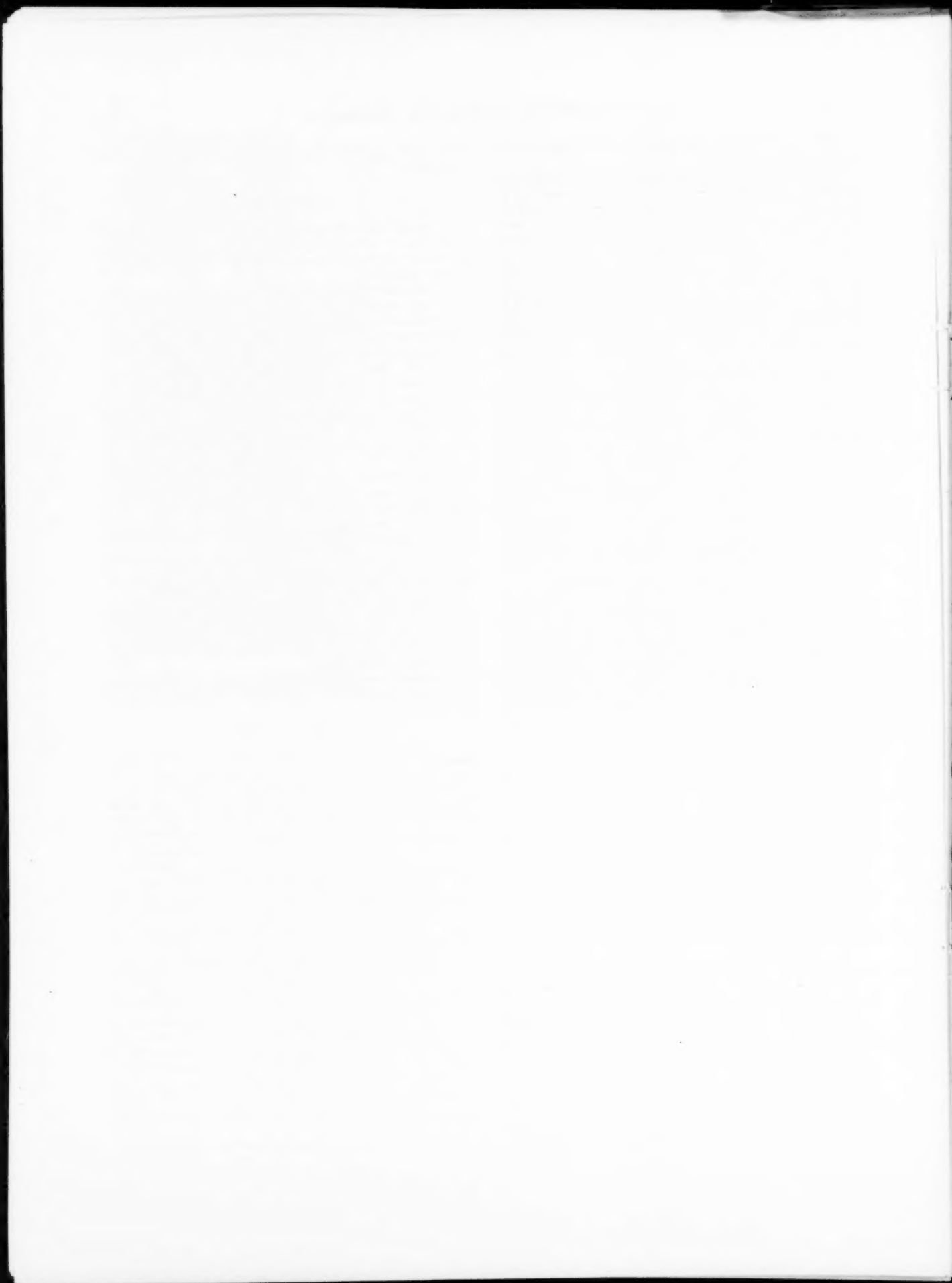
Evaluation of Transient Temperatures and Stresses

By R. J. FRITZ,[1] SCHENECTADY, N. Y.

Solutions to the one-dimensional, heat-conduction equation for arbitrary surface temperature transients are treated by superposition of other solutions and by a concept of thermal reflections. The maximum thermal stresses are given for a flat plate due to a given surface temperature change at a linear rate. Thermal stresses in thin cylindrical shells are discussed, and an example is evaluated.

Design factors are discussed briefly, mainly by citing critical problems and giving references. A comprehensive bibliography is presented.

NOMENCLATURE

The following nomenclature is used in the paper:

A = constant temperature, deg F

B = constant rate of temperature change, deg F per sec

$C = \dfrac{hL}{k}$

$D = \dfrac{EH^3}{12(1 - \mu^2)}$ = plate flexural rigidity, lb-in.

E = Young's modulus in psi; may be taken as 30×10^6 psi for steel

$f(nL + x, t)$ is a function of distance $nL + x$ and time t

$g(t)$ and $f(t)$ are arbitrary functions of time

h = film heat-transfer coefficient, Btu/hr sq ft deg F

H = shell thickness, ft

k = thermal conductivity, Btu/hr ft deg F

L = plate thickness, ft.

M = uniformly distributed (tangentially directed) moment around cylindrical shell, lb-in. per in.

m = thermal gradient, deg F per in.

P = uniformly distributed (radially directed) shear force, lb per in.

R = mean radius of thin cylindrical shell, in.

s = Laplace transform parameter

T = temperature, deg F

t = time, sec

ΔT = temperature difference treated as variable, deg F

ΔT_0 = constant temperature difference, deg F

x = distance, ft

y = deflection of cylindrical shell radially inward from stress-free dimension, in.

y' = slope of y, in. per in.

ϵ = thermal diffusivity in in²/sec or ft²/sec, equals thermal conductivity divided by thermal capacity per unit volume; it is about 52×10^{-6} ft²/sec for 18-8 stainless steels

α = linear coefficient of thermal expansion, per deg F; for ferritic steels it is about 7×10^{-6} per deg F while for austenitic steels it is about 10×10^{-6} per deg F

μ = Poisson's ratio; for Fig. 5 and Table 1, $\mu = 0.3$ is assumed which is a good value for most steels

θ = angle in radians

γ_n = root of $\gamma \tan \gamma = C$

ξ = x/L = normalized distance

σ = stresses, psi

λ = characteristic length for thin-walled cylinders, in.

$\quad = [3(1 - \mu^2)]^{-1/4} \sqrt{RH}$

$\quad = 0.778 \sqrt{RH}$ for $\mu = 0.3$

Subscripts:

x = longitudinal direction

ϕ = hoop or tangential direction

r = radial direction

o = outside of cylindrical shell wall

i = inside of cylindrical shell wall

INTRODUCTION

There are several trends in modern power-plant design and practice which make a knowledge of transient temperatures and stresses important. Long-time start-ups of stationary power plants are costly. The use of liquid metals in heat exchangers and nuclear reactors increases thermal stresses because of inherently high film heat-transfer coefficients. In these components as well as in the gas turbine and other heat engines an accurate evaluation of thermal stresses and distortions must be made in order to insure safe and reliable operation. It then becomes important to be able to calculate accurately transient temperature distributions and stresses in structural elements. This paper presents a discussion of design factors, graphs, and other data on transient-temperature distribution and thermal stresses which have been found helpful in design evaluations.

In general, the geometries that are met by the designer are complicated. The problem of thermal stresses is of most importance near structural discontinuities such as flanges, piping nozzles, and the like. The designer can choose to solve the exact geometry and make a career of slowly converging infinite series, or he can make simplifying and conservative assumptions and achieve a more rapid evaluation. An important simplification is to approximate the problem by assuming one-dimensional heat flow. Such an assumption will be made throughout this paper.

TRANSIENT CONDUCTION WITH ARBITRARY SURFACE TEMPERATURES

Semi-Infinite Media. We will first consider heat flow in semi-infinite isotropic media and then extend the solution to finite plates by the use of the concept of thermal reflections.

Fig. 1(a) presents the response to a step surface transient of a semi-infinite isotropic medium with zero initial temperature. Fig. 1(b) gives the response to a linear temperature change. Both of these curves are presented as functions of dimensionless parameters. The Appendix gives the solution from which the curves were drawn.
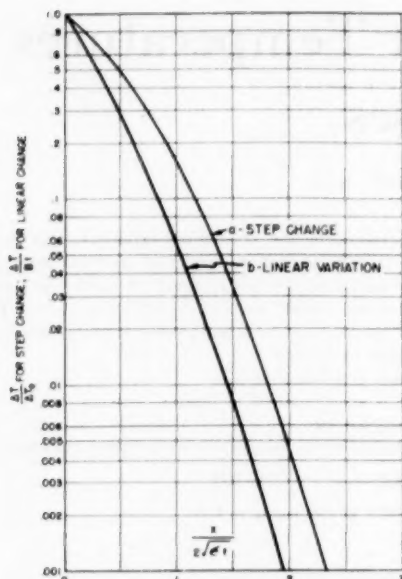
FIG. 1   TEMPERATURE DISTRIBUTION IN SEMI-INFINITE SLAB WITH ZERO INITIAL TEMPERATURE WHEN SURFACE TEMPERATURE—a, CHANGES INSTANTANEOUSLY BY ΔT_0; b, VARIES LINEARLY WITH TIME AT CONSTANT RATE B

An arbitrary surface-temperature transient can be fabricated by the use of steps and linear functions. For most practical cases two or three such linear functions normally suffice to approximate the specified surface variation. Figs. 2(a) and 2(b) give an example of the addition of three linear functions to approximate a specific surface transient. Each linear function is treated independently and the temperature responses added algebraically, taking cognizance of the time delays between functions. If several linear functions are superimposed it will be found that at times much larger than the initial temperature disturbance, trouble will be met in taking the difference of numbers that are practically equal. In these cases the linear functions are replaced by fewer linear functions or by step functions. This will present no difficulty to the reader if he remembers that, at times long after the application of a particular surface transient variation, details of shape of the surface variation are damped out.

Initial temperature distributions may be taken into account in the following manner. The boundary value problem may be formulated (1)[2]

$$\frac{\partial^2 T}{\partial x^2} = \frac{1}{\epsilon}\frac{\partial T}{\partial t}, \quad T = T(x, t), \quad t > 0, x > 0$$

$$T(0, t) = f(t); \quad T(x, 0) = g(x) \quad \dots\dots\dots [1]$$

Assume

$$T = T_1 + T_2 + A \dots\dots\dots\dots [1a]$$

where

$$\frac{\partial^2 T_1}{\partial x^2} = \frac{1}{\epsilon}\frac{\partial T_1}{\partial t}, \quad T_1 = T_1(x, t), \quad t > 0, x > 0 \dots [2]$$

$$T_1(0, t) = f(t) - A; \quad T_1(x, 0) = 0$$

and

$$\frac{\partial^2 T_2}{\partial x^2} = \frac{1}{\epsilon}\frac{\partial T_2}{\partial t}, \quad T_2 = T_2(x, t), \quad t > 0, x > 0 \dots [3]$$

_____
[2] Numbers in parentheses refer to the Bibliography at the end of the paper.
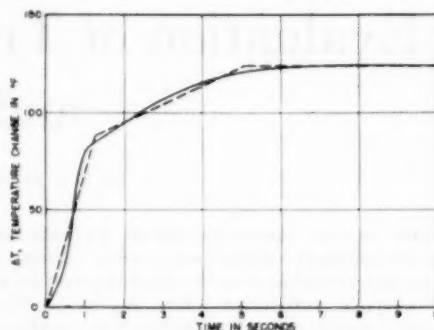

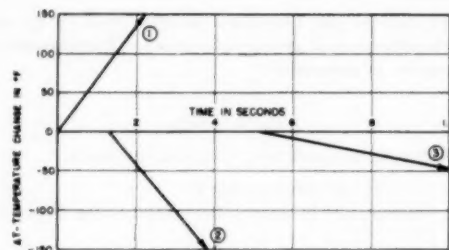FIG. 2(a)   ANALYSIS OF A SPECIFIED SURFACE TEMPERATURE INTO LINEAR COMPONENTS

FIG. 2(b)   ANALYSIS OF A SPECIFIED SURFACE TEMPERATURE INTO LINEAR COMPONENTS
(Linear components, when added give dashed curve of 2(a), which approximates solid curve.)

$$T_2(0, t) = 0; \quad T_2(x, 0) = g(x) - A$$

T_1 may be broken up into steps and linear components, and solved by superposition of solutions in Figs. 1 (a and b). The constant A is a datum of temperature which is chosen for convenience to minimize the calculations. Experience will show that for many problems A can be chosen so as to make an evaluation of stresses possible without the necessity of solving for T_2. This occurs when the $g(x) - A$ variations are small compared to the $f(t) - A$ variation. For example, suppose a steel pipe is initially at 1200 F with a variation of about 50 deg F through the pipe wall. Also, suppose that the surface is shocked to about 300 F. The datum A may be chosen at 1200 F. Then $g(x) - A$ is about 50 deg F; $f(t) - A$ is about 900 F. Then the former may be neglected with respect to the latter. At any rate, A in most cases may be chosen to insure a conservative thermal-stress calculation. If the initial temperature distribution must be taken into account it probably would be desirable to use a numerical method to solve the complete problem. Such methods are described by Dusinberre (2). The advantage of solving a problem by the superposition of known solutions rather than by using a numerical solution is that it is a quicker method, especially when solutions over a large time and distance range are necessary, for which the numerical methods become cumbersome.

THERMAL REFLECTIONS

In the repeated evaluation of the temperature distribution due to a specified surface transient it is convenient to be able to derive the distribution in a finite slab or plate in terms of the semi-infinite temperature distribution. For the problem of an isotropic medium of thickness L with a uniform (or nearly uniform) initial temperature distribution and with an arbitrary surface transient on one face and perfect insulation on the other face, the temperature distribution is

$$T = f(x, t) - f(2L + x, t) + f(4L + x, t) - \ldots$$
$$+ f(2L - x, t) - f(4L - x, t) + f(6L - x, t). \ldots [4]$$

where $f(x, t)$ is the solution for the temperature distribution for the semi-infinite solid due to the specific surface transient and referred to the initial uniform temperature as a datum. The physical interpretation of this is as follows:

When a thermal shock is imposed on the surface, the thermal wave travels into the medium. At an insulated face it may be imagined that an image shock wave is traveling toward the insulated face from the opposite direction. Thus the net heat flux passing the insulated face is the sum of equal and opposite heat fluxes which is zero. At this insulated face the thermal flux cancels, but the temperatures add. The direct wave continues its direction into the image medium, while the image wave propagates in the opposite direction. At the shocked surface (also at its image) the boundary condition is an arbitrary temperature which is a characteristic of the environment. To maintain this boundary condition it may be imagined that the wave is again reflected but with a change in sign, such that at the surface the net contribution from the returning wave is zero. A mathematical interpretation of this concept is given in the Appendix.

In many design investigations it may be convenient to calculate charts which give the response of a semi-infinite medium to a specified surface transient. Such a chart is shown in Fig. 3 which gives the temperature response of a semi-infinite slab of an 18-8 stainless steel to the indicated surface transient. This chart was calculated by superimposing two equal and opposite linear surface transients displaced by 100 sec. The response for a finite thickness may then be obtained by adding the series of reflections indicated by Equation [4]. The series converges quickly for plates of ordinary thicknesses so that usually employment of only the first two or three terms of the series is necessary. The problem of the slab of thickness L insulated on one face can be shown to be equivalent to a half-section of a slab of thickness $2L$ thermally shocked on both faces.

Although the concept of thermal reflections is fairly obviously implied by the differential equations (see Appendix), the concept has not been sufficiently called to the attention of the design engineer. However, a similar physical concept is commonly used in electrical transmission line and elastic-wave theory. The same may be said of the principle of superposition which may be applied to any system describable by a linear partial (or ordinary)

differential equation with constant coefficients (or with coefficients not a function of the dependent variable).

THERMAL STRESSES IN SHELLS

The problem of converting known temperature distributions to stresses is well known. A list of some important references on this subject is given at the end of this paper. Some examples of converting known temperature distributions into stresses will be given.

Fig. 4 presents the results of calculating the maximum biaxial surface stresses in a plate of thickness L, when one surface of the plate is washed by a fluid with heat-transfer coefficient h, and the other surface is perfectly insulated. The bulk temperature of the fluid changes linearly by ΔT_0 in time t_0, remaining constant thereafter. The plate is assumed restrained from bending and edge effects are neglected. Where bending is allowed, the stresses are reduced. These stresses apply to a thin-walled cylinder of wall thickness L, which automatically is restrained from bending by virtue of its shape. The biaxial stresses in this case are in longitudinal and hoop directions. The thermal disturbance is on the inner surface (or outer) of the cylinder wall, where the other surface is insulated. The results of this calculation also apply to a plate $2L$ in thickness shocked on both faces. By symmetry the plate does not bend. The Appendix indicates the mathematical derivation for this graph.

In using the results of Fig. 4, the analyst must choose the significant transient heat-transfer coefficient h. The phenomenon is too complicated (e.g., by phase changes as in the case of water, or by transient boundary layers in the case of constant phase fluids) for any quantitative descriptions here. The author knows of no reference on transient heat-transfer coefficients as such. The analyst probably can find published data on heat transfer to walls with nonuniform temperature, which may prove helpful for some cases, or heat-transfer coefficients near entrance regions where the boundary layer has not been stabilized, which may be helpful in others.

To evaluate stresses due to temperature differences in the thickness direction in a thin-walled cylinder or in a plate restrained from bending by its own symmetry or by supports, the following method is convenient. It may be shown that the biaxial surface stresses (except near discontinuities) are given by

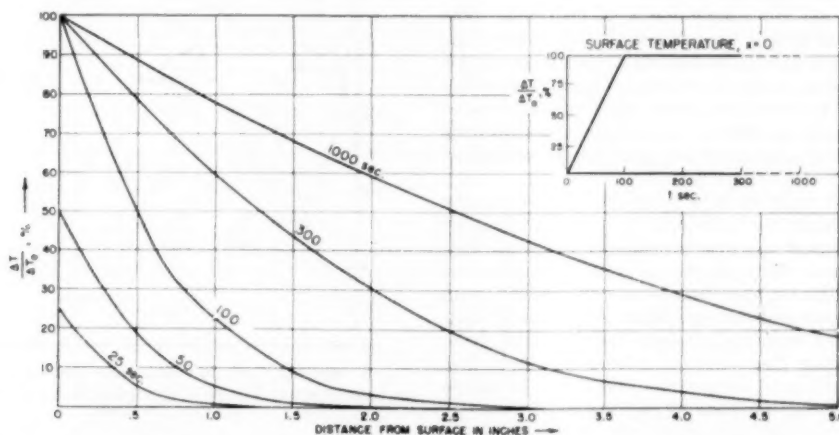$$\sigma = \frac{E\alpha\Delta T}{1 - \mu} \ldots \ldots \ldots \ldots [5]$$

FIG. 3   TEMPERATURE DISTRIBUTION IN 18-8 STAINLESS STEEL SEMI-INFINITE SLAB; THERMAL DIFFUSIVITY = 52×10^{-6} FT² PER SEC

(To refer curves to other materials, divide times by $\alpha/[52 \times 10^{-6}]$ where α is thermal diffusivity of other material in square feet per second.)

$$\sigma^* = \frac{\sigma}{\frac{E\alpha\Delta T_0}{1-\mu}}; \quad C = \frac{\hbar L}{k}; \quad S_0 = \frac{et_0}{L^2}$$
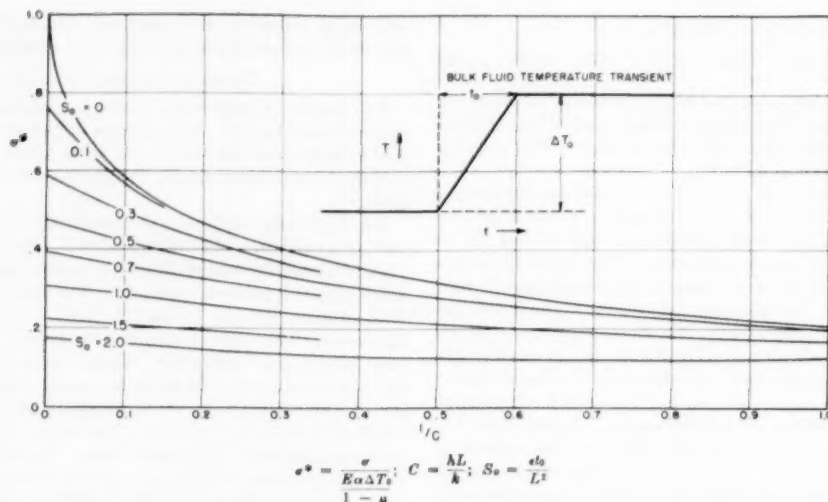
FIG. 4 MAXIMUM BIAXIAL SURFACE STRESS, AWAY FROM EDGES, OF SLAB OF THICKNESS L

(Slab initially at uniform temperature. One surface insulated; other surface in contact with fluid whose bulk temperature varies linearly by ΔT_0, as indicated. Heat-transfer coefficient from plate to fluid is $\hbar$.)

where ΔT is the temperature deviation from the average wall temperature for the point at which the stress is being evaluated. ΔT may be determined easily from a temperature plot.

Inspection of the temperature plot, Fig. 3, indicates that thermal transients are damped out with distance away from the disturbance. Therefore, to protect vital structural elements a thermal-shock shield may be used. This shield is a barrier to heat flow. Assume that the shield is constructed of the same material as the structure. If a thickness of shield is chosen, then the temperature distribution may be determined from a chart similar to Fig. 3 (neglecting any contact drop between shields, which is pessimistic in that it gives too big a temperature variation across the shield, except for structures immersed in liquid-metal coolants where the error is small). Knowing the temperature distribution in the shield plate, the stresses may be determined by Equation [5]. If the contact drop between the shield plate and the shielded structure is small, the temperatures and stresses also may be determined for the shielded structure.

Table 1 presents stresses and distortions for some important geometries which are not readily found in textbooks. The formulas listed were derived from Roark (6) and Hetenyi (3). The latter reference is valuable in forming a physical concept for distortions and stresses along a symmetrically loaded thin-walled cylinder. There it is shown that a thin-walled cylinder behaves as a beam on an elastic foundation; i.e., a longitudinal strip along the cylinder may be treated as a beam restrained by elastic hoop forces.

Any integral structure which is thermally stressed may be solved for these stresses by visualizing the structure cut apart with the components of the structure allowed to assume their stress-free dimensions. By application of suitable moments and forces on each component these components are brought into a shape compatible with neighboring components. After evaluating these forces and moments, one can calculate the stresses. This concept simplifies the analysis of thermal stresses in thin-walled cylinders with axial temperature variations. It will be illustrated in calculating the following problem:

Consider the case of a long thin-walled cylinder with an abrupt change in temperature gradient. The long cylinder may be imagined to be severed at the break in gradient. Moments and shear forces are applied to each half to make the rotation and the
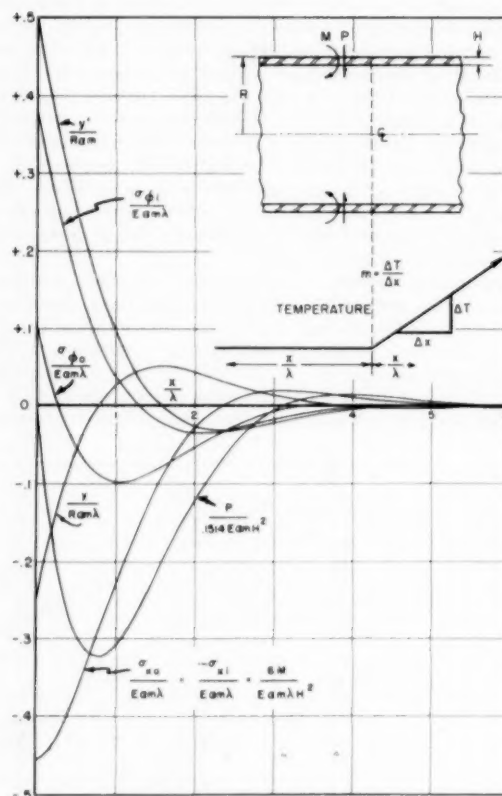

FIG. 5 STRESSES AND DEFORMATIONS DUE TO AN ABRUPT CHANGE OF LONGITUDINAL THERMAL GRADIENT ALONG A LONG THIN-WALLED CYLINDER

displacement continuous. In this particular case a distributed moment around the periphery is adequate to bring each half into continuity, since the break in temperature gradient brings about

an angular (i.e., slope) mismatch only. Then each half may be assumed to apply a moment to the other half to make up half of the total angular mismatch. The total angular mismatch is

$$\theta = \alpha Rm \dots\dots\dots\dots\dots\dots [6]$$

Therefore, since the flexibility of a cylinder is

$$\frac{\theta}{M} = \frac{\lambda}{D} \dots\dots\dots\dots\dots\dots [7]$$

The moment applied to each cylinder is

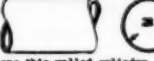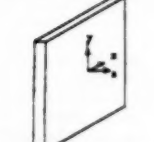$$M = \frac{D}{\lambda} \frac{\alpha Rm}{2} \dots\dots\dots\dots\dots\dots [8]$$

Hetenyi[3] formulates the response of the beam on an elastic foun-

[3] Reference (3), pp. 24-25.

dation to an end moment. When the corresponding elastic properties for a cylinder (described by Hetenyi) are cranked into these formulas, stresses and deformations can be evaluated and are shown in Fig. 5.

The meaning of "abrupt" and "long" can be implied from this graph. Any thin-walled cylinder is long which is over about 5λ in length. For $\mu = 0.3$ one obtains $\lambda = 0.778\sqrt{RH}$ (reference 3) so that a cylinder over $4\sqrt{RH}$ in length is essentially semi-infinite in that any disturbance along the cylinder is essentially damped out (to less than 1 per cent) in this distance. Also, any change in loading which takes place in a distance small with respect to λ may be considered abrupt. This distance may be taken as $0.05\sqrt{RH}$. Such an assumption will keep errors in calculated stresses to less than about 10 per cent. If the change is not abrupt, then the temperature gradient may be broken into linear

TABLE 1   STRESSES AND DISTORTIONS FOR VARIOUS GEOMETRIES

Form of Vessel	Loading and Case No.		Maximum Stresses
Long, joined thin-walled cylinders	A. Rotational misalignment between cylinders of amount θ	1. Break in longitudinal temperature gradient $\theta = \alpha R^2 \left(\frac{dT}{dx}\Big|_2 - \frac{dT}{dx}\Big|_1\right)$ 2. Constant temperature gradient but change in coefficient of thermal expansion $\theta = (\Delta\alpha)\,R\frac{dT}{dx}$ 3. Combination of 1 and 2	a. $R_1 = R_2 = R$ Max $\sigma_z = \pm 0.955\ E\theta\sqrt{\frac{R}{H}}$ Max Shear Stress $= \left|\frac{1}{2}(\sigma_z - \sigma_\varphi)\right| = 0.220\ E\theta\sqrt{\frac{R}{H}}$ b. $R_1 \gg R_2$ Max $\sigma_z = 1.41\ E\theta\sqrt{\frac{R_2}{H}}$ Max Shear Stress $= \left|\frac{1}{2}(\sigma_z - \sigma_\varphi)\right| = \left|\frac{1}{2}(\sigma_z - \sigma_\varphi)\right| = 0.71\ E\theta\sqrt{\frac{R}{H}}$
	B. Radial misalignment between cylinders of amount δ	1. Abrupt temperature change of ΔT between cylinders $\delta = R\alpha\Delta T$ 2. Differing coefficients of thermal expansion $\delta = RT\Delta\alpha$ 3. Combination of 1 and 2	a. $R_1 = R_2$ Max $\sigma_\varphi = 0.50\ E\frac{\delta}{R}$ Max Shear Stress $= \left|\frac{1}{2}(\sigma_\varphi - \sigma_z)\right| = \left|\frac{1}{2}(\sigma_\varphi - \sigma_z)\right|$ $= 0.25\ E\frac{\delta}{R}$ b. $R_1 \gg R_2$ Max $\sigma_\varphi = 1.82\ E\frac{\delta}{R}$ Max Shear Stress $= \left|\frac{1}{2}(\sigma_z - \sigma_\varphi)\right| = 1.13\ E\frac{\delta}{R}$
Long thin-walled cylinder (away from ends)	C. Uniform axial bending	1. Uniform second derivative of temperature variation $a = \frac{d^2T}{dx^2}$	Max $\sigma_z = 0.549\ E\alpha R H\,a$ Max Shear Stress $= \left|\frac{1}{2}(\sigma_z - \sigma_\varphi)\right| = \left|\frac{1}{2}(\sigma_z - \sigma_\varphi)\right|$ $= 0.275\ E\alpha R H\,a$
Element of any structure uniform wall thickness, restrained from bending, away from edges	D. Temperature varies across thin wall; surface temperature differs from volume average by ΔT		Max $\sigma_z = \sigma_\varphi = 1.43\ E\alpha\Delta T$ Max Shear Stress $= \left|\frac{1}{2}(\sigma_z - \sigma_y)\right| = \left|\frac{1}{2}(\sigma_\varphi - \sigma_y)\right|$ $= 0.71\ E\alpha\Delta T$
Same as C	E. Linear temperature variation through wall. Total temperature drop is ΔT		a. Away from ends. Apply Case D. Surface temperature differs from average by $\frac{\Delta T}{2}$. Max $\sigma_z = \sigma_\varphi = 0.71\ E\alpha\Delta T$ Max Shear Stress $= \left|\frac{1}{2}(\sigma_z - \sigma_y)\right| = \left|\frac{1}{2}(\sigma_\varphi - \sigma_y)\right|$ $= 0.36\ E\alpha\Delta T$ b. At free cylinder end Max $\sigma_\varphi = 0.89\ E\alpha\Delta T$ Max Shear Stress $= \left|\frac{1}{2}(\sigma_\varphi - \sigma_z)\right| = \left|\frac{1}{2}(\sigma_\varphi - \sigma_z)\right|$ $= 0.45\ E\alpha\Delta T$
Unrestrained thin-walled shell of uniform wall thickness, away from edges	F. Linear temperature variation of ΔT across thin wall		No stress, shell assumes spherical shape of radius $R = \frac{H}{\alpha\Delta T}$ (small deflections)
Any shape of isotropic material	G. Linear or constant temperature throughout structure		No stress

components as was done for temperatures in Figs. 2(a and b), and the stresses due to each component added algebraically. The analyst will be able to pick out the position of highest stress as being in the region of most severe temperature change. Only two or three linear components should suffice to obtain the net effect. For a situation where the temperature changes gradually, Case 2 of Table 1 ordinarily should suffice to give a fairly accurate evaluation of stresses.

MATERIAL BEHAVIOR

A brief discussion of material behavior is included here for the sake of completeness. Subjects relating to designing for thermal stresses are introduced for which references are given.

Failure due to thermal stresses may occur after but a few cycles in which the failure is usually referred to as due to thermal shock, or after many cycles in which the failure is due to thermal-stress fatigue. Shock failures ordinarily occur in brittle materials. Where ductile materials are involved, failure usually will be by thermal-stress fatigue. However, it must be recognized that a material which exhibits ductility in the tensile-bar test may be notch-brittle at the test temperature or may be almost completely brittle at lower temperatures. A good discussion of brittle behavior in metals is presented by E. Orowan (5).

In most cases brittle fractures may be correlated by the following dimensionless moduli

$$\frac{\sigma_B}{E\alpha\Delta T} = F\left(\frac{hL}{k}, \frac{tl}{L^2}\right) \quad\quad\quad [9]$$

where σ_B is the brittle fracture stress. L, ΔT, and t are the significant length, temperature change, and time parameters for the particular case. For instance, in the case of Fig. 4, the significant parameters obviously are the thickness of the plate L, the extent of the temperature change ΔT_0, and the time in which this temperature changes t_0. For longitudinal temperature distribution along a cylindrical tube, L would be the characteristic length, Fig. 5. To maintain similitude in scaling models of large components, these dimensionless moduli must be held constant. For a further discussion of similitude or the theory of models Hetenyi (4) may be consulted.

Fatigue failures in metals are rather complex and not completely understood. Nonlinearities of stress-strain relationships, fatigue "shakedowns," and other metallurgical changes complicate the picture. When a metal is strained thermally beyond the elastic limit and then the strain is removed or reversed, the stress-strain curve describes a hysteresis loop whose area measures the work of plastic deformation. The more the stress exceeds the elastic limit, the greater will be the area of the hysteresis loop and also the plastic-deformation energy per cycle. This energy of plastic deformation largely represents damage to the material. As the strain is cycled, the energy loop tends to decrease or shake down, due to strain hardening. Gensamer (5) aptly describes fatigue as a race between strain-hardening and damage. Coffin presents a detailed discussion of thermal fatigue in metals in reference (14).

For cyclic thermal stresses, the designer may use as a design basis what is known about stress fatigue. Briefly, according to Gensamer (5): (a) The safe range of cyclic stress for a given mean stress varies approximately linearly with the logarithm of the number of cycles to failure; (b) for some materials below a certain limiting range of stress known as the endurance limit, failure will not occur; (c) as the mean stress is increased, the safe range of cyclic stress diminishes, but not linearly; (d) the effects of combined stresses for ductile alloys are described adequately by the shear-strain-energy hypothesis; (e) the notch effect is caused by strain concentration; for hard steels, notches seem to have no

effects other than those calculable from known stress distributions; (f) the action of corrosion is apparently to sharpen the notch, or to make one if none existed, thus further localizing the strain; galling can have a similar effect by roughening surfaces and causing strain concentrations.

A rational approach to the choice of working stresses as suggested by C. R. Soderberg (4), analyzes the effects on ductile and brittle materials at normal and elevated temperatures of multi-axial static and cyclic stresses. However, thermal stresses are not specifically discussed. Obviously, it would be poor design to neglect the existence of thermal stresses altogether. On the other hand, the designer must choose some rational method of taking them into account. It would appear reasonable to treat cyclic thermal stresses no differently from cyclic stresses from other sources. However, where static thermal stresses are involved, it would not be reasonable to give thermal stresses based on elastic analysis the same weight as, say, pressure stresses. In general, the designer must consider the application and available service performance and test data in arriving at a reasonable basis.

There seems to be a definite size effect in determining the effect of fatigue-stress concentrations. Size effects for effective fatigue stress concentrations are indicated by Peterson (5). Effective fatigue-stress-concentration factors are usually lower than but may be as great as the theoretical or elastic-stress-concentration factors.

Thermal stresses combined with corrosion can cause failures by stress-corrosion cracking, involving static tensile stresses, or by corrosion fatigue, involving cyclic stresses. This possibility must be kept in mind by the designer in specifying materials for heat-exchanger vessels. An excellent report on corrosion is cited in reference (13). To minimize further the effects of thermal-stress fatigue and shock, care should be taken to produce structures essentially free from cracks and notches. Welding procedures should be selected which prevent cracking in the weldment. Low-quality materials, galling, and temperature-aging effects also cause a loss in resistance to thermal-stress failure. A general description of the effects of material properties on the resistance to thermal-stress failure is covered by Thielsch (10).

BIBLIOGRAPHY

1 "Conduction of Heat in Solids," by H. S. Carslaw and J. C. Jaeger, Oxford Press, New York, N. Y., 1947, pp. 33–44.
2 "Numerical Analysis of Heat Flow," by G. M. Dusinberre, McGraw-Hill Book Company, Inc., New York, N. Y., 1949.
3 "Beams on Elastic Foundation," by M. Hetenyi,University of Michigan Press, Ann Arbor, Mich., 1946. Applies beam on elastic foundation concept to cylinders. Contains tabulated solutions for many practical cases.
4 "Handbook of Experimental Stress Analysis," by M. Hetenyi, John Wiley & Sons, Inc., New York, N. Y., 1950. Edited by Hetenyi, text contains contributions from experts on mechanical properties of materials, working stresses, residual stresses, service fractures, models, and other important subjects.
5 "Fatigue and Fracture of Metals," by W. M. Murray. A Symposium held at M.I.T., June, 1950; Technical Press of M.I.T. with John Wiley & Sons, Inc., New York, N. Y., 1952.
6 "Formulas for Stress and Strain," by R. J. Roark, McGraw-Hill Book Company, Inc., New York, N. Y., second edition, 1943. Contains references to important papers on thermal stresses by J. N. Goodier, C. H. Kent, and others.
7 "Properties of Metals at Elevated Temperatures," by G. V. Smith, McGraw-Hill Book Company, New York, N. Y., 1950.
8 "Theory of Elasticity," by S. Timoshenko and J. N. Goodier, McGraw-Hill Book Company, Inc., New York, N. Y., second edition, 1951. Chapter 14 contains a thorough discussion of thermal stresses and their analysis. Discusses work by earlier authors on plates (J. N. Goodier, 1936, J. P. Den Hartog, 1936), cylindrical shells and cylinders (Den Hartog, ibid; C. H. Kent, 1931), modern general methods of analysis (M. A. Biot, 1935; Goodier, 1937; N. O. Myklestad, 1941).

SUMMARY REPORTS

9 "Behavior of Metals Under Conditions of Thermal Stress," by S. S. Manson, Heat Transfer Symposium, University of Michigan, Ann Arbor, Mich., 1952, p. 9–76.

10 "Thermal Fatigue and Thermal Shock," by H. Thielsch, Welding Research Council Bulletin, No. 10, April, 1952.

RECENT PAPERS AND REPORTS

11 "Thermal Stresses in a Rectangular Plate Clamped Along an Edge," by B. J. Aleck, *Journal of Applied Mechanics*, Trans. ASME, vol. 71, 1949, pp. 118–122.

12 "Centrifugal and Thermal Stresses in Disks and Stress Changes Due to Plastic Flow and Creep," by R. L. Brookling, J. Brown, and B. R. Atkins, National Gas Turbine Establishment, Great Britain, Report R 122, 1952.

13 "The Influence of Corrosion on the Cracking of Pressure Vessels," by H. R. Copson, *Welding Journal*, Welding Research Supplement, vol. 32, February, 1953, pp. 75-S–91-S.

14 "Study of the Effects of Cyclic Thermal Stresses on a Ductile Metal," by L. F. Coffin, Jr., published in this issue, pp. 931–950.

15 "Stresses in Boiler Tubes Subjected to High Rates of Heat Absorption," by W. L. De Baufre, Trans. ASME, vol. 55, paper FSP-55-6, 1933, pp. 73–103.

16 "Thermal Stresses in Long Cylindrical Bodies," by B. E. Gatewood, *Philosophical Magazine*, vol. 32, 1941, pp. 282–301.

17 "Experience With Austenitic Steels in High-Temperature Service in Petroleum Industry," by M. E. Holmberg, Trans. ASME, vol. 73, 1951, pp. 733–742.

18 "Transient Thermal Stresses in Disks and Cylinders," by G. Horvay, Trans. ASME, vol. 76, 1954, pp. 127–135.

19 "Thermal Stresses in Perforated Plates," by G. Horvay, Proceedings of the First National Congress of Applied Mechanics, June, 1951; published by ASME, 1952, pp. 247–257.

20 "The Plane-Stress Problem of Perforated Plates," by G. Horvay, *Journal of Applied Mechanics*, Trans. ASME, vol. 74, 1952, pp. 355–360.

21 "Temperature Stresses in Irregular Solids," by R. D. Hoyle, *Nature*, vol. 167, 1951, pp. 30–31.

22 "Thermal Stresses in a Partially Clamped Elastic Half-Plane," by J. H. Huth, *Journal of Applied Physics*, vol. 23, 1952, pp. 1234–1237.

23 "Analysis of Rotating Disks of Arbitrary Contour and Radial Temperature Distribution in the Region of Plastic Deformation," by S. S. Manson, Proceedings of the First National Congress of Applied Mechanics, June, 1951; published by ASME, 1952, pp. 569–577.

24 "Thermoelastic Stress in the Semi-Infinite Solid," by R. D. Mindlin and D. H. Cheng, *Journal of Applied Physics*, vol. 21, 1950, pp. 931–933.

25 "Stresses in Pipe Bundles," by H. Poritsky and G. Horvay, *Journal of Applied Mechanics*, Trans. ASME, vol. 73, 1951, pp. 241–250.

26 "Application of Bailey's Theory to Tube-Stress Calculations," by C. O. Rhys, Proceedings of the American Petroleum Institute, 8th Mid-Year Meeting, 1938, sect. 3, pp. 102–107.

27 "Safety Margins and Stress Levels in High-Temperature Equipment," by E. L. Robinson, Trans. ASME, vol. 73, 1951, pp. 89–99.

28 "Thermal-Shock and Other Comparison Tests of Austenitic and Ferritic Steels for Main Steam Piping," by W. C. Stewart and W. G. Schreitz, Trans. ASME, vol. 72, 1950, pp. 1043–1060.

29 "Cyclic Heating Test of Main Steam Piping Joints Between Ferritic and Austenitic Steels—Sewaren Generating Station," by H. Weisberg, Trans. ASME, vol. 71, 1949, pp. 643–664.

Appendix

SOLUTION FOR FIG. 1 (a AND b)

Fig. 1(a) shows the solution of the following boundary-value problem[4]

$$\frac{\partial^2 \Delta T}{\partial x^2} = \frac{1}{\epsilon} \frac{\partial \Delta T}{\partial t}, \quad x > 0, \ t > 0 \ldots\ldots\ldots [10]$$

$$\Delta T = \Delta T(x, t); \quad \Delta T(0, t) = \Delta T_0; \quad \Delta T(x, 0) = 0$$

Likewise, Fig. 1(b) shows the solution of

[4] Reference (1), p. 45.

$$\frac{\partial^2 \Delta T}{\partial x^2} = \frac{1}{\epsilon} \frac{\partial \Delta T}{\partial t^2}, \quad x > 0, \ t > 0 \ldots\ldots\ldots [11]$$

$$\Delta T = \Delta T(x, t); \quad \Delta T(0, t) = Bt; \quad \Delta T(x, 0) = 0$$

These solutions are as follows:
For Fig. 1(a) and Equation [10]

$$\frac{\Delta T}{\Delta T_0} = \mathrm{erfc} \frac{x}{2\sqrt{\epsilon t}} \ldots\ldots\ldots\ldots [12]$$

For Fig. 1(b) and Equation [11]

$$\frac{\Delta T}{Bt} = 4i^2 \, \mathrm{erfc} \frac{x}{2\sqrt{\epsilon t}} \ldots\ldots\ldots\ldots [13]$$

where the iterated erfc functions are defined by

$$i^n \, \mathrm{erfc} \, z = \int_z^\infty i^{n-1} \, \mathrm{erfc} \, r \, dr \quad n = 1, 2, \ldots$$

$$i^0 \, \mathrm{erfc} \, z = \mathrm{erfc} \, z$$

These latter functions are tabulated in Carslaw (1).

CONCEPT OF THERMAL REFLECTIONS

Thermal reflections in one-dimensional thermal conduction may be shown mathematically as follows: Consider the boundary-value problem

$$\frac{\partial^2 T}{\partial x^2} = \frac{1}{\epsilon} \frac{\partial T}{\partial t}, \quad T = T(x, t), \quad t > 0, \quad 0 < x < L \ldots [14]$$

$$T(x, 0) = 0$$
$$T(0, t) = g(t)$$
$$T_x(L, t) = 0$$

Taking the Laplace transform with respect to t and solving for $\bar{T}$ (transform of T) we obtain

$$\bar{T} = \bar{g}(s) \frac{\exp \sqrt{\frac{s}{\epsilon}} (L - x) + \exp - \sqrt{\frac{s}{\epsilon}} (L - x)}{\exp \sqrt{\frac{s}{\epsilon}} L + \exp - \sqrt{\frac{s}{\epsilon}} L}$$

$$= \bar{g}(s) \frac{\exp - \sqrt{\frac{s}{\epsilon}} x + \exp - \sqrt{\frac{s}{\epsilon}} (2L - x)}{1 + \exp - \sqrt{\frac{s}{\epsilon}} 2L} \quad \Big\} \ldots [15]$$

$$= \bar{g}(s) \sum_{n=0}^\infty (-1)^n \left\{ \exp - \sqrt{\frac{s}{\epsilon}} (2nL + x) + \exp - \sqrt{\frac{s}{\epsilon}} 2(n + 1) L - x \right\}$$

where $\bar{g}(s)$ is the transform of $g(t)$. If L is large, as for semi-infinite geometry, then the transform of T is

$$\bar{T} = \bar{g}(s) \exp - \sqrt{\frac{s}{\epsilon}} x \ldots\ldots\ldots\ldots [16]$$

If the solution for semi-infinite geometry is $f(x, t)$ then we can write for the solution of the slab of thickness L

$$T = \sum_{n=0}^\infty (-1)^n \{ f[2nL + x, t] + f[2(n + 1)L - x, t] \} \ldots [17]$$

The terms of this series may be interpreted as being due to re-

flections. A similar concept of reflection is common in transmission-line and elastic-vibration theory.

THERMAL STRESS IN PLATES

It can be derived from Carslaw[5] that the temperature response of an isotropic plate of thickness L with a uniform initial temperature with one surface insulated and the other in contact with a fluid of transfer coefficient h whose bulk temperature varies linearly with time is

$$\frac{\Delta T}{\Delta T_0} = 2 \sum_{n=1}^{\infty} \frac{\cos \gamma_n \xi}{\left(1 + \frac{\gamma_n^2}{C} + C\right) \cos \gamma_n}$$

$$\left[\frac{t}{t_0} - \frac{L^2}{\epsilon \gamma_n^2 t_0} + \frac{\exp - \frac{\gamma_n^2}{L^2} t}{\frac{\epsilon}{L^2} \gamma_n^2 t_0}\right] \dots [18]$$

where the linear bulk fluid temperature transient is

$$\frac{\Delta T_0}{t_0} t, \text{ and } \gamma_n \tan \gamma_n = C = \frac{hL}{k}$$

Superimposing a second linear transient at t_0 but with an opposite slope gives the temperature response for the bulk-fluid temperature pictured in Fig. 4.

In a flat plate restrained from bending, or a thin cylindrical shell, it can be shown that the biaxial thermal stress at a point ξ from the surface (away from edges) is

$$\sigma = \frac{E\alpha}{1-\mu} \left[\int_0^1 T(\xi)d\xi - T(\xi)\right] \dots [19]$$

The bracket can be recognized as the deviation from average temperature at the point ξ-distance from the surface.

If the temperature function is substituted, there results the expression for surface stress

$$\sigma^* = \sum_{n=1}^{\infty} \frac{2C\left(\frac{C}{\gamma_n^2} - 1\right)}{C + C^2 + \gamma_n^2}$$

$$\left[1 - \frac{\exp - \gamma_n^2 S}{\gamma_n^2 S_0}(1 - \exp - \gamma_n^2 S_0)\right] \dots [20]$$

where

$$S = \frac{\epsilon(t - t_0)}{L^2}, S_0 = \frac{\epsilon t_0}{L^2}, C = \frac{hL}{k}, \sigma^* = \frac{\sigma}{E\alpha \, \Delta T_0 / 1 - \mu}$$

The maximum surface stress was obtained by plotting this equation. Some difficulty was experienced with convergence as C became large. To obtain the maximum stresses for $1/C = 0$ the temperature response to a linear surface temperature was written using the concept of thermal reflections (earlier sections of appendix)

$$\frac{\Delta T}{\Delta T_0} = 4 \sum_{n=0}^{\infty} (-1)^n \left\{ i^2 \text{ erfc } \frac{2n + \xi}{2\sqrt{S_0}} + i^2 \text{ erfc } \frac{2(n + 1) - \xi}{\sqrt{S_0}} \right\}$$
$$\dots [21]$$

where ΔT is the temperature distribution at time t_0, at which time the surface temperature has changed ΔT_0. Substituting this distribution into Equation [19] gives the surface stress

---

[5] Reference (1), p. 102.

$$-\sigma^* = 1 - 0.7523 \sqrt{S_0} + 16 \sum_{n=0}^{\infty}$$

$$(-1)^n \sqrt{S_0} \, i^3 \text{ erfc } \frac{n + 1}{\sqrt{S_0}} \dots [22]$$

The definition for i^n erfc is given in the first part of the Appendix.

Discussion

M. P. HEISLER.[6] The author implies that thermal reflections as yet have found little use in the solution of heat-transfer problems because the concept has not been sufficiently called to the attention of the design engineer. It is not clear how he arrived at this conclusion since the principles are quite well known and are described clearly in a number of references on heat transfer, such as "Complex Variable and Operational Calculus" by N. W. Mclachlan, and "Operational Methods in Applied Mathematics" by Carslaw and Jaeger. There is also a comprehensive series of papers by George Green on this subject, although Green refers to the technique as the method of wave trains. These have been appearing in the *Philosophical Magazine* since the early 1930's, the latest appearing in vol. 38, 1947, pp. 97–115.

Possibly the real reason that the method is rarely applied to heat-transfer problems can be attributed to the fact that the techniques most commonly used, particularly the direct application of Laplace transforms, are both more general and more powerful. It would have been of some interest if the author had calculated the stresses in Fig. 4 from a general solution derived directly by the method of wave trains instead of using the conventional infinite-series form which he developed from Carslaw and Jaeger. Stress calculations of this type are facilitated by the use of "short-time" and "asymptotic" forms of solutions. In these it is seldom necessary to use more than one term in the numerical evaluation. With these the author would have experienced no convergence difficulties as C became large.

S. V. MANSON.[7] The evaluation of transient temperatures and stresses is a task that frequently confronts the designer, and aids to evaluation such as Mr. Fritz provides in his present paper, are correspondingly valuable. Discussion of the case of known surface temperature variation is particularly appropriate in view of the growing interest in liquid metals as heat-transfer fluids. The high heat-transfer coefficients obtainable with these fluids cause the surfaces which they contact to acquire temperatures close to the known liquid-metal temperatures.

The writer believes that it would be worth while if Mr. Fritz included the brief Laplace Transform proof of the validity of superposing temperatures resulting from successive linear transients. The superposition technique and the concept of thermal reflections appear to the writer to be of considerable value.

As is well known,[8] the general equation for thermal stress in a plate contains a term in addition to that indicated in Equation [5] of the present paper. As Mr. Fritz states, Equation [5] is valid when the plate is restrained against bending. Mechanical restraints are, of course, unnecessary if the temperature distribution is symmetrical about the plate center line; in other cases mechanical restraints would be required for a valid use of Equation [5].

---

[6] Senior Research Engineer, North American Aviation, Inc., Atomic Energy Research Department, Downey, Calif.

[7] Project Engineer, Wright Aeronautical Division, Curtiss-Wright Corporation, Wood-Ridge, N. J.

[8] "Theory of Elasticity," by S. Timoshenko, McGraw-Hill Book Company, Inc., New York, N. Y., 1934.

Author's Closure

The author is grateful for Mr. Heisler's and Mr. Manson's comments. As Mr. Heisler brought out, the concept of thermal reflections is already known to mathematicians, and is, as the author pointed out, fairly obviously implied by the differential equation of heat conduction. The author arrived at the presented methods by elimination of such methods as the direct application of the Laplace transform. Accuracy to less than a few per cent as may be given by the direct application of Laplace transforms is not feasible in light of the large factors of ignorance in materials behavior nor is it allowed by practical engineering schedules. Asymptotic solutions are in order in a mathematical treatise, but the present purpose was to generate a method by which the maximum stresses in a structure may be evaluated, which is obtained by short-time solutions.

As Mr. Manson pointed out, Equation [5] of the paper is valid only when the plate is restrained from bending. This is the case for cylindrical vessels away from ends and for plates with symmetrical temperature distributions for which applications the equations were derived.

The method of superposition may be stated mathematically as follows: Take for example the case

$$\frac{\partial^2 T}{\partial x^2} = \frac{1}{\epsilon} \frac{\partial T}{\partial t}, \quad x > 0, t > 0$$

$$T(0, t) = f(t); \quad T(x, 0) = 0$$

Assume

$$T = \sum_{n=1}^{m} T_n$$

where

$$\frac{\partial^2 T_n}{\partial x^2} = \frac{1}{\epsilon} \frac{\partial T_n}{\partial t}$$

$$T_n(0, t) = g_n(t); \quad T_n(x, 0) = 0$$

and

$$f(t) = \sum_{n=1}^{m} g_n(t)$$

$g_n(t)$ may be in the terms of delayed step functions, or in any arbitrary form, as long as the summation holds.

flections. A similar concept of reflection is common in transmission-line and elastic-vibration theory.

THERMAL STRESS IN PLATES

It can be derived from Carslaw[5] that the temperature response of an isotropic plate of thickness L with a uniform initial temperature with one surface insulated and the other in contact with a fluid of transfer coefficient h whose bulk temperature varies linearly with time is

$$\frac{\Delta T}{\Delta T_0} = 2 \sum_{n=1}^{\infty} \frac{\cos \gamma_n \xi}{\left(1 + \frac{\gamma_n^2}{C} + C\right) \cos \gamma_n} \left[\frac{t}{t_0} - \frac{L^2}{\epsilon \gamma_n^2 t_0} + \frac{\exp - \frac{\gamma_n^2}{L^2} t}{\frac{\epsilon}{L^2} \gamma_n^2 t_0}\right] \quad \ldots [18]$$

where the linear bulk fluid temperature transient is

$$\frac{\Delta T_0}{t_0} t, \text{ and } \gamma_n \tan \gamma_n = C = \frac{hL}{k}$$

Superimposing a second linear transient at t_0 but with an opposite slope gives the temperature response for the bulk-fluid temperature pictured in Fig. 4.

In a flat plate restrained from bending, or a thin cylindrical shell, it can be shown that the biaxial thermal stress at a point ξ from the surface (away from edges) is

$$\sigma = \frac{E\alpha}{1 - \mu} \left[\int_0^1 T(\xi)d\xi - T(\xi)\right] \quad \ldots \ldots [19]$$

The bracket can be recognized as the deviation from average temperature at the point ξ-distance from the surface.

If the temperature function is substituted, there results the expression for surface stress

$$\sigma^* = \sum_{n=1}^{\infty} \frac{2C\left(\frac{C}{\gamma_n^2} - 1\right)}{C + C^2 + \gamma_n^2} \left[1 - \frac{\exp - \gamma_n^2 S}{\gamma_n^2 S_0}(1 - \exp - \gamma_n^2 S_0)\right] \ldots \ldots [20]$$

where

$$S = \frac{\epsilon(t - t_0)}{L^2}, S_0 = \frac{\epsilon t_0}{L^2}, C = \frac{hL}{k}, \sigma^* = \frac{\sigma}{E\alpha \Delta T_0/1 - \mu}$$

The maximum surface stress was obtained by plotting this equation. Some difficulty was experienced with convergence as C became large. To obtain the maximum stresses for $1/C = 0$ the temperature response to a linear surface temperature was written using the concept of thermal reflections (earlier sections of appendix)

$$\frac{\Delta T}{\Delta T_0} = 4 \sum_{n=0}^{\infty} (-1)^n \left\{ i^2 \text{ erfc } \frac{2n + \xi}{2\sqrt{S_0}} + i^2 \text{ erfc } \frac{2(n + 1) - \xi}{\sqrt{S_0}} \right\} \ldots \ldots [21]$$

where ΔT is the temperature distribution at time t_0, at which time the surface temperature has changed ΔT_0. Substituting this distribution into Equation [19] gives the surface stress

[5] Reference (1), p. 102.

$$-\sigma^* = 1 - 0.7523 \sqrt{S_0} + 16 \sum_{n=0}^{\infty} (-1)^n \sqrt{S_0} \, i^3 \text{ erfc } \frac{n + 1}{\sqrt{S_0}} \ldots \ldots [22]$$

The definition for i^n erfc is given in the first part of the Appendix.

Discussion

M. P. HEISLER.[6] The author implies that thermal reflections as yet have found little use in the solution of heat-transfer problems because the concept has not been sufficiently called to the attention of the design engineer. It is not clear how he arrived at this conclusion since the principles are quite well known and are described clearly in a number of references on heat transfer, such as "Complex Variable and Operational Calculus" by N. W. Mclachlan, and "Operational Methods in Applied Mathematics" by Carslaw and Jaeger. There is also a comprehensive series of papers by George Green on this subject, although Green refers to the technique as the method of wave trains. These have been appearing in the *Philosophical Magazine* since the early 1930's, the latest appearing in vol. 38, 1947, pp. 97–115.

Possibly the real reason that the method is rarely applied to heat-transfer problems can be attributed to the fact that the techniques most commonly used, particularly the direct application of Laplace transforms, are both more general and more powerful. It would have been of some interest if the author had calculated the stresses in Fig. 4 from a general solution derived directly by the method of wave trains instead of using the conventional infinite-series form which he developed from Carslaw and Jaeger. Stress calculations of this type are facilitated by the use of "short-time" and "asymptotic" forms of solutions. In these it is seldom necessary to use more than one term in the numerical evaluation. With these the author would have experienced no convergence difficulties as C became large.

S. V. MANSON.[7] The evaluation of transient temperatures and stresses is a task that frequently confronts the designer, and aids to evaluation such as Mr. Fritz provides in his present paper, are correspondingly valuable. Discussion of the case of known surface temperature variation is particularly appropriate in view of the growing interest in liquid metals as heat-transfer fluids. The high heat-transfer coefficients obtainable with these fluids cause the surfaces which they contact to acquire temperatures close to the known liquid-metal temperatures.

The writer believes that it would be worth while if Mr. Fritz included the brief Laplace Transform proof of the validity of superposing temperatures resulting from successive linear transients. The superposition technique and the concept of thermal reflections appear to the writer to be of considerable value.

As is well known,[8] the general equation for thermal stress in a plate contains a term in addition to that indicated in Equation [5] of the present paper. As Mr. Fritz states, Equation [5] is valid when the plate is restrained against bending. Mechanical restraints are, of course, unnecessary if the temperature distribution is symmetrical about the plate center line; in other cases mechanical restraints would be required for a valid use of Equation [5].

Author's Closure

The author is grateful for Mr. Heisler's and Mr. Manson's comments. As Mr. Heisler brought out, the concept of thermal reflections is already known to mathematicians, and is, as the author pointed out, fairly obviously implied by the differential equation of heat conduction. The author arrived at the presented methods by elimination of such methods as the direct application of the Laplace transform. Accuracy to less than a few per cent as may be given by the direct application of Laplace transforms is not feasible in light of the large factors of ignorance in materials behavior nor is it allowed by practical engineering schedules. Asymptotic solutions are in order in a mathematical treatise, but the present purpose was to generate a method by which the maximum stresses in a structure may be evaluated, which is obtained by short-time solutions.

As Mr. Manson pointed out, Equation [5] of the paper is valid only when the plate is restrained from bending. This is the case for cylindrical vessels away from ends and for plates with symmetrical temperature distributions for which applications the equations were derived.

The method of superposition may be stated mathematically as follows: Take for example the case

$$\frac{\partial^2 T}{\partial x^2} = \frac{1}{\epsilon} \frac{\partial T}{\partial t}, \quad x > 0, \ t > 0$$

$$T(0, t) = f(t); \quad T(x, 0) = 0$$
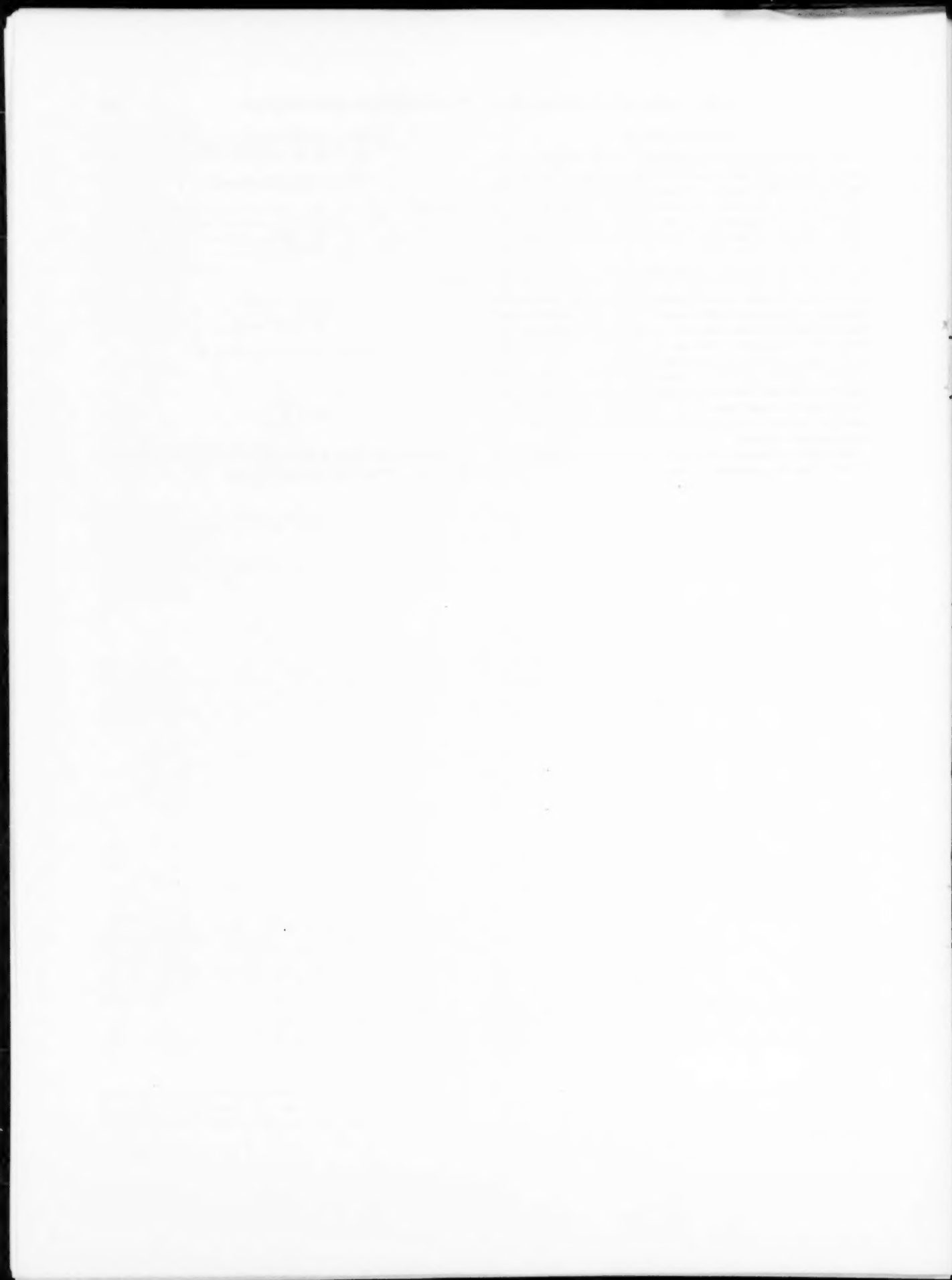
Assume

$$T = \sum_{n=1}^{m} T_n$$

where

$$\frac{\partial^2 T_n}{\partial x^2} = \frac{1}{\epsilon} \frac{\partial T_n}{\partial t}$$

$$T_n(0, t) = g_n(t); \quad T_n(x, 0) = 0$$

and

$$f(t) = \sum_{n=1}^{m} g_n(t)$$

$g_n(t)$ may be in the terms of delayed step functions, or in any arbitrary form, as long as the summation holds.

Apparatus for Study of Effects of Cyclic Thermal Stresses on Ductile Metals[1]

By L. F. COFFIN, JR.,[2] AND R. P. WESLEY,[3] SCHENECTADY, N. Y.

In cases in which very high rates of heat transfer exist, as in nuclear reactors, severe thermal stresses can be developed in structural metals. These stresses can be relieved by plastic flow and, consequently, are not regarded as serious when steady-state conditions prevail. Under the action of thermal oscillations, however, cyclic thermal stresses are developed. Depending on the frequency of thermal cycles and severity of the thermal stress, fatigue failure can result. Because of its low thermal conductivity and high thermal expansion, 18 per cent chromium-8 per cent nickel stainless steels are particularly prone to this effect. An investigation of this problem has been under way for some time. The object has been twofold: (*a*) To obtain information so that a particular material may be assessed critically for its resistance to thermal stress-fatigue damage under specified conditions, and (*b*) to investigate the fundamental aspects of the problem in order to learn more about the fatigue phenomenon. The paper describes the test apparatus developed for this study. A companion paper gives the test results to date and their interpretation.

INTRODUCTION

THERMAL stresses are generally defined as those stresses induced by differential expansions in a statically indeterminant system. Differential expansion can arise from temperature variations in the body or from differences in thermal-expansion coefficients when the body temperature is changed uniformly. Although many solutions exist in the literature for thermal stresses and strains in an elastic body of various configurations, the inclusion of thermal-stress considerations in design practice is often ignored. This is because in most practical applications they are generally too small to be of any significance. In addition, if one is dealing with a ductile material, excessive thermal stresses can relieve themselves by local plastic deformation to values not considered to be particularly serious.

In the design of nuclear reactors, however, thermal stresses and their effect on structural parts require more careful attention. There are many reasons for this. Because of the intense conversion of nuclear to thermal energy in fuel elements, thermal fluxes many times those encountered in conventional heat-transfer systems are required. Other sources of thermal flux may result from the absorption by materials of neutron, gamma, or other forms of irradiation. Apart from high thermal fluxes and the accompanying large temperature differentials existing in a steady-state operation of the reactor, the transient thermal problem can be equally important. Since the nuclear control of a reactor can take place much more rapidly than the control of the coolant flow, transient thermal stresses may result which can be extremely severe.

The principal problem that arises when one is concerned about the effect of thermal stresses on ductile structural materials is not necessarily the magnitude of thermal stress. If the material can deform plastically, then very severe thermal stresses will be modified or relieved through a process of plastic flow. The real problem arises when repeated thermal cycling occurs in the material. Now the high thermal stresses which were produced and relieved in one half of the cycle will reappear in the opposite direction in the remainder of the cycle as a direct consequence of the relief. Hence repeated thermal oscillations result in stress cycling which may be sufficiently severe to cause eventual damage of the part in question through a fatigue process.

The damage from fatigue which is of practical importance in the present problem occurs after a comparatively few cycles at high stress. This is a part of the fatigue problem which has received very little attention. Another complication is the fact that at the high temperature the stresses are of one sign while at the lower temperature, the stresses are of the opposite sign. The result is the introduction of the temperature as a variable during cycling. This is particularly important when one considers the nonelastic deformation which occurs per cycle.

Aside from the resistance of the material to repeated stress at elevated temperature, the physical properties of the material are important in assessing the seriousness of cyclic thermal stresses. Since these stresses initiate from strain gradients in the material, the thermal coefficient of expansion and the thermal conductivity of metal play an important role in the problem. Unfortunately, some useful high-temperature materials, such as austenitic stainless steels, combine a high thermal expansion with a low thermal conductivity. Thus for a given thermal condition (constant heat transfer or thermal shock) particular attention must be given to these metals in assessing the fatigue effect described.

Because of the lack of information both of a fundamental and design nature on the role of repeated thermal stresses on materials, an extended program pertaining to the problem has been undertaken. The present paper describes experimental apparatus developed for this study. A companion paper deals with test results and their interpretation from practical and theoretical views.

METHOD OF EXPERIMENTATION

If one is planning a program of experimentation for studying the fatigue characteristics of materials under thermal-cycling conditions, several testing methods would be available. One might, for example, submit the actual fabricated part to cyclic thermal shock by repeated immersions in a bath of high temperature interspersed by immersions in a low-temperature bath. After some length of time, failure, as manifested presumably by a fatigue crack, would very likely occur at the point of severest stress reversal. This would give a number for the life which would be applicable to that specific part only under the specific

test conditions. It would be valueless from the point of view of determining either design information or fundamental information on the fatigue process.

Another procedure would be to consider the problem basically as one of fatigue and to design an experiment whereby a simple part, such as a beam or a bar in uniaxial stress, is cycled at a constant temperature. The amplitude of the strain would be sufficient to produce a nonelastic deformation with each loading. This form of test would yield fundamental information and data which would be more generally useful to a variety of parts made of the material under test. However, since the specimen is held at constant temperature, the question arises as to the interpretation of this information to cases where both cyclic stress and temperature occur. However, there are many cases where thermal stresses can be cyclic in nature and yet where the temperature would remain essentially constant. An example of this would be the surface of some part subjected to radiation heating where a liquid-metal coolant is used. If the temperature of the coolant remains reasonably constant and independent of changes in irradiation, then the temperature of the outer surface of the part also would remain constant, and cyclic thermal stresses could be developed on the surface as the temperature of the interior changes with radiation flux.

Generally, the thermal stresses at a point in a body will be some nonlinear function of the temperature. To investigate this, another procedure would be thermally to cycle a constrained test specimen with a simple geometry so that the stresses are simple and readily determinable. This is essentially the same technique as the first method with the important difference that the stresses, strains, and temperature of the specimen are determinable at any point in the cycle.

A test apparatus has been developed which can, with very few modifications, be used for either the second or third testing procedure. Briefly, the method used consists of attaching a test specimen rigidly between two fixed plates which are held together by two columns. By heating and cooling the columns alternately, a displacement is produced between the two plates. Thus a test specimen connected in parallel with the columns is strain cycled at constant temperature. By fixing the temperature of the columns and temperature cycling the specimen, the specimen is constrained longitudinally and subjected to cyclic thermal stresses. In either case, it is possible to determine accurately the stress and strain amplitude for each cycle, so that the history of these quantities can be studied as a function of cycles of loading, temperature, or amplitude of loading.

The two methods are described in more detail in the text. The thermal-stress method is given more emphasis because most of the experimental work has been done on this equipment and because of its somewhat greater complexity.

DESCRIPTION OF THERMAL-STRESS TESTING APPARATUS

The apparatus for the present study of the effect of cyclic thermal stresses on the fatigue life of structural materials is shown in Fig. 1. The essential feature of the apparatus is the imposition of a complete longitudinal constraint on the test specimen so that any longitudinal thermal deformation of the specimen is converted directly to elastic or inelastic deformation. To accomplish this, the apparatus is designed to clamp each end of the test specimen rigidly to end plates so that longitudinal play in the clamps is reduced to a negligible amount (<0.0005 in.) when the specimen load is completely reversed. In addition, to prevent motion of the end plates relative to each other, the two plates are rigidly connected by heavy columns. The columns also serve as weighbars to give the instantaneous stress on the test specimen.

To develop a cyclic thermal stress in the test specimen, the

FIG. 1   THERMAL-CYCLING TEST APPARATUS

FIG. 2   TEST SPECIMEN

temperature of the specimen itself must be cycled. This has been accomplished most satisfactorily by allowing the specimen to serve as its own heater and by passing current through it. Cooling is accomplished by a radial gas stream using a diffuser consisting of a closed-end tube with several radial holes. Thus a tubular test specimen is required. The details of the test specimen are shown in Fig. 2.

The stiffness desired is accomplished, as shown in the exploded view of Fig. 1, by a somewhat complex assembly. The flanges at either end of the test specimen have slightly different outside diameters, allowing the specimen to be inserted, small end first, through the upper plate so that the large-diameter flange rests snugly in the counterbored hole in the top plate. A retainer plug is then screwed into this hole and when tightened by a wrench the top flange is pressed firmly in place. The smaller flanged end fits into a counterbored hole in the bottom plate and a split plate with a smaller central hole fits over the flange. A thin ring fits over the

split plate. The depth of the counterbore is such that the top face of the flange is raised slightly above the surface of the lower plate. Thus, when the split face and ring are in place and drawn down by the four bolts, as shown in Fig. 1, the end flange is clamped tightly in place. A glass specimen enclosure with an O-ring seal is used, if required, to maintain an inert-gas atmosphere around the test specimen.

Two columns (weighbars) separate the two end plates. These weighbars are threaded at both ends with square threads. The clearance between the bolts and holes in the end plates are kept to a minimum to facilitate the alignment. The plates are clamped to the bolts by means of nuts. Washers with spherical faces are used to prevent bending in the weighbars and insure tightness when the nuts are drawn up. In addition, two short bolts are used to clamp the bottom plate, split plate, and ring. Two resistance-wire strain gages are attached to each weighbar and the four gages are then connected in series to give the weighbar strain. Four dummy strain gages are attached to the upper plate and are used for temperature compensation. Strains are measured with a Baldwin, Type-L, SR-4 strain indicator. To prevent short-circuiting of the specimen during heating, the weighbars are insulated electrically from the upper plate. This is done with textolite washers and varnished cambric sleeves, as shown in Fig. 1.

The specimen temperature during the test is measured by a chromel-alumel thermocouple spot-welded to the tube at the midlength. A calibrated millivoltmeter is used for the purpose of measurement. The thermocouple is made from 10-mil wire so that the cooling effect from conduction along the wire is very small. Because of the good thermal contact introduced by spotwelding, the couple gives a reliable indication of the instantaneous temperature. There is no discernible lag in the indicated temperature cycle when compared to the actual heating and cooling cycle.

Good electrical contact is made by threading brass posts into either end of the test specimen. These posts have central holes to allow for the introduction of the gas diffuser and the escape of the coolant gas. Braided power cables are attached directly to these posts. From the specimen resistance and maximum heating rate desired, a current transformer with a secondary winding supplying 2 volts at 1000 amp is required.

The circuit diagram for the specimen heater (the specimen itself) is given in Fig. 3. Control is accomplished with a saturable
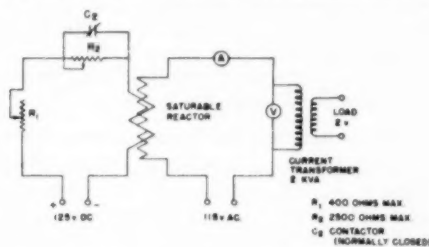
FIG. 3   CIRCUIT DIAGRAM FOR SPECIMEN HEATING

reactor in which the reactance in series with the primary of the current transformer can be varied by changing the degree of saturation of the reactor with direct current. Variable resistances R_1 and R_2 control the direct current to the reactor. R_1 is used to adjust the power during the heating cycle while R_2 controls the power during both the high and low-temperature "hold" phase of the cycle. C_2 is a contactor, normally closed, whose operation will be described more fully.

A solenoid-operated valve is used to supply the gas coolant to the diffuser during the cooling phase of the cycle. The position of

the solenoid in the control circuit producing the cyclic operation is shown in Fig. 4. The choice of coolant gas is determined by the oxidation rate of the metal at the maximum temperature of the test. For Type 347 stainless steel, N_2 was first used but later was replaced by air when it was found that the oxidation rate was too small to be a factor in the investigation.

Also in Fig. 4 is shown the relay circuit whereby the specimen can be cycled automatically between two predetermined temperatures. Basically, the cycle is broken down into four components: (1) heat, (2) hold at high temperature, (3) cool, (4) hold at low temperature. The time required for each component can be varied using adjustable time-delay relays. Three vacuum-tube time-delay relays are used, with the high and low-temperature hold times controlled by the same relay. With the existing relays, it is possible to adjust the time for each portion of the cycle from 1 to 60 sec. With the addition of external capacitance this time can be extended to 3 min.
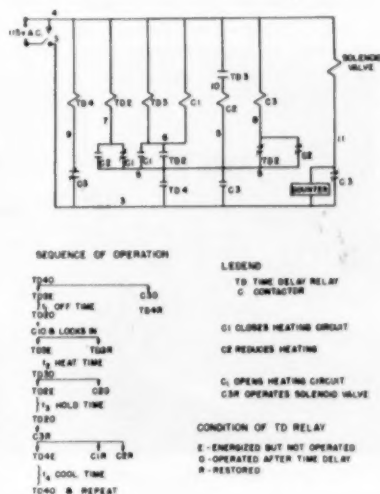
FIG. 4   CIRCUIT DIAGRAM FOR CONTROL OF THERMAL CYCLE

The sequence of operations of the various relays is shown in Fig. 4. Once switch 1 is closed, repetition of each cycle continues automatically until switch 1 is opened. The actual operation can be followed by tracing through the sequence of operations and the position of each relay and contact in the circuit diagram. A counter to record the number of cycles is in parallel with the solenoid, and this is energized during the cooling cycle.

The test apparatus and the control panel (actually the control panel for an adjacent stand is also included) are shown in Fig. 5. The three time-delay relays are mounted on the top of the panel. Immediately below are knobs for the two variable resistances R_1 and R_2 shown in Fig. 3. The voltage and amperage indicators in the primary circuit of the current transformer are located below these resistances and serve as a measure of the power to the specimen (if one assumes 100 per cent efficiency of the transformer and power factor of 1). To the right of the control panel is the portable strain indicator for measuring the instantaneous load on the specimen. The temperature indicator is located at the left of the test apparatus. The coolant-gas line is attached to the end of the gas diffuser at the top of the upper post. Various lead wires connect the active and dummy test specimens to the strain indicator.

Fig. 6 shows the arrangement of the thermal-stress testers in the laboratory and indicates the size of the unit. Shown in this
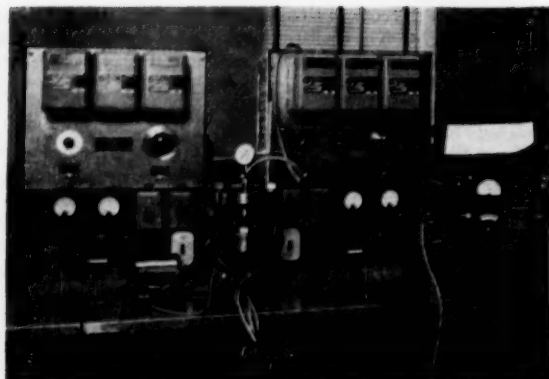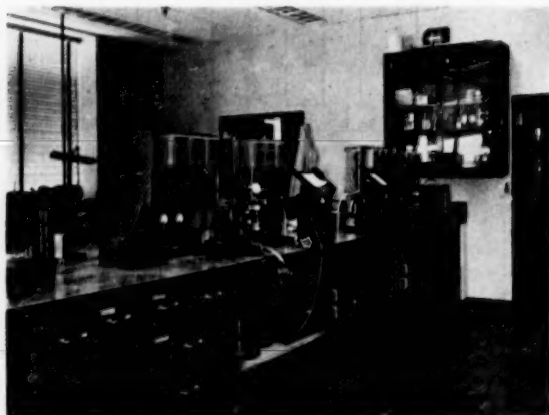
FIG. 5 THERMAL-CYCLING APPARATUS AND CONTROL PANEL

FIG. 6 GENERAL VIEW OF APPARATUS

figure are four control panels and only two test apparatus. A current transformer not in use can be seen just to the left of the left control panel, and the saturable reactors are shown on the floor underneath the laboratory bench.

OPERATION OF THERMAL-STRESS APPARATUS

Prior to insertion of a test specimen into the thermal-stress apparatus, a thermocouple is carefully spot-welded to the midpoint of the test length. The specimen is then inserted into the apparatus in the procedure described earlier. The lower nuts used to hold the bottom plate, split plate, and ring are tightened with the aid of two $1^5/8$-in. open-end wrenches. The upper flange of the specimen is also wrench-tightened against the retainer plug. The upper plate is initially allowed to float freely so that the specimen is unconstrained.

With the specimen thus unclamped, the temperature amplitude and frequency are adjusted to the desired values by manipulation of the time-delay relays and variable resistances. When suitable positions for these quantities have been found, several thermal cycles are completed to be sure that equilibrium conditions have been reached. It has been found that when the proper settings have been established, little further adjustment is required to maintain the required cycle.

Having established the desired temperature cycle, the balance point for zero stress on the specimen is found from the portable strain indicator. In addition, it will be necessary to measure the

relative displacement of the upper and lower plates prior to clamping so that the specimen thermal strain can be determined. This is done by means of a dial gage whose body is attached to a framework connected to the lower brass post and whose stylus is attached to the upper post. This measurement is made to the nearest 0.1 mil.

Complete clamping or constraint of the specimen can now be carried out. The question immediately arises as to the exact point in the cycle for the clamping. Should the top plate be clamped at the low temperature, the first stress will be compressive, while the stress will be tensile if the specimen is clamped in position when hot. As a standard procedure, the specimen is clamped by tightening the nuts against the upper plate during the high-temperature hold portion of the cycle. This point then is the reference or zero point for strain measurement.

Following the clamping operation, the stress change of the specimen between the high and low temperatures is obtained from the weighbar strain. This stress serves not only as a means of obtaining the elastic strain change but also as an indication of the strain-hardening variations during the test. Actually, the stress on the specimen at the low temperature and at the high temperature can be determined. However, since the unstressed balance point of the strain indicator will drift, the stress values themselves have less reliability than the stress change.

It is also desirable to measure the relative displacement of the upper and lower plates between the two temperatures after clamping. This is done in a manner identical with the measurement of the unclamped displacement. Usually this displacement is less than 1 mil. The deformations before and after clamping are necessary for the strain calculations discussed in the following section.

The test is continued until a fatigue failure in the test specimen results. When a crack is formed and grows, the cross-sectional area is reduced. The result is to increase the over-all specimen resistance and reduce the power fed to the specimen. However, the current density at the cross section of the crack increases. Consequently, the temperature rises in the region of the crack, and when the crack has progressed sufficiently far, the remainder of the cross section melts or burns off. If the thermocouple is located in the region of the crack, the temperature will fall. Because of the large number of cycles required for failure in most cases, the apparatus is run continuously. To determine the number of cycles for failure during off-hours, a photoelectric recording millivoltmeter is used in place of the temperature indicator. It is then a simple matter to count the oscillations from some reference point to the point where the temperature oscillations rise or fall and to determine the precise point of failure.

STRESS-STRAIN RELATIONSHIPS DURING THERMAL CYCLING

When a bar is subjected to end constraint and cycled thermally, the net strain is at all times zero (except for the small deflection of the supports). In order to better explore the behavior of the bar, the net strain can be broken into three strain components, each being cyclic in nature. These are (a) thermal strain, (b) elastic strain, and (c) inelastic strain. The thermal strain is the result of thermal-expansion effects only and is found directly by measurement of the motion of the specimen when subjected to temperature-cycling in the absence of end constraint. This measured value is actually an average, since the temperature distribution varies along the axis. The elastic strain is calculated from the measured load on the supporting columns, with the aid of the specimen dimensions and modulus of elasticity. Finally, the inelastic strain as defined here is a derived quantity found from the relationship

$$c_{thermal} + c_{elastic} + c_{inelastic} = c_{net} = 0 \ldots \ldots [1]$$

which is operative at all times. This strain is of considerable importance in an understanding of the problem.

As has been pointed out, the reference point for the various cyclic strains is established at the point at which the unstressed bar is clamped in place (generally the high-temperature hold phase of the cycle). With respect to this reference point, the thermal strains oscillate between zero and a negative value. Since these strains are only dependent on temperature, the zero point will not shift with the time. The zero point for elastic strains or stress will shift, very rapidly at first and then slowly as cycles of loading become established, from the temperature of clamping toward a temperature somewhere between the two extremes. The inelastic strain shifts its zero point with respect to temperature according to the behavior of both the thermal and elastic strain.

The stress-strain relationship during the first few cycles of testing is of interest for a better understanding of the phenomenon and is shown in Fig. 7. It is assumed that the thermal coefficient
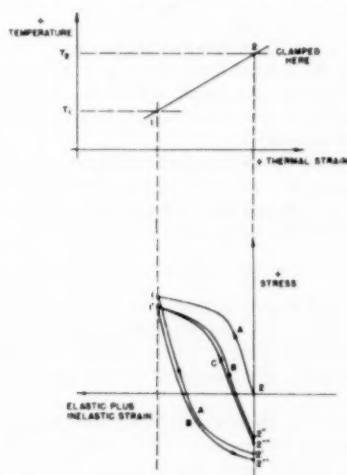
FIG. 7   STRESS-STRAIN RELATIONSHIP FOR FIRST FEW THERMAL CYCLES FOR BAR WITH LONGITUDINAL CONSTRAINT

of expansion of the material is constant over the temperature range of the test. The cycling is to be accomplished between temperatures T_1 and T_2. The temperature-thermal strain relationship is linear as shown in the upper figure. The lower figure shows the relationship between the stress and the sum of the elastic and inelastic strain of the specimen, which according to Equation [1] is the negative of the thermal strain if the net strain is small. The specimen is clamped into position at the temperature T_2 so that the point 2 in the lower figure is the origin of the stress-strain curve. As cooling occurs, the path A is followed such that first the deformation is elastic. There follows an elastic and an increasing inelastic deformation until point 1 is reached. During the hold time there will be little relaxation of the stress at point 1 as the specimen is held at T_1 (the low temperature). Upon heating, the stress reverses its directions and follows first an elastic path and then an inelastic path until point 2' is reached. It is evident that for this return path A inelastic deformation occurs prematurely in the compression zone. This is due to the well-known Bauschinger effect.[4] Since the specimen is now held at the high temperature, depending on the temperature and time at which the specimen is held at point 2', the stress will relax to some point, say, 2". Upon cooling, the path B is now followed;

[4] Doctor's thesis, by J. Bauschinger, Mitteilungen aus dem Mechanisher Technikisher Laboratorium in Munchen, 1886.

first elastically and then inelastically until the point 1' is reached. Again, assuming no relaxation at 1', upon heating path B is followed until the point 2''' is reached. Relaxation then takes place from 2''' to 2''. Upon cooling, path C is followed, and this path probably is very close to B. The stress-strain loop then settles down to a path somewhat similar to that of C and further changes will take place very slowly. The steady-stage stress-strain loop has inelastic deformation occurring in equal amounts during each half cycle but opposite in sign. Furthermore, a complete reversal in stress occurs for each cycle.

It will be seen that the steady-stage shape of the stress-strain hysteresis loop depends on many factors. Among the more important factors are the temperatures T_1 and T_2, the times at which the specimen is held at T_2 and to a lesser extent T_1, the rate of heating and cooling, the elastic properties of the material as affected by temperature, the inelastic properties of the material, and their temperature dependence. Among the inelastic properties which are of importance are the strain-hardening characteristics, the creep properties, and the inelastic properties. It will be appreciated, therefore, that a study of constant-temperature strain cycling must accompany a temperature-cycling program in order to separate out the effect of the various temperature-dependence factors.

DESIGN OF TEST SPECIMEN

There are several factors which must be taken into account in the proper design of a test specimen which will be subjected to a one-dimensional constraint from thermally induced strains. Of prime importance is the attainment of a satisfactory temperature distribution throughout the specimen during the various phases of the cycle. The radial variation of the temperature during heating and cooling must be minimized to reduce secondary thermal stresses produced by radial heat transfer. It is desirable to have a flat temperature distribution along the axis of the tube. In this way the maximum stress and strain effects will be felt by the specimen during the cycle. Also of importance is the magnitude of bending stresses produced near the end of the tube where there is a large longitudinal temperature gradient. These stresses must be kept small in order to prevent a fatigue failure from occurring at or near the end. Aside from temperature distribution, another factor for satisfactory design must be the fillets at the ends of the tube; these must be sufficiently smooth and gradual as to minimize stress-raising tendencies at these points.

Each of these effects is considered separately. First, we consider the thermal stresses which are induced by radial transfer during heating or cooling. In order to establish satisfactory heating and cooling rates without undue radial temperature variations, a thin-walled tube is used, Fig. 2. Since heating is accomplished by electrical means with the specimen itself as the resistance, a very uniform rate of heating occurs throughout the body and the thermal stresses induced thereby are exceedingly small. Cooling is accomplished primarily by the impingement of several distributed radial jets of gas onto the internal wall of the tube, Fig. 1. An average rate of cooling by this method is about 40 deg C per sec. One may then make approximate calculations of the tangential and longitudinal stresses induced thereby. An average heat-transfer rate of 10 watts per sq cm can be calculated from a knowledge of the cooling rate, the density of Type 347 stainless steel (about 8 g per cu cm), the wall thickness, and the specific heat of the metal (0.15 cal/g/deg C). From this calculated heat-transfer rate and the thermal conductivity of stainless steel (0.26 watts/cm/deg C), an average radial temperature gradient of 2 deg C is found. On the basis of

$$\sigma = E\alpha\Delta T/2(1 - \nu) \dots\dots\dots\dots\dots [2]$$

where σ is the axial or circumferential stress, E the modulus of elasticity, α the thermal coefficient of expansion, and ΔT the temperature gradient, a stress of about 720 psi can be obtained. This stress is negligibly small.

To determine the longitudinal temperature distribution, one must assume that there is uniform heat generation along the length of the specimen and that heat transfer occurs longitudinally by conduction and radially by convection and radiation. For the latter two modes of cooling, Newton's law of cooling is used. The problem is complicated by the fillet at the ends of the specimen, Fig. 2. To obtain an adequate solution to the problem, it is necessary to resort to an approximate method for evaluation of the temperature distribution. The method chosen was to assume that the temperatures at the center of the specimen and at the inside face of the specimen end flange are known and fixed. The specimen between these two points is then considered as a series of connected short cylindrical tubes with matched end temperatures and gradients. The tubes used are shown in Fig. 8. By trial and error the steady-stage temperature distribution[5] can be found for the entire tube, consistent with the thermal-heat generation and losses.
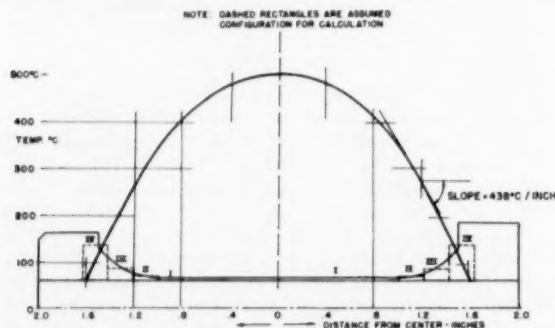
FIG. 8 CALCULATED TEMPERATURE DISTRIBUTION FOR TEST SPECIMEN

Fig. 8 shows the temperature distribution as calculated by the present technique. It is seen that a fairly flat temperature distribution exists over a central 1-in. length of the specimen. A flatter distribution could be obtained but this would introduce certain undesirable features. It can be shown[5] for a tubular specimen that the flatness of the temperature distribution depends on the quantity of ωl where

$$\omega = \sqrt{\frac{h}{kt}} \qquad\qquad [3]$$

and l is the half-length of the tube. In Equation [3], h is the Newton heat-transfer coefficient, k the thermal conductivity, and t the thickness of the tube. To increase the flatness of the temperature distribution it is necessary to increase h or l, or to decrease k and t. Since l and t are the only quantities easily adjustable for a given material, some flexibility in design exists. However, too severe a change in l or t may lead to a buckling problem and to manufacturing complications. Thus a compromise must be reached in the selection of these quantities. In addition, the flatter the distribution the more severe the bending stresses which are developed at the ends of the uniform section of the specimen.

The bending stresses induced by longitudinal variations in radial expansion are difficult to compute precisely because of the

fillets at the end of the specimen. However, an approximation of the constraint effect can be made. The specimen is first considered as a free-end tube with a length equal to the gage length and having a temperature distribution approximating that found in Fig. 8. Stresses and deformations produced in the tube by this temperature distribution can be found by using the beam on elastic foundation method, as treated by Den Hartog.[6]

The fact that the tube may be considered as semi-infinite in length may be ascertained from comparing the wave length of the stress and deformation functions to the tube length. The wave length is defined as

$$L_w = \frac{2\pi}{\beta} \qquad\qquad [4]$$

and β is defined[6] as

$$\beta = \frac{1.285}{\sqrt{rt}} \qquad\qquad [5]$$

where r and t are the radius and thickness of the tube, respectively. With the present dimensions, $\beta = 17.8$ 1/in. and $L_w = 0.352$ in. Since the tube length is 1 in. (to the center), and the stress and deflection waves are highly damped, the tube may be considered as semi-infinite.

To evaluate the stresses and deflections of the tube in the region of the free end, the tube may be considered as semi-infinite in length and the temperature distribution, as given in Fig. 8, is approximated by the relationship

$$\theta = (\theta_1 - \theta_0)(1 - e^{-\gamma x}) + \theta_0 \qquad\qquad [6]$$

where θ_1, θ_0, and γ are constants.

Applying reference[6] and using Equation [4], the bending stresses may be calculated. These stresses are negligible owing to the fact that the wave length of the thermal waves are so long in relation to L_w.

Superimposed on these stresses are those stresses arising from the constraint at the flanged ends. Calculation of these stress quantities would be quite simple if the effect of the fillet was neglected, since then the constraint would have infinite stiffness. With the large-radius fillet, however, a precise calculation is difficult, but an approximation can be made. Since the fillet results in a gradual change in wall thickness, the uniform tube can be thought of as extending somewhat farther than the actual tube and ending in an abrupt shoulder. This assumed configuration is shown in Fig. 9(b). The effectiveness of the fillet is determined by the amount of reduction of the bending stresses in the length of tube, x_{eff} in Fig. 9(b), assumed to replace the fillet.

The bending stress in the tube stemming from the end constraint is of the form

$$\sigma = \sigma_0 e^{-\beta x} \cos \beta x \qquad\qquad [7]$$

Thus the bending stress decreased rapidly from the constraint. For example, when

$$\beta x = 0, \ \sigma = \sigma_0; \ \beta x = 1.0, \ \sigma = 0.199\sigma_0;$$
$$\beta x = 2.0, \ \sigma = -0.056\sigma_0$$

it is assumed that the length of uniform tube replacing the fillet is one third the length of the fillet or $x_{eff} = 0.17$ in. Then, $\beta x_{eff} = 3.03$ or $\sigma = -0.049\sigma_0$. Consequently, any end effects associated with temperature variations will be reduced at least twentyfold at the point where the uniform tube actually begins.

For the assumed configuration of Fig. 9(b), the stress at the

[5] The basic problem is treated in "Conduction of Heat in Solids," by H. S. Carslaw and J. C. Jaeger, Clarendon Press, Oxford, England, 1947, pp. 136–140

[6] "Temperature Stresses in Flat Rectangular Plates and in Thin Cylindrical Tubes," by J. P. Den Hartog, *Journal of The Franklin Institute*, vol. 222, 1936, pp. 149–181.

built-in end of the thin-walled tube again can be calculated by the beam-on-elastic-foundation methods. This stress arises by assuming that the actual temperature distribution of Fig. 9(c) is replaced by that of Fig. 9(d). Correspondingly, the problem resolves itself into determining the edge bending moment and shearing force necessary to permit the tube to have the same deflection
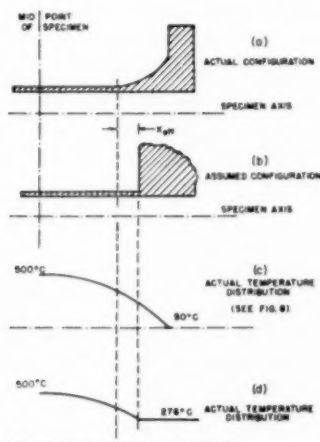

FIG. 9 ASSUMED CONFIGURATION FOR STRESS ANALYSIS

and zero slope as the very stiff flange. The edge bending moment and shear force necessary to match the end conditions are readily determined.[7] Using the temperature gradient given in Fig. 8, the bending stress at the fictitious built-in end is calculated to be 19,500 psi. The actual stress in the specimen (at the juncture of the fillet and tube), as discussed in the foregoing, is reduced by a factor of 20, so that the calculated bending stress in the actual tube at the fillet is about 1000 psi.

It is seen that the secondary stresses arising from radial or longitudinal temperature gradients are small in comparison to the primary longitudinal stress due to the end constraint. This stress, if completely elastic, is approximately

$$\sigma = E\alpha\Delta\theta = 150,000 \text{ psi} \dots\dots\dots\dots [8]$$

for a 300 deg C temperature change, a modulus of elasticity of 25×10^6 psi, and a thermal-expansion coefficient of $20 \times 10^{-6}/$ deg C. The maximum of these secondary stresses appears to be, from a highly conservative estimate, less than 0.7 per cent of the theoretically elastic stress due to longitudinal constraint.

The possibility of buckling of the thin-walled tube during the high-temperature portion of the cycle must be considered. Elastic buckling calculations show that the critical buckling stress is considerably above the yield stress, so that buckling occurs only after some plastic deformation. Experiments on tubes with the same dimensions as the test specimens reveal that a strain of several per cent is required before buckling occurs. Since the present apparatus does not permit strains greater than 1 per cent, plastic buckling is not a problem.

In the final analysis, actual testing of the specimen proves to be the best assurance that secondary effects are not important. Some 70 tests on specimens with a 2-in. gage length have been carried out on the thermal-cycling apparatus for a wide range of temperature and degree of cold work. Failures for these speci-

mens are all transverse and show complete randomness in their location as determined by the following distribution:

1 Twenty-four failures occurred on the central third region of the specimen including two starting at the thermocouple.

2 Twenty-three failures in the middle third of the specimen.

3 Twenty-three failures in the outer third of the specimen including six emanating from the fillet.

Thus no systematic secondary effect appears to be operating in the failure of these specimens.

CONSTANT-TEMPERATURE CYCLING APPARATUS

Because of the complications affecting the mechanism of plastic flow when temperature cycling is coupled with stress cycling, an investigation of constant-temperature stress cycling is extremely important. In this manner, effects due only to changes in temperature can be separated from those due to cyclic stresses. Such a comparison also would be valuable from a purely practical point of view. If the role played by temperature in thermal cycling were sufficiently understood, simpler experiments could be devised to test engineering components.

It is possible with a few simple modifications to convert the present thermal-stress apparatus to one in which a test specimen is strain-cycled between fixed limits at constant temperature. This is done by converting the two supporting columns to thick-walled tubes and cycling them thermally by current self-heating and internal gas cooling. A separate internal heater built to slide into the test specimen is used to control the temperature of the specimen at any level desired. Since it is no longer possible to attach strain gages to the columns, because of the temperatures, a weighbar in series with the test specimen is necessary. The columns are insulated from the balance of the apparatus at the top plate only, in the same manner as described earlier. Brass connecting posts are secured into the top of each column and these are joined by a copper bus bar and connected to the current transformer. The other transformer lead is connected to another brass post screwed into the lower end of the test specimen. No change in the control circuit is required.
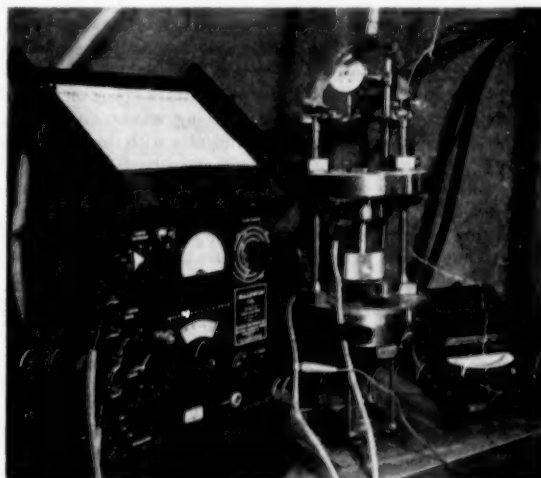

FIG. 10 CONSTANT-TEMPERATURE STRAIN-CYCLING APPARATUS

Fig. 10 shows the test assembly. The columns have been extended to allow for the introduction of the weighbar in series with the test specimen. Fig. 11 shows the construction of the weighbar. The assembly is such that it is not necessary to disassemble

[7] "Strength of Materials," by S. Timoshenko, D. Van Nostrand Company, Inc., New York, N. Y., part 2, 1947, p. 12.
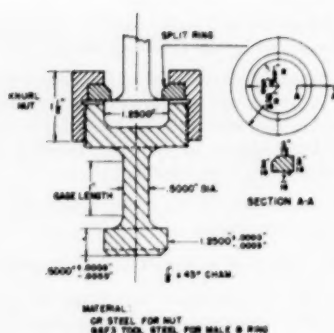
FIG. 11   WEIGHBAR FOR CONSTANT-TEMPERATURE STRAIN-CYCLING
APPARATUS

the apparatus completely in order to change specimens. This is effected by using a split ring-and-nut assembly which, when in place, clamps the flange of the specimen tightly to the weighbar and which, when the nut is unscrewed, permits the specimen to be withdrawn (provided the retaining plug in the upper plate is removed).

Since the specimen now undergoes a cyclic deformation, it is necessary to measure this displacement by means of a dial gage, as shown in Fig. 10. From this measurement the strain amplitude of the specimen can be determined.

The two columns are made of Type 347 stainless steel because of its corrosion resistance and high-temperature-strength properties. Dimensions must be chosen so that the stiffness of the weighbar is large with respect to that of the specimens and also have the proper electrical resistance to meet the design requirements of the current transformer. A stiffness ratio of almost 4 to 1 has been found satisfactory.

EXPERIMENTAL PROGRAM

As in all experimental work, some time was spent in making the equipment perform according to expectation. The principal sources of trouble lay in (a) play in the structure which prevented the thermal deformation of the specimen to be converted fully into elastic and inelastic deformation and (b) measurement of the stress change. First tests showed that the original design permitted excess motion at practically all points of attachment, and the final design, as described in the foregoing, was arrived at after considerable experimentation. The difficulty with the resistance-wire strain measurement stemmed from excessive 60-cycle pickup in the shielded leads during the heating cycle. Although many fairly involved techniques were tried to eliminate this trouble, the solution was obtained by twisting the lead wires carefully and avoiding any closed loops in the circuit near the apparatus in order to reduce the inductive effects to a minimum.

With the successful solution of the foregoing problems an experimental program was undertaken to explore the important parameters of the problem. A companion report[8] describes the ex-

[8] "A Study of the Effect of Cyclic Thermal Stresses on a Ductile Metal" by L. F. Coffin, Jr., published in this issue, pp. 931–950.

periments completed to date and their significance. The parameters investigated or to be investigated were selected to yield as much fundamental information as possible and at the same time to supply useful data for design purposes. A brief mention of them is made here to indicate the type of problem to which the apparatus can be applied.

In the program carried out to date, the fatigue life has been determined for Type 347 stainless steel as a function of temperature range of cycling. In doing this, the mean temperature $(T_{max} + T_{min})/2$ was maintained at a fixed level, and temperature changes of from 200 C to 500 C in 50-deg C steps have been performed on sufficient tests to establish the effect. For this investigation, the test specimens were first annealed by heating to 1100 C (2000 F) in dry hydrogen and cooled fairly rapidly to avoid formation of the sigma phase.

The effect of prestrain was investigated, not only as to amount but also as to kind. Test specimens were pulled in tension to strains of varying amounts up to 0.30 in. (ordinary strain) and in torsion to amounts of twist up to 1.57 in. per in. shear strain. Attempts to prestrain the thin-walled test specimens in compression resulted in failure, despite many and varied techniques, because of difficulties with plastic buckling. Prestrained specimens were then subjected to various ranges of thermal cycles and the relationship between temperature range and life to failure established for the various parameters of prestrain.

A third investigation was concerned with the role played by stress raisers in fatigue from cyclic thermal stresses. By drilling two diametrically opposed 0.040-in-diam holes through the tube wall at the mid-point of the specimen, a stress raiser was introduced. The elastic effect of the stress raiser was well known, since the effect was identical with that of a small hole in a plate in tension. Specimens so altered were then cycled with various temperature changes and the fatigue life established. From this it was possible to study the effect of stress concentration under severe cyclic stresses and to correlate these stress-concentrating effects with a cycling of a uniform tube.

Other parameters which are currently being studied include the effect of frequency of cycling and the effect of variations of the mean-temperature change. The first of these is accomplished by varying the hold times at the high and low temperatures of the cycle while keeping the heating and cooling times fixed. The effect of variation in the mean temperature is investigated by maintaining a fixed thermal-strain range in cycling and adjusting the mean temperature.

ACKNOWLEDGMENT

A Study of the Effects of Cyclic Thermal Stresses on a Ductile Metal

By L. F. COFFIN, JR.,[1] SCHENECTADY, N. Y.

The results of a study of cyclic strain and fatigue failure arising from cyclic thermal stresses are reported. By means of a test apparatus described in a companion paper, a cyclic temperature is imposed on a thin tubular test specimen subjected to complete longitudinal constraint. Hence, the cyclic strain is the independent variable. The following studies are reported: (a) Effect of thermal-stress cycling on strain hardening and life-to-failure for a fixed mean temperature, (b) effect of degree and kind of previous cold work on strain hardening and cycles-to-failure, (c) effect of mean temperature on thermal-stress cycling, (d) effect of period of cycle on cycles-to-failure, and (e) effect of prior strain cycling on stress-strain characteristics. The significance of factors such as hysteresis, Bauschinger effect, strain hardening, strain aging, and fatigue-crack formation is discussed, and a mechanism is described to relate these factors. Evidence is presented to show that strain hardening is not an important factor in the problem. The concept of total plastic strain is discussed.

INTRODUCTION

THERMAL stresses play an important role in the design of high-temperature apparatus. This is particularly true in nuclear reactors. Here the conversion of nuclear to thermal energy in realistic power reactors generally results in thermal fluxes many times those encountered in conventional heat-transfer systems. The cooling of structural materials exposed to intense neutron and gamma irradiation provides another source of high thermal flux.

The thermal stresses which arise as a result of these high thermal fluxes depend principally on the thermal-expansion coefficient, the modulus of elasticity, and the thermal conductivity of the heat-transfer path. One of the more widely used high-temperature materials is the 18 per cent chromium, 8 per cent nickel stainless steel. This material has the rather unusual property of incorporating a high coefficient of thermal expansion and modulus of elasticity with a low thermal conductivity. Thus, for the same amount of heat transferred, much higher thermal stresses can result than for most structural materials.

The problem then is concerned with assessing the damage done to the structural material by high thermal stresses. Here, on the first application of load the high thermal stresses are relieved by plastic flow, provided the material is ductile. As a result, provided static conditions prevail, the high stresses calculated on an elastic basis are reduced to a level which would not be considered to be serious.

The principal difficulty arises when the thermal effects become cyclic in nature. Here, as before, the stresses are first elastic, then become plastic for severe thermal effects. When the thermal load is removed the stresses are first reduced elastically. However, because of the previous plastic action, complete thermal unloading will cause the stresses to reverse their direction, and if the conditions are particularly severe, these stresses can cause a reversal in plastic flow. As a result, a cyclic thermal loading can cause cyclic thermal stresses which may be sufficiently severe to produce reversed plastic flow with each cycle. Consequently, the problem resolves itself into one in which eventual damage to the part in question can occur by fatigue.

This particular problem in fatigue has received very little attention. Primarily, failure occurs after a comparatively few cycles, whereas most fatigue testing is carried out for cycles-to-failure in excess of from 10 to 100,000 cycles. Then too, the period of the cycle is generally long and is measured in minutes or hours, while conventional tests are carried out for periods of loading in milliseconds. Also the problem involves cycling between fixed-strain values; conventional testing involves stress cycling. Finally, there is necessarily a temperature variation during the cycle, such that at high temperature the stresses are generally compressive, while at the lower temperature they become tensile.

Because of the lack of information, both of a fundamental and a design nature, an extended research program has been undertaken. A companion report (1)[2] has been prepared which describes the experimental apparatus developed for this study. The present report gives the results of pertinent tests which are useful from the point of view of design and information which may be helpful for the general problem of fatigue.

TEST APPARATUS

A detailed description of the test apparatus and its operation has been given in a companion paper (1), and this paper should be read to understand fully the method of testing. However, a brief review of this report appears to be in order here.

Basically, the method of testing consists of subjecting a flanged-end, thin-walled tubular test specimen to a temperature which is cyclic in nature. The specimen is clamped rigidly at each end to thick end plates and its thermal expansion and contraction prevented by two stiff bars attached firmly to the top and bottom plates. In this way the specimen is subjected to a cyclic longitudinal stress arising from its end constraint. Fig. 1 shows an assembly and exploded view of the apparatus, and Fig. 2 shows the test specimen used.

The temperature cycle of the specimen is divided into four parts: (a) heating, (b) high-temperature hold, (c) cooling, and (d) low-temperature hold. Heating is accomplished by passing a current through the test specimen so that the specimen serves as its own resistor. Cooling is carried out by means of a gas blast from a radial diffuser located internally. Temperatures are measured by a chromel-alumel thermocouple spot-welded to the tube wall, coupled with a millivoltmeter calibrated as a temperature

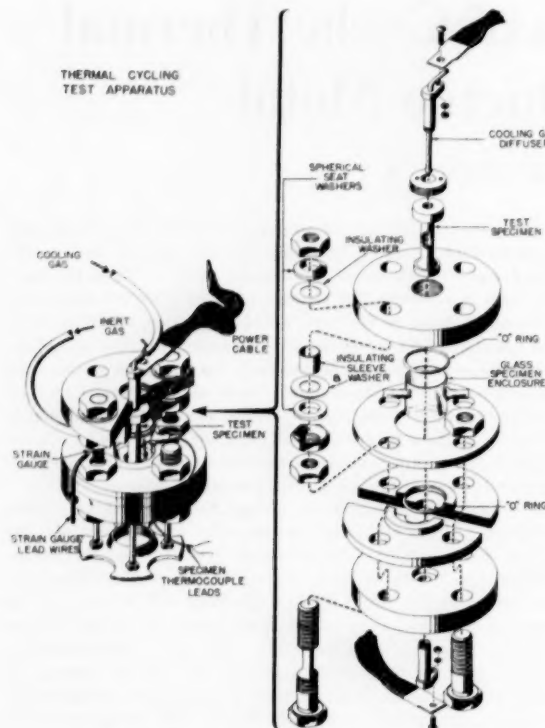[2] Numbers in parentheses refer to the Bibliography at the end of the paper.

FIG. 1   THERMAL-CYCLING TEST APPARATUS
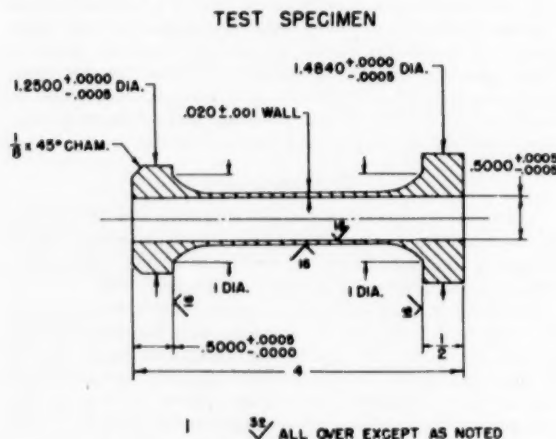
TEST SPECIMEN

FIG. 2   TEST SPECIMEN

indicator. A relay control circuit permits the continuous repetition of the cycle.

During the course of a particular test it is possible to measure and derive certain stress and strain quantities which are of importance in the study of the problem. First, the thermal deformation of the test specimen between the high and low temperatures of the cycle is found by cycling the test specimen first without, then with, end constraint, and subtracting the two quantities. The elastic strain component can be separated from this quantity from a knowledge of the change in stress of the specimen during the temperature oscillations. This stress

is in turn attained from strain gages mounted in the two supporting columns of the apparatus. From the strain-gage readings it is also possible to observe the strain-hardening effects which occur during the progress of a particular test.

When the apparatus has come to temperature equilibrium following the start of a particular test, no further adjustment in control has been found necessary to maintain the cycling between temperature limits set initially. Thus the test may be run continuously until the specimen has failed. To determine the number of cycles for failure should failure occur during off-hours, a recording millivoltmeter can be connected to the specimen thermocouple. When failure occurs, a change in temperature can be detected readily, and by counting oscillation back to a premarked reference point, the exact number of cycles can be determined.

Considerable attention has been given to the design of the test specimen with regard to temperature and stress distribution during the cycling operation. It can be shown that stresses and deformations, other than those desired, are minor in their effect. This is best demonstrated by the complete randomness in the location of the fracture found in some 75 test specimens.

The stress and strain behavior of the specimen during thermal cycling and longitudinal constraint is somewhat complicated. In order to interpret the test results of this report correctly, a clear understanding of the cycling process is essential.

When the test specimen is constrained and cycled, the net strain of the specimen is essentially zero, except for a small cyclic strain caused by the deflection of the supports. For the purpose of this discussion, this net strain will be taken to be zero. It can then be broken down into three strain components, each cyclic in its behavior. These components are (a) the thermal strain, (b) the elastic strain, and (c) the inelastic strain. The thermal strain is dependent only on the average temperature in the specimen and is found by measurement of the specimen deformation during thermal cycling in the absence of end constraint. The elastic strain is a calculated quantity, as discussed in the foregoing, being linearly related to the change in stress during cycling. The inelastic strain is a derived quantity and is found from the relationship

$$\epsilon_{thermal} + \epsilon_{elastic} + \epsilon_{inelastic} = \epsilon_{net} = 0 \dots \dots [1]$$

which is operative at all times.

The reference point for the various cyclic-strain components is established at the point at which the unstressed bar is constrained, usually during the time the specimen is at the maximum temperature. With this as the reference point, the thermal strain then oscillates between zero and the quantity $-\alpha \Delta T$, where α is the average thermal expansion coefficient and ΔT is the temperature change between the maximum temperature T_2 and the minimum temperature T_1.

The stress-strain relationship during the first few cycles of testing is shown in Fig. 3. It is assumed that the thermal coefficient of expansion of the material is constant over the temperature range of the test. Then T_2 is the maximum temperature and T_1 is the minimum temperature. The temperature versus thermal-strain relationship is shown in the upper figure. The lower figure shows the relationship between the stress and elastic plus inelastic strain. As mentioned before, the specimen is clamped at the maximum temperature (Point 2). This then is the origin of the stress-strain curve. As cooling occurs, Path A is followed in which an elastic tensile stress is first developed. As plastic flow occurs, an inelastic strain component is added to the elastic strain until the minimum temperature T_1 is reached. This is given by Point 1 on the curve. The temperature is then held at T_1. The change in elastic and inelastic strain during this interval is quite small and assumed, for practical purposes, to be
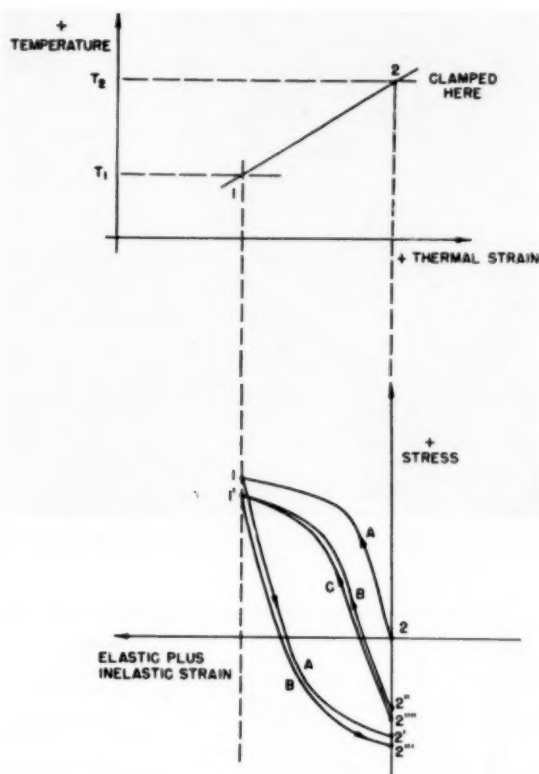
FIG. 3 STRESS-STRAIN RELATIONSHIP FOR FIRST FEW THERMAL CYCLES FOR BAR WITH LONGITUDINAL CONSTRAINT

zero, since the effects of anelasticity, viscosity, and plasticity in the metal which influence relaxation effects are strongly temperature-dependent, and at the low temperature T_1 they are diminishingly small.

Following the hold period at Point 1, heating of the specimen causes first an elastic decrease on stress along Path A. Now, however, because of the previous plastic effects, a reversal in inelastic behavior occurs prematurely. This is due to the well-known Bauschinger effect (2). Consequently, when Point 2 is reached at the high temperature, a portion of unloading Path A is inelastic although the amount of inelastic strain is not so large as occurred during the first loading. Thus, when Point 2' is reached, the specimen has a residual compressive stress. Because of this residual stress, the point in the cycle in which zero elastic strain occurs has shifted from T_2 to some point between T_1 and T_2.

During the hold interval at the elevated temperature T_2, relaxation effects will occur readily depending on the interval time and temperature. The stress-strain path then moves from 2' to 2''.[3] Upon the next cooling operation Path B is followed first elastically and then inelastically until Point 1' is reached. Again assuming no relaxation during the hold time at T_1, upon subsequent heating Path B is followed from 1' to 2'''. Here relaxation during the hold time at high temperature changes the path from 2''' to 2''''. With the next cooling operation Path C

[3] The fact that the relaxation occurs at constant strain in the lower figure of Fig. 3 is seen from Equation [1]. Here the elastic plus inelastic strain remains constant as long as the temperature and, hence, the thermal strain is constant regardless of any other change.

is very close to Path B. The stress-strain loop then settles down to a path similar to that of C and further changes take place very slowly. The steady-state stress-strain loop has inelastic deformation occurring in equal amounts and opposite in sign during each half cycle, provided the elastic modulus is the same for heating and cooling.

The fatigue phenomenon is strongly dependent on the size and shape of the stress-strain loop of the type given in Fig. 3, so that factors affecting this loop will markedly influence the fatigue behavior. Among the more important factors are the temperatures T_1 and T_2, the times at which the specimen is held at T_2 and to a lesser extent T_1, the rate of heating and cooling, the elastic properties of the material, the inelastic behavior of the material and its temperature dependence. Among the inelastic properties which would seem to be of importance are the plastic-flow characteristics, the creep properties (both slip and viscous processes), the anelastic properties, the aging behavior, and Bauschinger effect. To add to the complexity, these various effects are probably interrelated.

Some of the more important and easily controlled factors are considered in the present study. For a more complete investigation, these findings should be correlated with those obtained by strain cycling at constant temperature. However, this phase of the work is sufficiently advanced to report at the present time.

EXPERIMENTAL PROGRAM AND RESULTS

Effect of Thermal Cycling on Life-to-Failure and Strain Hardening for a Constant Mean Temperature. The first study of the effect of cyclic thermal stresses was undertaken to explore the influence of the temperature change ΔT on the fatigue life. In order to reduce the effect of temperature on the material properties to a minimum so that its principal effect would be one of producing a thermal strain, the mean temperature of the cycle $(T_1 + T_2)/2$ was maintained at a constant value. The material tested was Type 347 stainless steel in the annealed state. Annealing was performed on the finished specimens by heating to 1100 C (2012 F) in a dry hydrogen atmosphere and cooling rapidly to avoid a sigma-phase formation.

In this series of tests the mean temperature was maintained at 350 C (662 F). This temperature was chosen based on the practical consideration that the maximum useful temperature structurally is 650 C, while the minimum temperature for cooling by an air blast is 50 C; the average is 350 C. Values of T_1 and T_2 were then selected to maintain this temperature while giving temperature differences ΔT in 50-deg steps.

Fig. 4 shows the results of these tests. The data are presented in semilog co-ordinates with both the temperature dif-
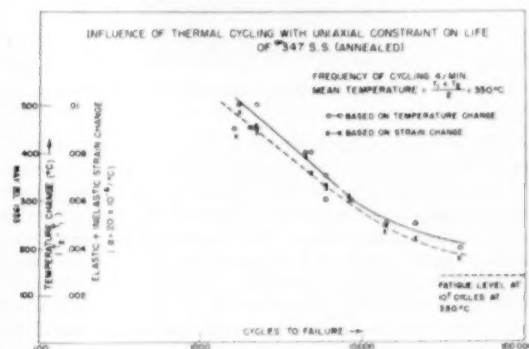

FIG. 4 INFLUENCE OF THERMAL CYCLING WITH UNIAXIAL CONSTRAINT ON LIFE OF NO. 347 SS (ANNEALED)

ference and strain change as ordinate and the logarithm of the cycles-to-failure as abscissa. Failure is defined as complete or nearly complete separation of the specimen by the rapidly growing crack. Similarity with conventional stress versus cycles-to-failure fatigue data is noted.

By plotting the data with the two different ordinates (temperature change and strain change), a difference in the scatter of experimental points is revealed. The two ordinates are approximately equal when $\alpha = 20 \times 10^{-6}/\deg$ C. In the ideal test, neglecting any deformation of the supports and assuming a uniform temperature distribution along the length of the tube, the elastic plus inelastic-strain change exactly equals $\alpha \Delta T$ for all conditions (see foregoing). Actually, however, there are several factors, some of which are compensating, which act to make the relationship only approximate. These include nonuniform longitudinal temperature distribution which varies with the temperature level, variations from specimen to specimen in tightness of clamping, variation in dimensions of specimens, and so on. The measured value of elastic plus inelastic strain is actually more closely related to the fatigue process in each specimen and hence gives a better fit for the test data than the temperature change. However, as indicated in Fig. 4, the difference is slight.

The fatigue strength for this material is in the range of 35,000 psi for 10^7 cycles at 350 deg C (3). Assuming a modulus of elasticity of 25×10^6 psi at this temperature, the elastic-strain change from tension to compression can be calculated. This strain value appears on Fig. 4. It can be seen that an extrapolation of the experimental curve to the elastic-strain change corresponding to the endurance limit is not unreasonable.

Scatter of test data for this series of tests is not particularly marked. However, at most only three specimens were tested at each condition so that the sample is too small to be conclusive. A later section gives more information on this subject.
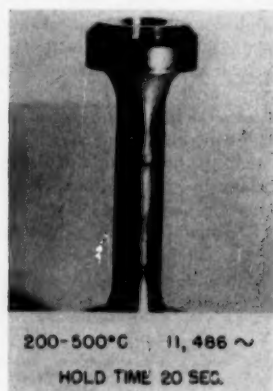
FIG. 5   FATIGUE CRACK IN ANNEALED TEST SPECIMEN

A typical fatigue crack is shown in Fig. 5. There is little evidence of ductility in the metal and the crack is quite characteristic of a fatigue failure. At both ends of the crack a plastically deformed region which progresses along with the crack can be observed on close examination. This region is fan-shaped in appearance and is a result of a concentration of slip planes arising from the discontinuity of the crack. Fig. 6 shows this area.

The strain-hardening characteristics of the material are of particular interest in this series of tests. As pointed out above, the hysteresis loop is established very quickly, and changes in the size and shape of the loop take place very slowly thereafter. Since the cyclic temperature change is fixed for the duration of
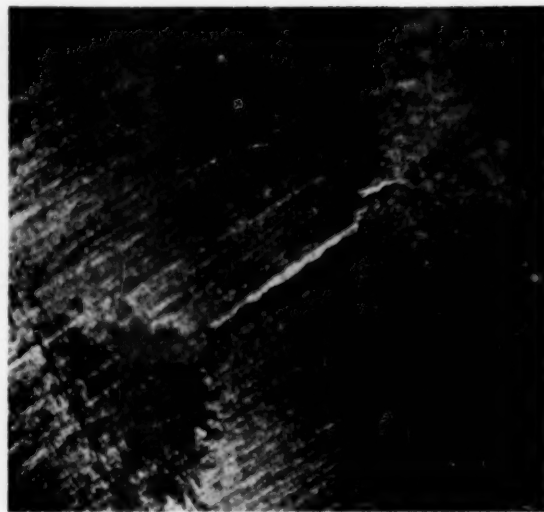
FIG. 6   MAGNIFIED VIEW OF FATIGUE CRACK IN NO. 347 STAINLESS STEEL
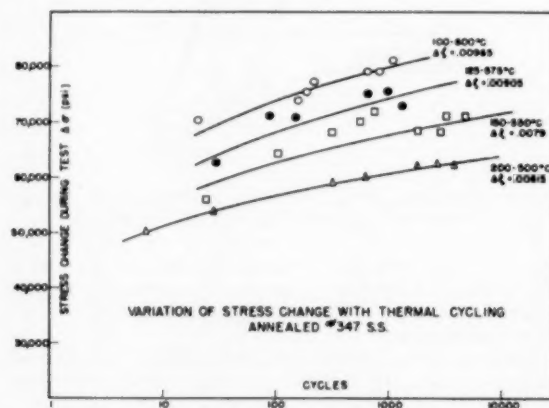
FIG. 7   VARIATION OF STRESS CHANGE WITH THERMAL CYCLING ANNEALED NO. 347 STAINLESS STEEL

the test, the elastic-plus-inelastic strain change in each cycle is likewise fixed. However, the stress change occurring in each cycle does vary slowly with time. This quantity can be measured throughout the test as shown in Fig. 7 for typical specimens subjected to various cyclic temperature changes. Here the stress change is plotted against the logarithm of the number of cycles corresponding to that stress change. It is of interest to note that the stress change is quite insensitive to the number of loading cycles, with only a slight rise found for each of the four temperature changes and a flattening of the curves noted even when plotted on semilogarithmic co-ordinates. It may be concluded that strain hardening for thermally strain-cycled annealed materials is not a pronounced effect.

It is also of interest to construct a type of stress-strain curve from the data of Fig. 7, by plotting for a particular specimen a nominal stress change occurring during the test versus a strain equal to the sum of the elastic plus inelastic strain. This curve is shown in Fig. 8 for the various specimens which have been tested at different strain levels. A comparison can be made with the
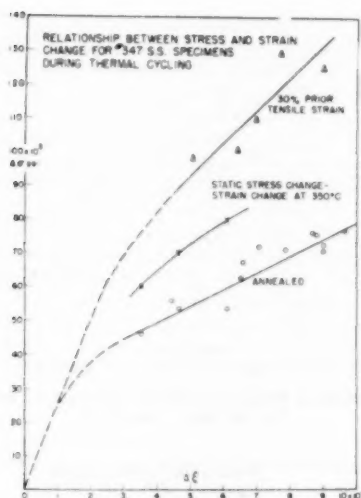
FIG. 8   RELATIONSHIP BETWEEN STRESS AND STRAIN CHANGE FOR No. 347 STAINLESS STEEL SPECIMENS DURING THERMAL CYCLING
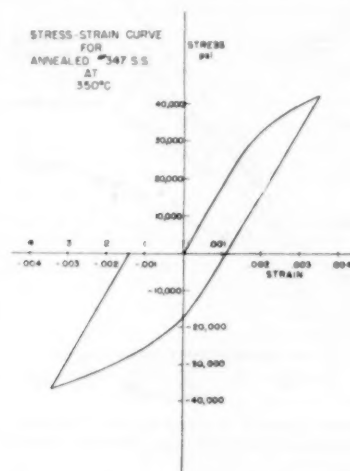

FIG. 9   STRESS-STRAIN CURVE FOR ANNEALED NO. 347 STAINLESS STEEL AT 350 C

data found from a single static test taken at the mean temperature.

Fig. 9 is the first stress-strain loop for annealed Type 347 stainless steel obtained in a static test at 350 C at a strain rate of about 0.1 per cent/hr. For comparison purposes, the first part of the stress-strain curve of Fig. 9 is replotted in Fig. 8. It will be seen that the data for the annealed, thermally cycled test specimens lie well below this static curve, indicating that the Bauschinger effect influences the size of the hysteresis loop.

Effect of Previous Cold Work on Cycles-to-Failure. Some early tests of an exploratory nature clearly showed that previous cold work played an important role in the life-to-failure of the thermal-stress cycled material. It was found that an inconsistency existed between specimens tested in the as-received condition (where annealing was performed on the original bar stock) and those annealed after machining. The former had a life of about 1800 cycles when cycled between 200 and 500 C, while the latter resisted some 8000 cycles before failing. The discrepancy was

resolved when a photomicrograph of the structure showed a heavily disturbed layer on the inner surface of the as-received specimens caused by the machining process. Subsequent annealing restored the disturbed region to its original structure. It was evident that fatigue cracks were originating prematurely in the cold-worked region and progressing through the annealed region to lower the life. This is in contrast to the familiar practice of purposely producing cold-worked surface layers to increase the fatigue resistance (4). As a result, a program of study was undertaken on the problem.

The investigation was started with annealed test pieces. Specimens were deformed plastically to various degrees by different kinds of deformation including simple tension and torsion. Compression was also attempted but no suitable method was found to avoid plastic buckling of the thin-walled tube. However, with the two kinds of cold work, it was possible to study the effect of type as well as degree of the effect.

Tension specimens were prepared by stretching annealed test specimens to 15 and 30 per cent uniform strain (in a 2-in. gage length) directly in the thermal-stress apparatus by screwing upward the bottom nuts of the top plate. The torsion process was carried out in a lathe by mounting the tube on a snugly fitted arbor and encompassing it by an external jacket to prevent buckling. One flanged end of the specimen was clamped to a fixed chuck, the other end clamped to a freely turning chuck. Deformations of 180 and 360 deg in 2 in. were obtained on the previously annealed specimens.

In a study of the type of cold work, a relationship of the equivalence between the various kinds of deformation is needed. This is conventionally done by relating effective strains, based on some plastic-flow criterion. Using the "distortion-energy" criterion, the effective strain, ϵ^*, is expressed as

$$\epsilon^* = \frac{\sqrt{2}}{3}\sqrt{(\epsilon_1 - \epsilon_2)^2 + (\epsilon_2 - \epsilon_3)^2 + (\epsilon_3 - \epsilon_1)^2} \dots \text{[2]}$$

where ϵ_1, ϵ_2, and ϵ_3 are principal strains (6). In the case of tension

$$\epsilon_1 = -2\epsilon_2 = -2\epsilon_3 = \log_e \frac{l}{l_0} \dots \dots \text{[3]}$$

where l_0 and l are the lengths between bench marks before and after stretching. Equation [3] is particularly applicable to large deformations, and the strain so calculated is referred to as the true strain.

For torsion, the shear strain is defined as

$$\gamma = \frac{d\phi}{2l_0} \dots \dots \dots \text{[4]}$$

where d is the diameter at which the shear strain is measured, ϕ the angular twist of the bar in radians, and l_0 the bar length. Poynting (5) has shown that for this case the principal strains are

$$\epsilon_1' = -\epsilon_2' = \log_e\left(1 + \frac{\gamma}{2} + \frac{\gamma^2}{8}\right) \dots \dots \text{[5]}$$

$$\epsilon_3' = 0$$

The equivalence between tension and torsion can then be found by using Equation [2], with the aid of Equations [3] and [5], resulting in the relationship

$$\epsilon_1 = \frac{2}{\sqrt{3}} \log_e\left(1 + \frac{\gamma}{2} + \frac{\gamma^2}{8}\right) \dots \dots \text{[6]}$$

between the true longitudinal strain in tension and the shear strain in torsion. The various deformations applied to the specimens prior to thermal cycling when connected to effective strain are given in Table 1.

TABLE 1 DEFORMATIONS APPLIED TO SPECIMENS

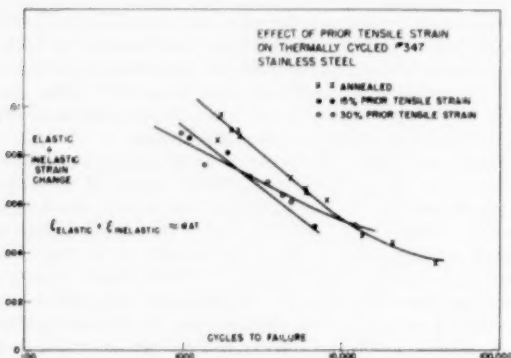| Amount and kind of deformation	Effective strain
15 per cent elongation in 2 in.	0.140
30 per cent elongation in 2 in.	0.262
180-deg twist in 2 in.	0.242
360-deg twist in 2 in.	0.443

Fig. 10 Effect of Prior Tensile Strain on Thermally Cycled No. 347 Stainless Steel
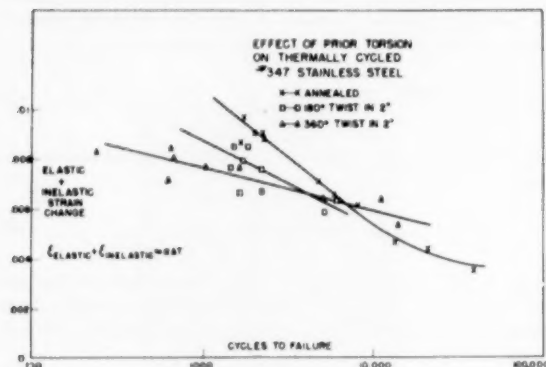
Fig. 11 Effect of Prior Torsion on Thermally Cycled No. 347 Stainless Steel

The effect of the amount of cold work on life-to-failure for constrained thermal cycling is shown in Figs. 10 and 11. In Fig. 10 comparison is made of life-to-failure for specimens given a previous tensile deformation of 15 and 30 per cent strain; in Fig. 11, specimens pretwisted to 180 and 360 deg are compared with those receiving no previous deformation. Contrary, perhaps, to expectation, it is seen that the previous cold work is beneficial only when the cyclic ΔT (or $\Delta\epsilon$) is less than a critical amount. Above this critical ΔT the previous deformation reduces the life-to-failure. Both effects depend monotonically on the amount of the previous deformation. The increase in life for cold-worked specimens subjected to below-critical temperature difference corresponds to an increase in endurance limit with cold work as reported in (4).

It should be pointed out that in Figs. 10 and 11 the ordinate is the temperature difference or its equivalent, the elastic plus inelastic strain. These data may be replotted using the nominal
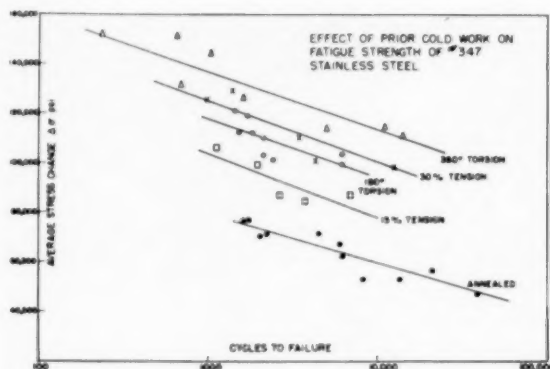
Fig. 12 Effect of Prior Cold Work on Fatigue Strength of No. 347 Stainless Steel
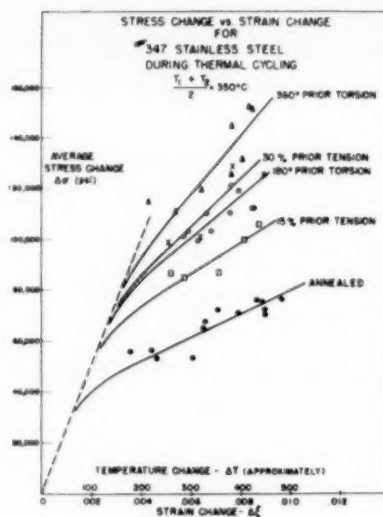
Fig. 13 Stress Change Versus Strain Change for No. 347 Stainless Steel During Thermal Cycling

stress change per cycle as ordinate and, as before, cycles-to-failure as abscissa. A pronounced difference in effect is now seen in Fig. 12, where the annealed and cold-worked curves are roughly parallel to one another such that increasing cold work raises the stress change that a particular specimen can withstand in fatigue. This figure bears a marked similarity to conventional fatigue data for effects of cold work.

The marked difference in appearance of Fig. 10 or 11, and Fig. 12, at first seems to indicate an ambiguity. The interpretation of Fig. 12 would be that cold work uniformly and monotonically increases the resistance of the material to cyclic thermal-stress effects. On the other hand, from Fig. 10 or 11 it appears that previous cold work may be either harmful or beneficial, depending on severity of the cyclic thermal stress. This difficulty can be clarified if curves of strain and stress change for various temperature changes are constructed for specimens with different degrees and kinds of cold work. This is done in Fig. 13. In this figure a comparison is made between no prestrain and 30 per cent tensile prestrain. From the curves in this figure and in Fig. 10 it is possible to construct the curves in Fig. 12 for these two states of prestrain. For a low number of cycles, for

example 1500 cycles, the corresponding strain values can be read from Fig. 10. It is seen that the strain for the annealed curve exceeds that for the 30 per cent strain curve. Referring to Fig. 13, however, these strain values correspond to values of stress in which the cold-work stress change exceeds that of the annealed. Considering the strain values for a large number of cycles, for example 15,000, it is seen that the strain for the cold-worked material exceeds that of the annealed metal. Referring again to Fig. 13, these strain values show that, as before, the stress change for the cold-worked state exceeds that of the annealed. Consequently, the annealed and cold-worked curves in Fig. 12 will not cross as they do in Figs. 10 and 11.

The importance of this finding lies in determining whether the stress or the strain is the independent variable in a fatigue test. If the stress is the independent variable, as in cyclic loading, it can be said that cold work increases resistance to fatigue without qualification. However, if the strain is the independent variable, as in cyclic thermal applications, such a statement is not correct. This will be discussed later.

The relationship between stress and strain change with each cycle, Fig. 13, is of particular interest in determining the size of the hysteresis loop. If there was a cyclic elastic behavior only (no hysteresis loop), the plotting of $\Delta\sigma$ against $\Delta\epsilon$ would result in a point falling on the dashed line in Fig. 13. When a hysteresis loop exists, the quantity $E - \Delta\sigma/\Delta\epsilon$ is a measure of the hysteresis.[4] From Fig. 13, $\Delta\sigma/\Delta\epsilon$ becomes the slope of the chord connecting the $\Delta\sigma - \Delta\epsilon$ origin with any other point on a particular curve, while E, the modulus of elasticity, is the slope of the dashed line. Consequently, the difference in these slopes gives the modulus of hysteresis. It will be seen for the same $\Delta\epsilon$ that the hysteresis loop will be quite narrow for materials heavily cold-worked prior to strain cycling, while annealed materials produce a large hysteresis loop.

The effect of the kind of cold work (tension versus torsion) prior to stress cycling is of considerable interest. Although a comprehensive study of this problem has not been made, enough tests have been completed to indicate a definite trend. Such a comparison can be made in Fig. 14 with reference to Table 1. From Fig. 14 it is seen that, of the various prestraining operations prior to thermal cycling, the 360-deg twist has the greatest

FIG. 14 SUMMARY OF EFFECT OF PRIOR COLD WORK ON THERMALLY CYCLED No. 347 STAINLESS STEEL

effect, while the 180-deg torsion and the 30 per cent tensile deformation seem to have a comparative effect on the number of cycles-to-failure. From Table 1 it is noted that on the basis of effective strains, a 180-deg twist should have slightly less effect

[4] This quantity is arbitrarily referred to as the modulus of hysteresis

than 30 per cent tension. It appears that pretwisting is actually about as effective as pre-extension on altering the fatigue characteristics of the material.

A similar interpretation can be made from a study of the stress change versus life-to-failure curve, Fig. 12. Here it is actually found that the 30 per cent tension and 180-deg twist give comparable results, while the 360-deg twist is the most effective and the 15 per cent tension least effective in changing the $\Delta\sigma$ versus cycles-to-failure characteristics.

The nature of the fatigue fracture is associated with the variation in cyclic thermal-stress resistance by previous cold work. Fig. 15 shows a typical fatigue fracture in a specimen with a 30
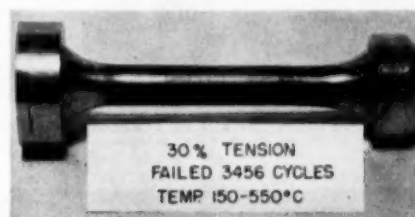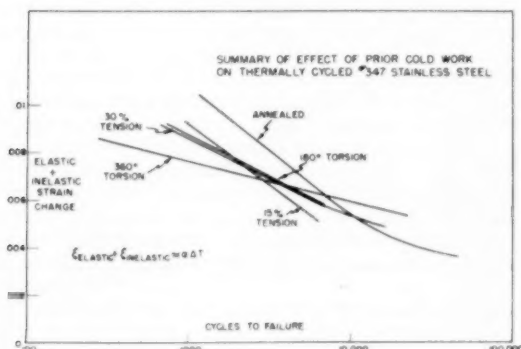

FIG. 15 FATIGUE CRACK IN TEST SPECIMEN WITH 30 PER CENT TENSILE PRESTRAIN

per cent tensile prior strain. All fractures found in the annealed case, Fig. 5, and in those specimens with prior tensile strains were brittle in appearance (except for a fan-shaped plastic region at the end of the crack) and transverse to the direction of cycling. However, when the direction of deformation is not coincident with the cyclic thermal-stress direction, an interesting effect appears, as is seen in Figs. 16 and 17. Fig. 16 shows the fracture obtained for specimens cycled with varying strain amplitudes (temperature change) following a 180-deg torsion, while specimens with 360-deg-torsion are shown in Fig. 17. It is seen that as the strain amplitude increases, a change in the fracture direction occurs quite suddenly from transverse to oblique. The effect is particularly striking for the 360-deg pretwist. It further appears that the angle of the obliquity seems to increase with the angle of pretwist[5] and, for the case of the 360-deg pretwist, is coincident with this angle. The details of the effect are currently being studied more thoroughly. As will be discussed later, however, similar behaviors have been noted by other investigators in static and fatigue testing.

The behavior of the stress change during thermal cycling on strain-cycled test specimens with various kinds of prestrain was of considerable interest. Earlier it was shown that annealed material underwent a slight strain hardening with thermal cycling, Fig. 7. With prior cold work, however, it was observed that the material actually strain softened; that is, the stress change during each cycle decreased with the number of cycles. Figs. 18 to 21 show this effect for specimens initially strain hardened by tension and torsion. It appears from these curves that the strain softening effect is more rapid at the beginning than at the end of the test. This would tend to disprove any mechanism for the behavior based on a structural disintegration which would be cumulative with cycling.

A careful study of Figs. 18 to 21 reveals that the strain softening is more pronounced for higher strain amplitudes (greater ΔT) indicating that the effect might be due to annealing resulting from the high-temperature portion of the cycling. To verify this possibility, specimens were prepared and strain-cycled manually at room temperature. The Rockwell B hardness of

[5] Defined as the pitch angle of an originally straight, longitudinally directed line on the tube after twisting.
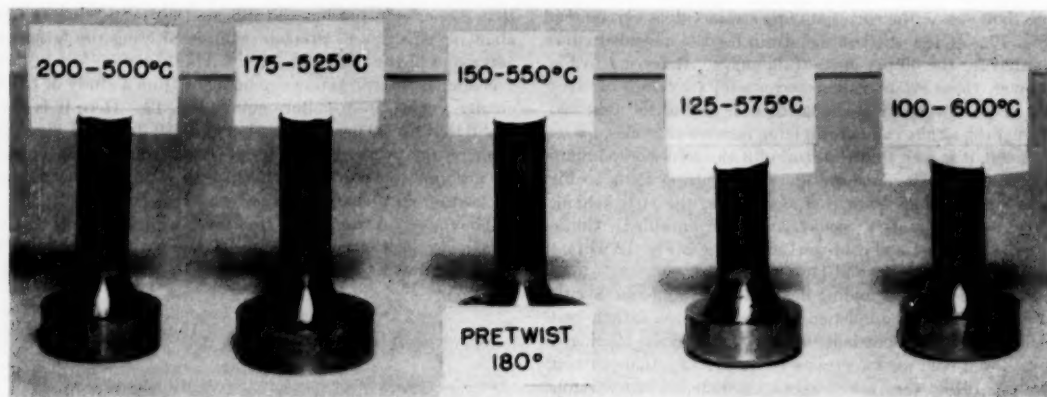
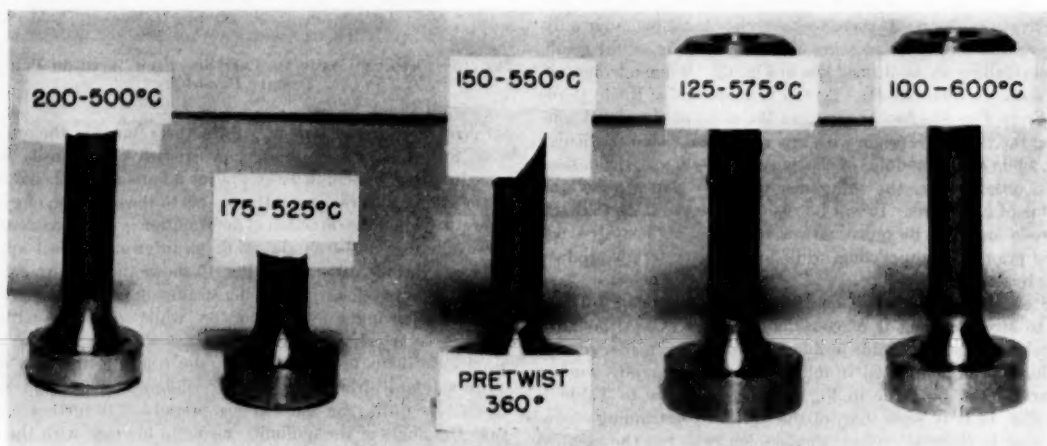FIG. 16   EFFECT OF TEMPERATURE CHANGE ON DIRECTION OF FRACTURE PLANE FOR 180-DEG PRETWIST

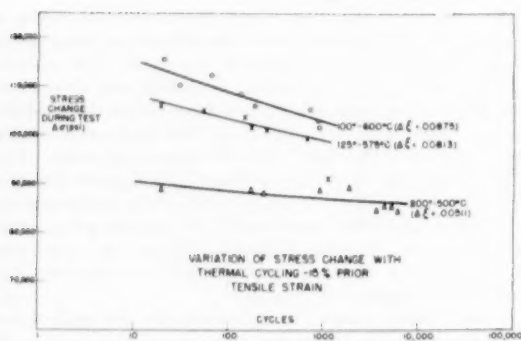FIG. 17   EFFECT OF TEMPERATURE CHANGE ON DIRECTION OF FRACTURE PLANE FOR 360-DEG PRETWIST

FIG. 18   VARIATION OF STRESS CHANGE WITH THERMAL CYCLING—
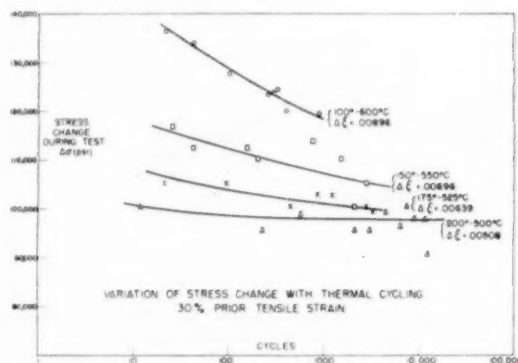15 PER CENT PRIOR TENSILE STRAIN

FIG. 19   VARIATION OF STRESS CHANGE WITH THERMAL CYCLING—
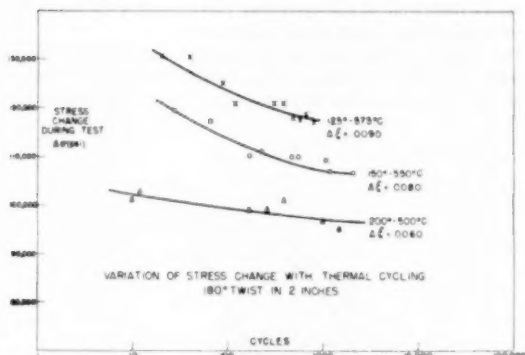30 PER CENT PRIOR TENSILE STRAIN

FIG. 20 VARIATION OF STRESS CHANGE WITH THERMAL CYCLING—180-DEG TWIST IN 2 IN.

FIG. 21 VARIATION OF STRAIN HARDENING WITH THERMAL CYCLING—360-DEG TWIST IN 2 IN.

the material was measured before each cycle of strain. Two specimens were strain-cycled in the annealed state while two other specimens were cycled following a 40 per cent tensile prestrain. Results are shown in Fig. 22. Strain amplitudes here are somewhat larger than those of the thermally cycled specimens, but the effect appears to be similar. It is seen that annealed specimens exhibit a progressive hardening with strain cycles, which appears to saturate with an increase in cycles of strain. Further, the rate of increase depends on the strain amplitude. However, in cold-worked specimens, the hardness decreases with a leveling off as the number of cycles of strain becomes large. The early rise followed by a leveling off and then a decrease exhibited by one of the cold-worked specimens is attributed to inaccuracies in measurement. It can be concluded that strain softening is a real effect.

Effect of Mean Temperature on Thermal-Stress Cycling. A series of tests was undertaken to investigate the effect of mean temperature in the cyclic thermal-stress problem. This corresponds approximately to the effect of temperature in conventional fatigue testing. In the present study, several specimens were tested at mean temperature $(T_1 + T_2)/2$, of 250 C, 350 C, and 450 C, while the temperature change $\Delta T = T_2 - T_1$ was maintained at about 300 deg C. Because of the slight nonlinearity of the coefficient of thermal expansion with temperature, the strain amplitude $\Delta\epsilon$ corresponding to a 300-deg C temperature change was greater when the mean temperature was 450 C than when it was 250 C. Since the strain change rather than the temperature was the important quantity, a slight adjustment in the temperature change was necessary to maintain a constant strain amplitude as the mean temperature was altered.

Fig. 23 gives the results of this study. It is seen that a marked decrease in cycles for failure occurs as the mean temperature increases. This decrease in fatigue resistance is similar to that found for constant temperature fatigue tests performed at high temperature.[6]

No significant difference was noted in the average stress change per cycle as a function of mean temperature. One might expect that with a higher mean temperature the lowered flow stress would decrease the stress change; however, another factor tends to compensate for this decrease in stress. With the higher temperature, the reduced flow stress of the material permits, for a particular strain change per cycle, a larger inelastic component. This increased inelastic strain leads to a slightly greater strain hardening with cycling as illustrated earlier in Fig. 13. Hence, the net stress change is not affected. For example, the stress change for a particular specimen is compared at 20 cycles and at
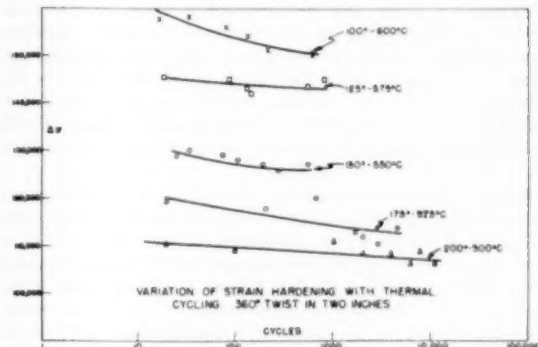
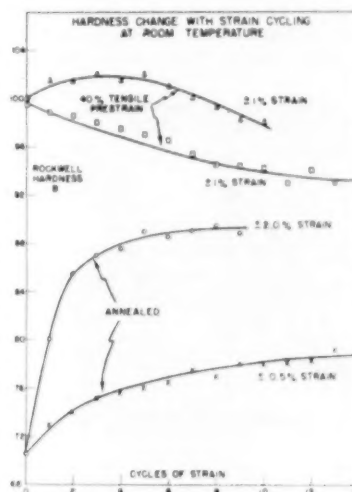[6] Reference (3); reference (4), appendix 5, p. 117.

FIG. 22 HARDNESS CHANGE WITH STRAIN CYCLING AT ROOM TEMPERATURE
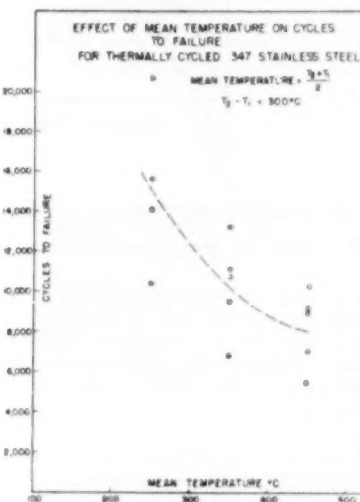
FIG. 23 EFFECT OF MEAN TEMPERATURE ON CYCLES-TO-FAILURE FOR THERMALLY CYCLED NO. 347 STAINLESS STEEL

1000 cycles of strain, and the difference is calculated. This difference in stress change is a measure of the strain hardening during the test. With increasing mean temperature, the average strain hardening increases from 6150 psi to 9280 psi. At the same time, the average stress change at 20 cycles decreases from 56,230 psi to 53,880 psi, while the average stress change at 1000 cycles remains essentially constant. Consequently, the effect in question appears to be operating.

Effect of Clamping on Cycles-to-Failure. A problem which arose in the cyclic thermal-stress tests was the effect of clamping on the life of the specimen. Two series of tests were undertaken in which (a) the specimens were clamped at 200 C and cycled between 200 and 500 C, and (b) specimens were clamped at 500 C and cycled between the same temperature limits. In the former, the initial loading on the specimen was compressive, while in the latter this initial loading was tensile. Thus, as seen in Fig. 24 (a), the specimen clamped at 200 C is cycled between stress values in which the compressive stress at 2 is larger in magnitude than the tension stress at 1. The reverse is true for the specimen clamped at 500 C as seen in Fig. 24 (b). Consequently, a variation in life is possible in view of these differences in sign despite the fact

EFFECT OF CLAMPING ON HYSTERESIS LOOP

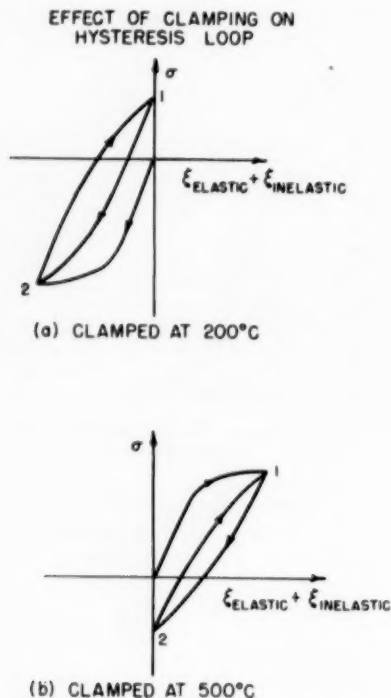

(a) CLAMPED AT 200°C

(b) CLAMPED AT 500°C

FIG. 24   EFFECT OF CLAMPING ON HYSTERESIS LOOP

that the stress change in each cycle is the same. The results of six tests carried out on each mode of testing reveal that when clamping occurred at 200 C, an average of 10,620 cycles was required for failure, while at 500 C, 10,000 cycles resulted in failure. From the agreement of the average values, it would appear that the difference between the two clamping procedures is negligible.

Effect of "Hold Time" on Cycles-to-Failure. A problem of considerable practical interest is the importance of the period of cycling in the thermal-stress-fatigue process. To investigate this, a program was undertaken in which the high and low-temperature hold time of the cycle was varied over wide limits while fixed temperature limits were maintained.

The results of this type of test might be anticipated by considering the effect of various hold times on the stress-strain cycle behavior. Fig. 25 shows this stress-strain hysteresis loop. For a
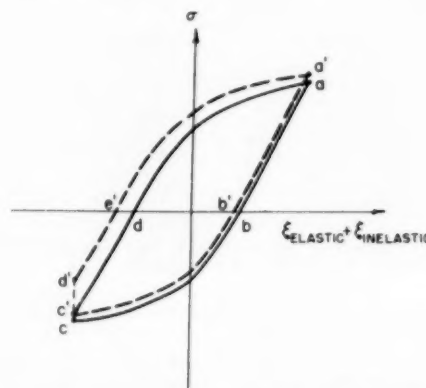

FIG. 25   HYSTERESIS LOOP FOR THERMAL-STRESS CYCLING WITH AND WITHOUT "HOLD TIMES" AT a AND c

rapid cycle (hold time = 0) the path is a-b-c-d. Point a is reached at the low temperature, while Point c is reached at the high temperature of the cycle.

If the specimen is now held for some time at the low temperature, the stress at Point a will relax very little since this is the low-temperature point in the cycle and creep relaxation depends exponentially on temperature. When held at the high temperature, however, a reduction in stress takes place with time. The new cycle then becomes a'-b'-c'-d'-e'. It can be seen that, although the strain change per cycle remains constant, the inelastic strain increases at the expense of the elastic strain. This increase is

$$\frac{\sigma_{e'} - \sigma_{d'}}{E}$$

where E is the modulus of elasticity and $\sigma_{c'} - \sigma_{d'}$ is the decrease in stress at c' resulting from relaxation. This additional inelastic strain is compressive; the same amount of additional tensile inelastic strain occurs along the path $d'-e'-a'$, since the net inelastic strain per cycle is zero. (Otherwise continuous growth or shortening of the tube would occur.)

Thus it appears that the greater the hold time, the greater the relaxation and the larger the inelastic strain change. Consequently, with longer hold times, failure by fatigue would be expected in fewer cycles.

The results obtained for this study are shown in Fig. 26 in which the cycles-to-failure are plotted against the hold time. Hold times used were 6, 18, 60, and 180 sec. The spread in test results for each hold time is quite wide because of such factors as uniformity of specimens, surface roughness, and accuracy of temperature measurements. There is also inherent scatter caused by internal effects in the fatigue process.

A precise interpretation of the test results given in Fig. 26 is difficult. A slight downward trend in fatigue life is observed with increasing hold time as predicted. However, it is observed that the data indicate a minimum in cycles-to-failure at a 60-sec hold time. Whether this is a real effect is uncertain.

From a practical point of view, the decrease in cycles-to-failure with increased hold times in the present tests is small. If the life of the part based on the elapsed time required for failure is
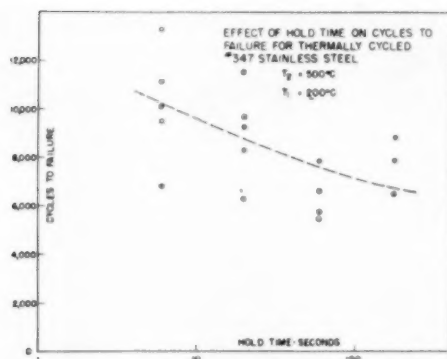
FIG. 26   EFFECT OF HOLD TIME ON CYCLES-TO-FAILURE FOR THER-
MALLY CYCLED NO. 347 STAINLESS STEEL

computed rather than cycles as in Fig. 27, it can be seen that this time increases with increased hold time. For example, extrapolating the data to a specimen with a hold time of 12 hr, failure after an elapsed time of 5200 days (14.2 years) will occur, other conditions of the test being equal.

With the exception of this present study on which the hold time was varied, the other studies considered in this report were carried out at a constant hold time of approximately 6 sec.

Effect of Prior Strain Cycling on Stress-Strain Characteristics. A study of the effect of prior thermal strain-cycling on the structural characteristics of annealed Type 347 stainless steel was undertaken to gain some information on the nature of fatigue damage. In this investigation, specimens were strain-cycled be-

tween 200 and 500 C for 2000 to 10,000 repetitions in 2000-cycle intervals. Following this, true stress-strain tests were carried out to observe structural changes in the material resulting from the previous cycling. For example, such a test would bring out clearly the progressive deterioration of the polycrystalline structure, or brittleness, or presence of fatigue cracks, should any of these possible modes of failure of the strength of the material occur progressively with strain cycling.

Fig. 28 shows some typical true stress-strain curves obtained after thermal-stress cycling. The test results may be summarized as follows. The general effect of prior strain cycling is to produce a small crack or several small cracks in the tube. These cracks act to cause premature failure by serving as stress raisers. Otherwise, the ductility of the material appears to be unimpaired. Another effect of the strain cycling is to cause a small elevation
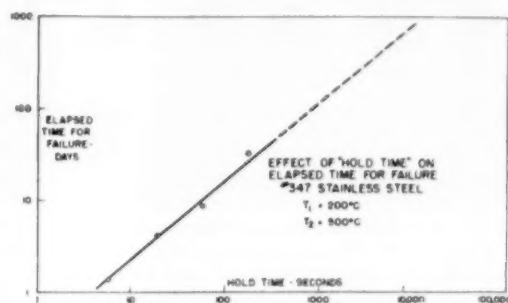

FIG. 27   EFFECT OF HOLD TIME ON ELAPSED TIME FOR FAILURE
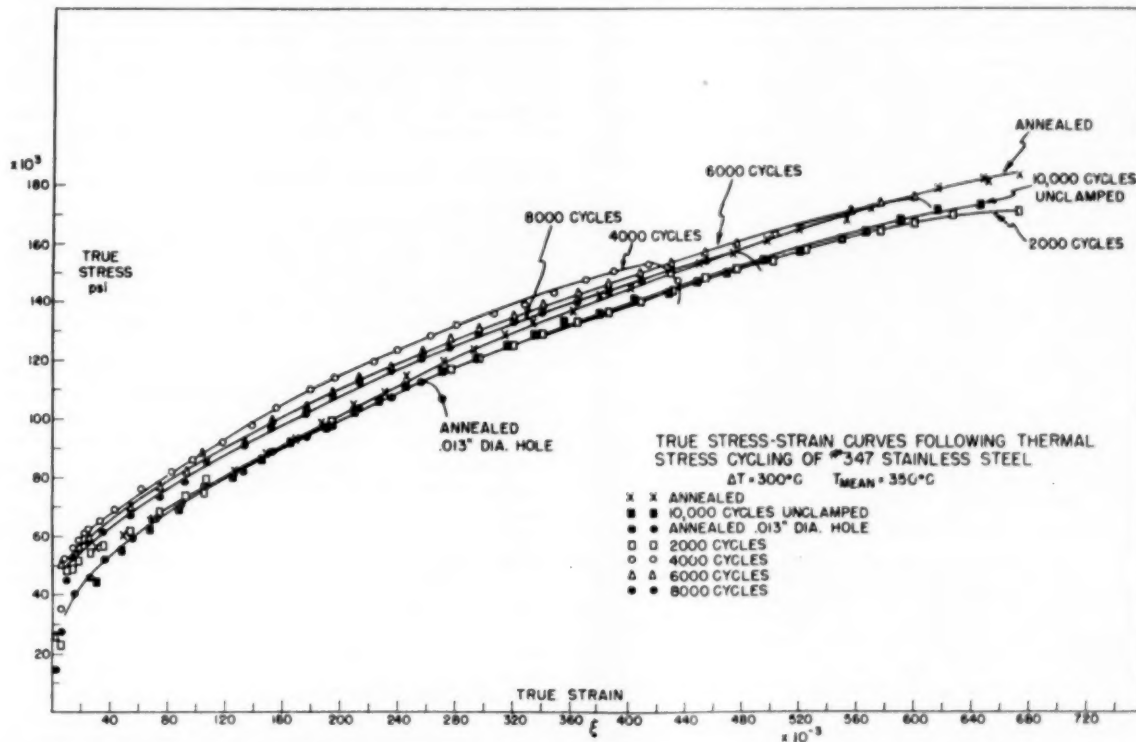OF NO. 347 STAINLESS STEEL

FIG. 28   TRUE STRESS-STRAIN CURVES FOLLOWING THERMAL-STRESS CYCLING OF NO. 347 STAINLESS STEEL
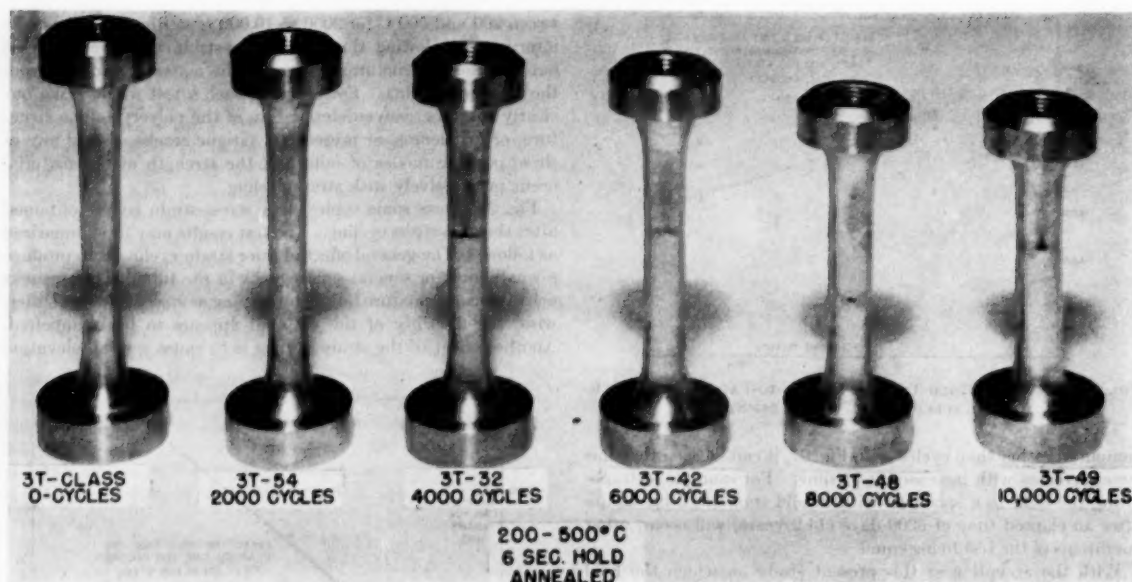
FIG. 29 CHARACTERISTIC TENSION FRACTURES FOR TUBULAR SPECIMENS OF TYPE 347 STAINLESS STEEL
WITH PRIOR THERMAL-STRESS CYCLING

in the stress-strain curve. This is consistent with the strain-hardening behavior as indicated in Fig. 7. As seen in Fig. 28 (for selected specimens), the larger the number of prior strain cycles, the less the strain value at which the fatigue crack causes an instability in the tensile loading and results in specimen failure. It would appear that these fatigue cracks occur quite early in the cyclic history, and with subsequent cycling these cracks grow and new cracks are formed. Consequently, the damaging effect from the cracks increases. Fig. 29 shows the same typical test specimens tested in tension following thermal strain cycling of from 0 to 10,000 cycles. The effect of the crack in causing a tearing of the tube wall can be seen in this photograph.

There is considerable evidence supporting the point of view that the crack was present in the specimens prior to static testing. First, in specimens tested to 10,000 cycles, a careful examination of the surface of the specimen usually shows some of these cracks. Subsequent tension testing causes these cracks to open up and become the direct cause of premature failure. A second, less direct proof comes from the test of a specimen with a 13-mil hole drilled radially through the tube wall at the midpoint of the specimen. The stress-strain curve for this test is shown in Fig. 28. The shape of the curve is exactly the same as the curve of the specimens with prior stress cycling. Further, there is no significant difference between this stress-strain curve and that of the homogeneous specimen, except for the fact that premature failure of the specimen occurs. This is manifested by a rapid drop in specimen load as tearing takes place from opposite edges of the hole.

It is concluded from these tests that fatigue cycling has little effect on the material properties except for a slight strain hardening of the metal. However, in a few isolated regions throughout the volume of the test specimen fatigue cracks nucleate and grow. Growth of these cracks progresses and new cracks appear with further cycling. From a structural point of view the gross volume of the material is not altered appreciably.

There is considerable experimental evidence that the bulk material is not greatly affected (in so far as its structural proper-ties are concerned). When a specimen has been severely strained in the tension test to the point that the cracks formed by the prior cycling begin to open up and grow, failure does not occur by a sudden propagation of the crack in a brittle fashion, but rather by a tearing action from the edges of the crack and a corresponding decrease in load. Thus the bulk material which has been strained heavily in the tension test has sufficient ductility to require that additional plastic-strain energy be expended by the material in order that the crack spread. This tearing action and the corresponding controlled decrease in specimen load are in contrast to the fracture of a specimen without prior cycling, where at the critical point failure is sudden and the crack is generated extremely rapidly.

Another factor indicating that prior cycling does not produce an appreciable effect on the bulk structural properties of the material is the considerable scatter in the fracture ductility. This is seen in Fig. 30 in which the fracture ductility is defined as the true strain at which the fatigue crack begins to grow by
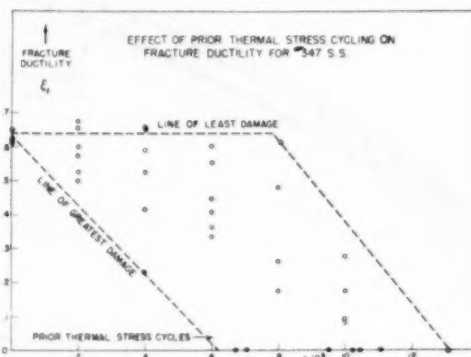

FIG. 30 EFFECT OF PRIOR THERMAL-STRESS CYCLING ON FRACTURE
DUCTILITY FOR NO. 347 STAINLESS STEEL

tearing with a simultaneous decrease in specimen load. For example, in Fig. 30 the fracture strain following 8000 repetitions of reversed thermal stress varies from zero to that corresponding to an annealed specimen without stress cycling. Thus some specimens are unaltered structurally (as determined by fracture ductility) while others are completely severed through the appearance and propagation of fatigue cracks. Only variations from specimen to specimen in the cycles required for the nucleation and growth of fatigue cracks could be responsible for these large differences in ductility.

The wide scatter found for this method of detecting fatigue cracks can be interpreted, from the point of view of engineering design, as follows. First, an upper and lower bound on the data can be drawn. These are referred to as lines of least and greatest damage. It is noted that the line of least damage is horizontal from 0 to about 8000 cycles (for these specimens no fatigue crack of any effective size is present). For further cycles, the line of least damage decreases rapidly until at 13,000 cycles it corresponds to a fracture ductility of zero. In this region the probability is that all specimens will have developed cracks and these become more severe with further cycling. Finally, at 13,000 cycles the probability approaches unity that all specimens will have failed by fatigue. The line of greatest damage, on the other hand, is observed to decrease linearly until at about 6000 cycles complete failure by fatigue will have occurred, indicating that cracks can occur in this range of cycling which will lower the ductility, the severity increasing with the number of cycles. Beyond 6000 cycles there is a finite probability that a complete fatigue failure can occur.

From the point of view of conservative design, the line of greatest damage is quite important since it indicates the lowest value of ductility which is finitely probable after thermal-stress cycling. In picking the point on this curve for intelligent design, it must be determined how important ductility (and crack propagation) is during and at the completion of the expected number of cycles. As an example, if 50 per cent of the ductility of the part in question must remain after this particular thermal-stress cycling, then some 3100 cycles under these test conditions can be absorbed by the part.

REVIEW OF PREVIOUS WORK

The method of studying the fatigue problem employed in the present report appears to be quite unique. However, since the results obtained are closely related to the general problem of fatigue, a detailed study of the pertinent literature is desirable.

Considerable experimentation has been carried out on the problem of fatigue in metals from an engineering point of view, and the literature on the subject is vast. The fundamental aspects of the problem also have been studied by several investigators but have received much less attention. Since this phase of the problem is pertinent here, some of the fundamental work will be reviewed in this section and will be compared with the results of the present investigations in the following section.

The fatigue problem in metals has been recognized for some time as being closely related to the problem of slip and plastic flow under static loading. The first study of the change in microstructure under cyclic-stress conditions was probably that of Ewing and Humpfrey (7). From their observations the "attrition" theory of fatigue was developed. Stanton and Bairstow (8) performed a similar investigation on iron and steel and interpreted their results in essentially the same manner. The attrition theory explains failure in metals by fatigue and a process of repeated sliding on the same slip band. This action results in an abrasion of the slip band, and the debris or attrited matter is forced to the surface. Consequently, a crack is formed on this plane which gradually spreads and leads to ultimate failure.

Such a theory requires that fatigue failure occur when the applied cyclic stress produces slip. Other investigators have not found this to be true. The work of Gough and Hansen (9) on the changes in microstructure in iron, steel, and copper under cyclic stresses showed that plastic deformation (slip) was found for cyclic stresses which did not lead to fatigue failure, as well as in those cases when fracture resulted. It was observed, however, that the fatigue crack was initiated in the region of slip. Hysteresis loops were noted in all cases and, although their magnitude changed with cycling, their existence was fundamental to the cycling process. It was found that regions of slip gradually increased with the number of repetitions of stress. This was true regardless of whether the applied stress was above or below the safe stress (that stress which would not produce a fatigue failure for an indefinite number of cycles). The process whereby regions of slip grow with further cycling was interpreted as being due to the hardening of particular planes following their slip, so that the deformation was then transferred to other slip planes. Failure was then regarded as the point at which some critical strain was reached.

Later studies by Gough and his co-workers (10) on single and multicrystalline metals under repeated cyclic stress indicated that the deformation process occurred in the same manner as for monotonic loading. It was found that the same slip planes and slip directions were operative for both cases. No basic difference in the characteristics of deformation and failure was observed in single and multicrystalline metals. Differences in degree, associated with grain boundaries which act to inhibit slip and influence the rate of propagation of fatigue cracks, did occur, however. The gradual growth of slip bands and the accompanying strain hardening with cycling was noted. For metals with stresses below that necessary to produce a fatigue crack, a limit to strain hardening was observed, while for specimens with stresses higher than the safe limit, new slip bands appeared even when fatigue cracks had occurred.

Gough concluded from these studies that the crystal as a whole did not attain a maximum value of strain hardening with cyclic stressing but rather hardened in certain local regions. It was argued that because of the local nonuniformity in strain, regions existed in which the strain might be higher by orders of magnitude than elsewhere. Thus rupture could occur in these regions when the lattice strain of the atomic bonds exceeded a critical value. The crack so produced would set up further high local strains at its edges and thus propagate itself by this mechanism.

Strain hysteresis with reversed cyclic stresses is quite well known (11). It has been shown (12) that the effect is present in the case of single crystals of aluminum as well as in polycrystalline metals. Because of the strain-hardening effects accompanying reversed stress cycling, the hysteresis loop will diminish in size with time. However, as pointed out previously, even up to the point where fatigue cracks occur, the loop is still present. Gough (13) has explained this behavior on the basis of a substructure or crystallites formed in the structure by cold work. With such a breakup in the crystal structure, atoms separating the crystallites are assumed to have alternative positions of stability. Under stress these atoms move to these new positions, thereby accounting for the strain-hysteresis effects observed.

An earlier interpretation of the hysteresis in metals with cyclic stresses was made by Rosenhain (14). Noting that slip bands were present when such effects were found, he attributed the behavior to a viscous behavior, as if the material within these slip bands had an amorphous structure with corresponding viscosity and mechanical properties. Zener (15) has suggested that this theory is not unlike one currently held, that hysteresis results from partial mobility of dislocations introduced by deformation.

The Bauschinger effect (2), another phenomenon closely related to hysteresis, is important in reversed cyclic stressing. The common interpretation of this effect is as follows: Because of anisotropy between the crystals in a polycrystalline structure when a stress sufficient to produce plastic flow is released, residual stresses are introduced between crystals. Upon reversed stress, certain grains are overloaded and flow with less applied stress than had the loading first been in that direction. Based on tests of Sachs and Shoji (16), in which the Bauschinger effect was found to be as marked for single crystals as in polycrystalline specimens, Zener (17) suggests that microscopic residual stresses associated with individual slip bands are responsible for the effect. Schwartzbart, Jones, and Brown (18) found a substantial Bauschinger effect in polycrystalline copper where all the crystals were aligned in the same direction (cubically aligned). Here, because of the preferential alignment, one would expect little residual stress between grains upon unloading following plastic deformation, so that the Bauschinger effect could only be attributed to residual stresses within each crystal.

The removal of hysteresis effects in strain-aging metals is well known (19). The Bauschinger effect also can be removed by aging (20). The mechanism by which both of these effects can take place has been studied by Corten and Elsesser (21), who conclude that a process similar to the Cottrell mechanism (22, 23) is responsible. Here impurity atoms such as carbon or nitrogen can diffuse to dislocations to reduce the potential energy in that region and lock the dislocations in place.

Ludwik (24) has carried out some experiments on stress cycling of metals, the results of which are quite pertinent to the present discussion. Torsion tests on copper and aluminum were performed monotonically, by cycling between zero and full stress and by completely reversed stress cycling. It was observed that deformation with each cycle (0 to full stress) following cold working decreased when the applied cyclic torque was less in value than the previous cold-working torque, whereas the deformation per cycle increased when the cyclic torque was larger than the previous monotonically applied torque.

Further, monotonic torsion tests following reversed cycling of varying amounts were fairly independent of the number of prior cycles, but the amount of fracture ductility was decreased with an increasing number of cycles. He attributed the foregoing results to a "structural loosening" brought about by reversed slip which causes a gradual "dissolving of molecular bonding."

Ewald and Polanyi (25) showed that rock salt did not strain-harden when subjected to reversed plastic bending. They concluded that reversed deformation neutralized the hardening produced by deformation of opposite direction.

Lui, Lynch, Ripling, and Sachs (26) have studied the effect of large reversed strain cycles on fatigue and on retained ductility of 24S-T aluminum alloy. For the most part, the strain amplitudes were considerably larger than reported here. A progressive decrease in fracture stress and retained ductility was noted with an increasing number of cycles and cyclic strain, while the cyclic stress-strain curve of the material did not change appreciably.

The results were interpreted as being due to two opposing processes—continuously increasing cold work with strain amplitude and cycles, balanced by structural deterioration.

Theories of fatigue have been developed by several authors. A mechanism for fatigue failure was suggested by Gough (10) and interpreted quantitatively by Orowan (27) on the basis of the flow curve for the material in question. Dehlinger (28) has proposed that the nonuniformity of structure found in a polycrystalline metal causes internal stresses when the metal is deformed and these can cause cracks to form. Machlin (29) assumes a distribution of microcracks (on an atomic scale) such

that under reversed stress, dislocations move from these cracks so as to permit growth of the cracks and eventual failure.

Several experimenters have considered the effect of prior fatigue cycling on subsequent mechanical properties. The so-called "damage line (30) is a manifestation of change of properties with prior fatigue cycling. Investigators (31, 32) have found a removal of the yield point in mild steel by prior cycling below the endurance limit, comparable to a small percentage of cold work. However, the effect in some cases is very small. Memmler and Laute (33) found that as the cyclic stress was increased above the endurance limit, the elongation was reduced and the stress-strain curve was raised. However, the reduction in area was not affected. It is significant, in view of the fact that the reduction in area is felt to be a better measure of ductility than the per cent elongation, that the overstressing did not appreciably alter this ductility measurement. Impact tests by Kies and Holshouser (34) on SAE X-4130 steel showed that there was no loss in impact strength from understressing, but a loss in impact strength accompanied by fatigue cracks upon overstressing. On the other hand, MacGregor and Grossman (35) have found a marked increase in brittle transition temperature in notched mild-steel specimens given prior stress cycling both below and above the endurance limit. Later Lessells and Jacques (36), in similar tests, found that fatigue cracks developed in such notched specimens and that these cracks propagated below as well as above the endurance limit for low-carbon steel. It was found that when the stress was reduced to 40 per cent of the endurance limit, cracks no longer occurred and virtually no change in the transition temperature was found.

DISCUSSION OF RESULTS

Experimental Results of Fundamental Significance. The type of test carried out here represents a definite departure from test techniques generally employed in fundamental studies of fatigue. The application of stress is unidirectional and statically determinate, in common with many basic investigations. However, because of the cyclic temperature, the test becomes somewhat more complicated than studies employing a constant temperature. It should be expected for the material and temperatures studied, however, that the difference in results should be in degree rather than kind for most metals. Large differences might be expected in cases in which a phase change is indicated in the range of temperature cycling, where the metal is metastable and a second phase might form, where marked strain-aging effects might occur, or where the crystal structure is such that a marked anisotropy in thermal expansion coefficients with orientation exits (37, 38, 39). This last effect seems to occur only in noncubic structures. Except for the possibility of some transformation of gamma iron to alpha iron with extreme cold work, none of the foregoing effects can occur for Type 347 stainless steel. It appears then that temperature cycling has only a secondary effect on the fundamental aspects of the problem. An additional proof of this is the true stress-strain characteristic of annealed Type 347 stainless steel after 10,000 temperature cycles between 200 and 500 C without longitudinal constraint. Fig. 28 compares these data with those of the annealed specimen without cycling. The difference is found to be that attributable only to experimental error.

A careful study of the experimental results obtained in the present report reveals several facts which are pertinent to the fatigue problem. These results in general seem to be in agreement with those of other experimenters as reported in the previous section. The first is, that for an annealed material the strain hardening is comparatively slight and tends to saturate, although a reasonable amount of inelastic strain occurs with each half cycle of loading. This is seen in Figs. 7 and 8. As a corollary to

this, the amount of strain hardening increases with increasing strain amplitude, but the rise is slight and saturation always occurs.

It is apparent that the hysteresis loop remains quite large for a particular reversed cyclic condition. As a consequence, a large amount of energy must be fed into the metal with each cycle and dissipated in the form of heat. The ability of the material to continue this process for thousands of cycles presents an interesting problem.

The effect of cyclic straining on the various physical, structural, and mechanical properties is of considerable interest. The program to date has included only the consideration of mechanical effects. It is found in Fig. 28 that the general ability of the material to resist stress (as measured by the flow curve) is not appreciably affected. It is shown in Fig. 30 that the fracture ductility is decreased, this being due, not to a loss in resistance to deformation generally, but to a few local fatigue cracks which have appeared in the structure.

Coupled with these observations is the strain-softening phenomenon which occurs when the material has been given a prior strain. This effect is seen in Figs. 18 through 21. Again a saturation of the behavior is found. This saturation would tend to refute any explanation of the effect in terms of a structural breakdown (24, 26). As yet, a study of the change in mechanical properties resulting from cyclic loading has not been completed for the cold-worked state of the material. However, preliminary results do indicate that there is no appreciable difference in the shape of the stress-strain curve of a heavily cold-worked specimen before and after cycling 800 times between 100 and 600 C with longitudinal constraint.

The test results indicate that the amount of prior cold work plays an important role in the life-to-failure. It is seen that with the type of cycling performed, for the same number of cycles the effect of cold work is such as to increase the strain change needed to develop fatigue failure when these strain changes are small, but to decrease the strain change required at high strains. It was seen that when the data were interpreted in terms of stress changes, the effect was such that prior cold work always increased the stress change required to produce failure in a certain number of cycles. Here then is an important distinction between fatigue resulting from cyclic thermal conditions and that resulting from cyclic stresses. Cold work can be detrimental or beneficial to the life of the material, depending on whether the strain or the stress is the independent variable in the particular application when the cyclic loading is severe.

From the tests at hand, the concept of plastic flow[7] may be developed by defining a quantity called the total plastic strain. This is found by adding up the entire plastic strain absorbed by the specimen to failure, regardless of sign. This is done for annealed and cold-worked metal subjected to different strain amplitudes and is included as Fig. 31. It will be seen immediately that the total plastic strain absorbed for a particular number of cycles-to-failure is reduced as the amount of prior cold work is increased.

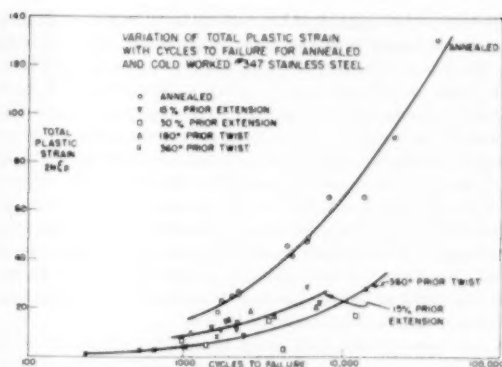Another interesting aspect of the results given in Fig. 31 is

FIG. 31 VARIATION OF TOTAL PLASTIC STRAIN WITH CYCLES-TO-FAILURE FOR ANNEALED AND COLD-WORKED NO. 347 STAINLESS STEEL

the fact that the total plastic strain increases with increasing slope when plotted against the logarithm of the cycles-to-failure. Thus, as the severity of the cyclic strain becomes less, the plastic strain per half cycle correspondingly decreases, but the total plastic strain absorbed prior to failure increases. Extrapolating the data for a large number of cycles, the total plastic strain capable of being absorbed by the metal appears to approach infinity.

A Mechanism for Strain Cycling. These various effects studied here have been observed in part by other investigators as reviewed in the previous section. Before a complete understanding of the fatigue problem can be reached, these effects as well as others not considered here must be satisfactorily explained. An attempt is made in the present report by postulating a tentative mechanism in terms of the widely accepted dislocation theory (41).

By this mechanism it is assumed that under the action of stresses sufficient to produce plastic flow, dislocations present in the crystal and those generated by the flow process move until they are blocked by some boundary or imperfection in the structure. Here they begin to pile up so that their density in this region increases, as does the local residual stress and resulting internal energy of the structure. When the stress direction is reversed, these dislocations can be moved readily because of the benefit of the residual stress set up by the prior stress directions. This is in accord with the ideas of Zener (15). As a result, observable plastic flow will occur fairly early in the reverse loading process as the dislocations move away from the barrier. As the reversed stress increases, the dislocations continue to move until a new barrier is met on the opposite end of their path; then the dislocations again begin to pile up and set up a region of high local internal energy. The general behavior of the dislocation reversal accounts for the commonly observed Bauschinger effect.

As the stress again changes direction, the process likewise reverses itself. In the steady state the dislocations can be thought of as moving back and forth from boundary to boundary, so that with each stress reversal the structure responds elastically and then plastically as the dislocation concentration begins to move from one barrier to the other. This process may be responsible for the hysteresis loop which is always found under conditions of cyclic stress. The energy which is fed into this loop is that required to generate the dislocations and to move them back and forth across the crystal from barrier to barrier, being continuously dissipated into the lattice as thermal vibration.

---

[7] In the present paper the inelastic behavior is principally considered to be a result of slip within the crystals of the metal. Other deformations such as twinning and viscous grain-boundary flow are small for this material at the temperatures employed. Anelastic effects (40) (recoverable inelastic strain) could account for a portion of the inelastic behavior during cyclic thermal straining, particularly when the strain changes are small. However, they become negligible, on the basis of data in reference (40), when the strain changes are of the order of 1 per cent. In the absence of viscous grain boundary effects, and keeping in mind the possibility of some anelasticity, the inelastic behavior found in cyclic loading in the present tests is termed plastic, a term generally reserved for completely permanent deformation.

The mechanism suggested here seems to be in accord with the observations found here and also reported by other investigators. By this mechanism, reversed plastic flow can occur without gross strain hardening and structural disordering. Actually the process could not be expected to be completely reversible,[a] particularly in the early cycles, because certain dislocations pass by some barrier, or might be annihilated, or might be too rigidly tied down after some motion to reverse their direction. Eventually a steady-state condition for this process is approached and further strain hardening becomes negligible. With large strain amplitudes in which many more dislocations are generated and moved, the degree of irreversibility would be higher. In such cases the level of strain hardening, reached as a steady-state condition is approached, would be higher.

In the case of cold work prior to strain cycling, where the strain-softening phenomenon is observed, considerable more stress would be required to move the dislocations because of the severe lattice distortion. With the severe lattice strain, a considerable amount of internal strain energy is absorbed in the lattice and at the grain boundaries. By the movement of dislocations from boundary to boundary, regions of distortion and high energy resulting from the cold work may be reduced in severity to permit an easier movement of the dislocations. A crude analogy to the process is the settling of gravel by vibration. The agitation to the lattice by the reversed motion of dislocations serves advantageously as the energy-minimizing process, just as the relative motion of the gravel during shaking causes a better packing and lowering energy.

The gradual growth of slip planes with increasing cycles of strain as observed microscopically by many investigators is consistent with the picture given here. Because of the irreversibility of the process, planes undergoing reversal will increase their resistance and other planes may then become active, tending to widen the slip area in conformity with observations from photomicrographs. The actual strain hardening, however, may not be too marked since it is presumed that there are many planes available for the process of reversal slip as pictured here, and little difference in stress from plane to plane is required to initiate the action.

The removal of the Bauschinger effect by strain aging as discussed above (19, 20, 21) is in agreement with the mechanism of dislocation cycling. When a previous stress has caused the dislocations to pile up at one barrier, a strain-aging heat-treatment can cause foreign atoms to diffuse to the dislocations and, by the Cottrell mechanism, interfere with their further motion. Thus, upon stress reversal a higher stress is required to start them in motion, resulting in reduction or elimination of the Bauschinger effect.

Fatigue-Crack Formation. The initiation of the fatigue crack is considerably more speculative. By the mechanism described here, there should be no limit to the number of times that the dislocations can flow from barrier to barrier, provided the process is reversible. As has been pointed out, it does not seem likely that complete reversibility would occur, even under very favorable conditions. Further, the degree of irreversibility would depend on the severity of the strain. Generally, certain regions in the structure would be under more severe strain than elsewhere so that the effects would vary quite markedly throughout each crystal. The irreversibility of the dislocation oscillation might be brought about by the interference of several dislocations or by some other process tending to disturb the ordered structure in the path of the oscillation discussed above. As this occurs, more stress is required for reversed slip and the process then spreads to neighboring planes (which would require this higher

stress for slip). Gradually the region of dislocation reversal grows. Within this region the fatigue crack is formed. The mechanism for the crack formation is not clear. Perhaps it is due to a running together of dislocations as they are halted at the barriers. It seems clear that, whatever the mechanism, it is closely related to the reversed dislocation motion.

A mechanism for the formation of a fatigue crack was proposed by Gough (10) and developed quantitatively by Orowan (27). By that mechanism, failure is considered to be a result of a reversal in strain at points of concentration. This produces local strain hardening and consequently increases the local stress until some critical stress to produce fracture is exceeded, resulting in a microcrack.

If the initiation of a fatigue crack was a result of the limit of local strain hardening in a metal, the observation of strain softening, as reported here and elsewhere, when cold-worked specimens are strain-cycled seems difficult to explain. One would expect, from the strain-hardening hypothesis, that reversed strain could further harden the slip planes, which would be partially compensated for by a thermal-softening process. It is difficult to see how a thermal-softening process would make a cold-worked metal softer with the addition of further strain cycling than it would have been had no additional strain been added.

Another observation of the present report, namely, the effect of prior strain cycling on the true stress-strain properties of the material seems inconsistent with the strain-hardening concept. With the amount of total plastic strain absorbed cyclically by the metal, as high as 100 to 120 in/in., on the basis of a strain-hardening hypothesis, one would expect a marked effect on stress-strain characteristics. The observation that the general stress-strain characteristics are only slightly altered (except for a reduction in ductility when a fatigue crack is present) would indicate that strain hardening is not the dominant factor in the fatigue process.

The interpretation of the tests of Lui, Lynch, Ripling, and Sachs (26) is not in accord with the present view. The mechanism whereby strain hardening is balanced by structural deterioration with strain cycling does not fit the facts of the present experiments. However, these tests were performed using quite large strain amplitudes and this may have obscured an interpretation which would be similar to that given here. The fact that specimens can absorb up to 8000 cycles of thermal strain without altering particularly the fracture ductility and fracture stress, Fig. 30, is ample evidence that structural damage has not occurred. The ductility exhibited by the tearing action of fatigue cracks when test specimens are pulled in tension is further proof. The asymptotic character of the strain-hardening curves of Figs. 18 to 21 does not indicate the progressive structural deterioration hypothesized by Lui, Lynch, Ripling, and Sachs.

It is well known that prior cold work causes a distinct disordering of the lattice. This disordering acts to inhibit dislocation motion when the cold-worked specimen is subjected to reversed stress cycling. As a result, the stress change per cycle, Fig. 13, increases for the same strain amplitude. It would appear reasonable that, when the stress is sufficiently severe to produce dislocation cycling, the process leads to the formation of a fatigue crack sooner, other conditions being equal, since with the greater disorder there would be more sites present to act as sources for the formation of these cracks. On the other hand, cold working can be beneficial when the cyclic-stress value is sufficiently low. In this case the dislocation motion is greatly reduced and the development and growth of cracks are inhibited. Thus, the observed effects on life-to-failure found in strain-cycling cold-worked test specimens, Figs. 10, 12, and 14, can be explained qualitatively.

The kind of cold work was found to be unimportant, Fig. 14.

---

[a] This word is not used in its thermodynamic sense.

Cold work by tension was about as effective as by torsion, other conditions being equal. It should be kept in mind, however, that the slip planes used in the prior tension are the same as those in strain cycling, while in the case of prior torsion they are not. It can be argued, then, that when strain cycling occurs in which the slip planes utilized differ from those of the prior cold work, relatively more cyclic strain can be absorbed by the structure than when the slip planes are the same. This assumes that the disorder and damage from the slip process are highly anisotropic, so that further disturbance to these planes more rapidly produces a fatigue crack than when other planes are involved. However, the difference between tension and torsion is apparently too small to show this effect.

The obliquity of the fatigue crack formed in strain-cycled specimens, Figs. 16 and 17, given prior torsion suggests similar results found statically by Swift (42). Here test specimens of mild steel, given prior torsion and then subjected to fracture by tension, were found to exhibit an unexpected effect when a shear strain of about 1 was reached. A marked decrease in fracture stress and ductility was noted at this point, and at the same time the appearance of fracture changed from the cup-and-cone type to a shear fracture 45 deg to the direction of loading. Significantly, when the torsion direction was reversed and the bar completely untwisted, the ductility, fracture stress, and cup-and-cone fracture reappeared.

To explain these results, a microcrack hypothesis has been introduced by Zener and Hollomon (43) whereby in deformation the random orientation of microcracks becomes preferential because of rotation of the cracks with flow. This action tends to weaken planes containing the highest density of these cracks and leads to the fracture planes observed. A more recent report by Backofen, Hundy, and Wulff (44) supports this theory. Such an explanation may also be applied to the present data. However, a more general application of the microcrack hypothesis to mechanical behavior has not been proved. An alternate explanation is suggested more in line with the mechanism of the present paper. It can be argued that the obliquity in the fatigue crack could occur if the direction of preferred slip became highly anisotropic. In torsion all crystals in the structure are subjected to plane shear, so that a rotation of all planes into the plane of shear takes place. This would cause the preferred slip direction of all crystals in the structure (except those already in that plane) to rotate toward that plane and produce the desired anisotropy. When this state exists, subsequent cyclic straining will preferentially produce a fatigue crack in this direction.

Fatigue and Total Plastic Strain. The effect of the total plastic-strain on fatigue failure is shown in Fig. 31. A replot of the data on log-log co-ordinates and an extension of the data to include static values (using fracture ductility and where $N = 1/4$) for both annealed and 360 deg prior torsion are given in Fig. 32. It is seen that a linear relationship approximates these data points for both the annealed and cold-worked materials. In fact, the two curves appear parallel. For the annealed material the relationship given in Fig. 32 can be expressed as

$$N^{0.5} \Delta\epsilon_p = 0.359 \dots\dots\dots\dots\dots [7]$$

The fact that a single relationship could be found experimentally for static and cyclic loading is of considerable interest in an understanding of the fatigue problem. As yet, there does not appear to be any theoretical method for deriving such a relationship. Moreover, such an expression must be more fully substantiated experimentally, particularly in the range of from 1 to 100 cycles and beyond 40,000 cycles.

One very important conclusion from such an expression is the nonexistence of an endurance limit. According to Equation [7], failure would result eventually no matter how low the applied
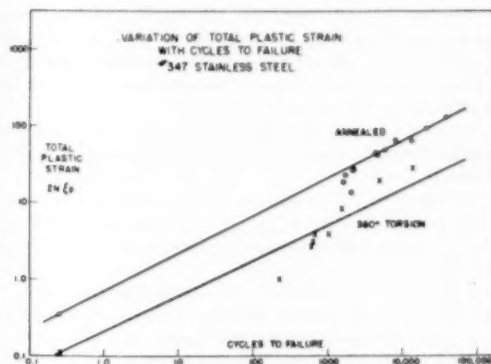

FIG. 32 VARIATION OF TOTAL PLASTIC STRAIN WITH CYCLES-TO-FAILURE

stress, provided there is reversed plastic flow. Since plastic flow can occur for stress levels well below the yield stress, fatigue failures should result for quite low stresses. This is not in accordance with fact for some metals, particularly ferrous alloys. Here a very distinct "endurance limit" is found in which the fatigue-stress versus cycles-to-failure curve levels off to a fixed stress after some million cycles of stressing. On the other hand, most nonferrous metals do not exhibit an endurance limit. Since iron and steel alloys are so widely used, it has been commonly accepted that the endurance-limit effect is the rule rather than the exception. The difference in behavior has not been resolved. Orowan (27) in his strain-hardening theory predicts an endurance limit for all metals. He explains the departure from an endurance limit in cold-worked copper and duralumin as caused by thermal softening or metallurgical instability.

The endurance limit, found principally in ferrous metals and in a few other materials, can be interpreted as resulting from strain aging of the metal. As discussed previously, diffusion of impurity atoms (principally carbon and nitrogen in iron) to dislocations acts to inhibit the reverse motion. Consequently, when the stress is sufficiently low, these dislocations are difficult to move and the accumulating effects toward development of a fatigue crack are reduced. When this occurs the stress versus cycles-to-failure curve exhibits a definite flattening, giving the observed endurance-limit effect. The mechanism is similar to that which explains the yield point in ferrous metals (22, 23). Consequently, metals which show a pronounced yield point in monotonic deformation should also reveal an endurance limit in fatigue testing.

CONCLUSIONS

The fatigue of Type 347 stainless-steel test specimens subjected to cyclic-temperature changes and unidirectional constraint has been studied under a variety of conditions. A significant feature of this type of loading is that the cyclic strain is constant, whereas in most fatigue testing the cyclic stress is constant during the test. For the present investigation the following specific characteristics were found.

1 For a fixed mean temperature, variations in the cyclic temperature change resulted in a characteristic fatigue curve of temperature change versus cycles-to-failure.

2 In contrast to cases in which stress is the independent variable, with thermal-stress cycling, prior cold work can reduce the number of cycles-to-failure when the strain is severe, but it is beneficial when the strain amplitude is low. When stress is the independent variable, cold work is beneficial (unless the material is damaged during the deformation).

3 The kind of prior cold work was found to be unimportant in thermal-stress cycling. For the same prior effective strain and cyclic-temperature change, specimens cold-worked by torsion withstood about the same cycles of thermal stress as specimens cold-worked by tension.

4 When the mean temperature is increased while a constant temperature change is maintained, a marked decrease in cycles-to-failure is found.

5 No significant difference in the life-to-failure was observed between specimens clamped in the test apparatus during the high-temperature hold phase of the cycle and the low-temperature phase.

6 A decrease in cycles-to-failure with increased hold time during thermal cycling was observed. However, the time for failure increased with increasing hold time.

7 Prior thermal-strain cycling was found to have little effect on the elevation of the subsequent true stress-strain curve. A marked decrease in fracture ductility occurred, however, as the number of prior strain cycles was increased. Scatter in ductility was quite wide. For example, after 8000 prior cycles, some specimens had failed completely while others maintained the ductility of the initially annealed specimens. The scatter was a result of the variations in occurrence and size of fatigue cracks formed during thermal-stress cycling. These cracks act as stress raisers during the tension test. This was substantiated by the strikingly similar behavior found in a test specimen containing a 13-mil hole and subjected to tension.

From the various measurements and observations made during the foregoing tests, certain general conclusions can be drawn regarding the fatigue process. For the most part these observations are in concurrence with those of other investigators.

(a) The significance of cyclic plastic strain as the basic cause of fatigue failure is confirmed in all of the tests carried out in this study.

(b) Strain hardening of the initially annealed material during strain cycling is very small and tends to saturate. The amount of strain hardening increases with increasing strain amplitude, but a saturation again occurs. Thus a fairly stable hysteresis loop is characteristic of the fatigue process.

(c) Prior cold working results in a strain softening of the material which depends on the strain amplitude and amount of prior cold work. The effect has been shown to be a result of strain cycling and not of an annealing effect in the metal. The asymptotic nature of the effect with strain cycles excludes the possibility of structural deterioration as an explanation.

(d) Prior cold work acts to reduce the ductility available for fatigue so that under the same plastic-strain amplitude the life of the material is actually less than that of annealed materials.

(e) The kind of prior cold work can alter the plane of fracture in fatigue. Severely twisted specimens exhibited a helical fracture when subjected to cyclic strain.

(f) Reversed plastic strain has little effect on mechanical properties until a fatigue crack has occurred. The crack then acts as a stress raiser to decrease the fracture ductility.

(g) A quantity defined as the total plastic strain can be calculated for each specimen tested. This strain is found to increase as the strain amplitude of the cycle decreases (or as the number of cycles-to-failure increases). A relationship between the total plastic strain and the cycles-to-failure is found to be linear when plotted on log-log co-ordinates. This line can be extrapolated for the present material to give a value which agrees with fracture ductility in simple tension. Other conditions being equal, the total plastic strain is reduced by prior cold work.

Based on the above observations, a mechanism for the behavior

of ductile metals under cyclic loading conditions is postulated. This is summarized as follows:

1 Under stress, dislocations move so as to concentrate at barriers such as grain boundaries. Upon reversed stress these dislocations reverse their direction and pile up against a barrier on the opposite side. Thus with cyclic stress a cyclic dislocation motion is set up. Such a mechanism accounts for the observed Bauschinger effect and hysteresis loop found in cyclic straining.

2 During the cyclic process some dislocations are tied down or pass beyond the barrier, so that there is a degree of irreversibility associated with the motion. This leads to the small amount of strain hardening and gradual growth of slip planes found during cyclic stressing. Furthermore, the irreversibility would be expected to increase with increased strain amplitude.

3 The reversed dislocation motion is considered as a process which permits regions of high energy in cold-worked metals to reduce their energy and thus allows the dislocations to move more freely. This accounts for the observed strain-softening effect.

4 The elimination of the Bauschinger effect by the Cottrell mechanism is consistent with the concept of reversed dislocation motion.

5 The cyclic dislocation motion can be regarded as the cause of fatigue cracks. By a mechanism not as yet described, cracks are developed along planes undergoing cyclic dislocation motion. There appears to be little evidence to support a strain-hardening mechanism as the cause of fatigue cracks.

6 According to the concept of total plastic strain, a fatigue crack will develop eventually, provided there is plastic strain in each cycle. To explain the endurance limit (as in ferrous metals) in which no fatigue crack will develop below a certain stress, a strain-aging process is suggested.

BIBLIOGRAPHY

1 "Apparatus for Study of Effects of Cyclic Thermal Stresses on Ductile Metals," by L. F. Coffin, Jr., and R. P. Wesley, published in this issue, pp. 923–930.

2 "Über die Veränderung der Elasticitätsgerenze und des Elasticitätsmoduls verschiedener Metalle," by J. Bauschinger, *Zivilingenieur*, vol. 299, 1881, col. 289–col. 348.

3 "Metals Handbook," Metals Handbook Committee, American Society for Metals, Cleveland, Ohio, 1948, p. 565.

4 "Prevention of the Fatigue of Metals Under Repeated Stress," by Battelle Memorial Institute Staff, John Wiley & Sons, Inc., New York, N. Y., 1941, Appendix 13.

5 "On the Pressure Perpendicular to Shear Planes in Finite Shear," by J. H. Poynting, Proceedings of the Royal Society of London, England, vol. 82, series A, 1909, p. 546.

6 "The Mathematical Theory of Plasticity," by R. Hill, Clarendon Press, Oxford, England, 1950.

7 "The Fracture of Metals Under Repeated Alternations of Stress," by J. A. Ewing and J. W. C. Humpfrey, Philosophical Transactions of the Royal Society of London, England, vol. 200, series A, 1903, p. 241.

8 "The Resistance of Materials to Impacts," by T. E. Stanton and L. Bairstow, Proceedings of the Institute of Civil Engineers, vol. 166, 1905-1906, part 4.

9 "Behavior of Metals Subjected to Repeated Stresses," by H. J. Gough and D. Hansen, Proceedings of the Royal Society of London, England, vol. 104, series A, 1923, p. 539.

10 "Crystalline Structure in Relation to Failure of Metals—Especially by Fatigue," by H. J. Gough, Proceedings of the ASTM, vol. 33, 1933, p. 3.

11 "On the Measurement of Small Strains in the Testing of Materials and Structures," by J. Ewing, Proceedings of the Royal Society of London, England, vol. 58, 1895, p. 123.

12 "The Behavior of Single Crystals of Aluminum Under Static and Repeated Stresses," by H. J. Gough, D. Hansen, and S. J. Wright, Philosophical Transactions of the Royal Society of London, England, vol. 226, series A, 1926–1927, p. 226.

13 "Note on Some Fatigue Phenomena With Special Relation to Cohesion Problems," by H. J. Gough, Trans. Faraday Society, vol. 24, 1928, pp. 137–148.

14 "Deformation and Fracture in Iron and Steel," by W. Rosenhain, Journal of the Iron and Steel Institute, vol. 70, 1906, p. 189.

15 "Elasticity and Anelasticity of Metals," by C. Zener, University of Chicago Press, Chicago, Ill., 1948, p. 137.

16 "Zug-Durchversuche an Messingkristallen," by G. Sachs and H. Shoji, Zeitschrift für Physik, vol. 45, 1927, p. 776.

17 Op. cit., by C. Zener, p. 146.

18 "Observations on Bauschinger Effect in Copper and Brass," by H. Schwartzbart, M. H. Jones, and W. F. Brown, Jr., NACA Research Memo E51D13, June 19, 1951.

19 "The Recovery of Iron From Overstrain," by J. Muir, Philosophical Transactions of the Royal Society of London, England, vol. 193, series A, 1900, pp. 1–46; "On the Effect of Low Temperature on the Recovery of Overstrained Iron and Steel," by E. Coker, Physical Review, vol. 15, 1902, p. 107.

20 "Overstrain of Metals," by A. E. Macrea, H. M. Stationery Office, London, England, 1930.

21 "The Effect of Slightly Elevated-Temperature Treatment Upon Microscopic and Submicroscopic Residual Stresses Induced by Small Inelastic Strains in Metals," by H. T. Corten and T. M. Elsesser, Trans. ASME, vol. 74, 1952, pp. 1297–1302.

22 "Effect of Solute Atoms on the Behavior of Dislocations," by A. H. Cottrell, Report of a Conference on Strength of Solids, University of Bristol, England, 1947.

23 "Mechanical Effects of Carbon in Iron," by F. R. N. Nabarro, Report of a Conference on Strength of Solids, University of Bristol, England, 1947.

24 "Changes in Strength of Properties of Metals With Stress Cycling," by P. Ludwik, Zeitschrift für Metallkunde, vol. 11, 1919, pp. 157–168.

25 "On the Hardening of Rock Salt in Bending Experiments," by W. Ewald and M. Polanyi, Zeitschrift für Physik, vol. 31, 1925, pp. 139–144.

26 "Low Cycle Fatigue of Aluminum Alloy 24S-T in Direct Stress," by S. I. Lui, J. J. Lynch, E. J. Ripling, and G. Sachs, Trans. AIME, vol. 175, 1948, p. 469.

27 "Theory of the Fatigue of Metals," by E. Orowan, Proceedings of the Royal Society of London, England, vol. 171, series A 1939, p. 79.

28 "Zur Theorie der Wechselfestigkeit," by V. Dehlinger, Zeitschrift für Physik, vol. 115, 1940, p. 625.

29 "Fracturing of Metals," by E. S. Machlin, American Society of Metals, Seminar, Cleveland, Ohio, 1948, p. 282.

30 Reference (4), p. 92; also Appendix 21.

31 "Fatigue Tests of Carburized Steel," by H. F. Moore and N. J. Alleman, Trans. American Society for Steel Treatment, vol. 13, 1928, pp. 405–419.

32 "Effect of Overstressing and Understressing in Fatigue," by J. B. Kommers, Proceedings of the ASTM, vol. 38, 1938, pp. 249–268.

33 "Dauerversuche an der Hochfrequenz-Zug-Druck-Maschine, Bauart-Schenck," by K. Memmler and K. Laute, Forschungsarbeiten auf dem Gebiete des Ingenieurwesens, vol. 329, 1930, 32 pp.

34 "Effects of Prior Fatigue Stressing on the Impact Resistance of Chromium-Molybdenum Aircraft Steel," by J. A. Kies and W. L. Holshouser, NACA TN 889, 1943.

35 "Some New Aspects of the Fatigue of Metals Brought Out by Brittle Transition Temperature Tests," by C. E. MacGregor and N. Grossman, Welding Research Supplement, Welding Journal, vol. 27, 1948, pp. 132–135.

36 "Effect of Fatigue on Transition Temperature of Steel," by J. M. Lessells and H. E. Jacques, Welding Research Supplement, Welding Journal, vol. 29, 1950, pp. 74–75.

37 "Crystal Growth in Cadmium," by C. H. Desch, discussion to paper by M. Cook, Trans. Faraday Society, vol. 19, 1923, p. 48.

38 "Thermal Fatigue of Metals," by W. Boas and R. W. K. Honeycombe, Nature, vol. 153, 1944, p. 494; vol. 154, 1944, p. 338.

39 "Deformation of Zinc Bi-Crystals by Thermal Ratcheting," by J. E. Burke and A. M. Turkalo, Trans. AIME, vol. 194, 1952, p. 651.

40 "The Role of Anelasticity in Creep, Tension, and Relaxation Behavior," by J. D. Lubahn, Trans. ASM, vol. 45, 1953, p. 787.

41 "Theory of Dislocations," by A. H. Cottrell, Progress in Metal Physics, vol. 1, 1949, p. 77.

42 "Tensional Effects of Torsional Overstrain in Mild Steel," by H. W. Swift, Journal of the Iron and Steel Institute, vol. 140, 1939, p. 181.

43 "Plastic Flow and Rupture of Metals," by C. Zener and J. H. Hollomon, Trans. ASM, vol. 33, 1944, p. 163.

44 "Mechanical Anisotropy in Some Ductile Metals," by W. A. Backofen, B. B. Hundy, and J. Wulff, Journal of the Institute of Metals, vol. 81, 1952, p. 433.

Discussion

HARRY MAJORS, JR.[9] This discussion is submitted to support the assertion in this paper that "the hysteresis loop is established very quickly, and changes in the size and shape of the loops take place very slowly thereafter," in which the net strain is zero while the temperature varies between fixed limits.

It is interesting to learn that the same observation has been verified for isothermal conditions in reversed torsion in which the total strain varied between fixed limits. Figs. 33[10] and 34[10] of

[9] Research Professor, Bureau of Engineering Research, College of Engineering, University of Alabama, University, Ala. Mem. ASME.

[10] This information was obtained in the summer of 1949, while the writer was on the M.I.T. staff in the Department of Mechanical Engineering, investigating fatigue under a low number of cycles.
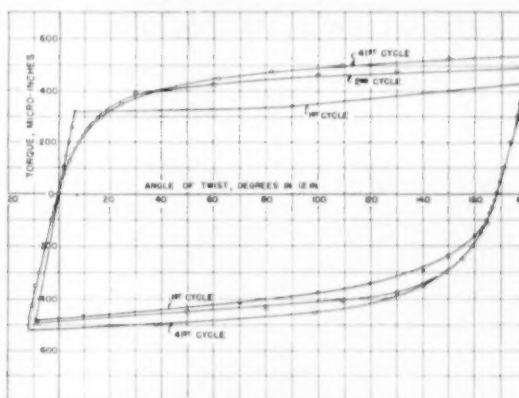

FIG. 33 HYSTERESIS LOOPS OF MILD STEEL IN REVERSED TORSION, ISOTHERMAL CONDITIONS

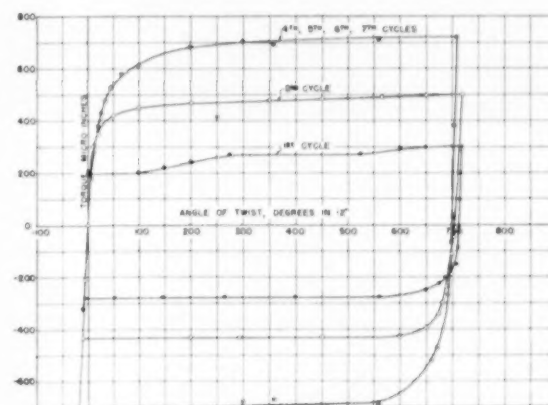(1 Microinch = 2 in-lb; maximum strain of each cycle, 180 deg per 12 in.)

FIG. 34 HYSTERESIS LOOPS OF MILD STEEL IN REVERSED TORSION, ISOTHERMAL CONDITIONS

(1 Microinch = 2 in-lb; maximum strain of each cycle, 720 deg per 12 in.)

this discussion are in support of this. Low-carbon steel, SAE 1020, originally annealed to a VHN of 120, was cycled under reversed torsion at room temperature and the hysteresis loops were found to stabilize after a few cycles into a constant area and shape.

These data were obtained on 0.750-in-diam rods, 21³/₄ in. long with a straight section of 12 in., reduced to 0.505 in. for torsion sectors. Torque in inch-pounds versus angle of twist in degrees in 12 in. was plotted until an angle of twist of 180 deg (in 12 in.) was obtained for Fig. 33, and 720 deg (in 12 in.) for Fig. 34. Then the data were plotted for decreasing torque to zero torque. Now, data were obtained for reversed torque up to 180 and 720 deg in 12 in., respectively; and then for decreasing torque to zero, which completed one cycle at constant reversed torsional strain. The total time to obtain the data for any cycle in Fig. 33, was 5 min and for Fig. 34 it was 10 min, so that the test is essentially an isothermal one at room temperature. A 60,000 in-lb Riehle torsion machine was converted to permit reversed torsion. The shank of the torsion specimen had a strain-gage bridge which was calibrated previously to measure torque. Circular sectors spaced 12 in. apart were used to measure the angle of twist.

As noted in Fig. 33, the second cycle approaches very closely the shape of the 41st cycle. Plots were made every fourth cycle after the tenth, and all were about the same shape and area. In Fig. 34 there was hardly any change during the fourth to seventh cycles. Rupture occurred on the eighth cycle.

A third series of reversed-torsion cycles on the same material were made to twists of 23 deg in 12 in. There were 332 cycles of reversed torsion. Stabilization was obtained on the seventh cycle in which plots after the seventh cycle were identical.

AUTHOR'S CLOSURE

The author wishes to thank Professor Majors for submitting additional supporting experimental information relating to the establishment of a hysteresis loop by cyclic straining. One comment regarding these data is of interest. In both Figs. 33 and 34 an increase in stress occurs during each of the first two or three cycles, but is particularly marked in Fig. 34. The effect is much more pronounced than what one would find in austenitic steels. Since the material is an annealed low-carbon steel, this behavior is strongly suggestive of strain aging, a phenomenon characteristic of this steel. As discussed in the paper, the Cottrell mechanism (22, 23) offers a plausible explanation of the effect. Once an equilibrium is reached between strain and strain aging, the hysteresis loop then remains fixed.

Evaluation of Bandsaw Performance

By

By L. V. COLWELL[1] and R. E. McKEE,[2] ANN ARBOR, MICH.

Methods of evaluating bandsaw performance are presented and typical performance characteristics are discussed. Tests indicate that bandsawing has orderly and predictable machinability characteristics very similar to other machining operations. Cutting speed and feed rate or feeding force are the more important variables requiring careful selection and control. Tests on sawing titanium show that positive power feed is almost a necessity to prevent premature breakdown of the band.

Introduction

THERE is considerable published information on machinability but knowledge of the subject has not advanced to the point where it is possible to make a few standardized tests and from the results calculate and predict performance characteristics for all of the many common machining operations. Thus, in the case of bandsawing as with turning, milling, tapping, and so on, it is necessary to run tests on the particular operation concerned. However, unlike turning and milling in particular, little work has been published on evaluating bandsaw performance. Consequently, one of the objectives of this study was to develop a procedure for analyzing and evaluating bandsaw performance. A further objective was to determine satisfactory conditions for bandsawing titanium and its alloys.

The immediate goals of the machine shop in connection with bandsawing are a high sawing rate and economically long saw life. A thorough study should include all variables which have significant influence on the objectives. This investigation was begun with little knowledge of the identity of the influential variables; therefore the program was limited by using only one type of commercial band and studying the effects of cutting speed, feed rate, and work material. Data were obtained on cutting forces and tool life as affected by the variables when sawing compositions of titanium and hot-rolled SAE 1045 steel.

Preliminary tests demonstrated the practical impossibility of sawing titanium alloys by either hand or dead-weight feeding. Consequently, a positive motion, mechanical feeding attachment was constructed for use on all subsequent tests.

Equipment

Fig. 1 shows the test setup. It consists of (1) Grobe, 24-in. metal-cutting bandsaw, (2) power-feed attachment, (3) force dynamometer, and (4) 2-channel strain recorder.

The bandsawing machine is a standard type and provides selectively variable band speed over a wide range. It was not modified in any way for these tests.

The power-feed attachment consists of a work-holding fixture, force dynamometer, lead screw, reduction gear, and a Master Electric infinitely variable drive. The force dynamometer is interspersed between the lead screw and the fixture.
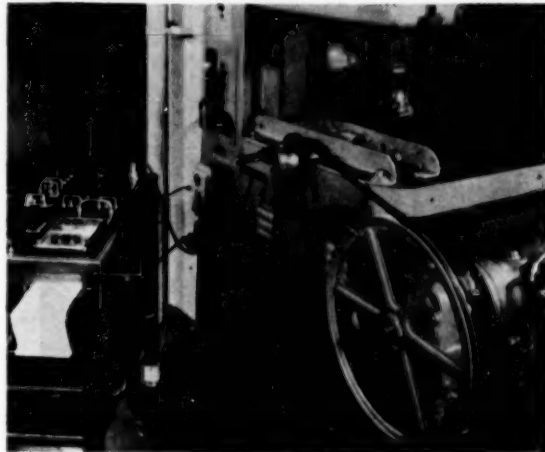
FIG. 1 A GROBE, 24-IN. BANDSAW EQUIPPED WITH POSITIVE FEED-SCREW MECHANISM AND DYNAMOMETER USED IN MEASURING FEEDING FORCES.

(Sanborn, twin-channel recorder-oscillograph for recording forces is shown at left.)
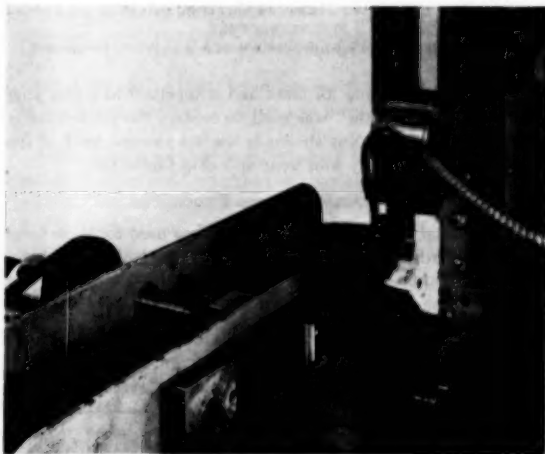

FIG. 2 CLOSE-UP VIEW OF FEEDING MECHANISM FOR POSITIVE INCREMENTS OF FEED AND DYNAMOMETER FOR MEASURING MAGNITUDE OF FEEDING FORCES IN BANDSAWING OPERATION

Fig. 2 is a close-up view of the work area showing a work specimen in position for cutting. The force dynamometer shown measures only the feeding force. Fig. 3 shows the 2-component dynamometer used to measure the cutting and feeding forces simultaneously. Since the feeding mechanism provides positive motion, the indicated force is a reaction to the motion and resistance at the cut. Consequently, any increase in this resistance, such as may result from tool wear, results in an increase in the indicated force.

Fig. 4 shows the auxiliary instruments necessary in conducting the tests. An indicating tachometer was used to determine the exact value of lineal cutting speed at cutting conditions. A stop
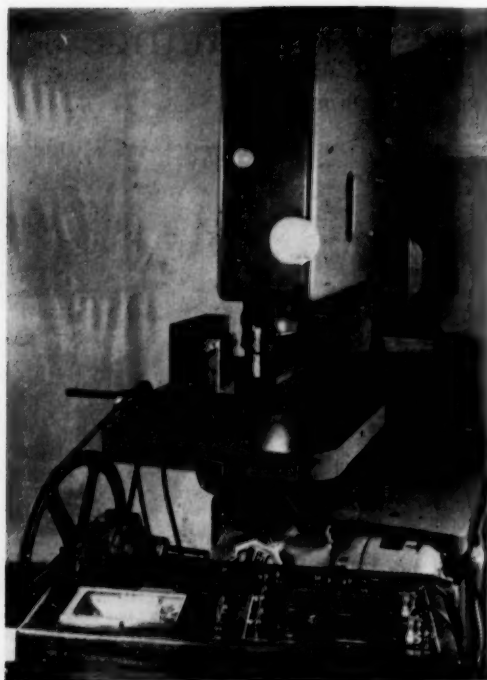
Fig. 3 Special, 2-Component Dynamometer Attached to Band-saw Feed Mechanism, to Measure Cutting and Feeding Forces Simultaneously
(Sanborn, twin-channel recorder-oscillograph is shown in foreground.)

Fig. 4 Sample Work Specimens, Indicating Tachometer, and Saw-Tension Used in Bandsawing Tests

watch was used to time all tests and a mechanical strain gage known as a "Simometer" was used to control the pre-tension in mounting the band. Not shown is the microscope used at frequent intervals to study tool wear and chip formation.

Test Conditions and Procedure

Tool Material. Only one type of saw was used for these tests. It was standard Simonds "Hard Edge," ³/₄ in. wide, 6 pitch roll stock. Individual bands were cut to length and butt-welded on the machine in the usual manner.

Work Material and Specimens. Five work materials were selected for study: (1) SAE 1045 steel (hot-rolled); (2) Ti 75A titanium (commercially pure); (3) RC 130A titanium (7 per cent manganese); (4) Ti 150A titanium (2.7 per cent chromium, 1.3 per cent iron); (5) RC 130B titanium (4 per cent aluminum, 4 per cent manganese).

Tensile properties of the work materials are given in Table 1. It will be noted that the three titanium alloys possess similar properties; it will be shown later that they differ substantially, however, in machinability ratings.

Work specimens of all materials were machined to dimensions of 2 in. × 4 in. × 1 in. thick. The saw cut was parallel to the 1-in. dimension. The cut was started and the teeth both entered and left through surfaces that previously had been machined. In other words, no sawing was done through surface oxides other than those formed during cutting.

Other Conditions. Cutting speed and feed rate were varied intentionally over broad ranges in order to evaluate their effects as continuous variables. All formal testing was done as dry cutting. Preliminary tests with liquid coolants and also with

TABLE 1 TENSILE PROPERTIES OF WORK MATERIALS

Material	Sample no.	Yield strength[a], psi	Tensile strength, psi	Breaking strength, psi	Per cent elongation	Per cent reduction of area
SAE 1045	1	48600	101200	91000	21.5	33.0
SAE 1045	2	48800	101800	92500	21.7	34.4
SAE 1045	3	53000	101700	98500	22.5	34.6
Ti-75A	1	60000	82000	56000	28.0	47.1
Ti-75A	2	57400	82100	65500	28.5	48.6
Ti-75A	3	57700	82000	65500	27.7	48.8
RC-130B	1	139000[b]	155500	122500	16.5	41.9
RC-130B	2	139400[b]	155000	126200	17.7	37.9
RC-130B	3	139400	155200	121700	18.3	46.3
Ti-150A	1	131700	141000	97200	25.0	55.8
Ti-150A	2	132500	140800	99200	24.7	54.5
Ti-150A	3	130000	140400	97400	25.0	55.1
RC-130A	1	131000[b]	140500	124000	22.7	38.1
RC-130A	2	134000[b]	142200	126000	22.0	38.1
RC-130A	3	135000	141600	126000	22.0	37.5

[a] Yield strength determined by 0.2 per cent offset method.

[b] Yield-point value.

VELOCITY: 52 FPM   MATERIAL: TI-150A   FEED RATE: VARIABLE - 10⁻⁶ INCHES PER TOOTH

VELOCITY: 52 FPM   MATERIAL: SAE-1045   FEED RATE: VARIABLE - 10⁻⁶ INCHES PER TOOTH

FIG. 5   SAMPLE FORCE CHARTS PRODUCED BY USE OF 2-COMPONENT DYNAMOMETER AND TWIN-CHANNEL RECORDER-OSCILLOGRAPH FOR VARIOUS FEED RATES OF WORK IN INCHES × 10⁻⁶ PER TOOTH

(Upper inverted curve shows record of cutting forces and lower curves show feeding forces.)

CO_2 indicated that cutting fluids were not appreciably effective when applied in the usual manner. It appeared that flood application might be needed to achieve the improvement usually found in turning. Flood application is difficult with vertical bandsawing machines.

Test Procedure. Two test procedures were used, one for tool-life studies and the other for cutting forces. In the first instance a test was started with preselected values of cutting speed and feed rate. These conditions were held constant throughout each test. The feeding force was recorded continuously and the test was allowed to proceed until the feeding force equaled or exceeded 100 lb. The cutting time required to reach this arbitrary limit was designated as the tool life. In all cases the 100-lb limit was in a region where the feeding force increased very rapidly so that the usual life of the band was all utilized and there was very little error in its extent as determined in this manner.

The second procedure was used for cutting-force studies. In this case the cutting speed was held constant at a conservative value but the feed rate was increased at short intervals so that corresponding forces could be obtained for a broad range of feeds. Both cutting and feeding forces were studied in this manner.

Fig. 5 shows the original chart records obtained from two typical tests. The upper chart was obtained for grade Ti 150A titanium cut at 52 fpm and at five different feeds ranging from 80 to 400 millionths of an inch per tooth. The feed rate in inches per tooth is determined by dividing the work-feed rate in inches per minute by the number of teeth of the same set (left set, for example) passing a given point in 1 min. The upper record line is deflected downward with an increase in cutting force while the lower record line is deflected upward for an increase in feeding force. The lower chart in Fig. 5 was obtained for SAE 1045

steel at the same cutting conditions as were used for the titanium. It is obvious that the titanium requires considerably higher feeding force.

Similar force records were obtained for the tool-life tests, the principal difference being that the feeding force increased steadily with elapsed cutting time and was permitted to continue up to and beyond 100 lb.

TOOL LIFE

The curves in Fig. 6 show the change in feeding force as the saw teeth wear when sawing Ti 75A titanium at a speed of 78 fpm. Each of four lines represents a different feed rate. As expected, the rate of increase is least with the smallest feed rate. The increase appears to be substantially linear with elapsed time until

FIG. 6   FEEDING FORCE IN POUNDS VERSUS TIME IN MINUTES FOR VARIABLE FEED RATES WHEN BANDSAWING TI 75A AT 78 FPM

FIG. 7   FEEDING FORCE IN POUNDS VERSUS TIME IN MINUTES FOR VARIABLE CUTTING SPEEDS ON TI 150A AT FEED OF 120 × 10⁻⁶ IN. PER TOOTH

FIG. 8   FEEDING FORCE IN POUNDS VERSUS CUTTING TIME IN MINUTES FOR SAE 1045 STEEL AND VARIOUS TITANIUM COMPOSITIONS, WHEN BANDSAWING AT SPEED OF 78 FPM AND FEED OF 120 × 10⁻⁶ IN. PER TOOTH
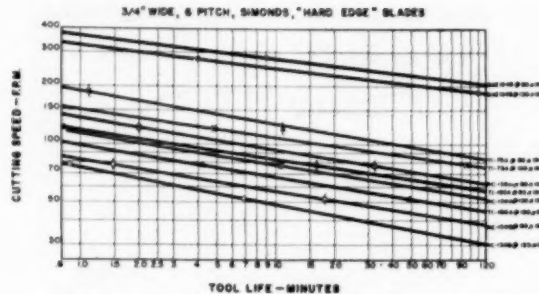

FIG. 9   LOGARITHMIC PLOT OF CUTTING SPEED IN FEET PER MINUTE VERSUS TOOL LIFE IN MINUTES FOR SAE 1045 STEEL AND VARIOUS COMPOSITIONS OF TITANIUM AT TWO FEEDS OF 80 × 10⁻⁶ AND 120 × 10⁻⁶ IN. PER TOOTH

FIG. 10   AREA OF CUT IN SQUARE INCHES VERSUS FEED RATE IN INCHES × 10⁻⁶ PER TOOTH FOR VARIOUS COMPOSITIONS OF TITANIUM AT 52 AND 78 FPM CUTTING SPEEDS

a critical level is reached after which the rate increases rapidly. The four lines in Fig. 6 demonstrate considerable sensitivity of tool life to feed rate. It would not be surprising if erratic performance accompanied hand feeding where it is difficult to control feeding pressure.

Fig. 7 shows a similar set of curves for grade Ti 150A titanium where each curve represents a different cutting speed at a constant feed rate of 120 millionths of an inch per tooth. These lines also demonstrate a marked sensitivity to cutting speed. Similar curves were obtained for all five work materials over ranges of both cutting speed and feed rate.

Fig. 8 gives a comparison of the work materials at a constant speed of 78 fpm and a constant feed of 120 millionths of an inch per tooth. RC 130B titanium gives the shortest life and SAE 1045 steel gives the longest life. In sequence of descending tool life, all five materials are in order of SAE 1045, Ti 75A, RC 130A, Ti 150A, and RC 130B. It is significant to note that the same order has been found for other machining operations.

Results of the tool-life tests are summarized in Fig. 9 where the tool life in minutes is plotted against the corresponding cutting speed on logarithmic co-ordinates. Drawing straight lines through the data points not only correlates the speeds and resulting tool life as continuous variables but it makes it possible to express correlation with an empirical equation of the type $VT^n = C$. This is the same equation used generally for tool life in turn-

ing. V is the cutting speed in fpm, T is the tool life in minutes, and n and C are constants whose values depend on other conditions.

The results in Fig. 9 can be expressed in terms of area sawed instead of minutes of tool life. A 1-in-long cut in 1-in-thick material would be 1 sq in. of cut area. Sample curves of this type are shown in Fig. 10. However, all necessary data are shown in the previous figure.

A further analysis of the tool-life curves shown in Fig. 9 is given in Tables 2 to 5, inclusive. Table 2 summarizes the cutting speeds necessary to give a 1-hr band life. The speeds are expressed both in fpm and per cent of the speed for SAE 1045 steel. It will be noted that the percentage ratings differ very little as between the two different feed rates. Previous experience has shown that the same percentages apply almost equally well to turning, milling, and so on, for identically the same materials. Consequently, it is reasonable to assume that any relative machinability ratings that are known to be valid for turning or milling can be used for bandsawing.

Table 3 summarizes the values of n and C of the equation $VT^n = C$ for all of the test conditions represented in Fig. 9. It will be noted that the exponents n for titanium average about 0.16 and a value of 0.12 holds for the SAE 1045 steel. This can be interpreted as meaning that in titanium, mechanical and chemical "wear" are more important than temperature when compared with steel.

Tables 4 and 5 compare the tool life for the various titanium alloys when sawed at the same cutting speeds. SAE 1045 steel is

TABLE 2   CUTTING SPEED ($V60$) FOR 60-MIN TOOL LIFE AT 80μ AND 120μ IN. FEED

| Material | $f=80 \times 10^{-6}$ ipt=80~ | | $f=120 \times 10^{-6}$ ipt=120~ | |
	Vel 60 min TLØ 80~ in.	Per cent 1045	Vel 60 min TLØ 120~ in.	Per cent 1045
SAE 1045	218	100	197	100
Ti 75A	98	45	85	43
Ti 130A	70	32	59	30
Ti 150A	65	30	51	26
Ti 130B	43	20	35	18

TABLE 3   VALUES OF n AND C FOR WORK MATERIALS ($VT^n = C$)

| Material | n | | C | |
	80 in.	120 in.	80 in.	120 in.
SAE 1045 . . .	0.123	0.122	388	326
Ti 75A . . .	0.155	0.142	182	151
RC 130A . . .	0.180	0.156	140	112
Ti 150A . . .	0.152	0.164	120	99
RC 130B . . .	0.165	0.190	84	76

TABLE 4   COMPARISON OF AREAS CUT FOR TITANIUM ALLOYS

| Material | Area cut - square inches | | | |
| | 52 fpm | | 78 fpm | |
	80 in.	120 in.	80 in.	120 in.
Ti 75A	420	294	49	21
RC 130A	42	19.9	7.2	2.4
Ti 150A	19.8	10.4	3.7	1.2
RC 130B	1.8	1.0	0.34	0.2

TABLE 5   TOOL LIFE AND AREA CUT FOR VARIOUS MATERIALS

| Material | Feed rate, in. $\times 10^{-6}$ tooth | Tool life, min | | | | Area cut, sq in. | | | |
| | | 52 fpm | | 78 fpm | | 52 fpm | | 78 fpm | |
		Min	Per cent of Ti 75A	Min	Per cent of Ti 75A	Sq in.	Per cent of Ti 75A	Sq in.	Per cent of Ti 75A
Ti 75A	80	4200	100	215	100	420	100	49	100
	120	1960	100	92	100	294	100	21	100
RC 130A	80	420	10	32	15	42	10	7.2	15
	120	133	6.8	10.8	12	20	6.8	2.4	12
Ti 150A	80	195	4.7	16.5	7.7	19.8	4.7	3.7	7.6
	120	69	3.5	5.2	5.7	10.4	3.5	1.2	5.7
RC 130B	80	17.8	0.42	1.5	0.7	1.8	0.42	0.34	0.7
	120	6.9	0.35	0.88	0.96	1.0	0.35	0.2	0.96

Note: SAE 1045 steel not included, because of excessive extrapolation at these speeds.

not included in this comparison because of the considerable extrapolation required at such relatively low speeds. Table 4 compares the areas cut. Table 5 gives comparisons in units of time and areas cut as well as per cent of the performance of commercially pure titanium. Both tables demonstrate the futility of trying to cut all titanium alloys at the same speeds. Instead, the cutting speed should be selected in a range appropriate to the alloy as indicated in Table 2.

It was pointed out earlier that the titanium grades RC 130A, Ti 150A, and RC 130B have substantially the same tensile strength; this is shown in Table 1. On the other hand, Table 2 shows that RC 130A can be cut at speeds about 60 per cent higher than the corresponding speeds for RC 130B despite approximately equal strength. This difference when translated into tool life at the same speed shows that tools would last from three to four times as long cutting RC 130A compared to RC 130B. Ti 150A is intermediate but approaches the performance of the RC 130A.

While it is difficult to evaluate quantitatively, it should be pointed out that the mill scale or surface oxides on titanium produce exceptionally high rates of tool wear and should be avoided in every practical way. Such oxides are always present in significant quantity even after machining operations. This is be-

lieved to be one of the major reasons why titanium alloys cannot be sawed satisfactorily with hand feed. Saw teeth are not of uniform height and hand feeding permits the work to float or adjust itself to these irregularities. This action accompanied with relatively small feeding force results in erratic cutting or no cutting at all, thus giving the oxides a chance to cause very rapid wear of the flanks of the saw teeth. Positive motion, mechanical feeding mechanisms are recommended strongly for sawing titanium. This recommendation is consistent with the exceptional rigidity found to be necessary for satisfactory machining of titanium by other operations.

CUTTING FORCES

Usually, the machine shop is not interested in cutting force data per se, since they can be used only to determine whether or not a machine has adequate power capacity for the job to be done on it. However, such data have considerable interest for the engineer and research worker because similar data from many sources when considered together are gradually revealing the fundamentals of what happens when metal is cut. It is hoped that the force data obtained from this investigation will be useful in furthering this objective. In addition to this, it does reveal
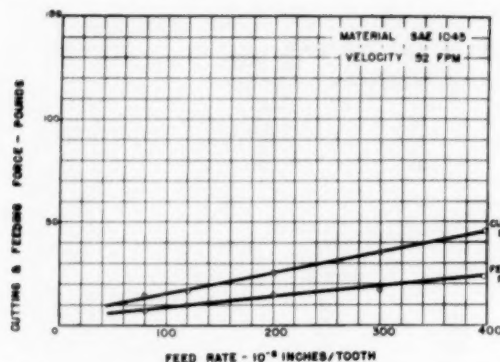
FIG. 11 CUTTING AND FEEDING FORCES PLOTTED VERSUS FEED
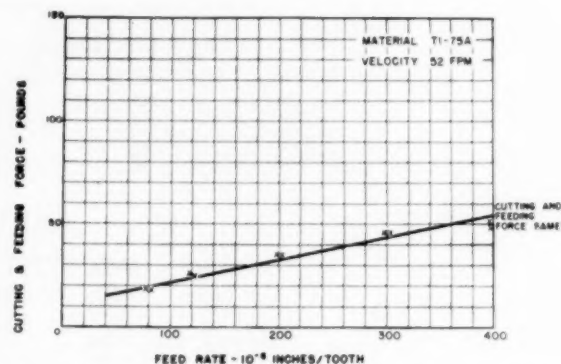RATE IN INCHES × 10^{-6} PER TOOTH FOR SAE 1045 STEEL AT 52 FPM

FIG. 12 CUTTING FORCES PLOTTED VERSUS FEED RATE IN INCHES
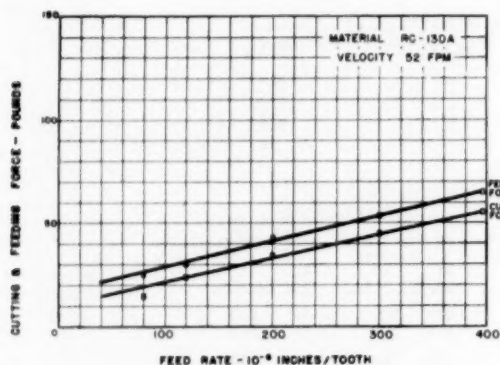× 10^{-6} PER TOOTH FOR TITANIUM TI 75A

FIG. 13 CUTTING AND FEEDING FORCES PLOTTED VERSUS FEED
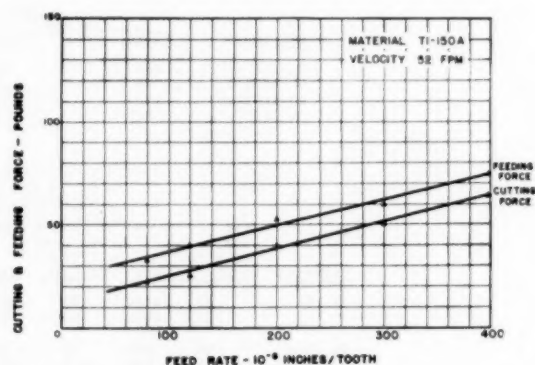RATE IN INCHES × 10^{-6} PER TOOTH FOR TITANIUM RC 130A

FIG. 14 CUTTING AND FEEDING FORCES PLOTTED VERSUS FEED
RATE IN INCHES × 10^{-6} PER TOOTH FOR TITANIUM TI 150A

significant attributes of the sawing process and unique properties
of titanium alloys.

Figs. 11 to 15, inclusive, show the cutting and feeding forces
obtained for each of the five work materials at a constant cutting
speed of 52 fpm and over a wide range of feeds. The forces are
representative of sharp cutting edges since the speed was rela-
tively low and the saws were used for relatively short times at
each feed rate. The data points are plotted on Cartesian co-
ordinates and are represented reasonably by straight lines.
Two properties of these lines appear to be significant.

First it will be noted from Fig. 11 for SAE 1045 steel, that the
cutting force is approximately twice the feeding force, while
Fig. 15, which is for RC 130B, shows the cutting force to be sub-
stantially less than the feeding force. This reversal occurs in
all of the titanium alloys while the two force components are equal
for Ti 75A. A further comparison of the steel and RC 130B at a
feed of 300 millionths of an inch per tooth shows that the cutting
force for titanium is only twice that for steel while the feeding
force is more than $4^{1}/_{2}$ times as great as that for steel; once more,
this demonstrates the need for greater rigidity when machining
titanium. This is particularly important for interrupted cuts
where the greater feeding force delays achieving full-chip thick-
ness, thus simulating dull tools and augmenting the high rate of
wear associated with this condition.   A corollary to greater ri-
gidity is the maintenance of sharper tools. Thus, in general,
titanium calls for initially sharper tools where possible which
should not be permitted to wear excessively before regrinding.
The latter policy is obviously impossible with saws and other
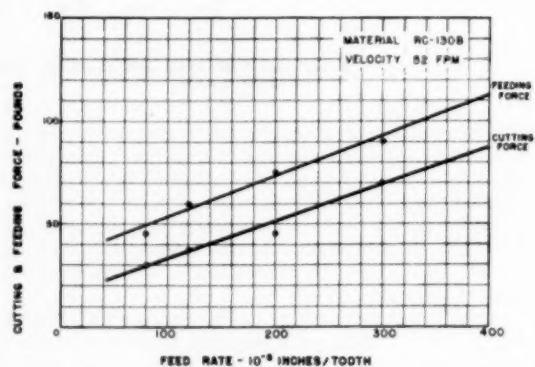
FIG. 15 CUTTING AND FEEDING FORCES PLOTTED VERSUS FEED
RATE IN INCHES × 10^{-6} PER TOOTH FOR TITANIUM RC 130B

tools which cannot be reground economically.   That the mate-
rials differ more in feeding force than in cutting force is shown
graphically in Fig. 16 and 17.

The second significant property of the curves in Figs. 11 to
15 is that the straight lines when extrapolated to zero feed rate
all intersect the force axis at positive values. Consequently,
the equations for the lines must be written in the form $F = F_0$
$+ Kf$, where F_0 is the residual value at zero feed.   The equations
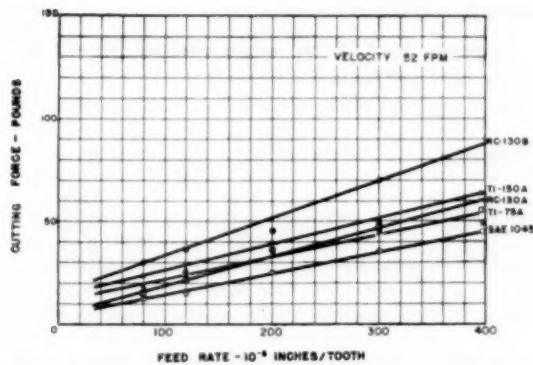
FIG. 16 CARTESIAN CO-ORDINATE PLOT OF CUTTING FORCE IN POUNDS VERSUS FEED RATE IN INCHES $\times 10^{-6}$ PER TOOTH FOR SAE 1045 STEEL AND VARIOUS COMPOSITIONS OF TITANIUM AT CUTTING SPEED OF 52 FPM
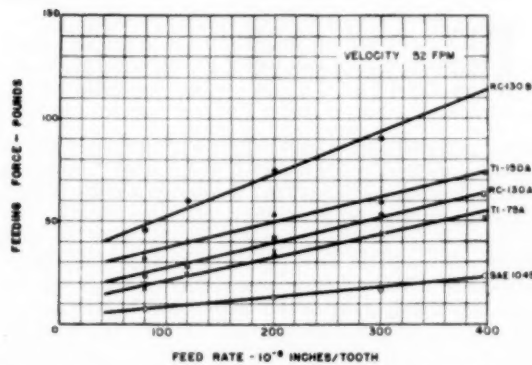
FIG. 17 CARTESIAN CO-ORDINATE PLOT OF FEEDING FORCE IN POUNDS VERSUS FEED RATE IN INCHES $\times 10^{-6}$ PER TOOTH FOR SAE 1045 STEEL AND VARIOUS COMPOSITIONS OF TITANIUM AT CUTTING SPEED OF 52 FPM

for all the force lines in Figs. 11 to 15 are summarized in Tables 6 and 7.

The fact that the force lines do not go through the origin is not surprising since no cutting edge is perfectly sharp and some force must be built up before cutting can begin. The values of F_0 in Tables 6 and 7 give a relative measure of the property. Where no metal is cut, the ratio F_{c0}/F_{f0} is a crude measure of the coefficient of friction between the saw and the work material. These ratios are summarized in Table 8. All three titanium alloys give coefficients of 0.5 while Ti 75A gives 1.0 and the steel gives 1.5. This evidence is at variance with some claims that the coefficient of friction between cutting tools and titanium chips is greater than when steel is cut. The relative values given in Table 8 are confirmed by the fact that titanium invariably produces larger shear angles than steel; this is consistent with current metal-cutting theory.

CARTESIAN CO-ORDINATES VERSUS LOGARITHMIC CO-ORDINATES

The question is frequently asked as to which is valid for plotting cutting-force data—Cartesian co-ordinates or logarithmic co-ordinates. The answer is that both are valid. Cartesian co-ordinates make it easier to analyze and interpret data while logarithmic co-ordinates lead to the exponential type of equation which is a concise and compact expression of the data that is

TABLE 6 CUTTING FORCES[a]

$$F_c = F_{c0} + K_c f$$

where F_c = force of cutting, lb

F_{c0} = initial force of cutting at 0 feed

f = feed rate, in. $\times 10^{-6}$ per tooth

Material	V = 52 fps	
	F_{c0}	K_c
SAE 1045	6	0.100
Ti 75A	11.5	0.105
RC 130A	7.5	0.125
Ti 150A	12	0.130
RC 130B	15.5	0.180

[b] Same note as on Table 7.

TABLE 7 FEEDING FORCES[a]

$$F_f = F_{f0} + K_f f$$

F_f = force of feed, lb

F_{f0} = initial force of feed in pounds at 0 feed

f = feed rate, in. $\times 10^{-6}$ per tooth

Material	V = 52 fps	
	F_{f0}	K_f
1045	4	0.0425
75A	11	0.105
130A	14	0.125
150A	21.5	0.130
130B	22	0.195

[a] For 6-pitch band, 0.035 in. kerf, 1-in. thick plate.

F_0 and K should be adjusted linearly for other values.

TABLE 8 COEFFICIENT OF FRICTION FOR VARIOUS MATERIALS

$$M = \frac{F_{c0}}{F_{f0}}$$

Material	F_{c0}	F_{f0}	M
SAE 1045	6.0	4.0	1.5
Ti 75A	11.5	11.0	1.05
RC 130A	7.5	14.0	0.54
Ti 150A	12.0	21.5	0.56
RC 130B	15.5	22.0	0.47

easier to apply. In brief, one type of co-ordinates is better for analysis; the other is better for application. This idea is developed with the data already presented for bandsawing.

The data plotted originally on Cartesian co-ordinates in Figs. 11 to 15 are replotted on logarithmic co-ordinates in Figs. 18 and 19. Again the data are represented reasonably well by straight lines which, in this case, can be defined by equations of the type $F = Cf^a$ where a is the slope of the line measured from the feed axis. Appropriate values of C_c and a, and C_f and b are given for the cutting forces and feeding forces, respectively, in Tables 9 and 10.

The unique advantage of this type of equation is that it is transformed readily into a simple equation for unit power. The power required for feeding is negligible so that only the cutting force need be considered. An equation for unit power is derived as follows:
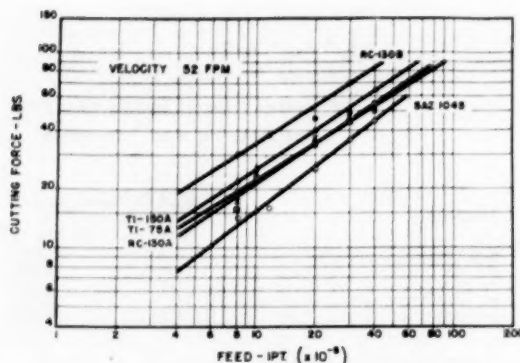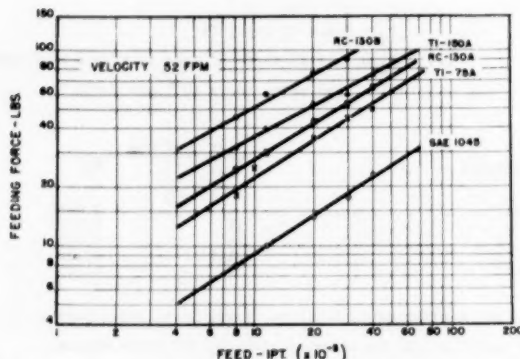
Fig. 18 Logarithmic Plot of Cutting Force in Pounds Versus Feed Rate in Inches × 10⁻⁶ Per Tooth for SAE 1045 Steel and Various Compositions of Titanium at Cutting Speed of 52 Fpm

Fig. 19 Logarithmic Plot of Feeding Force in Pounds Versus Feed Rate in Inches × 10⁻⁶ Per Tooth for SAE 1045 Steel and Various Compositions of Titanium at Cutting Speed of 52 Fpm

$$HPu = \frac{\text{Cutting force (lb)} \times \text{cutting speed (fpm)}}{33,000 \times \text{cu in. per min}}$$

$$= \frac{C c f^a \, V c}{33,000 \times \frac{72}{3} \, V c \times f \times 0.055 \times 1 \times 10^{-6}}$$

$$= 22.9 \, C c f^{a-1}$$

where 0.055 is the kerf and 72/3 is the number of teeth per minute for teeth of similar set. For sawing the RC 130B titanium the equation becomes

$$HPu = 41.3 f^{-0.36}$$

For a feed of 80 millionths of an inch per tooth

$$HPu = 41.3 \times 80^{-0.36}$$

$$= \frac{41.3}{4.85}$$

$$= 8.6$$

TABLE 9 EXPONENTIAL EQUATIONS FOR CUTTING FORCE

Formula: $F_c = C_c f^a$ for various materials, where f is in in. x 10^{-6}/tooth

Material	C_c	a
SAE 1045	0.4	0.79
Ti 75A	1.07	0.65
RC 130A	0.66	0.74
Ti 150A	1.3	0.65
RC 130B	1.8	0.64

TABLE 10 EXPONENTIAL EQUATIONS FOR FEEDING FORCE

Formula: $F_f = C_f f^b$ for various materials where f is in in. x 10^{-6}/tooth

Material	C_f	b
SAE 1045	0.39	0.67
Ti 75A	1.05	0.65
RC 130A	1.52	0.62
Ti 150A	3.3	0.52
RC 130B	4.5	0.53

Similar values for all five work materials at feeds of 80 and 320 millionths are given in Table 11. It is significant that the unit power for bandsawing is from 4 to 7 times as great as that required for turning, milling, and other "thick-chip" operations.

Current theory of cutting forces as developed for orthogonal cutting predicts forces as straight lines through the origin on Cartesian co-ordinates. The corresponding exponential equations would have a slope or exponent of unity. A more exact theory is needed to predict actual performance. At least two major factors have not been treated in classical analyses of cutting forces.

The first of these is the inherent dullness of cutting edges as manifest in the fact that data do not extrapolate to zero. Second, and probably more important, the boundary conditions which can be neglected in orthogonal cutting assume a dominant role in the most common metal-cutting operations, including sawing. As the width of cut is decreased for a given thickness, more of the interior of the chip has greater freedom to flow thus requiring proportionately less force to deform the metal in forming the chip. This phenomenon would cause the force curve to be convex upward on Cartesian co-ordinates and linear correlation with cut thickness would be impossible. However, the same data plotted on logarithmic co-ordinates could be represented by a straight line with a slope less than unity. This conforms with common experience.

The exponents a and b in Tables 9 and 10 are all significantly less than unity. A small part of the differential between the actual value of the exponent and unity is due to the inherent dullness manifest in residual forces at zero rate of metal removal. The remainder of the differential is probably due to the extra degree of freedom at the boundaries. The exponential equation may mask the causes of deviations from linear theory but it is a

TABLE 11 UNIT HORSEPOWER FOR VARIOUS MATERIALS

Material	F_{c80}	F_{c320}	HPu 80 in. x 10^{-6} tooth	HPu 320 in. x 10^{-6} tooth
SAE 1045	14	27.5	4.0	2.6
Ti 75A	20	44.5	5.7	4.0
RC 130A	17.5	47.5	5.0	3.5
Ti 150A	22.5	53.5	6.4	4.5
RC 130B	30	75	8.6	6.0

more exact expression of performance in addition to being a convenient form for the use of force information.

Conclusions

1 Bandsawing done with positive power feed is orderly and predictable.

2 An exponential equation of the type $VT^a = C$ can be used to express the relationship between cutting speed and tool life for bandsaws.

3 The exponents n of the equation $VT^a = C$ are of the same magnitude for both turning and bandsawing.

4 The relative machinability of the five materials studied is about the same for bandsawing as it is for turning.

5 Titanium alloys can be sawed more satisfactorily by using positive motion, power feed.

6 The end of useful tool life in bandsawing is accompanied by an abrupt increase in the feeding force required to sustain the same rate of metal removal.

7 Both cutting and feeding forces vary substantially linearly with the feed rate except for residual values at zero rate of metal removal.

8 The feeding force for sawing SAE 1045 steel is approximately half that required in the cutting direction.

9 The feeding force for commercially pure titanium is the same as that for cutting.

10 The feeding force for titanium alloys is substantially greater than that required in the cutting direction.

11 The coefficient of sliding friction between titanium and the bandsaw material appears to be significantly less than for SAE 1045 hot-rolled steel.

12 The exponential equation appears to be a more realistic form for expressing cutting-force data for metal cutting in general.

Acknowledgment

Grateful acknowledgment is made to the Watertown Arsenal and its laboratory staff for support and encouragement in undertaking this investigation.

Discussion

C. J. Oxford, Jr.[3] The authors are to be commended upon their ingenuity in devising performance criteria for such an unpredictable tool as the bandsaw. The success of their approach is evident in the correlation of their bandsawing data with that from other machining operations—and metal-cutting research to date indicates that this correlation should exist even in the case of the extremely thin chips encountered here. Positive feed has made this possible; it is unfortunate that positive feed is not more generally used in bandsawing nearly all metals. The increased tool life to be attained by operating under controlled conditions would appear to be worth while, particularly on the tougher metals.

The selection of feeding force as a tool-life criterion is very good. This force component reflects both flank wear and taper or loss of set on the sides of the blade. The writer has found that feeding force is a very sensitive indicator to tool-dulling on another light chip-load tool—small end mills. Here an increase in feeding force above a certain experimentally established value has nearly always indicated that the end mill is producing an unsatisfactory slot, either from the standpoint of size or surface finish.

The selection of the 100-lb feeding force as the failure point might be criticized in that this value is above the bend in the

feed force-tool life curves. However, since bandsaws generally are not resharpened, there would appear to be no disadvantage to running to nearly total destruction. This technique is probably representative of actual shop-operating practice.

G. H. Sheppard.[4] Several questions are left unanswered in the paper, such as, the type of saw set, clearance angle, rake angle, back angle, camber, twist, and analysis of the steel in the bands tested. All of this should be considered when formulating a procedure for tests of this nature. The writer would conclude that if information of this type is to be fundamentally reliable from a standpoint of basic engineering, facts such as mentioned cannot be overlooked. It may be that these facts were not overlooked but they are not contained in the paper.

A paper of this type should be the result of a thorough investigation confined to one material only with known analysis and homogeneity, rather than one including several materials. The test should be run on a machine with maximum control of horsepower delivered to the point of cut, good mechanical ability, band-tensioning adjustment, power feed, proper guide setup, coolant facilities, and an identifiable band tool.

For comparison purposes we would like to suggest further that it would be advisable to conduct tests using constant lineal work-travel rate and also constant feeding force. We could offer many suggestions based on thousands of tests already conducted which might be of value in establishing testing procedures for the evaluation of bandsaw performance for the use of basic engineering. The writer will be pleased to co-operate in supplying information on these tests if desired.

C. A. Sluhan.[5] The authors state that a solution of sodium nitrite in water was an extremely effective material for the sawing of titanium. In their opinion, is this effect due to a chemical reaction between sodium nitrite and titanium or is it due to the fact that a solution of sodium nitrite in water has a greater heat-conducting capacity than does plain water?

Authors' Closure

The authors wish to thank Messrs. Oxford, Sheppard, and Sluhan for their interest and observations. Mr. Oxford points out that the limiting feeding force of 100 lb would appear to be arbitrary and might be criticized for that reason but also, as he indicates, it was selected simply because it is well beyond that value of feeding force at which the increase in force is precipitous. Consequently, almost any convenient value above the bend will result in slight error where the objective is to determine the end of useful tool life. Obviously an appropriately larger or smaller force should be selected for larger or smaller cuts respectively. The significant conclusion is that trend in the feeding force is a sensitive criterion of tool life.

Mr. Sheppard raises several questions regarding details of the bandsaws used for these tests. Details concerned with set, clearance angle, rake angle, and so on, were not stated explicitly but were implied in the statement that the sizes were standard Simonds "Hard Edge," $^3/_c$-in-wide 6-pitch roll stock. This material is available to anyone and leaves no secrets regarding the details questioned by Mr. Sheppard.

We assume that Mr. Sheppard is expressing a personal opinion rather than stating a question when he says that a technical paper of this type should be the result only of an investigation confined to one material of known analysis and homogeneity. However, we must disagree, in that we believe any investigation intended to develop or verify the soundness of a technique must of neces-

[3] Research Engineer, National Twist Drill & Tool Co., Rochester, Mich.

[4] Director of Research, The DoALL Company, Des Plaines, Ill.

[5] President, Master Chemical Corporation, Toledo, Ohio.

sity include the common variables such as are encountered in the industrial shop; it goes without saying that the work material is a common variable.

Mr. Sheppard goes further in stating, "the test should be run on a machine with maximum control of horsepower delivered to the point of cut, good mechanical ability, band-tensioning adjustment, power feed, etc.". The context of our paper indicates that these conditions were met but we question how one accomplishes control in the delivery of horsepower when it is recognized that the power is a reaction to the resistance encountered during the motion of the saw and in the components of the machine.

Mr. Sheppard suggests, "it would be advisable to conduct tests using constant lineal work-travel rate." It was pointed out early in the paper that constant lineal work-travel rate was used for this investigation. Further, it was pointed out that constant feeding force could not be used successfully in sawing the titanium alloys. The authors would be pleased to receive the results offered by Mr. Sheppard from the "thousands of tests already conducted" since a thorough analysis of them not only would be interesting but also would be very useful to industry. We would urge Mr. Sheppard to publish the results of these works for the benefit of all.

We wish to correct an apparent misinterpretation by Mr. Sluhan. The authors did not state that a solution of sodium nitrite in water was extremely effective for sawing titanium. As a matter of fact, it is stated explicitly that all tests were conducted dry.

The Momentum Principle Measures
Mass Rate of Flow

By V. A. ORLANDO[1] AND F. B. JENNINGS,[1] WEST LYNN, MASS.

The operation of a flowmeter which accurately measures
the mass flow of fluid is described. Compared with con-
ventional flowmeters, this instrument has many advan-
tages, including a linear torque output easily adaptable to
direct reading, remote indication, or control initiation.
It is more easily installed in pipe lines than most flow-
meters and can be mounted in any attitude. It has high
accuracy, low pressure loss, small size, and light weight.
The sample was tested using liquid petroleum fuels of
various viscosities and densities, giving errors less than 0.5
per cent of full scale.

INTRODUCTION

FOR many years, experimenters have explored means of meas-
uring the rate of fluid flow on a true mass basis. Mass-flow
measurements are required in such applications as the com-
bination of reagents in chemical processes; the transportation of
different fluids in pipe lines; and the measurement of fuel con-
sumption in aircraft. Conventional flowmeters used to measure
mass-flow rate are compensated for errors due to density and
viscosity changes of the fluids. The magnitude of the density errors
is shown in Fig. 1. These errors arise because the responses of
familiar flowmeters are not independent of the density of the
most fluids being measured. The volumetric flowmeter responds to
the ratio of the mass-flow rate and density; the simple orifice
responds to the ratio of the mass-flow rate and the square root of
density, and the tapered tube and bob which is widely used
for measuring mass flow over specified density and viscosity
ranges responds to the ratio of the mass-flow rate and a function
of density.

In developing a true mass flowmeter a fundamental approach
is to introduce a constant velocity into the fluid. The resulting
changes in energy or momentum are directly proportional to the
mass-flow rate. Measurable effects can be formed which are
proportional to the mass-flow rate. The measurement is usually
accomplished by measuring one of the following: Input power
of the rotating source, pressure, force, or torque generated by
the fluid.

An early flowmeter operating in this way was developed in the
Technical University of Delft about 1941.[2] In this flowmeter
a cylinder is placed in the middle of the fluid stream with its
axis perpendicular to the direction of flow. This divides the
fluid stream into two equal parts which flow around the cylinder
when the cylinder is not rotating. By driving the cylinder about
its axis with a constant angular velocity, a circulation is added to

RESPONSE VS. DENSITY RELATIONS ARE AS FOLLOWS:

A. VOLUMETRIC FLOWMETER $R = M/\rho$

B. ORIFICE & VENTURI $R = M/\sqrt{\rho}$

C. TAPERED TUBE & BOB $R = M/\sqrt{\rho(K - \rho)}$

D. MASS FLOWMETER $R = M$

WHERE R = RESPONSE, M = MASS RATE, ρ = DENSITY, AND
K = CONSTANT.

FIG. 1 THEORETICAL ERROR OF VARIOUS FLOWMETERS

the fluid. This circulation, added to the axial flow of the fluid,
increases the flow on one side of the cylinder and decreases the
flow on the other side, producing a pressure difference which is
proportional to the mass-flow rate.

The first flowmeter developed in conjunction with the work to
be reported here imparted a constant velocity to the fluid by
causing the fluid to flow through an arrangement similar to the
familiar rotary lawn sprinkler. The radiating pipes, however,
were straight and were driven at a constant angular speed. This
rotating arrangement, with necessary baffling and detection
means, was placed in a housing which kept the fluid line closed.
The fluid entered at the axis of rotation with little or no angular
velocity, experienced a Coriolis acceleration, and left the outer end
at the tip velocity of the rotating tubes. The torque necessary
to accelerate the fluid is a true measure of the mass-flow rate.

A sample of this flowmeter gave excellent results in actual tests,
and work on it would have been carried further if the flowmeter
which is the subject of this paper had not been conceived.
Messrs. Y. T. Li and S. Y. Lee of the Massachusetts Institute
of Technology independently investigated the Coriolis flowmeter
and reported on certain versions of it.[3]

The reason the present authors looked beyond the Coriolis
flowmeter was to find, if possible, a principle which allowed a
simpler, more flexible mechanical-instrument design. The
fundamental momentum theories, of which the Coriolis accelera-
tion is a special case, were studied and the concepts evolved were
incorporated in the sample shown in Fig. 2. The results of tests
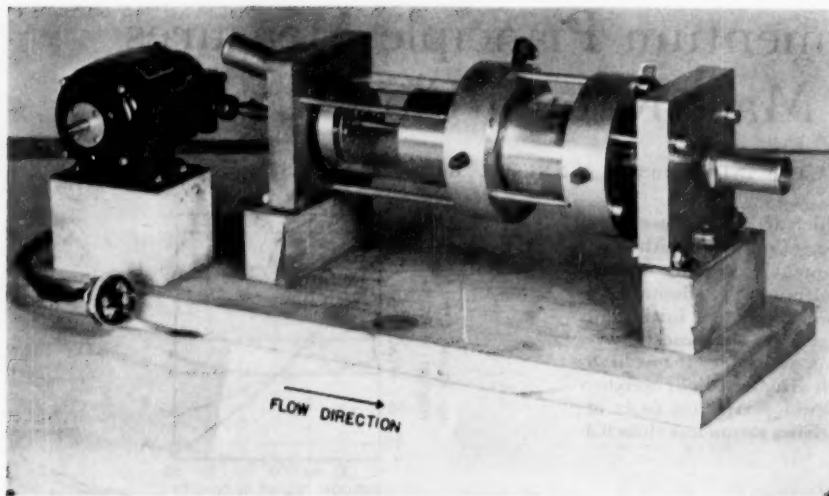on aircraft fuels showed the instrument to have the following
features:

FIG. 2 (*left*)   SAMPLE FLOWMETER

1   Flow measurement on a mass basis independent of fluid density and viscosity.

2   Linear response which can be adapted for direct reading, remote indication, or control initiation.

3   Low pressure loss.

4   Small size and weight.

5   Operates in any attitude, independent of acceleration.

6   Does not require auxiliary flow-straightening devices.

7   Pressure and flow rates unaffected by malfunction of the instrument.

8   Scale range of the instrument is easily changed.

Theoretical considerations show the flowmeter to be unaffected by variations in pressure and temperature and also that the average value of rapidly pulsating fluid flow is measured correctly.

PRINCIPLE OF OPERATION

Fig. 3 is a schematic representation of the sample shown in Fig. 2. The unit consists of two similar cylinders placed end to end so that the two axes coincide. The instrument housing closely fits the outer diameter of the cylinders. Around the periphery of the cylinders are located a number of passages, the axes of which are parallel to the axes of the cylinders. Fluid moving through the pipe line enters the passages in the first cylinder, proceeds through the passages in the second cylinder, and continues along the pipe line. By driving the upstream cylinder, termed the impeller, at a constant angular velocity about its axis, the fluid is given a constant velocity at right angles to the fluid flow. This angular velocity constitutes a change in momentum of the fluid. The second cylinder, termed the turbine, is designed to remove all the angular momentum from the fluid. In doing so, a torque is exerted on it in accordance with Newton's second law of motion. This torque deflects a spring restraining the turbine. The angular deflection of the turbine is a measure of the mass rate of flow.

The equation relating the torque output and mass rate of flow is derived as follows. Newton's law applied to rotating bodies may be written

$$T = \frac{dH}{dt} \dots\dots\dots\dots\dots\dots\dots\dots [1]$$

where T is the torque and H is the angular momentum of the rotating body.

Consider a small mass of fluid dm, which leaves the impeller in the time interval dt. Fig. 4 shows an impeller having N-passages. In this case, dm consists of N-wafers of fluid of thickness $V\,dt$. The flow velocity V is considered to be uniform across

FIG. 3 (*right*)   DIAGRAM SHOWING PRINCIPLE OF MASS FLOWMETER
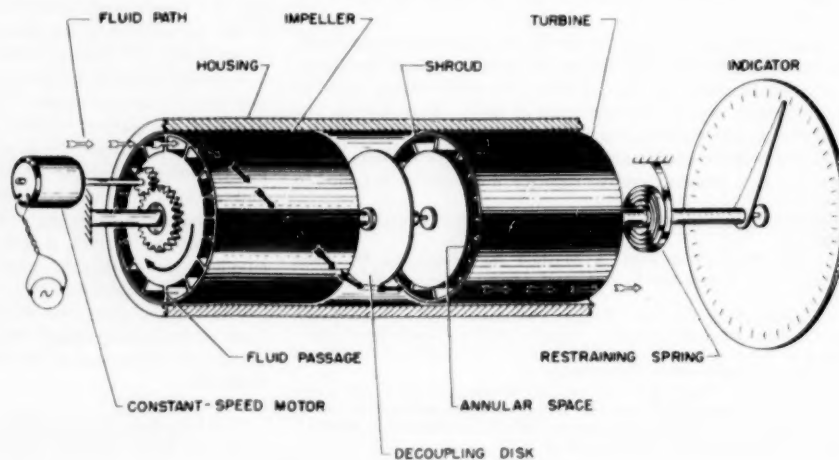
the impeller passages. As these fluid wafers rotate with the impeller, their angular momentum can be expressed as

$$dH = \omega dI \dots\dots\dots\dots\dots\dots [2]$$

where ω = angular velocity of impeller; dI = moment of inertia of N fluid wafers shown in Fig. 4 about the axis of the impeller.
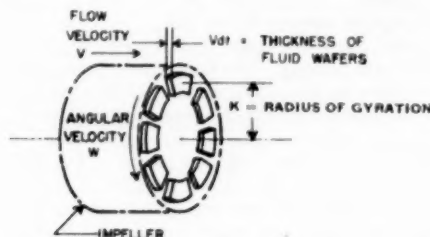
FIG. 4   DIAGRAM SHOWING FLUID WAFERS OF MASS, dm

It is convenient to express the moment of inertia in terms of a radius of gyration k which depends mainly on the distance between the rotation axis and the center of the passages and only to a small extent on the shape of the passages

$$dI = k^2 dm \dots\dots\dots\dots\dots\dots [3]$$

On substituting this in Equation [2] and dividing by the time interval, dt, the rate at which fluid angular momentum leaves the impeller and enters the turbine is given by

$$\frac{dH}{dt} = \omega k^2 \frac{dm}{dt} \dots\dots\dots\dots\dots [4]$$

where dm/dt is the mass rate of fluid flow.

Since the turbine is designed to remove all the angular momentum from the fluid, the rate at which angular momentum is lost to it is equal to the entrance rate given by Equation [4]. Thus the torque exerted by the fluid on the turbine is by Equation [1]

$$T = \omega k^2 \frac{dm}{dt} \dots\dots\dots\dots\dots [5]$$

Equation [5] shows that the torque received by the turbine is proportional to the mass rate of flow, and that the proportionality constant, ωk^2, depends only on the angular velocity and dimensions of the impeller. The torque output does not depend on fluid density. In practice, the equation applies for liquids or gases and whether the flow is laminar or turbulent.

In the case of pulsating flow, the linear torque equation implies that the average turbine deflection measures the average flow rate. If the pulsation frequency is higher than the natural frequency of the turbine, the oscillations will be small and the turbine deflection will indicate the average rate of flow.

TEST RESULTS

In the sample, the impeller and turbine shown in Fig. 5 are almost identical, being $2\frac{1}{2}$ in. diam $\times$ $2\frac{1}{2}$ in. long. The impeller is driven by a synchronous motor at 60 rpm. The turbine is restrained from turning by a spiral spring having a torsion constant of 0.0042 oz-in. per deg. The cylindrical surface of the turbine is marked in degrees and the readings of the instrument are made by noting the rotation of the turbine with respect to lines scribed on the glass housing. Pressure taps are placed in the instrument before the impeller and behind the turbine.

Fig. 6 shows a calibration curve of the flowmeter using kerosene and jet-engine fuel. All of the test points are accurate to within 0.5 per cent of the full-scale range. The accuracy of the
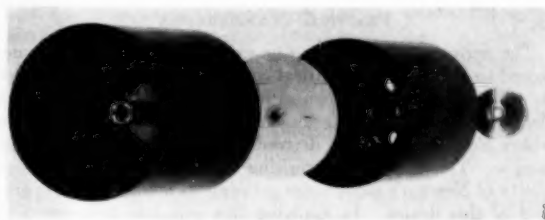
FIG. 5   IMPELLER, DECOUPLING DISK, TURBINE, AND RESTRAINING SPRING
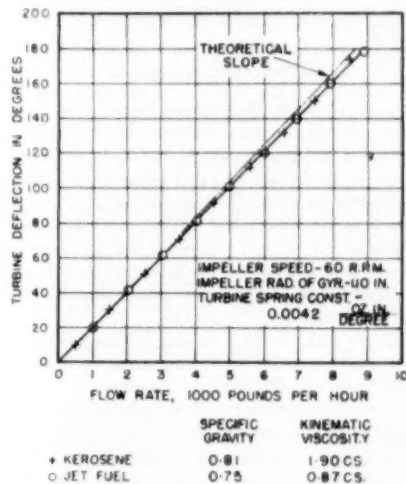
FIG. 6   CALIBRATION OF SAMPLE WITH TWO FUELS

test equipment was 0.5 per cent of point. The close agreement between the experimental and theoretical curves shown in Fig. 6 is a significant indication of the inherent accuracy of the device.

The maximum pressure drop across the cylinders was less than $\frac{1}{4}$ in. of water. This indicates that the pressure loss across an instrument will depend on the inlet and outlet arrangement of the particular design.

The highest flow rate measured with the sample flowmeter was 18,000 lb per hr. There was no indication that the torque would not remain linear at higher values of flow.

The response time of the sample flowmeter was about 4 sec to come within 1 per cent of the steady-state indication. There were slight transient oscillations of the turbine at low flow rates, but at high flow rates it was overdamped. Any motion of the turbine with flow existing imparts momentum to the fluid as it leaves the turbine, and this action produces a damping torque proportional to both the turbine velocity and the flow rate. The magnitude of the damping torque is given by Equation [5] where, in this case, k is the radius of gyration of the passages in the turbine and ω is the turbine angular velocity.

Tests were made on the flowmeter in all attitudes, without appreciable error. When the impeller motor was switched on and off, no change was detected in the actual flow rate or in the pressure drop across the instrument, showing that malfunction of the motor cannot interfere with the flow of fluid in the pipe line.

The test data taken were limited to liquid petroleum fluids. In view of the close agreement between the theoretical and experimental results of these tests, it is reasonable to expect that other liquids as well as gases can be measured with considerable accuracy by a properly designed flowmeter of the present type.

Practical Consideration

The performance which can be expected from any device designed to apply a mathematical equation depends on the degree to which the physical design satisfies the assumptions on which the equation is based. Results indicate that the assumptions on which Equation [5] was derived were applicable to the test sample. This is not too surprising when one considers the simplicity of Newton's momentum principle as applied in the operation of this device. In applying this principle to a practical design, it is merely necessary to determine where undesirable torques may be developed and where momentum may be gained or lost, and design the flowmeter to minimize these unwanted conditions. The more important considerations are discussed in the following.

Impeller Design

As has been indicated, the primary function of the impeller is to impart a constant angular velocity to the fluid. Equation [5] shows that if the impeller speed varies, an error is introduced in the device which is equal to this per cent variation in speed. It is no problem to maintain constant angular velocity where power from a modern electrical utility is available, since a synchronous motor can be used; however, for the cases where only direct current is available or the alternating-current frequency varies, a small constant-frequency power supply has been developed to drive the impeller motor.

To be certain that the fluid leaving the impeller is rotating at the same angular velocity as the impeller, it is necessary that flow straighteners, in the form of passages, be built into this cylinder. This is the reason that no external flow straighteners are required in the flowmeter installation. The dimensions of the passages found most effective in flow straightening are long and have only a small cross-sectional area. The shape of the passages is not particularly important, except as it affects pressure drop in the instrument. Where improper flow straightening is present, the angular velocity of the fluid leaving the impeller might be either greater or less than the impeller speed. With properly designed flow-straightening passages in the impeller, stationary flow straighteners upstream of the impeller were found unnecessary, even when swirling fluid was introduced.

It is important that the axis of the passages be parallel to the axis of rotation of the cylinders. Skewed holes tend to introduce angular momentum into the fluid which results in torques that vary as the product of the density and the square of the fluid velocity. These torques are undesirable because they introduce the same density errors as an orifice, as shown in Fig. 1.

Angular Momentum Effects

In the construction of the flowmeter, clearance is required between the cylinders and the housing and fluid leaks through this gap. The magnitude of the resulting error has been found to be very small. With the low pressure drops encountered across these cylinders, a gap of 0.020 in. has been found to have an undetectable effect on a calibrated flowmeter.

The radius of gyration k in Equation [4] is a function of both the circulation of the fluid about the axis of rotation and the swirling or rotation of the fluid in each passage. The amount of rotation introduced in the fluid is a function of its viscosity and therefore the angular momentum also depends on viscosity. If the flow velocity is kept relatively high and the fluid passages are placed at relatively large distances from the axis of the cylinders, viscosity effects become very small. In such a design the radius of gyration is very nearly the distance from the rotation axis to the middle of the radial width of the passages.

Several tests were made to determine the need for shrouds on the impeller and turbine, shrouds being the outer coverings on the cylinders shown in Fig. 3. Impellers without shrouds were found to give low torque outputs and extreme nonlinearities at low flow rates. There are probably several reasons for this:

1 The fluid tends to remain fixed to the housing and passes from one passage to the next between the edges of the partitions and the housing. This leakage has the effect of imparting insufficient angular velocity to the fluid.

2 Another effect also results from the viscosity of the fluid in contact with the housing. The fluid in each passage is set rotating in a manner similar to the way snow rolls when pushed with a plow. A little consideration shows this rotation to be in a direction that subtracts angular momentum from the fluid. Since the fluid is in these openings longer at low flow rates, it gains more of this type of rotation, resulting in low torque outputs over this range of operation. Turbines without shrouds were also found to give low torque outputs and nonlinearities at low flow rates. One reason for this, no doubt, is the leakage effect described for the impeller. But a much more important reason is that, through viscous effects, angular momentum is lost to the housing in the space between the cylinders. This loss is greater at low flow rates because the fluid is in this space for a longer time. By adding the shroud to the turbine and keeping the distance between it and the impeller shroud very small, this effect is eliminated.

In deriving the equation of the flowmeter, the fluid velocity was assumed constant across the cross section of the passages. Theoretically, the radius of gyration should be slightly different for laminar and turbulent flow. However, because of the turbulence set up as the fluid enters the cylinders, the flow in the passages is turbulent even at Reynolds numbers considerably below the critical. For this reason, even though the flow rate in the pipe line may be extremely low, the turbulent effects of the fluid entering the passages in the flowmeter justify the assumption of constant fluid velocity across the passages.

Eliminating Stray Torques

In the theory of operation of the flowmeter, the torque necessary to supply momentum to the fluid equals the torque necessary to remove it; therefore, to obtain a measure of the mass flow rate, it is only necessary to measure the torque required to drive the impeller as the fluid passes through it. However, because of the viscous torque that would be developed in the small gap between the housing and the rotating impeller, an error would result. To prevent this error, the momentum is removed from the fluid by the turbine, the resulting torque driving the turbine to a stationary position. In the design of the turbine, all of the points of construction for the impeller apply. However, it is of value to emphasize that the turbine is designed solely to remove angular momentum from the fluid. The impeller is designed to supply the required angular momentum for the desired torque output of the instrument.

When one considers that the rotating impeller is only a small distance from the stationary turbine, the viscous coupling between these two cylinders is immediately appreciated. By placing a stationary disk between these two cylinders, as shown in Fig. 3, this effect is greatly reduced.

Equation [5] indicates that the torque developed by the device and, therefore, the full-scale range of the instrument, can be changed by merely changing the impeller speed. At high speeds, a large error can be introduced by a torque which develops between the impeller and turbine in a manner similar to that employed in an automotive fluid coupling. It is due to the centrifugal force on the fluid revolving with the impeller. In tests made driving the impeller at different speeds, it was found that the slopes of the

linear portion of the calibration curves were directly proportional to the speed of rotation but that the angular deflection of the turbine at zero flow rate was excessive at the higher impeller speeds. This effect was noticeably reduced by reducing the width of the passages in the radial direction and removing a short length of the partitions at the upstream end of the turbine as shown in Fig. 3. In the sample flowmeter this effect is less than 1 per cent of full scale at zero flow rate. Since tests show this error to decrease with increase in fluid viscosity, it is concluded that the centrifugal-force effects are greater than the viscous-coupling effect. When the instrument is once calibrated, errors resulting from these effects are negligible.

The results of all the effects discussed here indicate that an accurate flowmeter should have long cylinders with passages having small cross-sectional areas located at relatively large distances from the center of rotation. The rotation of the impeller should be slow. Both cylinders should have shrouds, the adjacent ends of which are located as close together as practical. A stationary disk should separate the cylinders. Results of repeated tests show that such a design will give consistent data and nothing in the construction will have a critical effect on the operation of the instrument.

DESIGN POSSIBILITIES

An important feature of the flowmetering principle described in this paper is the possibility of applying it to designs satisfying various specific flowmetering applications. A few of these designs that show promise of useful application are the following:

For control initiation, remote indication and recording, or totalizing, it is often useful to have the output in the form of an electrical voltage which is proportional to the flow rate. A suitable signal can be obtained with low friction from a variable-ratio transformer whose armature is supported on the turbine shaft. Such signals from two or more flowmeter outputs can be added by connecting them in series and the totalized flow rate can be presented as a separate indication.

The total mass of fluid which is passed through the flowmeter can be measured by integrating the flow rate with respect to time. One of the simpler means of accomplishing this is to use a servomotor to drive both a tachometer and a counter which indicates the total mass of fluid. The error signal which is amplified to operate the servomotor would be the difference between the tachometer output and the signal from the flowmeter.[4]

CONCLUSIONS

The many features which are offered by this flowmeter have been applied to the measurement of fuel to the engines of aircraft.[5] The system in production incorporates a constant-frequency power supply and remote indication. Work is under way to develop flowmeters for aircraft with ranges up to 600,000 pph which will indicate the total fuel delivered during any given time.

A method of presenting on one indicator the total flow rate of fuel through several flowmeters also is being developed. Sample flowmeters have been built to measure the flow rate of gases as well as the total flow of gases in pounds. Tests on these units have been satisfactory.

It is expected that mass flow of liquid and gases will be indicated or recorded in whatever way is most convenient for the application. Such instruments hold promise of finding many applications in the chemical, aircraft, and other industries.

---

[4] "Velodyne," by F. C. Williams and A. M. Uttley, *Journal of the Institution of Electrical Engineers*, V-93, IIIA, 1946, p. 1256.

[5] "Fuel Mass Flowmeter Meets Needs of Aircraft Operation," by H. T. Wrobel and R. F. Buckley, *Aviation Age*, December, 1953, p. 136.

The Viscosity, Thermal Conductivity, and Prandtl Number for Air, O_2, N_2, NO, H_2, CO, CO_2, H_2O, He, and A

By JOSEPH HILSENRATH[1] and Y. S. TOULOUKIAN[2]

The low-pressure viscosity and heat-transfer parameters—thermal conductivity and Prandtl number—are tabulated for air, nitrogen, oxygen, hydrogen, argon, carbon monoxide, carbon dioxide, nitric oxide, steam, and helium. The values reported are based on recent critical correlations of the thermodynamic and transport properties of these gases at the National Bureau of Standards. The properties are tabulated for atmospheric pressure and extend from 100 K (180 R) to as high as 2000 K (3600 R) in some instances. The effect of pressure on the viscosity is presented in tabular form for oxygen, nitrogen, hydrogen, steam, carbon dioxide, and argon for pressures up to 100 atm in the experimental range of temperatures. The Prandtl numbers for air given in this work are compared with existing published and unpublished values which are in extensive use. Plots are included showing the scatter among the experimental data and deviations between them and the tabulated values. They present a very clear picture of the extent and concordance of the experimental data. A nomogram is included for obtaining fractional powers of the Prandtl number.

Introduction

AN increasing number of heat-transfer problems ranging from the design of heat exchangers to the aerodynamic heating of planes and missiles require among other data a precise knowledge of the transport properties, the heat capacity, and the Prandtl number of gases. A brief survey of the extent of the experimental viscosity and thermal conductivity data for 12 gases available in 1948 was given by G. A. Hawkins (1).[3] Later F. G. Keyes (2) published a more detailed review of these experimental data for nine gases, giving correlating equations and a theoretical discussion on the calculation of viscosities for nonpolar molecules from the characteristic Lennard-Jones parameters for the gas in the manner of Hirschfelder, Bird, and Spotz (3).

This paper reports some of the results of a comprehensive compilation and correlation of thermal data—thermodynamic as well as transport properties—for gases undertaken by the authors and their colleagues at the National Bureau of Standards with the co-operation of the National Advisory Committee for Aeronautics. Tables and charts are presented of dynamic and kinematic viscosity, thermal conductivity, specific heat, and Prandtl number for the gases—air, nitrogen, oxygen, hydrogen, argon, carbon

monoxide, carbon dioxide, nitric oxide, steam, and helium.

This paper is the third in a series of publications resulting from the NBS-NACA Thermal Tables Series. The two previous publications by Harold W. Woolley concerned themselves with an improved method for correlating data of state for nonpolar molecules (4) and with a resonance method for measuring the ratio of specific heats, C_p/C_v, (5). A National Bureau of Standards circular is in preparation, as are also a number of NACA Technical Notes covering this work.

The NBS-NACA Tables of Thermal Properties of Gases, the prospectus for which was discussed by Harold J. Hoge (6), were issued in loose-leaf form to a group of research activities soon after the inception of the project to insure quick access to the data by research workers. As the project approached completion and the publication of these tables in a more durable form was in sight, the effort expended in preparing loose-leaf tables seemed less justifiable. It is not anticipated therefore to issue further tables in this series until they appear in a National Bureau of Standards Circular (7).

The tables of properties are based primarily on analytical correlations, some empirical and other semitheoretical, of the existing experimental data. Correlating equations are given for viscosity and thermal conductivity for most of the gases. Composite plots for each of the properties show pictorially the temperature variations of the properties for each of the gases. Even more interesting are the deviation plots which show not only the abundance or paucity, the concordance or discordance of the experimental data, but also the extent and trend of the extrapolated portions of the tables.

The kinematic viscosities in Table 2 were obtained by dividing the values in Table 1 by the relative densities obtained from the correlation of the data of state for these gases to be reported in reference (7).

Correlation of Experimental Viscosity Data

(a) *Dry air.* The dynamic viscosities of dry air at atmospheric pressure were calculated from the equation

$$\eta(10)^7 = 145.8(T)^{3/2}/(T + 110.4) \qquad [1]$$

where η is in poise and T in degrees Kelvin. The calculated values are shown in Table 1 in the dimensionless form η/η_0 where η_0 is the value of the viscosity at 0 C and 1 atm. The value of η_0 is taken as 1716×10^{-7} poise, selected by F. C. Morey (7) as an average value of the work of twenty observers (references 13 to 32). Departures of the experimental data of eleven workers (references 8 to 18) from the tabular values are presented in Fig. 2.

The effect of pressure on the viscosity of air has been investigated by Kellstrom (19) at 20 C over the pressure range 1–29 atm; by Nasini and Pastonesi (33) at 14 C and pressures of 70–200 atm; by Iwasaki (34) at 50, 100, 150 C and pressures to 200 atm; by Golubev (35) at 0, 16, 50, 100 C and pressures to 300 atm; and more recently by Kestin and Pilarczyk (36) at room temperature and pressures to 70 atm. The large discrepancies

TABLE 1 DYNAMIC VISCOSITY AT ATMOSPHERIC PRESSURE

T°K	η/η_0 Air	η/η_0 Nitrogen	η/η_0 Oxygen	η/η_0 Helium	η/η_0 Hydrogen	η/η_0 Argon	η/η_0 Carbon monoxide	η/η_0 Carbon dioxide	η/η_0 Nitric oxide	$\eta \times 10^5$ Steam, poise	T°R
100	0.4038	0.413	0.4050	0.511	0.5006	0.3906	0.3966	0.787	0.3906		180
200	0.7742	0.779	0.7743	0.812	0.6100	0.7647	0.7692	1.091	0.7648		360
300	1.076	1.074	1.0751	1.065	1.0652	1.0795	1.0076		1.079?	9.81	540
400	1.232	1.322	1.3216	1.292	1.292	1.349	1.340	1.410	1.348	13.42	720
500	1.556	1.546	1.5595	1.500	1.503	1.588	1.574	1.697	1.587	17.03	900
600	1.758	1.752	1.7680	1.696	1.699	1.806	1.787	1.958	1.804	20.64	1080
700	1.942	1.943	1.9622	1.881	1.884	2.008	1.986	2.199	2.006	24.25	1260
800	2.112	2.125	2.1447	2.068	2.061	2.198	2.172	2.425	2.196	27.86	1440
900	2.271	2.295	2.3181	2.227	2.230	2.379	2.349	2.637	2.377	31.70	1620
1000	2.420	2.461	2.485	2.391	2.392	2.551	2.519	2.840	2.548	35.85	1800
1100	2.562	2.619	2.648	2.549	2.549	2.717	2.682	3.029	2.714	39.72	1980
1200	2.696	2.771	2.803			2.876	2.842	3.218	2.874	43.27	2160
1300	2.824	2.918	2.951			3.024	2.995	3.394		46.46	2340
1400	2.947	3.061	3.096			3.186	3.142	3.570		49.28	2520
1500	3.066	3.200	3.237			3.321	3.285	3.737		51.74	2700
1600	3.180		3.374					3.903			2880
1700	3.290		3.509					4.062			3060
1800	3.397		3.640								3240
1900	3.501		3.770								3420
2000			3.897								3600

TABLE 2 KINEMATIC VISCOSITY AT ATMOSPHERIC PRESSURE

T°K	ν/ν_0 Air	ν/ν_0 Nitrogen	ν/ν_0 Oxygen	ν/ν_0 Helium	ν/ν_0 Hydrogen	ν/ν_0 Argon	ν/ν_0 Carbon monoxide	ν/ν_0 Carbon dioxide	ν/ν_0 Nitric oxide	Steam centistokes	T°R
100	0.1451	0.1484	0.1450	0.187	0.1831	0.1299	0.5620	1.200	0.1310		180
200	0.5659	0.5694	0.5658	0.596	0.5931	0.5588	1.184	2.075	0.559		360
300	1.182	1.180	1.181	1.172	1.170	1.1860	1.964	3.125	1.186	24.18	540
400	1.952	1.939	1.952	1.898	1.892	1.977	2.884		1.98	38.62	720
500	2.851	2.832	2.858	2.839	2.749	2.910			2.91		900
600	3.867	3.852	3.888			3.972	3.920	4.329	3.97	56.29	1080
700	4.982	4.983	5.035			5.152	5.095	5.674	5.15	77.22	1260
800	6.192	6.223	6.289			6.445	6.368	7.152	6.44	101.4	1440
900	7.491	7.568	7.647			7.848	7.748	8.749	7.84		1620
1000	8.868	9.017	9.109	3.752	3.730	9.350	9.252	10.471	9.34		1800
1100	10.23	10.55	10.67			10.95	10.61	12.28	10.94		1980
1200	11.85	12.18	12.32			12.65	12.49	14.29	12.65		2160
1300	13.45	13.89	14.06			14.45	14.26	16.26			2340
1400	15.12	15.70	15.88			16.34	16.11	18.42			2520
1500	16.86	17.58	14.79			18.31	18.05	20.66			2700
1600	18.64		19.78								2880
1700	20.49		21.86								3060
1800	22.40		24.01								3240
1900	24.27		26.25								3420
2000			28.56								3600

TABLE 2(a)   VISCOSITY AT STANDARD CONDITIONS (1 atm, 0 C)

Gas	$\eta_0 \times 10^7$	$\eta_0 \times 10^2$	ν_0	ν_0
	g sec^{-1} cm^{-1}	lb hr^{-1} ft^{-1}	cm^2 sec^{-1}	ft^2 hr^{-1}
Air	1716	4.151	.1327	.5142
Nitrogen	1662	4.022	.1330	.5154
Oxygen	1919	4.643	.1343	.5204
Helium	1863	4.507	1.044	4.046
Hydrogen	841.1	2.035	.9358	3.626
Argon	2125	5.140	.1191	.4615
Carbon monoxide	1657	4.008	.1325	.5134
Carbon dioxide	1370	3.314	.0693	.2685
Nitric oxide	1792	4.335	.1337	.5181
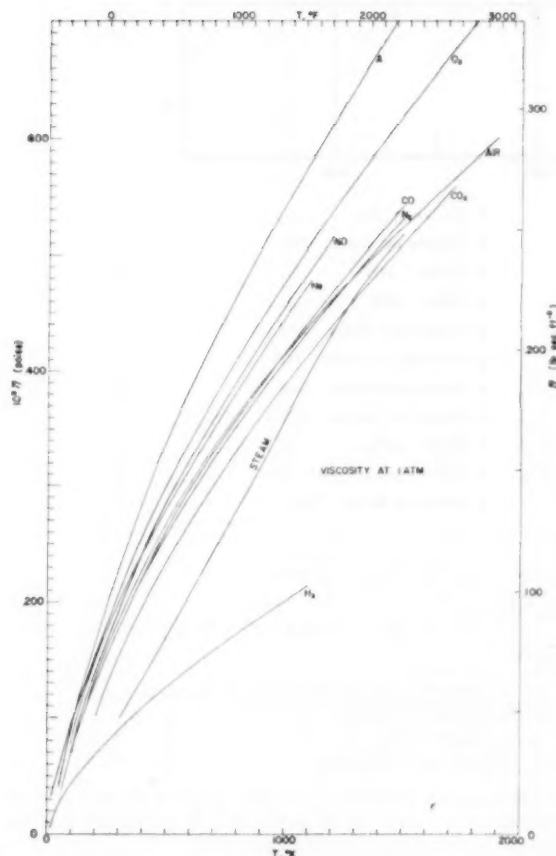
FIG. 1   VISCOSITY OF TEN GASES AT LOW PRESSURE

between the two sets of data at higher temperatures are not immediately resolvable. Therefore, the tabulation for air has been deferred pending the completion of an analysis. In the interim, Fig. 3 should suffice where approximate values are desired.

(b) *Nitrogen.* The dynamic viscosities of nitrogen were calculated using the Lennard-Jones approximation to nonpolar molecules, as applied by Hirschfelder, Bird, and Spotz (3), in which the potential energy of interaction between the two molecules is given by

$$\epsilon(r) = 4\epsilon_m[(r_0/r)^{12} - (r_0/r)^6]$$

where ϵ_m is the maximum energy of attraction and r_0 is the low-velocity collision diameter. The coefficient of viscosity for a single gas is given by

$$\eta(10)^7 = 266.93 V \sqrt{MT}/[r_0^2 W^{(2)}(2)] \ldots \ldots [2]$$

where M is the molecular weight, T is the temperature in degrees Kelvin, and V and $W^{(2)}(2)$ are functions of kT/ϵ. Hirschfelder, et al., have calculated the collision integrals needed for the computation of the transport properties, tabulated the functions V and $W^{(2)}(2)$, and have suggested the parameters for 45 gases (3) on the basis of the more accurate viscosity data in the lower temperature region. For nitrogen they are $\epsilon/k = 91.46$ and $r_0 = 3.681$ Å. The computation of the values of dynamic viscosity given in Table 1 were based on these parameters. The values of the reference viscosity, η_0, is taken as 1662.5×10^{-7} poise at 1 atm pressure and 0 C.

The tabulated values of viscosity are reliable within 5 per cent. A graphical comparison of the tabulated values with the experimental data is shown in Fig. 4. The decided trend of the experimental data at high temperatures would suggest that a modification of the force constants ϵ/k and r_0 is in order. If the constants are chosen as $r_0 = 3.8$ angstroms and $\epsilon/k = 80$, the deviations can be reduced to within 2 per cent. While this choice improves the fit at the higher temperatures, it introduces larger departures in the lower temperature region where the experimental data are probably more precise. Numerical adjustments may be made to the tables on the basis of the deviations shown in Fig. 4, which would bring the values within a few tenths per cent of the experimental data.

The viscosities of nitrogen at higher pressures given in Table 3 were calculated by Hilsenrath and Touloukian (7) from the equation

$$\eta/\eta' = 1 + 0.175(b\rho) + 0.8651(b\rho)^2 \ldots \ldots [3]$$

where b is the viscosity covolume, in cm^3 g^{-1} given by the relation
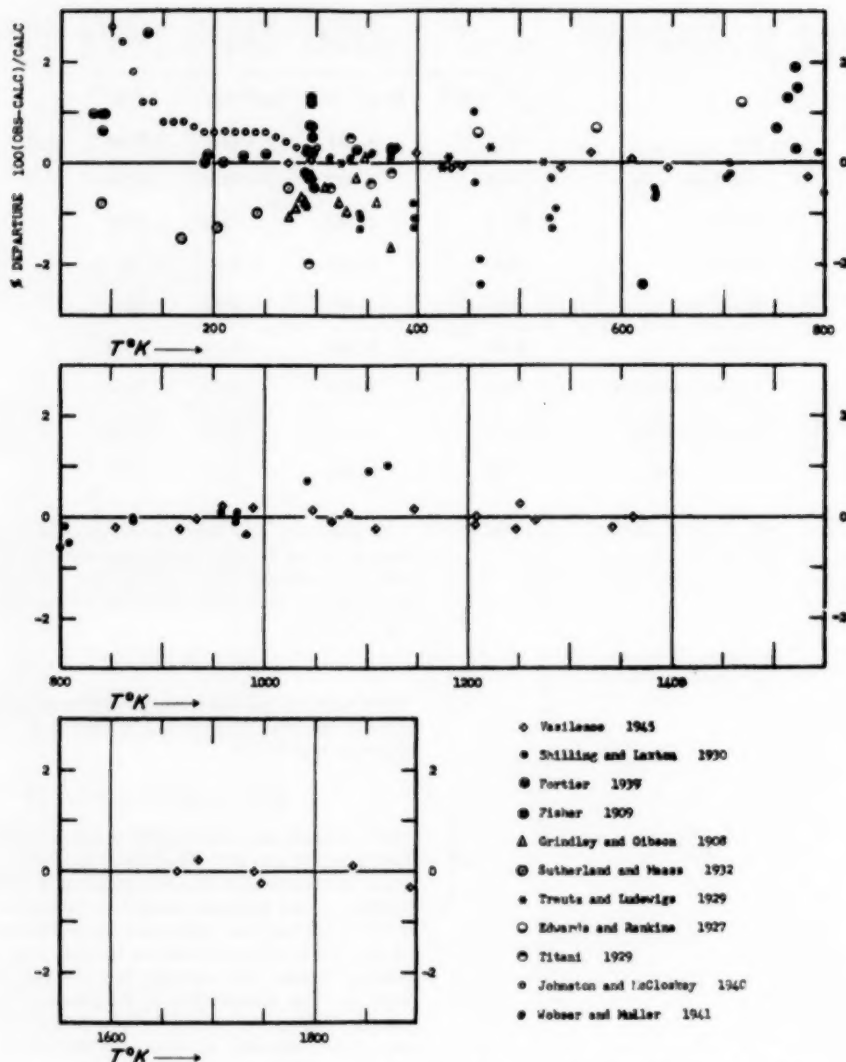
FIG. 2 COMPARISON OF LOW-PRESSURE VISCOSITY DATA FOR AIR WITH VALUES IN TABLE 1

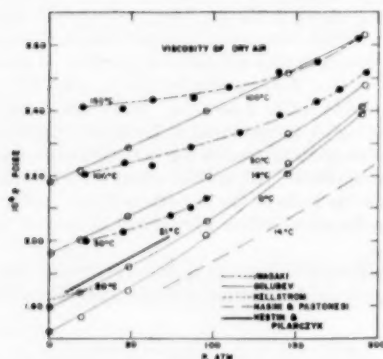FIG. 3 EXPERIMENTAL DETERMINATIONS OF VISCOSITY OF AIR AT ELEVATED PRESSURES

$$b(10)^7 = 1.783 M^{-1/6} (\sqrt{T}/\eta')^{2/3}$$

where

η' = viscosity at 1 atm and T deg K, in poise

M = molecular weight

ρ = density, g cm^{-3}

T = temperature, deg K.

The foregoing equations are based on the theoretical work of Enskog and are given by K. A. Gardner in his discussion of the work of Sibbitt, Hawkins, and Solberg (37).

The departures of the high-pressure viscosity data of Boyd (38), Michels and Gibson (39), and Sibbitt, et al. (37) from this equation are given in Fig. 5. The recent data of Kestin and Pilarczyk (36) at room temperature are in agreement with this correlation within 0.2 per cent up to 40 atm. Above this pressure the departure increases gradually to 1 per cent at 70 atm.

(c) *Oxygen.* The dynamic viscosity data for oxygen were

correlated by R. L. Powell (7) in a manner similar to those of nitrogen, and the values are given in Table 1. For oxygen the characteristic parameters ϵ/k and r_0 were redetermined by fitting to the data of Johnston and McCloskey (17) and Trautz and Zink (40) in the ranges 90 to 300 K and 300 to 1100 K, respectively. The

TABLE 3   VISCOSITIES OF GASES UNDER PRESSURE, $\eta \times 10$

T	1 atm	20 atm	40 atm	60 atm	80 atm	100 atm
°C	poise	poise	poise	poise	poise	poise
			Nitrogen[1]			
20	1.75	1.78	1.84	1.90	1.97	2.05
50	1.88	1.90	1.93	1.97	2.01	2.05
100	2.21	3.11	2.13	2.16	2.20	2.23
200	2.47	2.49	2.51	2.53	2.55	2.58
400	3.14	3.16	3.17	3.19	3.20	3.22
600	3.74	3.75	3.75	3.77	3.78	3.80
800	4.29	4.29	4.30	4.31	4.32	4.23
1000	4.79	4.79	4.80	4.81	4.83	4.83
1200	5.25	5.27	5.27	5.28	5.29	5.30
			Oxygen[2]			
25	2.06	3.16	2.26	2.38	2.50	(2.65)
50	2.20	2.28	2.36	2.48	2.59	(2.72)
100	2.45	3.51	2.59	2.67	2.77	(2.88)
150	2.68	3.72	2.78	2.84	2.92	(3.01)
200	2.90	2.94	2.98	3.04	3.10	(3.17)
			Hydrogen[3]			
-150	4.81	4.90	4.98	5.06	5.18	5.34
-100	6.11	6.15	6.18	6.21	6.25	6.30
0	8.37	8.40	8.43	8.45	8.50	8.55
100	10.35	10.39	10.40	10.42	10.45	10.47
200	12.16	12.18	12.20	12.23	12.25	12.29
300	13.85	13.85	13.87	13.90	13.92	13.94
			Argon[2]			
25		2.28	2.35	2.42		
50	2.41	2.46	2.53	2.61	2.71	
100	2.71	2.75	2.79	2.87	2.97	(3.06)
150	2.95	2.99	3.04	3.10	3.19	(3.31)
200	3.20	3.24	3.30	3.37	3.45	(3.56)
300	3.62	3.65	3.69	3.75	3.82	(3.93)
			Carbon Dioxide[2]			
50	1.60	1.68	1.81	2.05	2.42	
100	1.83	1.87	1.97	2.14	2.55	
150	2.05	2.09	2.16	2.37	2.61	
200	2.25	2.31	2.39	2.52	2.70	
250	2.45	2.50	2.57	2.66	2.80	
300	2.64	2.68	2.75	2.82	2.91	
			Steam[1]			
25	0.0974					
50	1.064					
100	1.255					
200	1.606					
300	1.967	1.978	1.996	2.022		
400	2.328	2.337	2.350	2.364	2.386	2.410
500	2.689	2.698	2.708	2.720	2.734	2.750
600	3.056	3.070	3.079	3.089	3.100	3.112
700	3.477	3.482	3.489	3.497	3.505	3.517
800	3.871	3.876	3.886	3.891	3.899	3.907
900	4.235					
1000	4.563					
1100	4.856					
1200	5.111					

[1] This correlation.
[2] Smoothed values from reported data of Kiyama and Makita [42].
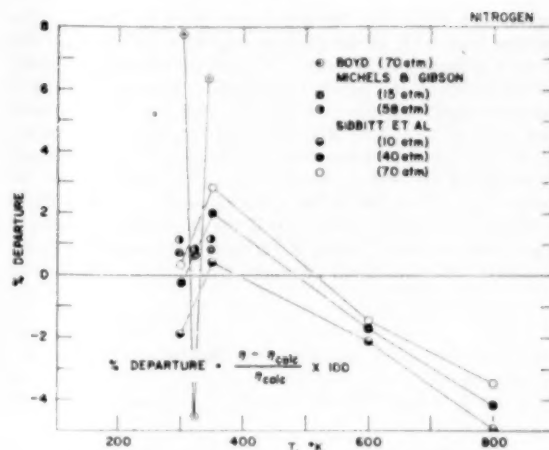[3] Based on Woolley, Scott, and Brickwedde [43].

Fig. 5   Comparison of High-Pressure Viscosity Data for Nitrogen with Equation [3]

values thus obtained were $\epsilon/k = 100$ and $(1/r_0^3)\sqrt{M\epsilon/k} = 4.621$.

The value of η_0 at 1 atm and 0 C was chosen as 1919.2×10^{-7} poise. This value is in close agreement with the determination by Johnston and McCloskey (17) who found the viscosity to be 1918.4×10^{-7} poise at 0 C, based on the value 1833.0×10^{-7} poise as the viscosity of dry air at 296.1 K.

A graphical comparison of the experimental results of six authors (17, 18, 25, 26, 40, 41) is given in Fig. 6. The viscosity values in the table are reliable within 1 per cent below 1000 K. The extrapolated values to 2000 K are reliable within 2 per cent.

Kiyama and Makita (42) have recently measured the viscosity of oxygen from 25 to 200 C and pressure up to 96 atm. The values reported for oxygen in Table 3 were read from smooth isotherms drawn through their reported data.

(d) *Hydrogen*. The dynamic viscosities of hydrogen were calculated from the empirical formula given by Woolley, Scott, and Brickwedde (43)

$$\eta/\eta_0 = 0.1017 \frac{T^{3/2}}{(T+19.55)} \frac{(T+650.39)}{(T+1175.9)} \qquad [4]$$

where the value η_0, the viscosity at 1 atm and 0 C, is taken to be 841.1×10^{-7} poise. In Fig. 7, which is reproduced from reference (43) with minor changes, are plotted deviations of experi-
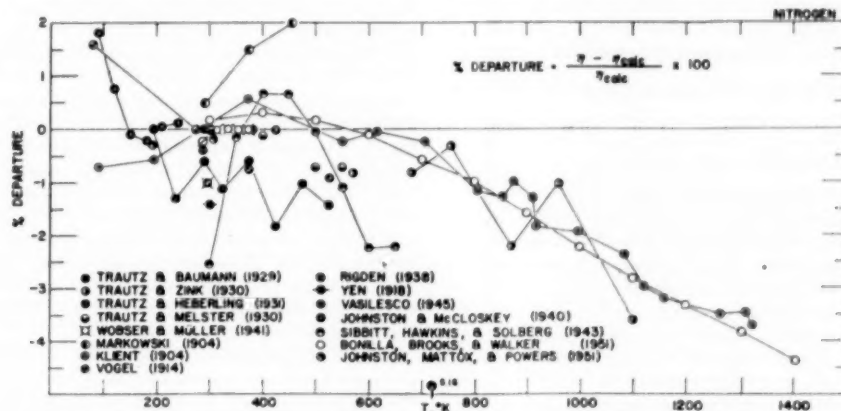

Fig. 4   Comparison of Low-Pressure Viscosity Data for Nitrogen with Values in Table 1

mental data from the viscosity values given in Table 1. No
changes were made in the experimental data for the small dif-
ferences of density from 1 atm. To limit the crowding of experi-
mental points in the figure, those plotted represent only data
published since 1928, but a few data obtained after 1928 also have
been omitted. The data of Trautz, et al. (14, 40, 41, 44, 45, 46, 47,
48, 49) would be in better agreement with the zero line if increased
by about 0.5 per cent for the revision in the value for the vis-
cosity of air. From 200 to 400 K the values adopted are reliable
to within 0.5 per cent. Below 100 K the uncertainty is probably
as great as 1 per cent. Above 400 K there is also considerable un-
certainty. For this region allowance was made for the revision
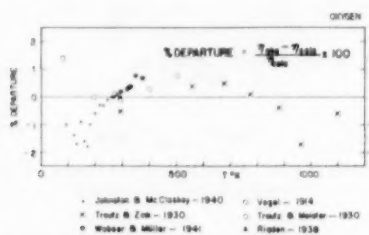
Fig. 6 Comparison of Low-Pressure Viscosity Data for
Oxygen With Values in Table 1

of the old values for the viscosity of dry air, in terms of which the
principal experimental values were obtained. The values adopted
for the higher temperature region may need to be reduced slightly.
A reduction of 2 or 3 per cent in the temperature range from 500
K to 1000 K is to be found in the correlation of Hirschfelder, et
al. (50). It appears quite possible that the theoretical treatment
of Hirschfelder provides the better extrapolation to still higher
temperatures. The differences obtained apparently would be
several per cent.

It has been pointed out by others that the Sutherland formula

$$\eta/\eta' = (T/T')^{3/2}(T' + C)/(T + C)$$

does not fit the data for hydrogen over an extended range of tem-
peratures. This may be seen in Fig. 7, in which the deviations
of the Sutherland formula from values of Table 1 are represented by
the curve below the zero line. The constant C in the foregoing
equation was evaluated at 300 K to represent the trend of the
best data.

The effect of pressure on the viscosity of hydrogen is discussed
by Woolley (43), who gives formulas based on the theoretical
work of Enskog, in accordance with which the ratio of viscosity
at any pressure η, to the viscosity at low pressure (1 atm)η' is
represented adequately over a considerable range of densities by

$$\eta/\eta' = 1 + 0.175(b\rho\chi) + 0.7557(b\rho\chi)^2 - 0.405(b\rho\chi)^3 \ldots [5]$$

where

$$(b\rho\chi) = Z - 1 + T(dZ/dT)$$

Z being the compressibility factor, PV/RT.

There is fairly good quantitative agreement between experi-
mental and theoretical values of η/η' for hydrogen at tempera-
tures immediately above 0 C. The recent data of Kestin and Pilar-
czyk (36) at room temperature, and pressures up to 70 atm are
in excellent agreement with the foregoing correlation on which the
values in Table 3 are based.

(e) *Argon.* The dynamic viscosities of argon were calculated
by Fano and Queen (7) in a manner similar to those of nitrogen.
The values are given in Table 1 in the dimensionless form η/η_0,
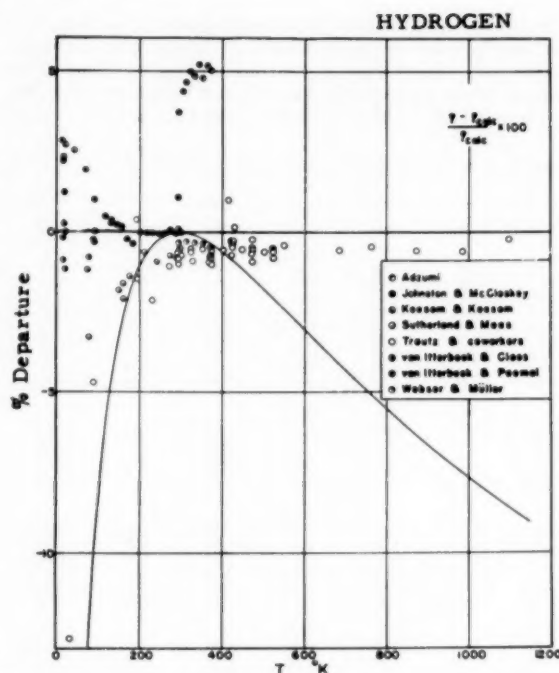where η_0 is taken as 2125×10^{-7} poise at 0 C and 1 atm. The

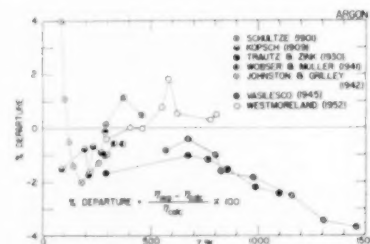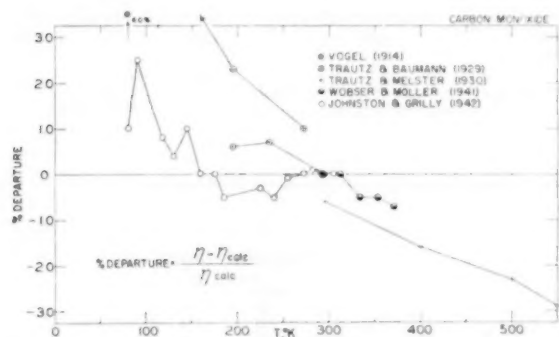Fig. 7 Comparison of Low-Pressure Viscosity Data for Hydro-
gen With Values in Table 1

Fig. 8 Comparison of Low-Pressure Viscosity Data for
Argon With Values in Table 1

characteristic parameters $\epsilon/k = 119.5$ and $r_0 = 3.421$ for argon
were obtained from a complete correlation of the thermodynamic
and transport properties of argon and were used by Beckett and
Fano (7) to calculate the thermodynamic properties of argon.

A graphical comparison of the tabulated values and the experi-
mental data of seven authors (8, 18, 40, 51, 52, 53, 54) is given in
Fig. 8. The viscosities tabulated are reliable to within 2 per cent
between 200 and 600 K and within 3 per cent at higher tempera-
tures. Below 200 K the uncertainties increase from 3 to 10 per
cent. The higher temperature values probably could be improved
by adjusting the assumed force constants for the molecule. The
low-temperature values, however, are insensitive to changes in the
force constants (55). Furthermore, it is not yet established that
the Lennard-Jones 61: 2 potential gives an adequate representa-
tion for argon at lower temperatures.

Recent determinations of the viscosity of argon at elevated
pressures have been reported by Kiyama and Makita (42) over
the temperature range 50-300 C and for pressures up to 96 atm.
Kestin and Pilarczyk (36) also measured the viscosity of argon to

70 atm at room temperature. The values reported in Table 3 were read from smooth isotherms drawn through the reported data.

(f) *Carbon Monoxide.* The dynamic viscosities of carbon monoxide were calculated by Hilsenrath (7) in a manner similar to nitrogen, and the values are given in Table 1 in the dimensionless form η/η_0, where η_0 is taken as 1656.8×10^{-7} poise at 0 C and 1 atm. This value is in close agreement with the determination by Johnston and Grilly (51).

The characteristic parameters $\epsilon/k = 110.3$ and $r_0 = 3.590$ used for carbon monoxide were those recommended by Hirschfelder, et al. (3).

A graphical comparison of the tabulated values with experimental results of five authors (18, 25, 41, 51, 56) is shown in Fig. 9. The tabulated values should be reliable within 2 per cent except at temperatures above 500 K where the uncertainty may exceed 3 per cent. The values undoubtedly could be improved over the entire range by a readjustment of the force constants.

read from smooth isotherms drawn through their data. A discussion of the comparison with the limited data of Phillips (57), Stakelbeck (58), Comings, Mayland, and Egly (60), and Naldrett and Maass (59) is to be found also in reference (42).

(h) *Nitric Oxide.* The dynamic viscosities of nitric oxide were calculated by Hilsenrath (7) in a manner similar to nitrogen, and the values are given in Table 1 in the dimensionless form η/η_0, where η_0 is taken as 1792×10^{-7} poise at 0 C and 1 atm. This value is in close agreement with the determination by Johnston and McCloskey (17), who found the viscosity to be 1790×10^{-7} poises at 0 C, based on the value 1833.0×10^{-7} poise as the viscosity of dry air at 296.1 K. The characteristic parameters $\epsilon/k = 119$ and $r_0 = 3.47$ used for nitric oxide were those recommended by Hirschfelder, et al. (3).

A graphical comparison of the tabulated values with the experimental data (17, 18) is shown in Fig. 11. The tabulated values fit the limited experimental data well within 1 per cent. The values
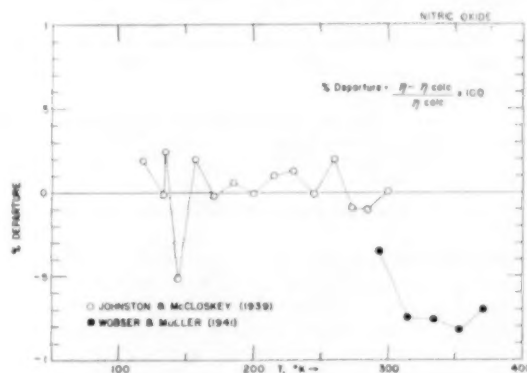

FIG. 9 COMPARISON OF LOW-PRESSURE VISCOSITY DATA FOR CARBON MONOXIDE WITH VALUES IN TABLE 1

FIG. 11 COMPARISON OF LOW-PRESSURE VISCOSITY DATA FOR NITRIC OXIDE WITH VALUES IN TABLE 1

FIG. 10 COMPARISON OF LOW-PRESSURE VISCOSITY DATA FOR CARBON DIOXIDE WITH VALUES IN TABLE 1

There are no data on the variation of the viscosity of carbon monoxide at moderate pressures.

(g) *Carbon Dioxide.* The dynamic viscosities of carbon dioxide were calculated in a manner identical to those of nitrogen, and the values are given in Table 1 in the dimensionless form η/η_0, where η_0 is taken as 1370.1×10^{-7} poise at 0 C and 1 atm. The characteristic parameters ϵ/k and r_0 used for carbon dioxide are 200 and 3.952 Å, respectively.

A graphical comparison of the low-pressure values with experimental data of four authors (8, 13, 17, 41) is shown in Fig. 10. The tabulated values are believed to be accurate within 2 per cent.

Kiyama and Makita (42) recently have reported extensive measurements (50–300 C and 1–96 atm) of the viscosity of carbon dioxide. The values given for carbon dioxide in Table 3 were

above 300 K are extrapolated beyond the experimental range and are believed reliable within 2 per cent.

There are no data on the variation of the viscosity of nitric oxide with pressure.

(i) *Steam.* The viscosity of steam at 1 atm (Table 1) was computed from the equations given by Bonilla, et al. (61)

$$\eta = 0.361T - 10.2 \text{ for } T \leq 800 \text{ K} \dots \dots [6]$$

and

$$\eta = \frac{39.37T^{1/2}}{33.15 - T + 0.0011587T^2} \text{ for } T \geq 800 \text{ K} \dots [7]$$

where T is the Kelvin temperature and η is in micropoise. A graphical comparison of the low pressure values with the experimental data (61–67) is given in Fig. 12, from which a reliability of approximately 2 to 4 per cent may be adduced.

The viscosity of steam at higher pressures was computed by Hilsenrath and Touloukian (7), according to the Enskog theory, from the equations given by Gardner (68)

$$\eta/\eta' = 1 + 0.175b\rho + 0.8651b^2\rho^2 \dots \dots [8]$$

where

$\eta' = 1$ atm viscosity at T deg K, in poise

$\rho = $ density in g/cm³

$$b = \frac{1.783}{M^{1/4}} \left(\frac{\sqrt{T}}{\eta'} \right)^{1/2} \times 10^{-7}$$
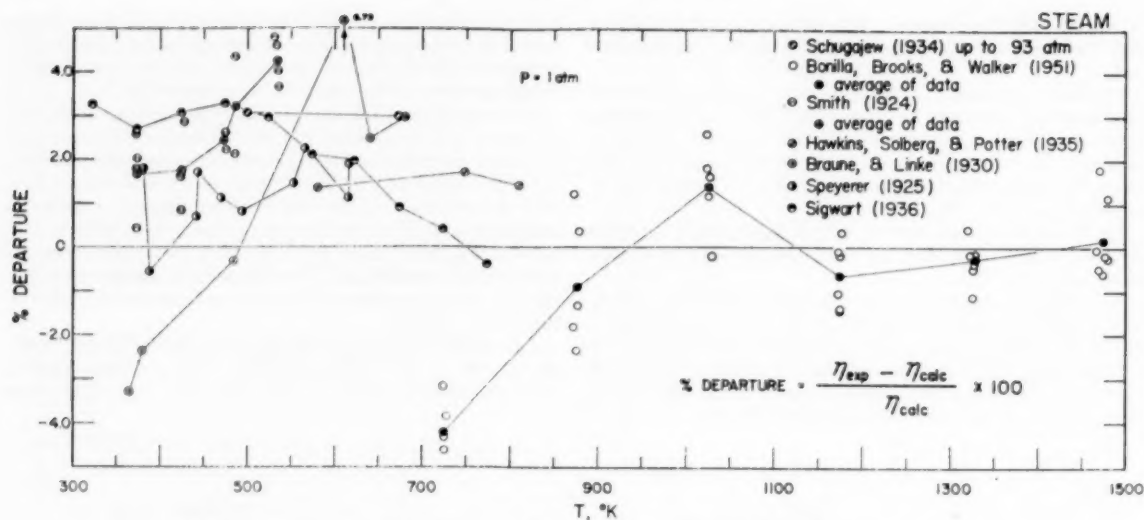
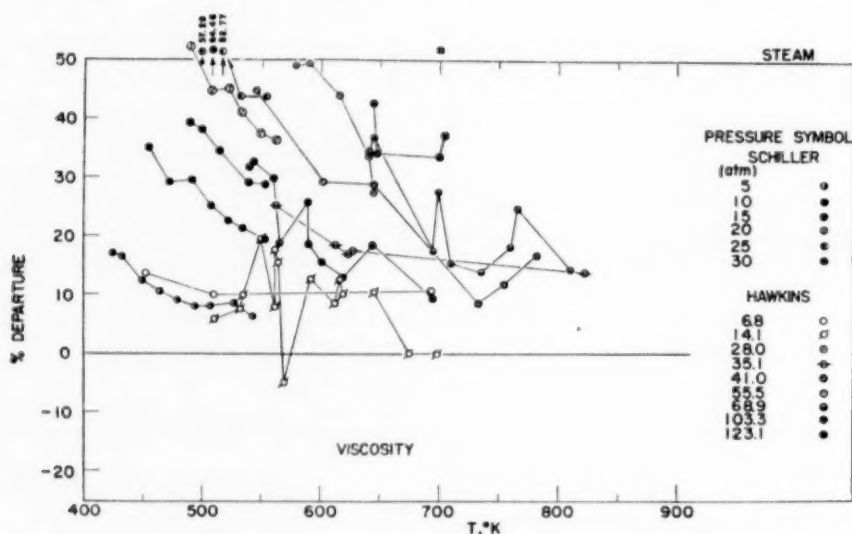FIG. 12   COMPARISON OF LOW-PRESSURE VISCOSITY DATA FOR STEAM WITH VALUES IN TABLE 1

FIG. 13(a)   COMPARISON OF HIGH-PRESSURE VISCOSITY DATA FOR STEAM WITH VALUES IN TABLE 3

where

M = molecular weight, T = Kelvin temperature.

The scatter of the bulk of the experimental data for steam at high pressure from the correlating equation is approximately 10 per cent. Some data, however, are as much as 50 per cent different from the values obtained in the foregoing correlation. Figs. 13(a) and 13(b) show the departures of the pressure data (69–74).

(j) *Helium*. The dynamic viscosities of helium were computed by R. L. Nuttall (7) from the relationship

$$\eta = \frac{4.2295T^{3/2}}{T^{0.826} - 0.409} \quad \dots \dots \dots \dots \dots \dots [9]$$

where η is the viscosity in micropoise and $\eta_0 = 1953 \times 10^{-7}$

poise. Equation [9] is an empirical representation of the experimental data. The deviations from the experimental results (40, 51, 75) are illustrated in Fig. 14.

The only determinations of the effect of pressure on the viscosity of helium are those of Kestin and Pilarczyk (36) whose measurements at 20 C extend to 70 atm. These authors represent their results by the empirical equation

$$\eta/\eta' = 1 + 7.753 \times 10^{-5}(P - 14.7)$$
$$- 0.1711 \times 10^{-8}(P - 14.7)^2 \quad . . [10]$$

where P is the pressure in psi and $\eta' = 1957 \times 10^{-7}$ poise.

CORRELATION OF EXPERIMENTAL THERMAL-CONDUCTIVITY DATA

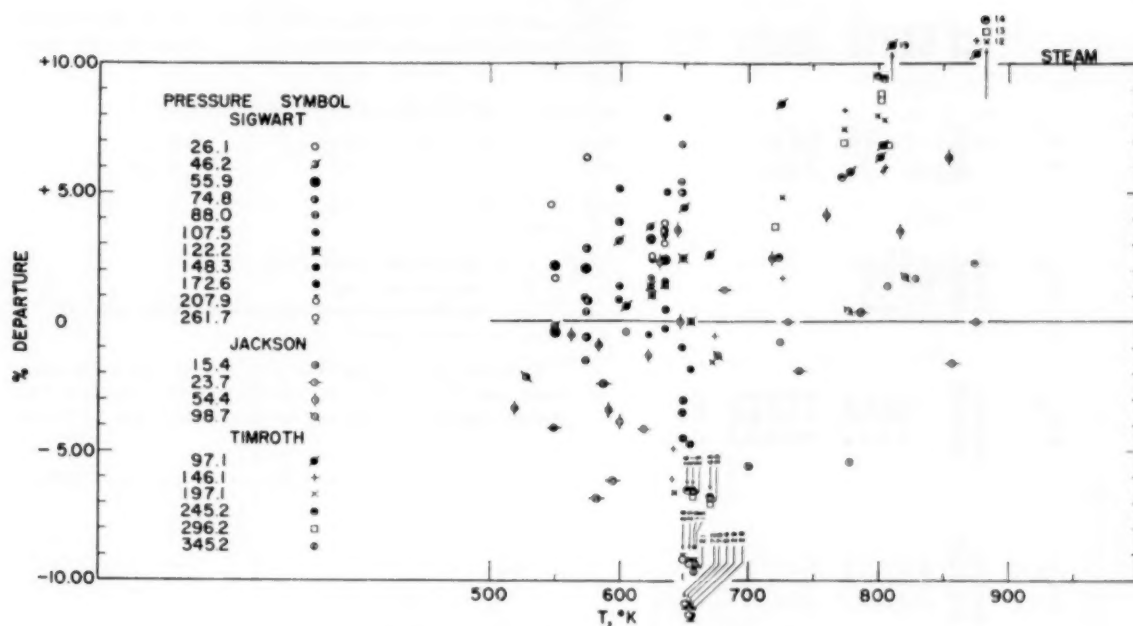The low-pressure thermal conductivity of air, nitrogen, oxygen,

FIG. 13(b) COMPARISON OF HIGH-PRESSURE VISCOSITY DATA FOR STEAM WITH VALUES IN TABLE 3

argon, carbon dioxide, carbon monoxide, and helium were computed by R. L. Nuttall (7) from the equation

$$k/k_0 = 1/k_0 \left[\frac{a\sqrt{T}}{1 + \frac{b \times 10^{-c/T}}{T}} \right] \dots \dots [11]$$

where T is the Kelvin temperature, k_0 is the thermal conductivity at standard conditions (1 atm and 0 C), and the constants a, b, c, are as shown in Table 5. There are incorporated also in this table references to the experimental data and to the figures wherein these are compared with the values given in Table 4.

For nitrogen above 300 K the tabulated values of the thermal conductivity were obtained from the equation given by D. W. Stops (83) based on his data extending to 1000 C.

$$k/k_0 = 1 + 3.13 \times 10^{-3}t - 1.33 \times 10^{-6}t^2$$
$$+ 2.63 \times 10^{-10}t^3 \dots [12]$$

where t is the temperature in degrees Celsius. The value of k_0, thermal conductivity at 0 C and 1 atm, was taken as 5.77×10^{-5} cal cm^{-1} sec^{-1} °C^{-1}. The two representations, Equations [11] and [12], yield values which are in close agreement between 300 and 700 K.

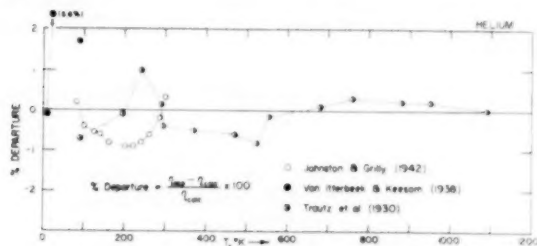The pressure dependence of the thermal conductivity of nitrogen has been investigated by N. Vargaftig (100) in the temperature range 40 to 53 C at pressures to 87 atm; by J. M. Lenoir and E. W. Comings (102) at 41 C and 1 to 206 atm; by F. G. Keyes, et al (99, 103, 104) from 0 to 401 C and pressures up to 150 atm; and by A. Botzen (101) at 25, 50, 75 C and pressures up to 2500 atm.
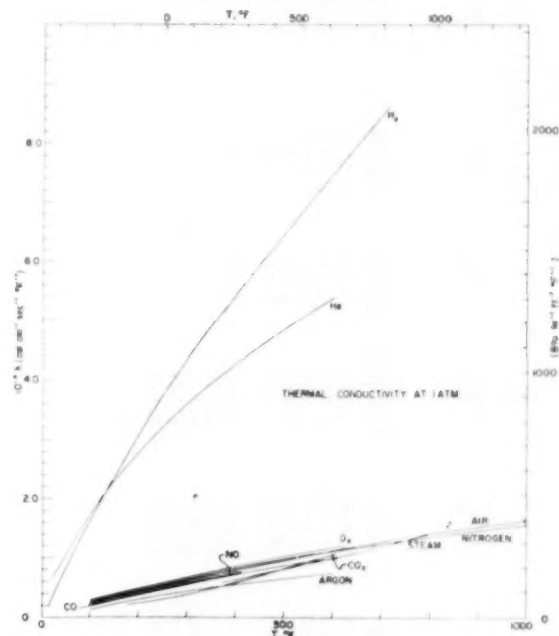

FIG. 15 THERMAL CONDUCTIVITY OF NINE GASES AT LOW PRESSURE

FIG. 14 COMPARISON OF LOW-PRESSURE VISCOSITY DATA FOR HELIUM WITH VALUES IN TABLE 1

TABLE 4   THERMAL CONDUCTIVITY AT ATMOSPHERIC PRESSURE

T°K	Air k/k_θ	Nitrogen k/k_θ	Oxygen k/k_θ	Helium k/k_θ	Hydrogen k/k_θ	Argon k/k_θ	Carbon monoxide k/k_θ	Carbon dioxide k/k_θ	Nitric oxide k/k_θ	Steam k/k_θ	T°R
100	0.3831	0.390	0.368	0.5155	0.395	0.394	0.374				180
200	0.7494	0.765	0.743	0.8218	0.762	0.765	0.750	0.659	0.579		360
300	1.087	1.081	1.06	1.059	1.080	1.081	1.087	1.159	0.7480		540
400	1.394	1.377	1.41	1.258	1.356	1.365	1.389	1.691	1.0907	1.641	720
500	1.674	1.645	1.70	1.432	1.616	1.616	1.664	2.304	1.421	2.139	900
600	1.921	1.890	1.97	1.588	1.871	1.846	1.914	2.888		2.660	1080
700	2.169	2.114			2.128			3.388		3.192	1260
800	2.392	2.318						3.848		3.728	1440
900	2.600	2.504						4.274			1620
1000	2.792	2.673						4.666			1800
1100		2.828						5.030			1980
1200		2.968						5.367			2160
1300								5.674			2340

The thermal conductivities of hydrogen given in dimensionless form in Table 4 were calculated by R. L. Nuttall from the equation

$$k/k_0 = 1/k_0[(0.4780 + 0.000505T)(C_p - 4.968) + 3.722]\frac{\eta}{1 + \frac{5.9}{T} 10^{-10/T}} \quad \dots \dots [13]$$

where

k_0 = 40.21 × 10^-5 cal cm^-1 sec^-1 °C^-1
T = temperature, deg K
C_p = specific heat at constant pressure, in cal mole^-1 C^-1
η = viscosity, poise

Equation [13] is of the same form as that used by Woolley, Scott, and Brickwedde (43) except that the constants were changed slightly by including the more recent data of Ubbink
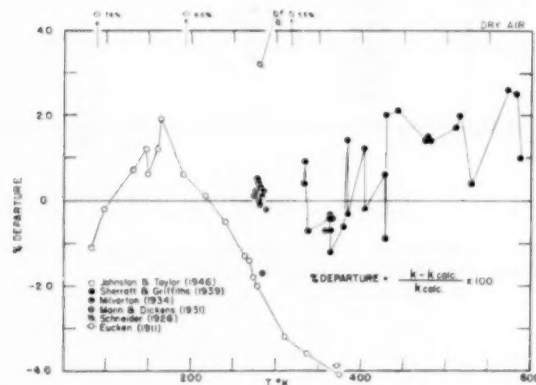

FIG. 16   COMPARISON OF LOW-PRESSURE THERMAL-CONDUCTIVITY DATA FOR AIR WITH VALUES IN TABLE 4

(90) and of Johnston and Grilly (89). The values of C_p and η were those given by Woolley, Scott, and Brickwedde.

Fig. 19 shows the deviations of the tabulated values from experimental data (80, 81, 89, 92, 93, 94). The values of thermal conductivity for hydrogen given in Table 4 are considered to be reliable within 6 per cent.

The thermal conductivities of nitric oxide given in Table 4 are the smoothed values of Johnston and Grilly (89). The tabulated values were made dimensionless by dividing by $k_0 = 5.674 × 10^{-5}$ cal cm^-1 sec^-1 °C^-1, the thermal conductivity at 0 C and 1 atm.

Fig. 23 shows the deviations of the tabulated values from existing experimental data (89, 98). The values given in Table 4 are considered reliable within 0.3 per cent.

The thermal conductivities of steam given in dimensionless form in Table 4 were calculated by R. L. Nuttall (7) from the following equations

$$k/k°0 = \frac{1}{k°0}[k° + 1.097 × 10^{-5}(10^{0.934 × 10^9 P/T^4} - 1)] \dots [14]$$

and

$$k° = \frac{1.5466\sqrt{T} × 10^{-5}}{1 + \frac{1737.3}{T} 10^{-12/T}}$$

where P is the absolute pressure in atmospheres, $k°0 = 3.789 ×$

TABLE 5 CONSTANTS FOR THERMAL-CONDUCTIVITY EQUATION [11]

Gas	Experimental scatter, per cent	a x 10^5	b	s	k_0 x 10^5 cal cm^{-1} sec^{-1} °K^{-1}	k_0 x 10^5 Btu ft^{-1} hr^{-1} °F^{-1}	Fig. No.	Ref
Air	4	0.6325	254.4	12	5.770	1395.0	16	72 - 78
Nitrogen*	5	0.604	224.0	12	5.77	1400.0	17	78,79,80,82, 84,85,97
Oxygen	2	0.6725	265.9	10	5.867	1419.0	18	78, 81 - 85
Argon	2	0.3790	179.59	10	3.905	944.2	20	78,82,83,88
CO	2	0.5862	217.6	7.75	5.549	1342.0	21	82,85,86, 92,93
CO$_2$	10	4.608	6212.0	10	3.477	840.7	22	74,79,82,86, 92,94
Helium	2	2.347	42.54	10	33.63	8130.0	23	78, 82 - 86, 89,95

* See text for the representation above 300 K.
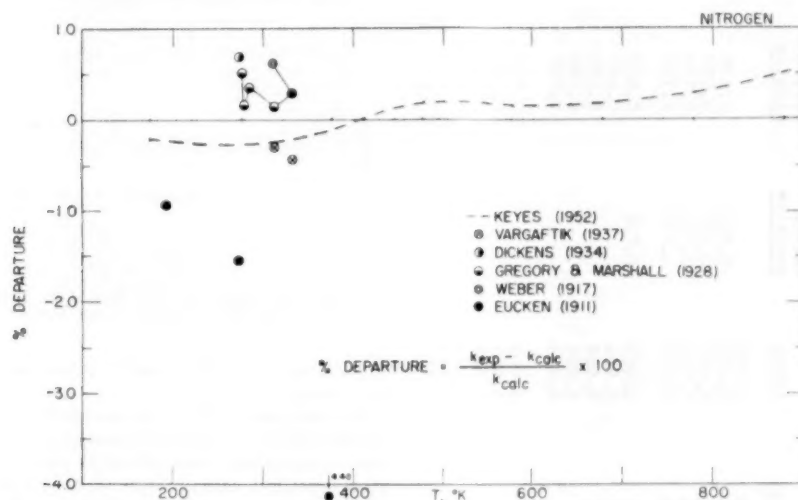
FIG. 17 COMPARISON OF LOW-PRESSURE THERMAL-CONDUCTIVITY DATA FOR NITROGEN WITH VALUES IN TABLE 4
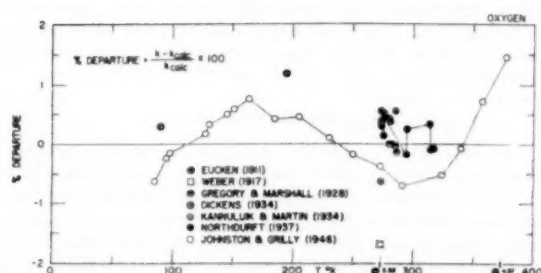
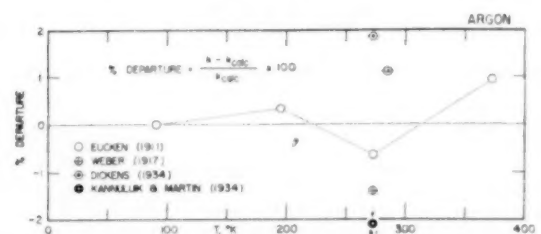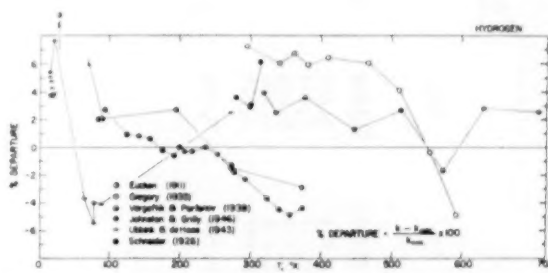FIG. 18 COMPARISON OF LOW-PRESSURE THERMAL-CONDUCTIVITY DATA FOR OXYGEN WITH VALUES IN TABLE 4

FIG. 19 COMPARISON OF LOW-PRESSURE THERMAL-CONDUCTIVITY DATA FOR HYDROGEN WITH VALUES IN TABLE 4
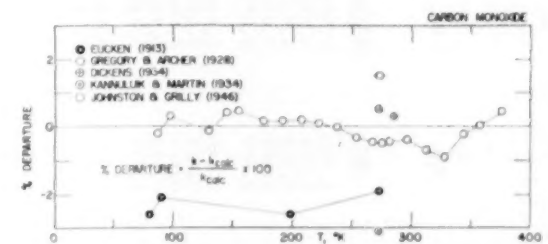

FIG. 20 COMPARISON OF LOW-PRESSURE THERMAL-CONDUCTIVITY DATA FOR ARGON WITH VALUES IN TABLE 4

FIG. 21 COMPARISON OF LOW-PRESSURE THERMAL-CONDUCTIVITY DATA FOR CARBON MONOXIDE WITH VALUES IN TABLE 4

TABLE 6 PRANDTL NUMBER

$$N_{Pr} = \eta c_p / k$$

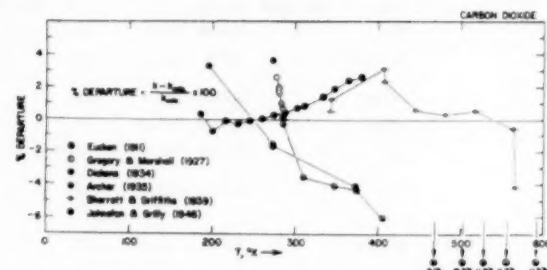| T°K	Air N_{Pr}	Nitrogen N_{Pr}	Oxygen N_{Pr}	Helium N_{Pr}	Hydrogen N_{Pr}	Argon N_{Pr}	Carbon monoxide N_{Pr}	Carbon dioxide N_{Pr}	Nitric oxide N_{Pr}	Steam N_{Pr}	T°R
100	0.770	0.786	0.815	0.677	0.712	0.692	0.764				180
200	0.739	0.747	0.745	0.674	0.719	0.676	0.737	0.830	0.789		360
300	0.708	0.715	0.729	0.686	0.706	0.670	0.722	0.770	0.745		540
400	0.689	0.691	0.696	0.700	0.690	0.664	0.718	0.738	0.729	1.037	720
500	0.680	0.684	0.697	0.715	0.675	0.658		0.702		0.995	900
600	0.680	0.686	0.703	0.729	0.664	0.655	0.724	0.685		0.992	1080
700	0.684	0.695			0.661	0.654		0.687		1.000	1260
800	0.689	0.708			0.660	0.655		0.692		1.015	1440
900	0.696	0.725				0.654		0.698			1620
1000	0.702	0.740				0.654		0.705			1800
1100		0.757				0.656		0.712			1980
1200		0.774				0.657		0.721			2160
1300						0.659		0.729			2340
1400						0.661					2520
1500						0.663					2700

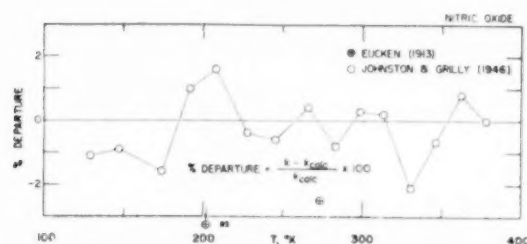FIG. 22 COMPARISON OF LOW-PRESSURE THERMAL-CONDUCTIVITY DATA FOR CARBON DIOXIDE WITH VALUES IN TABLE 4

FIG. 23 COMPARISON OF LOW-PRESSURE THERMAL-CONDUCTIVITY DATA FOR NITRIC OXIDE WITH VALUES IN TABLE 4

10^{-5} cal cm^{-1}sec^{-1}, °C^{-1}, and $k°$ is the thermal conductivity at zero pressure.

The foregoing equations are essentially as given by Keyes and Sandell (99) as the best representation of their measurements. The constants have been altered to give values in terms of the thermochemical calorie taken to be 4.1840 abs joules. The values of thermal conductivity of steam in Table 4 are, therefore, in very close agreement with the results of Keyes and Sandell (99) whose experimental data extend to 625 K and 150 atm. The values differ appreciably from the earlier data reported by Vargaftig, et al. (74,100) whose data are as much as 38 per cent higher in certain regions. The departures of their low-pressure data are indicated in Fig. 24.

SPECIFIC HEATS OF GASES

Experimental data on heat capacity are too sparse to provide a satisfactory direct correlation over an appreciable temperature and pressure range. Fortunately, extensive and reliable values can be calculated from the existing data of state (pressure-volume-temperature data), which are relatively abundant. The thermodynamic properties derived from good PVT data usually are in very satisfactory agreement with the experimental data.

If the PVT data are fitted by means of a virial equation of state such as

$$Z = PV/RT = 1 + B_1 P + C_1 P^2 + D_1 P^3 + \ldots\ldots\ldots\ldots [15]$$

the specific heat can be expressed by the equation

$$\frac{C_p}{R} = \frac{C_p°}{R} - (2B'_1 + B''_1)P - \frac{(2C'_1 + C''_1)}{2}P^2 - \frac{(2D'_1 + D_1'')}{3}P^3 \ldots\ldots [16]$$

the first term on the right being the specific heat of the ideal (or perfect) gas. The remaining terms are corrections for the gas imperfection. The primes denote derivative functions as follows
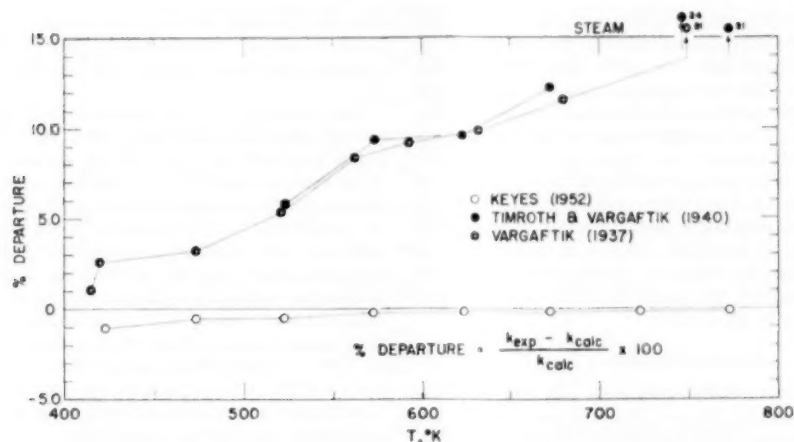
FIG. 24 COMPARISON OF THERMAL-CONDUCTIVITY DATA FOR STEAM WITH EQUATION [14]
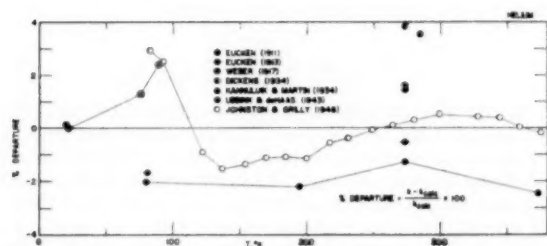

FIG. 25 COMPARISON OF LOW-PRESSURE THERMAL-CONDUCTIVITY DATA FOR HELIUM WITH VALUES IN TABLE 4

B'_1, C'_1, D'_1 are $\dfrac{TdB_1}{dT}, \dfrac{TdC_1}{dT}, \dfrac{TdD_1}{dT}$

B''_1, C''_1, D''_1 are $\dfrac{T^2 d^2 B_1}{dT^2}, \dfrac{T^2 d^2 C_1}{dT^2}, \dfrac{T^2 d^2 D_1}{dT^2}$.

Corresponding formulas can be written when the virial equation is given in terms of density. If the specific heats at constant volume also are desired, the following formulas apply: If

$$Z = PV/RT = 1 + B\rho + C\rho^2 + D\rho^3 + \ldots\ldots$$

the specific heat at constant pressure can be computed from

$$C_p/R = (C_p - C_v)/R + C_v/R$$

where

$(C_p - C_v)/R$
$$= \frac{[1 + (B + B')\rho + (C + C')\rho^2 + (D + D')\rho^3]^2}{1 + 2B\rho + 3C\rho^2 + 4D\rho^3} \ldots [17]$$

and

$C_v/R = C^\circ_p/R - 1 + (C_v - C^\circ_v)/R$
$= C^\circ_p/R - 1 - (2B' + B'')\rho + (C'' + C''/2)\rho^2$
$\qquad\qquad + (2D'/3 + D''/3)\rho^3 \ldots [18]$

The primes denote derivative functions as defined previously.

Alternatively, if the data of state are not correlated through a power series, it may be more advantageous to compute the heat capacities directly from the tabulated compressibility values and their derivatives. In this case, the dimensionless specific heat of the real gas can be computed from
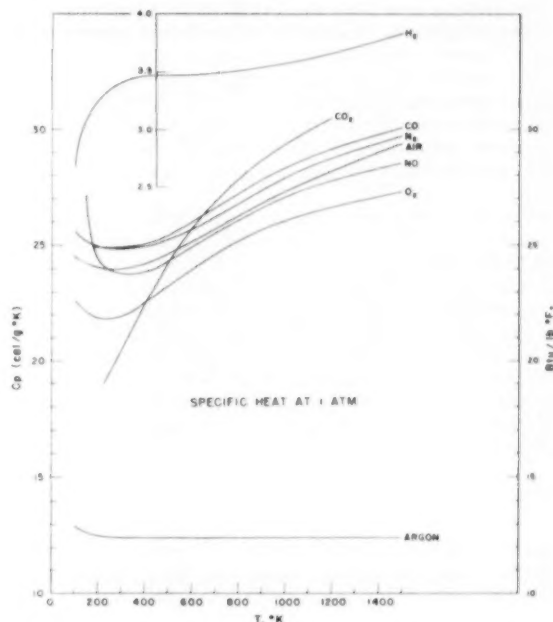

FIG. 26 SPECIFIC HEATS OF EIGHT GASES AT ATMOSPHERIC PRESSURE

$C_p/R = C^\circ_p/R - 1 - 2 \int_0^\rho [T(dZ/dT)_\rho/\rho]d\rho$
$\qquad - \int_0^\rho [T^2(d^2Z/dT^2)_\rho/\rho]d\rho$
$\qquad + [Z + T(dZ/dT)_\rho]^2/[Z + \rho(dZ/d\rho)_T] \ldots [19]$

Corresponding relationships are derivable from the thermodynamic identities when the compressibility is tabulated in terms of temperature and pressure.

The specific-heat values for the gases used in this paper were computed in the foregoing manner at the National Bureau of Standards and are tabulated in the NBS-NACA series (7) from low pressure to 100 atm and to temperatures as high as 5000 K in some instances. The values given in Fig. 26 are an abridgment

of the NBS-NACA Tables for atmospheric pressure. A survey of the experimental determinations of the specific heats for these gases is given in a recent review by J. F. Masi (105) who also tabulates the specific heats to temperatures approaching 3000 K.

The reliability of the specific-heat values used in the calculation of the Prandtl numbers varies slightly with the gas and the temperature. In general, however, the uncertainties are 3-10 per cent of the corrections for gas imperfection $(C_p - C_p°)$ which at atmospheric pressure are small, when compared with the value of the ideal gas. The resulting uncertainties in the specific heat are only a few tenths of a per cent which is at least an order of magnitude better than the viscosity and thermal-conductivity data. A fuller discussion of the specific heats for these gases is to be found in the review by Masi (105).

PRANDTL NUMBER

The Prandtl numbers reported previously (82, 106, 107) were computed with the specific heats of the ideal gas. The values given here were computed with the real-gas specific heats. The difference, however, is small at atmospheric pressure and well within the experimental uncertainty of the thermal conductivity. The effects are most pronounced at the lowest temperatures.

The reliability of the Prandtl numbers can be assessed readily from the deviation plots for the viscosity and thermal conductivity. Lack of extensive and accurate thermal-conductivity measurements limits the scope and reliability of the Prandtl numbers.

The uncertainty in the Prandtl number for air is less than 2 per cent at temperatures below 700 K and considerably higher at higher temperatures where use was made of extrapolated values of the thermal conductivity. The uncertainty is correspondingly decreased in the decreasing powers of N_{Pr} employed in heat-transfer calculations. This tabulation agrees with those of Keenan and Kaye (107) and Tribus and Boelter (108) up to 500 K but departs gradually (see Fig. 28) from that point until at 1000 K it exceeds their values by approximately 7 per cent of the tabulated values. Above 500 K this tabulation is lower by 10 per cent than values obtained from the theoretical relationship $N_{Pr} = C°_p/(C°_p + 1.25R)$ which yields Prandtl numbers in the neighborhood of 0.75. A more favorable comparison is obtained against a formula based on a theoretical relationship of Chapman and Cowling (109) for the thermal conductivity

$$k = [U_{11}C°_p + (3.75 - 2.5U_{11})R]\eta/M \ldots \ldots [20]$$

From this the Prandtl number can be written

$$\frac{\eta C_p}{R} = \frac{C°_p/R}{(U_{11}C°_p/R) + (3.75 - 2.5\,U_{11})} \ldots \ldots [21]$$

If U_{11} (the ratio of the mean free paths for diffusion and viscosity) is taken as 1.204 as for smooth elastic spheres, the resulting Prandtl numbers for air are in the neighborhood of 0.71 or 0.72 over the higher temperature range. Calculations based on the recent experimental measurements of the thermal conductivity at 1000 C by Stops (83) seem to corroborate the 0.72 value. In any event, at elevated temperatures the Prandtl number for air should be considerably higher than the values in current use (107, 108, 110, 111).

Estimates of the Prandtl number for these gases at elevated temperatures can be made on the basis of the foregoing theoretical assumptions. Table 7 gives the Prandtl numbers corresponding to a smooth elastic sphere ($U_{11} = 1.204$), a Maxwellian molecule ($U_{11} = 1.55$), and the Eucken approximation ($U_{11} = 1$).

CONCLUSIONS

The existing thermal-conductivity and viscosity data are reviewed, correlated, and presented for low pressures with reasonable extrapolations to higher temperatures. These data are combined with the specific heats to obtain the Prandtl numbers for the gases treated. Although estimates are given for the Prandtl numbers at high temperatures, based on the Chapman and Enskog relationships, much more is required in both theoretical and experimental lines before data at the elevated temperatures can be considered reliable. It is hoped that more accurate experimental data for viscosity and thermal conductivity will become available at temperatures approaching 1000 K. From these the transport properties can be calculated from fundamental principles to even higher temperatures.

With the exception of air, hydrogen, steam, and helium, for which the data were correlated either graphically or empirically, the low-pressure viscosities were computed on the basis of force constants, for each gas considered as obeying a Lennard-Jones, 6:12 interaction potential function. The force constants were chosen largely on the basis of reliable viscosity data in the moderate temperature region where the data may be presumed most reliable. In the case of argon, the force constants chosen also provided the best fit of the experimental PVT data. Where data are available at higher temperatures, it is observed (see Figs. 3, 7, 8) that the Lennard-Jones model yields viscosity values which
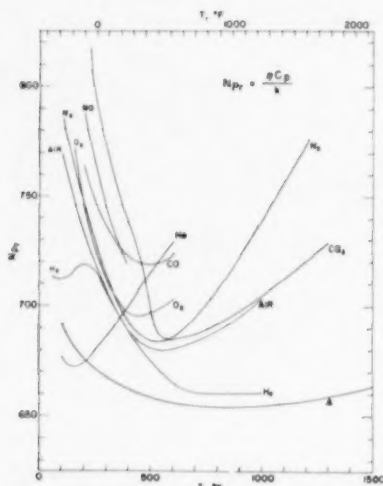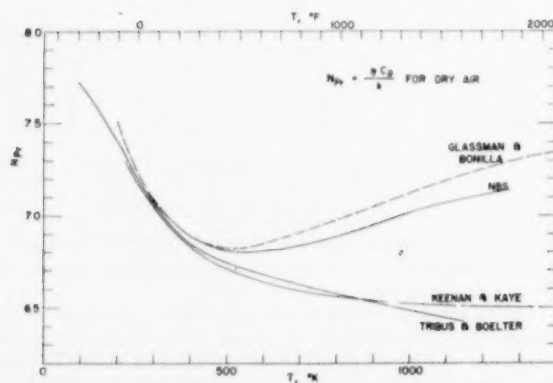

FIG. 27   PRANDTL NUMBER FOR NINE GASES

FIG. 28   COMPARISON OF PRANDTL NUMBERS FOR AIR

TABLE 7 ESTIMATED PRANDTL NUMBERS AT ELEVATED TEMPERATURES
(500 – 5000 K)

Gas	Prandtl Number		
	$U_{11} = 1.55$	$U_{11} = 1.304$	$U_{11} = 1$
	Maxwellian molecule	Smooth elastic sphere	Eucken approximation
Air	.66	.71 – .74	.74 – .78
N_2	.66	.72 – .73	.74 – .78
O_2	.66	.71 – .74	.75 – .80
H_2	.66	.71 – .74	.74 – .78
A	.67	.67	.67
CO	.66	.71 – .73	.74 – .78
CO_2	.66	.74 – .78	.81 – .85(at 2000°K)
NO	.66	.72 – .73(at 3000°K)	.76 – .78(at 3000°K)
He	.67	.67	.67

FIG. 29 NOMOGRAM FOR FRACTIONAL POWERS OF PRANDTL NUMBER

were computed from the Enskog equation. For argon, oxygen, and carbon dioxide, tabulations were effected by reading values from smooth isotherms drawn through the reported data. The pressure dependence of helium, having been measured only at one temperature, has been represented by an empirical equation fitted to the data by the investigators (36). No experimental data were found on the pressure variation of viscosity for carbon monoxide and nitric oxide.

It is encouraging indeed to note the continuing or renewed investigations on the transport properties of gases carried on in the established laboratories of F. G. Keyes at M.I.T., A. Michels at the University of Amsterdam, E. W. Comings at the University of Illinois, B. H. Sage and W. N. Lacy at the California Institute of Technology, and G. A. Hawkins at Purdue University, and of measurements underway in new laboratories of H. S. Bean and R. L. Nuttall at the National Bureau of Standards, A. W. Lawson at the University of Chicago, and R. Kiyama at Kiyoto University in Japan. While striking advances have been made along theoretical lines, in the final analysis the theories are dependent on accurate experimental data.

ACKNOWLEDGMENT

BIBLIOGRAPHY

1 "Brief Review of Available Data on the Dynamic Viscosity and Thermal Conductivity for Twelve Gases," by G. A. Hawkins, Trans. ASME, vol. 70, 1948, pp. 655–659.

2 "A Summary of Viscosity and Heat Conduction Data for He, A, H_2, O_2, N_2, CO, CO_2, H_2O, and Air," by F. G. Keyes, Trans. ASME vol. 73, 1951, pp. 589–596.

3 "Viscosity and Other Physical Properties of Gases and Gas Mixtures," by J. O. Hirschfelder, R. B. Bird, and E. L. Spotz, Trans. ASME, vol. 71, 1949, pp. 921–937.

4 "The Representation of Gas Properties in Terms of Molecular Clusters," by H. W. Woolley, J. Chem. Phys., vol. 21, 1953, p. 236.

5 "Note on the Resonance Method of Measuring the Ratio of Specific Heats of a Gas, C_p/C_v," by H. W. Woolley, Canadian J. Physics, vol. 31, 1953, p. 604.

6 "Compilation of Thermal Properties of Wind-Tunnel and Jet-Engine Gases at the National Bureau of Standards," by H. J. Hoge, Trans. ASME, vol. 72, 1950, pp. 779–783.

7 "NBS-NACA Tables of Thermal Properties of Gases," by

in the high-temperature region may be too high by about 2 to 5 per cent. This situation could be corrected by adjusting the force constants to vary with temperature. At the present time this does not seem necessary either for theoretical or practical purposes.

The variation of viscosity with pressure has been discussed, and abridged tables are given where sufficient experimental data were found. In the case of nitrogen, steam, and hydrogen, the tables

Joseph Hilsenrath, editor, National Bureau of Standards, Washington 25, D. C. (To be published shortly.)

8 "Recherches Expérimentales sur la Viscosité des Gaz Température Élevées," by V. Vasilesco, *Annales de Physique*, vol. 20, Séries 11, 1945, pp. 137, 292.

9 "The Effect of Temperature on the Viscosity of Air," by W. G. Shilling and A. E. Laxton, *Phil. Mag.*, vol. 10, 1930, p. 721.

10 "Sur la Determination de la Viscosité des Gaz et de la Constante de Sutherland," by A. Fortier, Comptes Rendus, vol. 203, 1936, p. 711; ibid. vol. 208, 1939, p. 506.

11 "The Coefficients of Gas Viscosity," by W. J. Fisher, *Phys. Rev.*, vol. 28, 1909, p. 73.

12 "On the Frictional Resistances to the Flow of Air Through a Pipe," by J. H. Grindley and A. H. Gibson, Proceedings of the Royal Society of London, England, vol. 80, series A, 1908, p. 114.

13 "Measurement of the Viscosity of Gases Over a Large Temperature Range," by B. P. Sutherland and O. Maass, *Canadian J. Research*, vol. 6, 1932, p. 428.

14 "Viscosity, Thermal Conductivity, and Diffusion in Gas Mixtures, VI. Viscosity Determinations on Pure Gases by Direct Measurement and by Measurements on Their Mixtures," by M. Trautz and W. Ludewigs, *Ann. Physik* (5), vol. 3, 1929, p. 409.

15 "On the Effect of Temperature on the Viscosity of Air," by R. S. Edwards and A. D. Rankine, Proceedings of the Royal Society of London, England, vol. 117, series A, 1927, p. 245.

16 "Viscosity of Organic Compounds," by T. Titani, Bull Chem. Soc., Japan, vol. 4, 1929, p. 68.

17 "Viscosities of Several Common Gases Between 90°K and Room Temperature," by H. L. Johnston and K. E. McCloskey, *J. Phys. Chem.*, vol. 44, 1940, p. 1038.

18 "Die Innere Reibung von Gasen und Dämpfen und Ihre Messung im Höppler-Viskosimeter," by R. Wobser and F. Müller, *Kolloid-Beihefte*, vol. 52, 1941, p. 165.

19 "Die Innere Reibung von Luft im Druckgebeit 1–30 kg/cm²," by G. Kellstrom, *Arkiv. för Matematik, Astronomi och Physik*, vol. 27, series A, 1941, p. 1.

20 "The Flow of Air Through Capillary Tubes," by I. M. Rapp, *Phys. Rev.* vol. 2, 1913, p. 363.

21 "Viscosity of Air," by W. N. Bond, *Motive*, vol. 137, 1936, p. 1031.

22 "Coefficient of Viscosity of Air," by V. D. Majundar and M. B. Vajifdar, Proc. Ind. Acad. Sci., vol. 8, series A, 1938, p. 171.

23 "A Precision Determination of the Viscosity of Air," by J. A. Bearden, *Phys. Rev.*, vol. 56, 1939, p. 103.

24 "Die Bestimmung der Elecktronenladung und die Viskosität der Luft," by G. B. Banerjea and B. Plattaniak, *Zeit. Physik*, vol. 110, 1938, p. 676.

25 "Über die Viskosität Einiger Gase und Ihre Temperaturabhängigkeit bei Tiefen Temperaturen," by H. Vogel, *Ann. Physik*, vol. 43, 1914, p. 1235.

26 "The Viscosity of Air, Oxygen, and Nitrogen," by P. J. Rigden, *Phil. Mag.*, vol. 25, 1938, p. 961.

27 "The Viscosity of Air," by W. V. Houston, *Phys. Rev.*, vol. 52, 1937, p. 751.

28 "The Viscosity of Air," by E. L. Harrington, *Phys. Rev.*, vol. 55, 1939, p. 230.

29 "The Coefficients of Viscosity and of Slip of Air and of Carbon Dioxide by the Rotating Cylinder Method," by K. S. Van Dyke, *Phys. Rev.*, vol. 21, 1923, p. 250.

30 "An Absolute Determination of the Viscosity of Air," by L. Gilchrist, *Phys. Rev.*, vol. 1, 1913, p. 124.

31 "Die Koeffizienten der Inneren Reibung bei Gemischen von Helium und Wasserstoff," by A. Gille, *Ann. Physik*, vol. 48, 1915, p. 799.

32 "Viscosity of Air," by J. L. Hogg, Proc. Amer. Acad. Arts and Sci., vol. 40, 1905, p. 609.

33 "Viscosity of Air up to 200 Atmospheres," by A. G. Nasini and G. Pastonesi, *Gazz. Chimica Italiana*, vol. 63, 1933, p. 821.

34 "Measurement of Viscosities of Gases at High Pressure. I. Viscosity of Air at 50°, 100°, and 150° C," by H. Iwasaki, Scientific Reports, Tohoku University, Japan, vol. 3, series A, 1951, p. 247.

35 "The Viscosity of Gases and Gaseous Mixtures at High Pressures. I," by I. F. Golubev, *Journal of Technical Physics*, USSR, vol. 8, 1938, p. 1932.

36 "Measurement of the Viscosity of Five Gases at Elevated Pressures by the Oscillating Disk Method," by J. Kestin and K. Pilarcsyk, Trans. ASME, vol. 76, 1954, pp. 987–999.

37 "The Dynamic Viscosity of Nitrogen," by W. L. Sibbitt, G. A. Hawkins, and H. L. Solberg, Trans. ASME, vol. 65, 1943, pp. 401–405.

38 "The Viscosity of Compressed Gases," by J. H. Boyd, Jr., *Phys. Rev.*, vol. 35, 1930, p. 1284.

39 "The Measurement of the Viscosity of Gases at High Pressures. The Viscosity of Nitrogen to 1000 atm," by A. Michels and R. O. Gibson, Proceedings of the Royal Society of London, England, vol. 134, series A, 1931, p. 288.

40 "Gasreibung bei Höheren Temperaturen," by M. Trautz and R. Zink, *Ann. Physik* (5), vol. 7, 1930, p. 427.

41 "Die Reibung von H₂, N₂, CO, C₂H₄, O₂, und Ihren Binaren Gemischen," by M. Trautz and A. Melster, *Ann. Physik*, vol. 7, 1930, p. 409.

42 "The Viscosity of Carbon Dioxide, Ammonia, Acetylene, Argon, and Oxygen Under High Pressures," by R. Kiyama and T. Makita, *Rev. of Phys. Chem.*, Japan, vol. 22, 1952, p. 49.

43 "Compilation of Thermal Properties of Hydrogen in Its Various Isotopic and Ortho-Para Modifications," by H. W. Wooley, R. B. Scott, and F. G. Brickwedde, J. Research NBS, vol. 41, 1948, p. 379, RP 1932.

44 "Die Reibung, Wärmeleitung, und Diffusion in Gasmischungen. XVII. Die Reibung von NH₃ und Seinen Gemischen mit H₂, N₂, O₂, C₂H₄," by M. Trautz and R. Heberling, *Ann. Physik*, vol. 10, 1931, p. 155.

45 "Die Reibung, Wärmeleitung, und Diffusion in Gasmischungen. III. Die Reibung von H₂-C₂H₄ Gemischen," by M. Trautz and F. W. Stauf, *Ann. Physik*, vol. 2, 1929, p. 737.

46 "Die Reibung, Wärmeleitung, und Diffusion in Gasmischungen. VIII. Die Reibung von H₂, He, Ne, A und Ihren Binaren Gemischen," by M. Trautz and H. E. Binkele, *Ann. Physik*, vol. 5, 1930, p. 561.

47 "Die Reibung von H₂, N₂O, CO₂, und C₃H₈ und Ihren Binaren Gemischen," by M. Trautz and F. Kurz, *Ann. Physik*, vol. 9, 1931, p. 981.

48 "Die Reibung, Wärmeleitung, und Diffusion in Gasmischungen. XVI. Die Reibung von H₂, CH₄, C₂H₆, C₃H₈ und Ihren Binaren Gemischen," by M. Trautz and K. G. Sorg, *Ann. Physik*, vol. 10, 1931, p. 81.

49 "Die Reibung, Wärmeleitung, und Diffusion in Gasmischungen XXV. Die innere Reibung von Xenon und seinen Gemischen mit Wasserstoff und Helium," by M. Trautz and R. Heberling, *Ann. Physik*, vol. 20, 1934, pp. 118–120.

50 "The Transport Properties for Non-Polar Gases," by J. O. Hirschfelder, R. B. Bird, and E. L. Spotz, *J. Chem. Phys.*, vol. 16, 1948, p. 968.

51 "Viscosities of CO, He, Ne, and Argon Between 80–300° K. Coefficients of Viscosity," by H. L. Johnston and E. R. Grilly, *J. Phys. Chem.*, vol. 46, 1942, p. 948.

52 "Über der Koeffizienten der Inheren Reibung von Wasserstoff und Argon bei Niederen Temperaturen," by W. Kopsch, Dissertation, Halle, 1909. (Quoted in Trautz and Nonath.)

53 "Die Innere Reibung von Argon und Ihre Änderung mit der Temperatur," by H. Schultze, *Ann. Physik*, vol. 5, 1901, p. 140.

54 J. C. Westmoreland, unpublished data.

55 "On the Determination of Molecular Fields, I. From the Variation of the Viscosity of a Gas With Temperature," by J. E. Lennard-Jones, Proceedings of the Royal Society of London, England, vol. 106, series A, 1924, p. 441.

56 "Die Innere Reibung von Gasen und Dampfen und Ihre Messung im Hoppler-Viskosimeter," *Kolloid Beihefte*, vol. 52, 1941, p. 165.

57 "The Viscosity of Carbon Dioxide," by P. Phillips, Proceedings of the Royal Society of London, England, vol. 87, series A, 1912, p. 48.

58 "Über die Zähigkeit Vershiedener Kältemittel in Flussigen und Dampfförmigen Zustand in Abhängigkeit von Druck und Temperatur," by H. Stakelbeck, *Z.F.D. ges. Kalte-Ind.*, vol. 40, 1933, p. 33.

59 "The Viscosity of CO₂ in the Critical Region," by S. N. Naldrett and O. Maass, *Can. J. Research*, vol. 18, series B, 1940, pp. 322–332.

60 "Viscosity of Gases at High Pressures," by E. W. Comings, B. J. Mayland, and R. S. Egly, Univ. Illinois Engr. Exp. Sta. Bull., series 354, 1944, p. 7.

61 "The Viscosity of Steam and Nitrogen at Atmospheric Pressure and High Temperatures," by C. F. Bonilla, R. D. Brooks, and P. L. Walker, Jr., Proceedings of the General Discussion on Heat Transfer, The IME and the ASME, Section II, Sept., 1951, p. 167.

62 "An Experimental Study of the Viscous Properties of Water Vapour," by C. J. Smith, Proceedings of the Royal Society of London, England, vol. 106, series A, 1924, p. 83.

63 "Die Bestimmung der Zähigkeit des Wasserdampfes," by H. Speyerer, *Zeit. des Ver. Deut. Ing.*, vol. 69, 1925, p. 747.

64 "Die Zähigkeit des Wasserdampfes bei Hohen Drucken," by W. Schugajew, *Phys. Zeit. der Sowjetunion*, vol. 5, 1934, p. 659.

65 "The Viscosity of Water and Superheated Steam," by G. A.

Hawkins, H. L. Solberg, and A. A. Potter, Trans. ASME, vol. 57, paper FSP—57-11, 1935.

66 "Über die Innere Reibung Einiger Gase und Dampfe, III. Einfluss des Dipolmoments auf die Grösse der Sutherlandschen Konstanten," by H. Braune and R. Linke, Zeit. Phys. Chem., vol. 148, series A, 1930, p. 195.

67 "Messungen der Zähigkeit von Wasser und Wasserdampf bis ins Kritische Gebiet," by K. Sigwart, Forsch. auf. dem. Geb. des. Ing., vol. 7, series B, 1936, p. 125

68 See discussion by K. A. Gardner, of the paper "The Dynamic Viscosity of Nitrogen," by W. L. Sibbitt, G. A. Hawkins, and H. L. Solberg, Trans. ASME, vol. 65, 1943, pp. 404-405.

69 "Zähigkeit von Wasser und Überhitztem Dampf.," by K. Sigwart, Forsch. auf. dem. Geb. des. Ing., vol. 7, 1926, p. 310.

70 "Viscosity of Superheated Steam," by G. A. Hawkins, H. L. Solberg, and A. A. Potter, Trans. ASME, vol. 62, 1940, pp. 677–688.

71 "Determination of the Viscosity of Steam and Water at High Temperatures and Pressures," by D. L. Timrot, J. Phys., (USSR), vol. 2, 1940, p. 419.

72 "Bestimmung der Zähigkeit von Wasserdampf," by W. Shiller, Forsch, auf. dem Geb. des. Ing., vol. 5, series A, 1934, p. 71.

73 "The Viscosity of Steam," by T. W. Jackson, PhD thesis, Feb., 1949, School of Mech. Engr., Purdue University, Lafayette, Ind.

74 "Thermal Conductivity and Viscosity of Steam at High Temperatures and Pressures," by D. L. Timrot and N. Vargaftig, J. Phys. (USSR), vol. 2, 1940, p. 101.

75 "Measurements on the Viscosity of Helium Gas Between 293 and 1.6° K," by A. van Itterbeek and W. H. Keesom, Physica, vol. 5, 1938, p. 257, also Commun. Lab. Leiden, No. 252 a.

76 "An Improved Hot-Wire Cell for Accurate Measurements of Thermal Conductivities of Gases Over a Wide Temperature Range. Results With Air Between 87° K and 375° K," by W. J. Taylor and H. L. Johnston, J. Chem. Phys., vol. 14, 1946, p. 219.

77 "A Hot-Wire Method for the Thermal Conductivity of Gases," by G. G. Sherratt and E. Griffiths, Phil. Mag., vol. 27, 1939, p. 68.

78 "Experimental Determination of the Thermal Conductivity of Air Between 0° and 100°," by S. W. Milverton, Phil. Mag., vol. 17, 1924, p. 397.

79 "The Thermal Conductivities of the Saturated Hydrocarbons in the Gaseous State," by W. B. Mann and B. G. Dickins, Proceedings of the Royal Society of London, England, vol. 134, series A, 1931, p. 77.

80 "Über die Wärmeleitung von Luft und Wasserstoff," by E. Schneider, Ann. Physik, vol. 79, 1926, p. 177.

81 "Über die Temperaturäbhangigkeit der Wärmeleitfähigkeit Einiger Gases," by A. Eucken, Phys. Zeit., vol. 12, 1911, p. 1101.

82 F. G. Keyes, U. S. Navy, U. S. Air Force, Project Squid, Technical Report 37, April 1952.

83 "Effect of Temperature on the Thermal Conductivity of Gases," by D. W. Stops, Nature, vol. 164, 1949, p. 966.

84 "Zur Absolutemessung des Wärmeleitvermögens von Gasen," by W. Northdurft, Ann. Physik, vol. 28, 1937, p. 137.

85 "The Effect of Accomodations on Heat Conduction Through Gases," by B. G. Dickins, Proceedings of the Royal Society of London, England, vol. 143, series A, 1934, p. 517.

86 "The Thermal Conductivity of Some Gases at 0° C.," by W. G. Kannuluik and H. L. Martin, Proceedings of the Royal Society of London, England, vol. 144, series A, 1934, p. 496.

87 "Experimentelle Untersuchungen über die Wärmeleitfähigkeit der Gase," by S. Weber, Ann. Physik, vol. 54, 1917, p. 325.

88 "Thermal Conductivities of Oxygen and Nitrogen," by H. S. Gregory and C. T. Marshall, Proceedings of the Royal Society of London, England, vol. 118, series A, 1928, p. 594.

89 "The Thermal Conductivities of 8 Common Gases Between 80° K and 380° K," by H. L. Johnston and E. R. Grilly, J. Chem. Phys., vol. 14, 1946, p. 233.

90 "Thermal Conductivity of Gaseous Hydrogen and Gaseous Deuterium," by J. B. Ubbink, Physica, vol. 14, 1948, p. 165.

91 "Über die Wärmeleitfähigkeit der Gase," S. Weber, Ann. Physik, vol. 82, 1927, p. 479.

92 "An Apparatus to Measure the Specific Thermal Conductivity of Gases at Low Temperatures," by J. B. Ubbink and W. J. de Haas, Physica, vol. 10, 1943, p. 451.

93 "Effect of Temperature on the Thermal Conductivity and the Accommodation Coefficient of Hydrogen," by H. S. Gregory, Proceedings of the Royal Society of London, England, vol. 149, series A, 1935, p. 35.

94 "Heat Conductivity of Hydrogen at High Temperatures," by N. B. Vargaftig and I. D. Parfenov, J. Exp. Phys. (USSR), vol. 8, 1938, p. 724.

95 "Experimental Determination of the Thermal Conductivity of Gases," by H. S. Gregory and C. T. Archer, Proceedings of the Royal Society of London, England, vol. 110, series A, 1926, p. 91.

96 "The Thermal Conductivity of Carbon Dioxide," by H. S. Gregory and S. Marshall, Proceedings of the Royal Society of London, England, vol. 114, series A, 1927, p. 354.

97 "The Thermal Conductivity and the Accommodation Coefficient of Carbon Dioxide," by C. T. Archer, Phil. Mag., vol. 19, 1935, p. 901.

98 "The Thermal Conductivity, the Specific Heat, and the Viscosity of Gases," by A. Eucken, Phys. Zeit, vol. 14, 1913, p. 324.

99 "New Measurements of the Heat Conductivity of Steam and Nitrogen," by F. G. Keyes and D. J. Sandell, Jr., Trans. ASME, vol. 72, 1950, pp. 767–778.

100 "The Dependence of the Coefficients of Thermal Conductivity of Gases and Vapors on the Pressure," by N. Vargaftig, Tech. Phys. (USSR), vol. 4, 1937 p. 343.

101 "The Thermal Conductivity of Gases at High Pressures," by A. Botzen, PhD Dissertation, 1952, University of Amsterdam.

102 "Measurement of Thermal Conductivity of Gases at High Pressures," by J. M. Lenoir and E. W. Comings, Chemical Eng. Progress, vol. 47, 1951, p. 223.

103 "Measurements of the Heat Conductivity of Nitrogen-Carbon Dioxide Mixtures," by F. G. Keyes, Trans. ASME, vol. 73, 1951, pp. 597–603.

104 "Additional Measurements of Heat Conductivity of Nitrogen, Carbon Dioxide, and Mixtures," by F. G. Keyes, Trans. ASME, vol. 74, 1952, pp. 1303–1306.

105 "Survey of Experimental Determinations of Heat Capacity of Ten Technically Important Gases," by J. F. Masi. ASME Paper No. 53—A-206.

106 "Relationships Between Transport Properties of Gases," by E. R. Grilly, Amer. J. of Physics, vol. 20, 1952, p. 447.

107 "Gas Tables," by J. H. Keenan and J. Kaye, John Wiley and Sons, New York, N. Y., 1948.

108 "An Investigation of Aircraft Heaters, II. Properties of Gases," by M. Tribus and L. M. K. Boelter, NACA Report W-9, Oct., 1942.

109 "The Mathematical Theory of Non-Uniform Gases," by S. Chapman and T. G. Cowling, Cambridge University Press, 1939.

110 "Heat Transmission," by W. H. McAdams, second edition, McGraw-Hill Book Company, Inc., New York, N. Y., 1942.

111 "Airplane Air Conditioning Engineering Data—Heat Transfer," SAE Aeronautical Information Report 24, Society of Automotive Engineers, 1952.

Discussion

E. WHALLEY.[4] It is quite evident from the deviation curves presented that the authors have not obtained good correlating equations for most of the gases treated.

Theoretical equations for gas properties based on an assumed form of intermolecular potential have two distinct and at the present time partly independent uses. The one is to examine the validity of the assumed form of the potential considered as an approximation to the true potential; the other is to obtain some guidance about the best equation to be used for interpolating and extrapolating the available experimental data. The Lennard-Jones 12:6 potential, though probably one of the closer approximations to the true potential which is yet fairly easily usable for calculating transport properties, does not provide a good method for correlating viscosity data.[5,6,7] This is quite evident from the deviation curves of Hilsenrath and Touloukian. Dr. Schneider and the writer[7] have investigated in some detail the viscosity of several simple nonpolar gases in relation to the 12:6 potential. We showed that at temperatures above 500–1000 K depending on

[4] Division of Applied Chemistry, National Research Council of Canada, Ottawa.

[5] "Determination of Intermolecular Forces From Transport Phenomena in Gases, II." by T. Kihara and M. Kotani, Proceedings of the Physical Mathematical Society, Japan, vol. 25, 1943, pp. 602–614.

[6] "A Summary of the Viscosity and Heat-Conduction Data for He, A, H₂, O₂, N₂, CO, CO₂, H₂O, and Air," by F. G. Keyes, Trans. ASME, vol. 73, 1951, pp. 589–595.

[7] "The Lennard-Jones 12:6 Potential and the Viscosity of Gases." by E. Whalley and W. G. Schneider, Journal of Chemical Physics, vol. 20, 1952, pp. 657–661.

the gas, it was impossible to obtain any 12:6 parameters to fit the viscosity data for argon, nitrogen, oxygen, and carbon dioxide. This is further illustrated in Fig. 30 of this discussion, where the apparent ϵ/k for a 12:6 potential is plotted against temperature for nitrogen, oxygen, and argon. A similar graph for carbon dioxide was given in footnote 7.
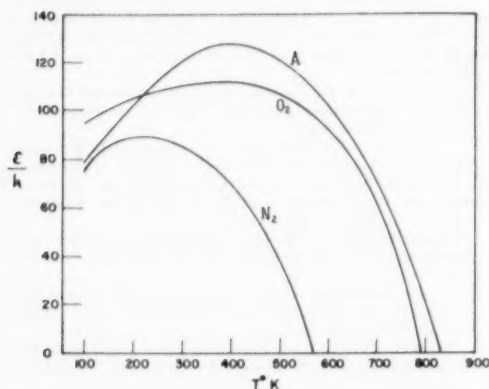

FIG. 30   VARIATION OF ϵ/k FOR A 12:6 POTENTIAL WITH TEMPERATURE FROM VISCOSITY DATA

Keyes[8] has shown that a modified Sutherland equation containing three constants provides a much better correlation of viscosity data over a wide temperature range than the 12:6 potential. At higher temperatures this reduces to the unmodified Sutherland equation used by the authors to correlate the viscosity of air reasonably satisfactorily. Recently the writer tried to correlate the viscosity of simple gases using the theory of corresponding states.[9] On the usual assumptions of this theory and the kinetic theory of gases, for gases which have an intermolecular potential $\varphi(r)$ at a distance r given by

$$\varphi(r) = \epsilon f(r/r_0).\ldots\ldots\ldots\ldots\ldots[22]$$

where ϵ is an energy, r_0 a length, and f a universal function, the reduced viscosity η_r, defined as $\eta V_c{}^{2/3}/\sqrt{MT}$, where V_c is the critical volume should be a universal function of the reduced temperature T_r ($= T/T_c$, where T_c is the critical temperature). Almost all the simple gases investigated fell close to a single curve indicating that Equation [22], herewith, is a good approximation to the true potential. The exceptions, which did not fall on the curve, were hydrogen, helium, and neon, and this is probably due, in part at least, to the occurrence of appreciable quantum effects in both the viscosity and the critical properties. Since it seems likely that the viscosity can be reasonably well correlated by a potential of Type [22] the following were investigated to determine their usefulness: Sutherland potential with an inverse 6th power attractive term,[9] Sutherland equation, 12:6 potential, and exponential:6 potential.[10]

The two parameters involved were adjusted to fit the experimental curve at $T_r = 1$ and $T_r = 10$. In Fig. 32[a] the experimental and calculated curves are compared. The Sutherland potential is omitted from the graph for clarity. Up to $T_r = 3$ it follows roughly curve 5 and above $T_r = 10$ it follows curve 2. It

[8] E. Whalley, Canadian Journal of Chemistry, in press.

[9] "Determination of Intermolecular Forces From Transport Phenomena in Gases," by M. Kotani, Proceedings of the Physical Mathematical Society, Japan, vol. 24, 1942, pp. 76-95.

[10] Transport Properties of Gases Obeying a Modified Buckingham (Exp-6) Potential," by E. A. Mason, University of Wisconsin Naval Research Laboratory Report ONR-1, June 12, 1953.
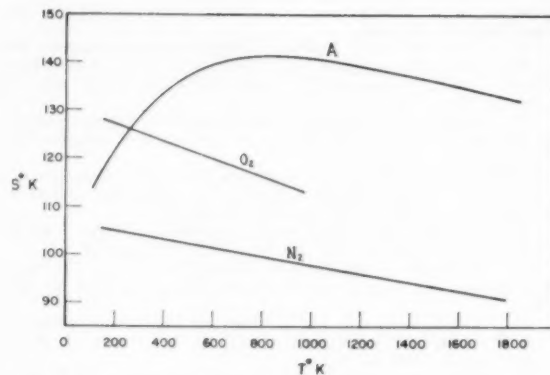
FIG. 31   VARIATION OF SUTHERLAND CONSTANT WITH TEMPERATURE

1- CURVE OF FIG. 1
2- SUTHERLAND EQ
3- 12:6
4- EXP:6 $\alpha = 12$
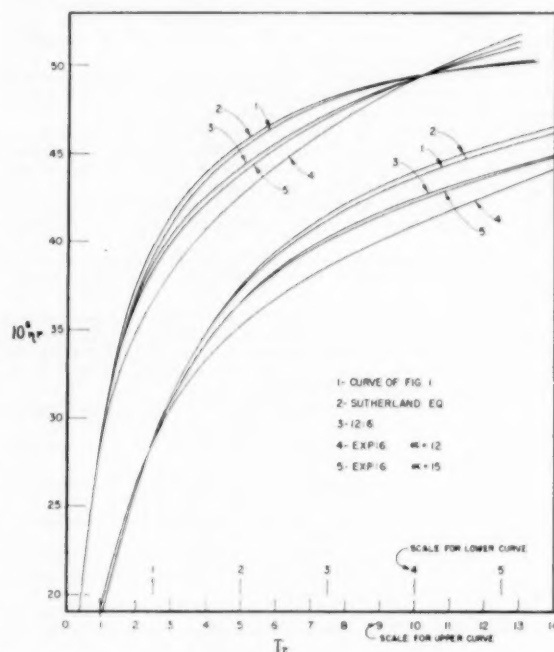5- EXP:6 $\alpha = 15$

FIG. 32   REDUCED VISCOSITY—REDUCED TEMPERATURE CURVES
(Comparison of experimental and theoretical curves fitted at $T_r = 1$ and $T_r = 10$. Curve 1 is experimental.)

is easily seen that the best fit over the rather wide range of reduced temperature is obtained with a simple Sutherland equation.

It seems fairly evident to the writer that the Sutherland equation, or some modification of it, will give the best method for correlating viscosity data over a wide temperature range, and for extrapolating data beyond their present temperature limit. This is illustrated in Fig. 31 of this discussion, where the Sutherland constant S is plotted against temperature for oxygen, nitrogen, and argon. The variation in S is only a few per cent. For predicting the viscosities of simple nonpolar gases the experimental curve in Fig. 31 should give reasonably good values.

Finally, in correlating viscosity and other gas properties it should be the aim of the tabulator to give the best values obtainable using the available experimental data and to extrapolate the values if necessary, distinguishing clearly between extrapolated

and interpolated values. If data are measured by comparative methods, e.g., viscosity by comparison with that of air, the data should be reduced to one common basis. The data then can be correlated and "best" values tabulated, either by using large-scale graphs as was done for the viscosity data used in footnote 7, or better though more tediously correlated by a suitable correlating equation. The equation used should be that which gives the minimum variance of the calculated from the observed data. The method of least squares preferably should be used weighting each value according to its estimated reliability. If data over a wide temperature range are under consideration, the best values probably would be obtained by correlating separately over several smaller but overlapping temperature ranges.

Authors' Closure

The authors wish to express their thanks to Dr. Whalley for directing attention to his forthcoming work on the viscosity of gases using the theory of corresponding states. We await with interest the publication of this work of the Canadian National Research Council.

Dr. Whalley states that "it is evident from the deviation curves presented that the authors have not obtained good correlating equations for most of the gases treated." It is assumed from his subsequent discussion that this criticism is directed at the use of the Lennard-Jones 12:6 intermolecular potential for calculating the viscosity of six of the ten gases presented (O_2, N_2, NO, CO, CO_2, and A). The experimental data for NO, CO_2, and O_2 are fitted by the 12:6 model to within 2 per cent and only in the case of argon and nitrogen did the model depart seriously from the experimental points at high temperatures.

It is clear that a purely empirical correlation of experimental data can always be made to achieve as close a fit as the concordance of the data will allow. This technique was, in fact, used for all the thermal conductivity tables and for the viscosity of air, H_2, He, and H_2O. The viscosities of the six non-polar gases were computed at a time (1952) when the use of the Lennard-Jones 12:6 potential offered certain advantages in calculation—it being the only reasonable potential function for which convenient tables of collision integrals were then available. This model was also successful in representing thermodynamic properties, and resulting viscosities had some theoretical interest. The systematic departures of calculated viscosities from the experimental points at high temperatures were at once apparent, and this is indeed reflected in the deviation plots. This departure was not considered serious enough for engineering purposes to change the tabulated values when this paper was being prepared for publication. It is the opinion of the authors that, for such engineering applications as require it, the tables in question (viscosity of nitrogen and argon) can be readily adjusted by means of these deviation plots to suit the requirements of the user, as was stated in the text.

TABLE 8 COMPARISON OF CALCULATED VISCOSITIES FOR CO_2 FROM DATA CORRELATED BY VARIOUS METHODS

Force Constants		Remarks	$\eta \times 10^7$				
			300°	600°	900°	1200°	1500°
$r_0 \times 10^8$ Å	ϵ/k °K	F. G. Keyes [2] temperatures fitted	poise	poise	poise	poise	poise
3.955	196.1	273°:373°	1505	2692	3632	4419	5134
3.938	202.8	373 :473	1497	2692	3629	4429	5151
3.909	212.2	473: 573	1489	2698	3648	4448	5188
3.874	224.8	573 :673	1478	2703	3690	4491	5228
3.850	235.4	673 :773	1466	2702	3675	4507	5253
3.952	200	This work	1495	2683	3613	4409	5120
3-constant equation (F. G. Keyes [2])			1493	2708	3667	4472	5175

One would infer from Dr. Whalley's Figs. 30 and 31 that the temperature variation of ϵ/k in contrast to that for the Sutherland constant S should disqualify the 12:6 potential as a means for computing gas viscosities. The viscosity, however, depends not only on the choice of ϵ/k but also on the value of r_0 which, if plotted against temperature, shows an opposite variation. In addition, the resulting viscosities are not very sensitive to the choice of force constants when these are properly paired.

F. G. Keyes (2) has fitted the experimental data for CO_2 in different temperature regions and obtained values of ϵ/k varying from 196.1 K to 235.4 K with correspondingly different values of r_0. These differing force constants yield viscosities which are quite concordant among themselves and with the values tabulated here—based on 200 K for ϵ/k and 3.952 Å for r_0. Thus, in spite of the temperature variation of ϵ/k, it is possible to obtain a reasonable fit of the experimental data. Table 8 gives viscosities for CO_2 computed at 300, 600, 900, 1200, 1500 K from different choices of force constants and from a three-constant Sutherland equation.

For argon, F. G. Keyes reports (in a private communication) that at 1000 K, calculations based on the 12:6 model yield values within 2 per cent of those calculated from an empirical fit of his recent experimental data covering the range 90–400 K.

The authors take this opportunity to correct Fig. 17 of the preprint for the erroneous listing of experimental points ascribed to F. G. Keyes. The curve in the present Fig. 17 is taken from a recent correlation of thermal-conductivity data for nitrogen by F. G. Keyes (82). The experimental points of Keyes and Sandell (99) for nitrogen have been omitted from Fig. 17 since they have now been shown to be in error (see F. G. Keyes' closure, Trans. ASME, vol. 73, 1951, p. 602). The viscosity of helium at standard conditions was erroneously listed in Table 2(a) of the preprint. This has been corrected to read $\eta_0 \times 10^7 = 1863$ g sec^{-1} cm^{-1}. Slight changes have also been made in Table 3.
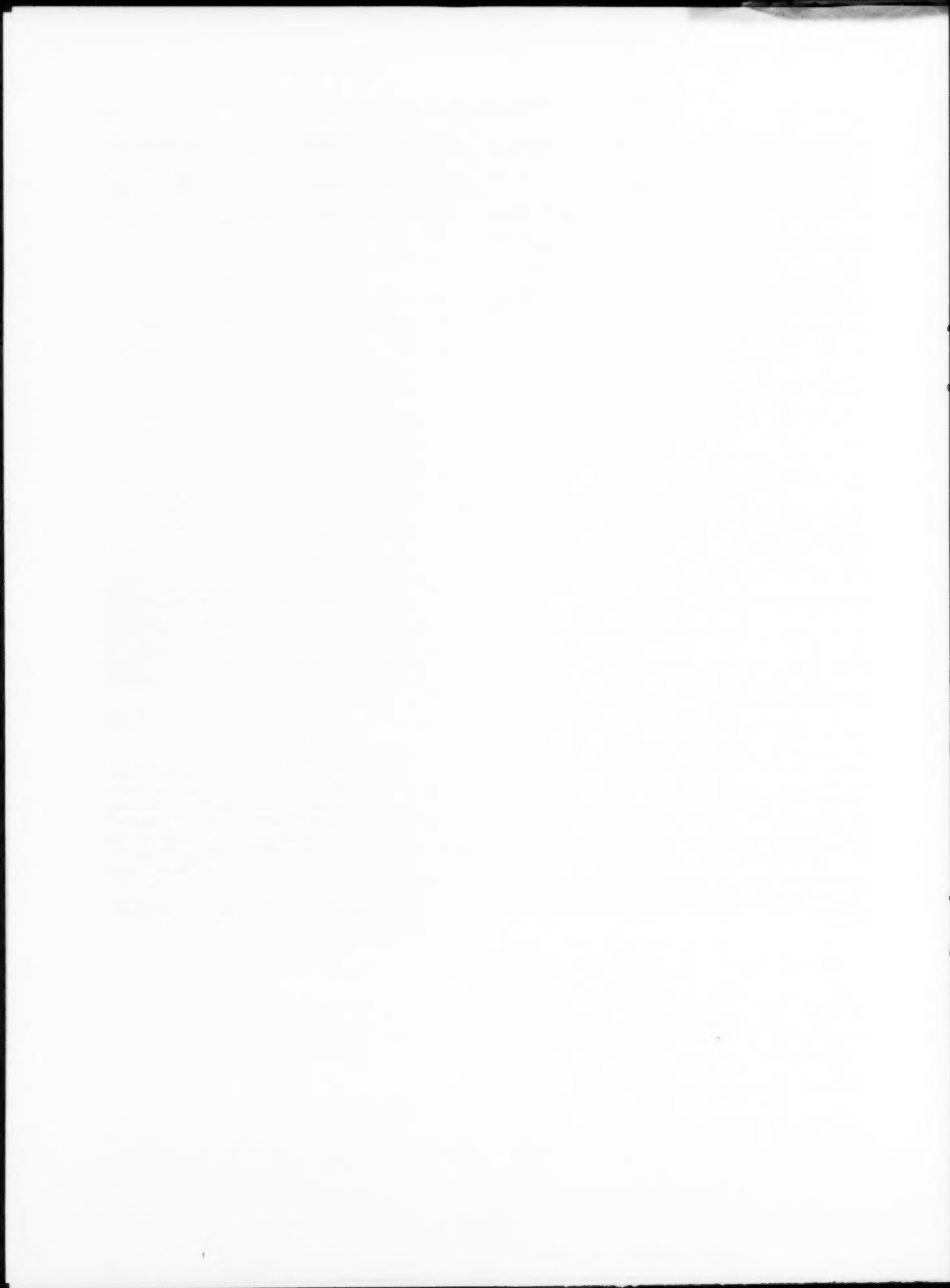
Measurement of the Viscosity of Five Gases at Elevated Pressures by the Oscillating-Disk Method

By J. KESTIN[1] and K. PILARCZYK[2]

The paper describes the measurement of the influence of pressure on the viscosity of five commercially pure gases: air, nitrogen, hydrogen, argon, and helium, in a range up to about 70 atm (1000 psi) at room temperature (20 or 21 C). The viscosity was measured by observing the period of oscillation and the logarithmic decrement of an optically ground quartz disk of 70 mm diam suspended on a thin rhodium-platinum wire between two fixed optically ground quartz plates with a separation of 1 mm and performing torsional oscillations. The data were evaluated on the basis of Macwood's equations, but the instrument proved capable of a higher accuracy of measurement than the 1 per cent inherent in the theory. The scatter of experimental data did not exceed 0.1 per cent and repeatability was of the same order of accuracy. In view of the mathematical difficulties no attempt is made to improve the theory of the instrument but it is shown that the motion of the disk is nonlinear and that the relation between the period of oscillation and the logarithmic decrement is not that which would be expected on the assumption of simple damped harmonic motion.

INTRODUCTION

THE recent survey of available data concerning the thermal properties of substances which was carried out in the NBS-NACA Tables (1)[3] reveals the existence of considerable gaps. In particular, accurate data on the influence of pressure on the viscosity of gases are still very scarce.

The present investigation was undertaken to supply some additional carefully measured values of the viscosity of air, nitrogen, hydrogen, argon, and helium at elevated pressures. At the time of measurement no data on argon and helium were available.

It was decided to use the oscillating-disk method because of its extreme simplicity from the point of view of design and construction. However, in spite of the fact that many workers (2, 3, 4, 5, 6, 7) attempted to derive an acceptable theory of this type of measurement, no completely satisfactory solution has been given so far. The data were evaluated on the basis of Macwood's equations (5), but the instrument proved to be capable of a higher accuracy of measurement than that inherent in the existing theory.
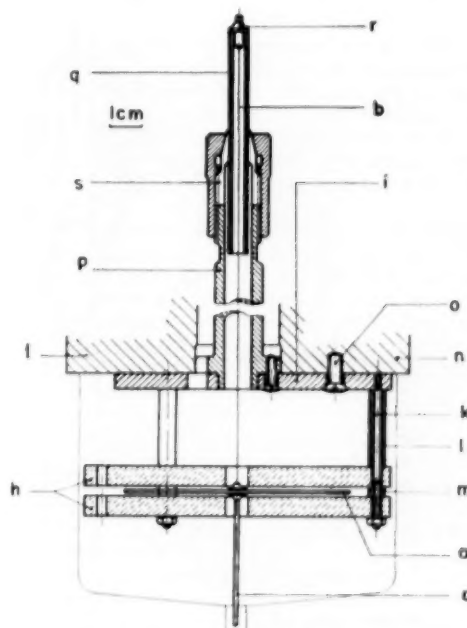
The viscosity of five commercially pure gases was measured in a range of pressures from atmospheric to about 70 atm (1000 psi); the measurements were made at ambient temperature and were

later corrected to 20 C or 21 C, whichever was closer to the mean for a given gas. The measurement consisted in observing the logarithmic decrement of an optically ground quartz disk, 70 mm diam, which was made to perform torsional oscillations on a suspension wire between two fixed quartz disks, equally optically ground, and allowing for a spacing of about 1 mm. The oscillating disk was enclosed in an insulated steel vessel designed to withstand 500 atm pressure.

Some inconsistencies between observed facts and the assumptions made in existing theories of the oscillating-disk viscometer were noted, and by the use of simple mathematical considerations it was shown that the oscillating motion of the disk is nonlinear. It is noted that, owing to the absence of a completely satisfactory theory, the final values of viscosity given cannot be regarded as more accurate than within 1 per cent, whereas the deviation of the experimental results from a smooth mean curve did not exceed 0.1 per cent.

THE OSCILLATING-DISK VISCOMETER AND EXPERIMENTAL PROCEDURE

The oscillating-disk type of viscometer was used by a large number of research workers (3, 4, 6 to 22). The present design differs in many details from previous instruments, most changes

a, Oscillating disk   h, Fixed plates
b, Suspension wire   m, Spacing bushes

FIG. 1 OSCILLATING SYSTEM

Fig. 2   General Viscometer
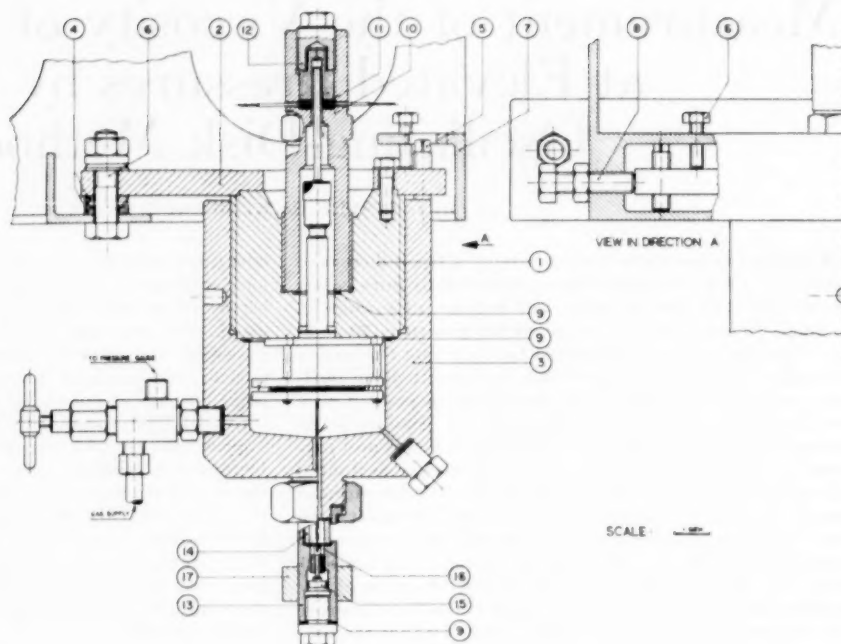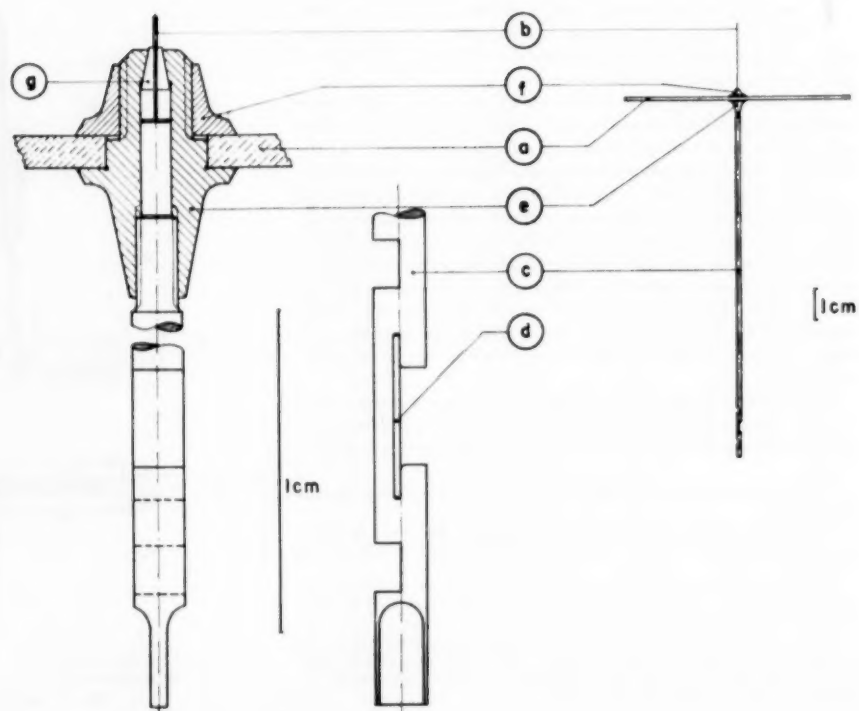Assembly

VIEW IN DIRECTION A

SCALE:

Fig. 3   Details of Oscillating
System

1cm

1cm

1cm

being conducive to higher accuracy and to the handling of high pressures.

The oscillating system, Fig. 1, is accommodated in a suspension holder partially compensated for thermal expansion. The suspension holder is attached to the container head 1 as shown in the general assembly drawing, Fig. 2. Thus the oscillating system remains accessible to measurement and checking for alignment before the viscometer is sealed by screwing on the container 3.

The oscillating system consists of a disk a made of carefully selected, bubble-free, transparent fused quartz of over 99.8 per cent SiO_2 whose diameter (at 15.3 C) $2R = 6.9984 \pm 0.0005$ cm and whose thickness $s = 0.1084 \pm 0.0001$ cm. The disk was optically ground and was flat to $\pm 0.5 \mu$ and parallel to $\pm 15''$. The disk was suspended by means of a rhodium-platinum wire b of diameter $d_w = 0.00508$ cm and length $l = 23.25$ cm, giving a period of oscillation of about $\tau = 33$ sec. All grips were mechanical in order to avoid evaporation which may occur when glues or resins are used.

A long rod c is rigidly attached to the bottom of the disk and bears on its lower end a small aluminized and optically worked flat mirror 5 mm $\times$ 1.5 mm $\times$ 0.25 mm. It is shown to a larger scale in Fig. 3. The two grooves above and below the mirror insure good balancing and a flat bottom end is provided to engage the electromagnetic-starter mechanism.

The miniature collet which grips the suspension wire and fixes the disk is seen in greater detail in Fig. 3. When put together, the conical jaws g which grip the suspension wire b have the minute dimensions of 0.87 mm diam at the base and a length of 2 mm.

The two fixed plates h in Fig 1 are made of the same material as the oscillating disk and their working faces were optically ground and are flat to $\pm 0.12 \mu$. The two plates are held together and attached to the base plate i by means of three screws k and two sets of accurately and simultaneously ground spacing bushes l and m. The separation between disk and fixed plates can be adjusted by changing the bushes.

All parts of the suspension holder were made of mild steel and were free from stresses due to high pressure. The differential axial displacement of the disk was estimated to be 0.00004 cm/deg C and could be ignored completely in the present series of measurements.

The oscillating-system assembly is fixed to the head 1, Fig. 2, which is in turn, rigidly connected to a heavy triangular base plate 2. The base plate is supported on three points and secured to the frame 7. The frame was welded from channel-section steel and rigidly fixed to the 4-ft external wall of the laboratory, thus insuring complete freedom from external vibration.

The assembly is closed at the top with a cap 10 which accommodates klingerit washers 11 for the passage of four thermocouples made of 40 swg nichrome and constantan wire. The thermocouples were calibrated against a standard thermocouple bearing a certificate from the National Physical Laboratory at Teddington. The emf was measured with the aid of a Tinsley potentiometer accurate to 1 μv. Two of the four thermocouples were placed between the fixed plates at an adequate distance from the oscillating disk and the remaining two were placed near the top and bottom of the container, respectively. A final run was started only after the indication of the four thermocouples differed by less than 0.1 deg C and rejected if the variation during a run exceeded 0.1 deg C. No radiation correction was found necessary.

The bottom end of the viscometer is closed by a tube 13 which houses the cylindrical quartz window 14 and the magnetic starter 15. The magnetic starter consists of a brass needle 16 which engages the flattened bottom of the rod attached to the oscillat-

ing disk. The needle is attached to a bar made of soft iron which could be raised and lowered by a powerful Alcomac external magnet 17, with cylindrically shaped poles.

In order to obtain a large angle of vision, good strength, and small dimensions, the window was made of optically worked quartz tubing 4.2 mm thick, 12.5 mm long, and 10.5 mm bore. The tube was sealed with the aid of two lead washers and its optical effect was compensated by a cylindrical lens mounted in front on a special holder.

a, Light source
b, Cylindrical lens
c, Mirror
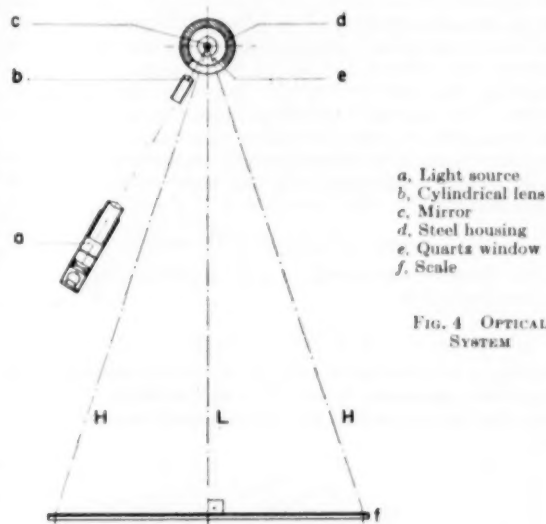d, Steel housing
e, Quartz window
f, Scale

FIG. 4 OPTICAL SYSTEM

The optical system, Fig. 4, is a standard arrangement consisting of a light source, fitted with a fiber strand, which shines on the mirror through a system of lenses. The scale 156 cm long was made of three standard transparent celluloid scales mounted on a rigid frame. As the surface of the mirror rotates in the axis of the cylindrical quartz tube the central ray is always normal to the surface of the quartz tube, removing the need for any corrections.

The pressure was measured by means of two Budenberg Bourdon-type precision test gages, each of which was calibrated against a dead-weight tester at 18 C. The first, with a 6-in. dial, was graduated in kg/cm² and covered a range up to 10 kg/cm² with an accuracy of ± 0.025 kg/cm². The second, with a 7-in. dial, was graduated in psi and covered the remainder of the range with an accuracy of ± 2.5 psi. In all experiments the pressure in the viscometer was set by raising it only.

The time of oscillation was measured with two Swiss stop watches, one giving an accuracy of 0.01 sec, the other one of 0.1 sec. Both stop watches were new and carried the maker's usual guarantee; they were checked carefully against each other, but showed no noticeable deviation. During each run two mean values of the period of oscillation were obtained and the difference never exceeded 0.01 sec.

The instrument was insulated with kapok wool.

Before filling the container with a given gas, the air was extracted from it with the aid of a two-stage "Speedivac" high-vacuum pump down to a pressure of 10^{-3} mm Hg. Further, the container was flushed for several minutes to insure purity of charge. The container was freshly charged whenever the temperature fluctuation in the laboratory exceeded 2 C per day.

PRELIMINARY TESTS

In order to test the system against distortion which might have set in when the cap was screwed on and tightened, and in order to test the wire for stretching, the following preliminary tests were performed:

The relative position of the oscillating disk and the fixed plate was measured carefully with the aid of a traveling microscope, before tightening the container and after its removal. Next the logarithmic decrement was measured three times under atmospheric conditions; when the container was screwed on but not tightened, when the container was tightened in position, and finally when the window was assembled. The maximum deviation in the logarithmic decrement did not exceed 0.07 per cent and was due rather to a change in the temperature of the surroundings from 18.81 C to 18.91 C than to any distortion of the system. The spacing of the disk and plates showed no measurable change either in these preliminary experiments, or later when they were measured at 3-week intervals, during which comparatively violent oscillations of the disk were started on several occasions.

ABSOLUTE INSTRUMENT CONSTANT

The viscosity was calculated from Macwood's equation (5) for small separation

$$\eta_1 = C(\lambda/\tau - \lambda_0/\tau_0) \dots \dots \dots \dots [1]$$

where η_1 is the uncorrected value of the absolute viscosity, λ the logarithmic decrement, τ the period of oscillation, λ_0, τ_0 their respective values in vacuo, and the instrument constant is given by

$$C = \frac{2I}{\pi R^4} D \dots \dots \dots \dots [2]$$

where I is the moment of inertia of the oscillating system, R the radius of the disk, and D the harmonic mean separation

$$D = \frac{2d_1 d_2}{d_1 + d_2} \dots \dots \dots \dots [3]$$

with d_1 and d_2 denoting the upper and lower separation, respectively, which were set as nearly equal as possible. The value η_1 was subsequently corrected for edge effect from

$$\eta = \eta_1(1 - \epsilon) \dots \dots \dots \dots [4]$$

where η denotes the final value of viscosity, and the correction ϵ, as given in Macwood's second paper (5), is calculated from

$$\epsilon = \frac{4sD \sqrt{\pi\rho/\tau\eta_1}}{2sD \sqrt{\pi\rho/\tau\eta_1} - R} \dots \dots \dots \dots [5]$$

s denoting the thickness of the oscillating disk.

As seen from Equation [2], the absolute value of the viscometer constant can be determined easily by weighing and by linear measurement because of the simple geometry of the oscillating system. The results are as follows: Moment of inertia of oscillating system $I = 55.6317 \pm 0.0004$ g/cm², disk radius $R = 3.4992 \pm 0.00025$ cm, mean separation $D = 0.096 \pm 0.002$ cm, instrument constant $C = 227.831 \times 10^{-4} \pm 0.00005$ g/cm. Owing to the fact that the experimental logarithmic decrement was taken to the base 10, the modulus of natural logarithms must be taken into account, and

$$C = 524.599 \times 10^{-4} \pm 0.0001 \text{ g/cm}$$

In order to be in a position to make absolute measurements it would be necessary to determine the term λ_0/τ_0 in Equation [1],

but this proved impracticable with the available vacuum pump. Furthermore from preliminary experiments with air it became clear that an absolute determination of viscosity would be impossible owing to the lack of precision associated with Equations [1], [4], and [5]. The resulting values of the viscosity of air were about 9 per cent higher than the accepted values. A similar effect was noted already by Meyer (7) and others,[4] pointing to the fact that a higher degree of damping was observed than that implied by the equations used, as discussed in more detail later. Consequently, it was decided to perform comparative measurements, as is usual, and to calibrate both C and λ_0/τ_0 in air and hydrogen.

CALIBRATION

Calibration was performed with two gases, air and hydrogen, as their viscosities at atmospheric conditions were considered to be known to a reliable degree of accuracy. With both gases, calibration was performed under atmospheric pressure and at three slightly differing temperatures.

The values for air were taken from the NBS-NACA Tables (1), and those for hydrogen were taken from the work of Woolley, Scott and Brickwedde (23) and reproduced in the same tables, as both sets represent averages of carefully selected data.

Calibration yielded

$$C = 475.5 \pm 0.25 \text{ g/cm}, \quad \lambda_0/\tau_0 = 0.581 \pm 0.031 \text{ per sec}$$

The values of C were in very good agreement with each other, the maximum deviation being about 0.05 per cent. The comparatively large discrepancies in λ_0/τ_0 can be accepted in view of the smallness of the term whose relation to λ/τ, e.g., for air, was of the order of 0.15 per cent.

The discrepancy between the absolute and calibrated values of the viscometer constant C amounts to 9 per cent, as already mentioned in relation to absolute-viscosity measurement.

ACCURACY

Without repeating here the lengthy but standard estimates, and on the assumption that Macwood's theory can be accepted as valid, it may be stated that the maximum errors in the final values of viscosity, and due to experimental errors alone, were estimated as follows:

Hydrogen at atmospheric pressure and about 18 C, 0.17 per cent
Argon at 1000 psia pressure and about 19.5 C, 0.23 per cent

The accuracy of the remaining values ranges between these two.

From the detailed analysis referred to, it became apparent that the magnitude of the error depended primarily on the error in the determination of the logarithmic decrement, and, to a lesser degree, on that associated with the instrument constant C. In any case these errors are much smaller than the error due to approximation in Macwood's equation (5), i.e., 1 per cent.

LOGARITHMIC DECREMENT

As stated before, the most important quantity from the point of view of accuracy was the logarithmic decrement. Consequently, considerable thought was devoted to reducing the error of its determination.

1 Great care was taken in aligning the optical system and in insuring rigidity. The lamp and scale were assembled on a heavy laboratory bench under the suspended viscometer. The bench was attached to the floor with the aid of four steel brackets and braced to the wall with a diagonal cable. A marking plug was

---

[4] It was also confirmed in a private communication from Prof. A. de Troyer of Leiden, Holland.

located with the cathetometer exactly in the axis of suspension of the oscillating system to facilitate the measurement of the distance L, Fig. 4, from the mirror to the scale. The scales were calibrated and found to be uniform, but the absolute value of a unit (1 cm) was a little too large. In order to eliminate this error, all linear measurements were referred to the scale, as the measurement of the logarithmic decrement involves only ratios.

The scale was placed 200 units away from the mirror, making sure that the optical axis was perpendicular to the scale at its zero point. Perpendicularity was achieved by setting the hypotenuses H, Fig. 4, equal with the aid of a special test bar. The lamp was so adjusted as to make the beam of light pass in the same horizontal plane as the mirror. A final check gave $L = 200.0 \pm 0.025$ units of the scale.

2   Precautions were taken to eliminate zero-adjustment errors of the light spot. Denoting by α_0, α_1, α_2...the successive angular amplitudes of the damped harmonic oscillation, the logarithmic decrement appearing in Equation [1] was defined as

$$\lambda = -\ln(\alpha_2/\alpha_0) = -\ln(\alpha_3/\alpha_1) = \dots \dots \dots \quad [6]$$

where even suffixes refer to one and odd suffixes to the other side on the scale with respect to the zero position. Since accurate zero setting of the light spot was difficult to achieve, the logarithmic decrement was evaluated from the sums of successive amplitudes, $\alpha_0 + \alpha_1, \alpha_2 + \alpha_3 \dots$

3   As is well known, the measurement of the logarithmic decrement from successive amplitudes is inaccurate, and it is necessary to work with mean values over a number of complete oscillations, m. Hence

$$\lambda = -\frac{1}{m}\ln(\theta_{n+m}/\theta_n)$$

where

$$\theta_n = \alpha_{n-1} + \alpha_n$$

In the present experiments $m = 5$, so that for most experiments

$$\theta_n/\theta_{n+m} \approx e$$

Since the accuracy of the product m decreases with decreasing angular deflection, the values of m obtained for each of the five oscillations in an experiment were multiplied by weighting factors $w_n = 6, 5, 4, 3, 2$, corresponding to the ratios $\theta_1 : \theta_2 : \theta_3 \dots$ This method of evaluating the logarithmic decrement is similar to the one used by Mason and Maas (19).

When any of the five calculated values m in a run differed by more than 0.5 per cent from the mean, the run was rejected. In this way it was estimated that the accuracy of the accepted values of λ ranged from 0.12 to 0.21 per cent.

Experimental Results

Scope of Experiments.   The present series of experiments were conducted with five gases in the ranges indicated as follows:

	Psi
Air	14.07 to 1007.1
Hydrogen	14.78 to 1003.8
Helium	16.65 to 749.1
Nitrogen	15.39 to 1009.4
Argon	15.60 to 1009.7

The five gases were standard industrial products, supplied in high-pressure cylinders by the British Oxygen Company Ltd., London. The analyses given in the succeeding sections were provided by the makers.

In the range from atmospheric to 150 psi, readings were taken in steps of about 25 psi. The steps were increased to about 50 psi in the range 150–500 psi, and to 75 psi for the range 500–1000 psi. As mentioned, all viscosities were corrected to 21 C or 20 C.

Air.   The air supplied was dry and untreated. It contained the following impurities:

	Per cent
Carbon dioxide	0.03
Water vapor	0.02
Increasing as cylinder is emptied to	0.13

All experiments were carried out by filling the viscometer from a container whose pressure was not allowed to decrease below 120 atm, so that the amount of water vapor was never higher than 0.02 per cent.

The experimental results are given in Fig. 5. Values of density entering into Equation [5] were taken from the equation

$$\rho = \frac{1}{Z}\frac{P}{RT} \dots \dots \dots \dots \dots \quad [7]$$

where Z is the compressibility factor, and R is the gas constant. The latter was assumed as $R = 29.27$ kg m/kg deg C and the compressibility factors were evaluated from the data in the International Critical Tables.
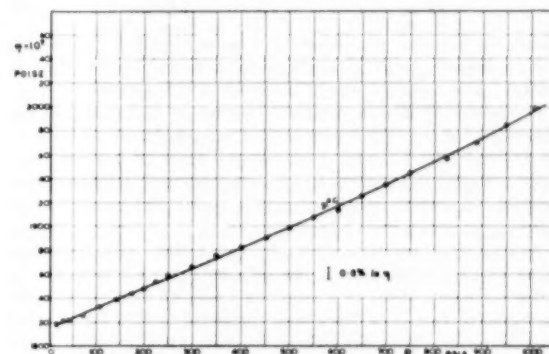

Fig. 5   Pressure Effect on Viscosity of Dry Air at 21 C

The experimental viscosity data were corrected to 21 C assuming a linear temperature coefficient in the range 18 C to 25 C from the following data:

4.78×10^{-7} poise/deg C; NBS-NACA (1), selected from 21 sets of experimental results

4.75×10^{-7} poise/deg C; Johnston and McCloskey (17), experimental

4.75×10^{-7} poise/deg C; Hirschfelder, Bird and Spotz (24, 25), calculated

4.93×10^{-7} poise/deg C; Rigden (26), experimental

4.38×10^{-7} poise/deg C; Vasilesco (27), experimental

The value given in the NBS-NACA Tables finally was adopted. From the data it is possible to deduce the empirical formula

$$\eta/\eta_a = 1 + 90.44 \times 10^{-6}(P - 14.7)$$
$$- 48.25 \times 10^{-10}(P - 14.7)^2$$
$$+ 13.56 \times 10^{-12}(P - 14.7)^3 \text{ at 21 C} \dots [8]$$

Here η denotes the viscosity at pressure P psi, and η_a the viscosity at atmospheric pressure, all at 21 C. The deviation of the values from Equation [8] from the experimental points does not exceed 0.1 per cent. At atmospheric pressure

$$\eta_a = 1817 \times 10^{-7} \text{ poise}$$

which compares well with the following values:

1818 × 10^{-7} poise from the empirical equation in the NBS-NACA
　　　　Tables (1)

1823 × 10^{-7} poise measured by Vasilesco (27) at 21.30 C and cor-
　　　　rected

1819.5 × 10^{-7} poise measured by Houston (28) at 22 C and cor-
　　　　rected

This agreement should be expected because of the proximity
of the temperature to the calibration temperature. It supplies,
however, a measure of the excellent repeatability and the ab-
sence of scatter in the experimental results.

The effect of pressure on the viscosity of air was measured pre-
viously by Iwasaki (22), Kellström (29), Golubev (30) and Nasini
and Pastonesi (31).

Iwasaki's measurements were organized in a way very similar
to the present ones, except that he used infinite disk separation,
but he also based his calculations on Macwood's theory. His
measurements were carried out at three temperatures: 50, 100,
and 150 C and at pressures up to about 200 atm, the accuracy
being 1 per cent. Kellström (29) used a rotating-cylinder vis-
cometer and covered a range of pressures up to about 30 atm, re-
ducing all values to 20 C. His results can be represented by
the equation

$$10^7\eta_{20} = 1819.2 + 1.188p + 0.0128p^2 \ldots \ldots [9]$$

where the pressure p is in atm and η_{20} is in poise.[5] When cor-
recting linearly to 21 C the first term should be increased to
1824.0. His accuracy was of the order of 0.5 per cent.

Golubev (30) used a capillary viscometer and measured the
viscosity of air up to 300 atm at four temperatures: 0 C, 16 C,
50 C, and 100 C, with a maximum error of 1.5 per cent.
Finally Nasini and Pastonesi (31), who also used a transpiration
method, covered the range of up to about 200 atm at 14 C,
claiming an accuracy of 0.5 per cent.

Not all these results are directly comparable with the values
given in Fig. 5, because of the difference in temperature. In
order to reduce them to a common basis, all results, with the
exception of Iwasaki's, have been corrected to 21 C by applying
a linear term. They are plotted together with Iwasaki's values
for 50 C in Fig. 6. Lines of ±0.5 per cent in η for the present
results also are shown.

From Fig. 6, it can be seen that excellent agreement exists with
the three values within our range reported by Golubev. Kell-
ström's values agree very well in the range 1–20 atm, but he
reports a smaller slope, so that at 40 atm his values become
smaller by 1 per cent, compared with the present ones. The
values measured by Nasini and Pastonesi are smaller, the deviation
reaching about 7 per cent at 70 atm. Their rate of pressure in-
crease is considerably smaller in the range 1–35 atm, becoming
only slightly smaller at higher pressures.

Iwasaki's results have not been reduced to 21 C because of the
rather large difference in temperature, but they are compared
with Golubev's data for the same temperature. It is noteworthy
that the rate of increase in his results is smaller than that meas-
ured by the authors at 21 C, as well as by Golubev at 50 C.

Nitrogen The composition of the gas was as follows:

	Per cent
Nitrogen	99.9
Helium	0.03
Neon up to	0.07
Hydrogen up to	0.008
Argon less than	0.005
Oxygen less than	0.001
Carbon compounds less than	0.0005

---

[5] The authors are indebted to Mr. J. Hilsenrath of the National
Bureau of Standards, Washington, for a private communication cor-
recting a misprint in Table 2.39 and in reference (12) of the NBS-
NACA Tables.
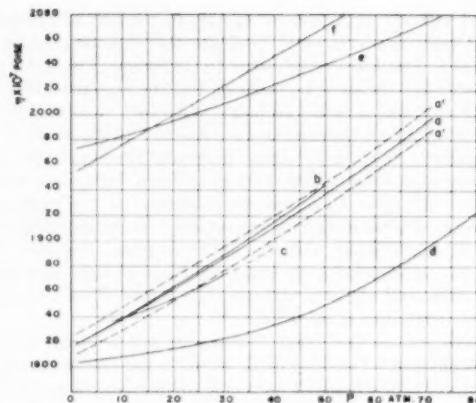
a, Present values　　　　　　　c, Kellström 21 C
a', 0.5 per cent deviation　　　d, Nasini and Pastonesi 21 C
　　from present values　　　　e, Iwasaki 50 C
b, Golubev 21 C　　　　　　　f, Golubev 50 C

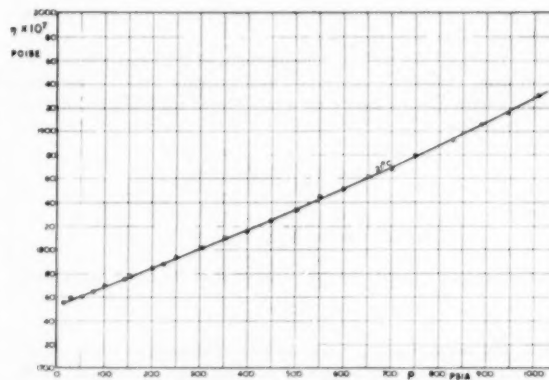FIG. 6　COMPARISON OF RESULTS FOR AIR

FIG. 7　PRESSURE EFFECT ON VISCOSITY OF NITROGEN AT 21 C

The experimental data are collected in Fig. 7.

The density was calculated from Equation [7] and the Inter-
national Critical Tables with $R = 30.257$ kg m/kg deg C, whereas
the temperature coefficient was taken as 4.55 × 10^{-7} poise/deg
C, which is a mean value between 4.5 × 10^{-7} poise/deg C given
by Johnston and McCloskey (17) and 4.6 × 10^{-7} poise/deg C
calculated by Hirschfelder, Bird, and Spotz (25). The value of
4.76 × 10^{-7} poise/deg C quoted by Rigden (26), the mean value
in the range 0–280 C of 3.90 × 10^{-7} given by Vasilesco (27), and
the value of 4.84 × 10^{-7} in the range 25–50 C given by Michels
and Gibson (32) appeared too high.

The experimental results can be reproduced within 0.1 per
cent by the empirical equation

$$\eta/\eta_a = 1 + 88.79 \times 10^{-6}(P - 14.7) + 9.168 \times 10^{-10}(P - 14.7)^2$$
$$+ 10.86 \times 10^{-12}(P - 14.7)^3 \ldots \ldots \ldots [10]$$

At atmospheric pressure and 21 C

$$\eta_a = 1755 \times 10^{-7} \text{ poise}$$

This value can be compared with the following determinations:

(1738.2 ± 0.73) × 10^{-7} poise at 17 C, Rigden (26)
　　　　1756 × 10^{-7} poise corrected linearly to 21 C from
　　　　　　　　Rigden's measurements

1748 × 10⁻⁷ poise at 21 C interpolated from calculated data; Hirschfelder, et al. (25)

1760 × 10⁻⁷ poise at 21 C interpolated from measured data; Johnston and McCloskey (17)

1758 × 10⁻⁷ poise at 21 C corrected linearly from 0 C on the basis of Vasilesco's (27) measurements

The agreement appears to be excellent, as the largest discrepancy with measured values does not exceed 0.2 per cent, which is well within the experimental error. This agreement provides an additional check on the accuracy of calibration, at least at pressures near atmospheric.

The pressure dependence of the viscosity of nitrogen was measured by Sibbitt, Hawkins, and Solberg (33), Michels and Gibson
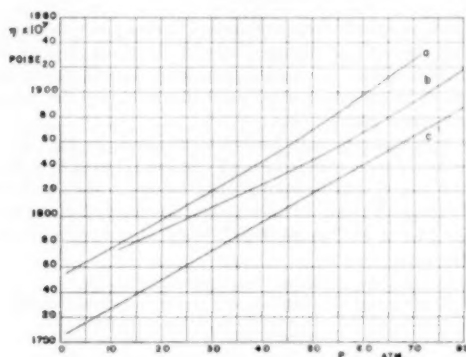
a, Present results
b, Michels and Gibson
c, Sibbitt, Hawkins, and Solberg

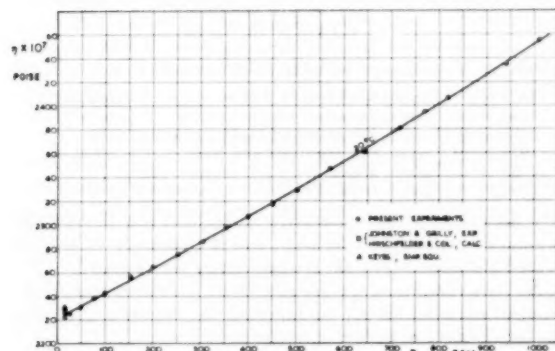FIG. 8   COMPARISON OF RESULTS FOR NITROGEN

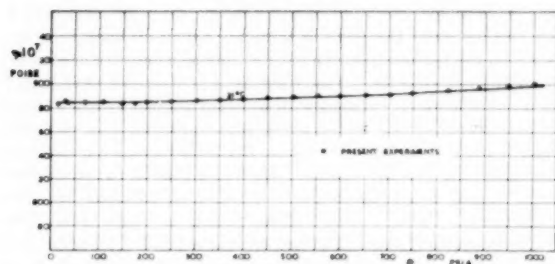FIG. 9   PRESSURE EFFECT ON VISCOSITY OF ARGON AT 20 C

FIG. 10   PRESSURE EFFECT ON VISCOSITY OF HYDROGEN AT 21 C

(32), and Boyd (34). The results are compared in Fig. 8, Rigden's value at 1 atm also being shown.

Sibbitt, et al., measured the viscosity of nitrogen by the capillary-flow method in the range 68 deg to 923 deg F and 14.7 to 1020 psi. The curve shown in Fig. 8 is a smoothed curve which represents their extensive experimental data with an accuracy of 1.6 per cent. Although their values are some 3 per cent lower than the present results, there is excellent agreement as regards slope. However, it appears that the results of Sibbitt, et al., suffer from a calibration error, as their value at 1 atm is obviously too low, considering the excellent agreement between the various determinations of η_a as mentioned previously.

Michels and Gibson (32) used a Rankine-type capillary viscometer and determined the viscosity of nitrogen at 25, 50, and 75 C in the range of 10–1000 atm. The agreement in the range of lower pressures 10–15 atm is excellent, the discrepancy being less than 0.5 per cent. However, Michels and Gibson's values are lower by about 2 per cent at 70 atm and the slope is slightly smaller.

Boyd's values (34) were obtained with a transpiration viscometer at 30, 50, and 70 C in the range from 75 to 180 atm. However, in view of the large scatter the results cannot be usefully compared.

In conclusion it might be worth noting that the slope for nitrogen is the same as that for air.

Argon. The analysis of the gas supplied was as follows:

	Per cent
Argon	99.8
Nitrogen	0.2

The experimental results for argon are given in Fig. 9. For the calculation of density from Equation [9] with compressibilities taken from the International Critical Tables the value $R = 21.248$ kg m/kg deg C was used. The temperature correction 6.37×10^{-7} poise/deg C was averaged from the following data:

6.55×10^{-7} poise/deg C summary by Keyes (35)
6.25×10^{-7} poise/deg C measured by Johnston and Grilly (18)
6.30×10^{-7} poise/deg C calculated by Hirschfelder, et al. (25)

The empirical formula for the viscosity of argon at 20 C becomes

$$\eta/\eta_a = 1 + 91.08 \times 10^{-6}(P - 14.7)$$
$$+ 108.75 \times 10^{-10}(P - 14.7)^2$$
$$+ 1.959 \times 10^{-13}(P - 14.7)^3 \quad [11]$$

with a deviation not exceeding 0.1 per cent.

At atmospheric pressure we have

$$\eta_a = 2225 \times 10^{-7} \text{ poise at 20 C}$$

which can be compared with the following data interpolated from published tables:

2227 × 10⁻⁷ poise: Johnston and Grilly (18), measured
2226 × 10⁻⁷ poise: Hirschfelder, et al. (25), calculated
2231 × 10⁻⁷ poise: Keyes (35), empirical formulation
2211 × 10⁻⁷ poise: Vasilesco (27), measured

The largest discrepancy is only about 0.64 per cent, and the agreement can be considered very satisfactory. This circumstance, as was the case with nitrogen, confirms the accuracy of the calibration of the instrument.

No comparative data on the pressure effect on the viscosity of argon were traced.

To conclude this section, it might be of interest to note that the slope of the viscosity-pressure curve is slightly greater than for air or nitrogen.

Hydrogen. The composition of the hydrogen used was as follows:

	Per cent
Hydrogen	99.9
Oxygen	0.05
Nitrogen up to	0.05
Carbon monoxide	0.001
Carbon dioxide	0.001
Carbon compounds	0.002

The experimental results for hydrogen are given in Fig. 10. The values of density were determined from the NBS-NACA Tables, and the temperature coefficient of viscosity for correction was taken as 2.00×10^{-7} poise/deg C, as given in the same Tables (2.03×10^{-7}), as well as by Woolley, Scott, and Brickwedde (23), (2.02×10^{-7}), Johnston and McCloskey (17) (2.03×10^{-7}), Hirschfelder, Bird, and Spotz (25) (2.0×10^{-7}). The following empirical formula fits the present results in the usual way

$$\eta/\eta_a = 1 + 4.647 \times 10^{-6}(P - 14.7) + 1.256 \times 10^{-9}(P - 14.7)^2 \dots \dots [12]$$

at 21 C. At atmospheric pressure

$$\eta_a = 884.4 \times 10^{-7} \text{ poise}$$

which compares well with the value selected during calibration and shows the absence of scatter. It agrees with Johnston and McCloskey's value 884.1×10^{-7} poise corrected from 293 K, as well as with the Leiden value of 884×10^{-7} poise.

Woolley, Scott, and Brickwedde have reviewed the viscosity data at higher pressures measured by Boyd (34) and Gibson (36)[*] and compared the results with Enskog's (23, 32) theory. In view of the large amount of numerical work involved, no direct comparison with Enskog's formulas is given at present either for hydrogen or for the other gases. In the case of hydrogen, however, the present results are compared with those given by Woolley in the NBS-NACA Tables for 300 K at 1, 50, and 100 atm. The results have been linearly corrected to 21 C and are shown in Fig. 11. It is seen that the two sets of data agree within
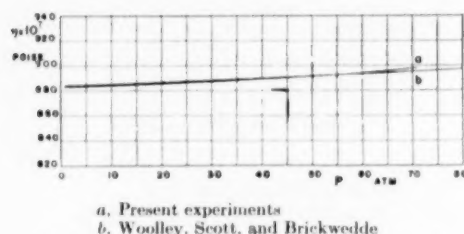

a, Present experiments
b, Woolley, Scott, and Brickwedde
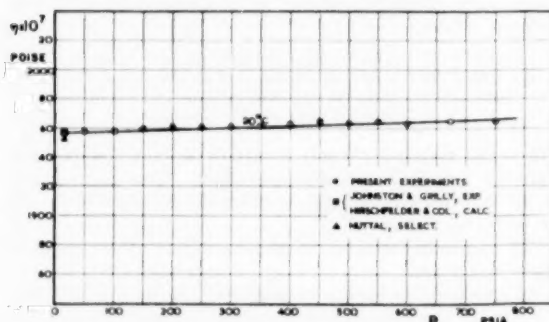FIG. 11 COMPARISON OF RESULTS OF HYDROGEN

FIG. 12 PRESSURE EFFECT ON VISCOSITY OF HELIUM AT 20 C

[*] The authors could not obtain access to this work.

0.1 per cent up to about 48 atm. At higher pressures the present curve has a slightly steeper course, so that at about 68 atm the present value is some 0.5 per cent higher, which, however, is still within the limits of accuracy claimed.

As expected, the influence of pressure on the viscosity of hydrogen is comparatively very small.

Helium. The composition of the gas was as follows:

	Per cent
Helium	98
Nitrogen	1.8
Oxygen	0.1
Hydrogen	0.1
Carbon monoxide	Trace
Carbon dioxide	Trace
Carbon compounds	Trace

The comparatively large amount of nitrogen was tolerated because the viscosity of nitrogen is only about 20 per cent lower than that of helium. Assuming proportional parts, the estimated influence of the presence of nitrogen was to reduce the measured values by about 0.35 per cent.

The experimental results for helium are given in Fig. 12. The density data were calculated from Equation [7] with $R = 211.954$ kg m/kg deg C and compressibility factors from the International Critical Tables. The temperature correction factor was taken as 4.64×10^{-7} poise/deg C, which is an average from the following data:

4.81 poise/deg C; Keyes' empirical equation (35)
4.95 poise/deg C; Johnston and Grilly, experimental (18)
4.35 poise/deg C; Hirschfelder, et al., calculated (25)
4.46 poise/deg C; NBS-NACA Tables, averaged (1)

The results can be represented by the empirical equation

$$\eta/\eta_a = 1 + 7.753 \times 10^{-6}(P - 14.7) - 0.1711 \times 10^{-8}(P - 14.7)^2 \dots \dots [13]$$

at 20 C in the same way as before. At atmospheric pressure

$$\eta_a = 1957 \times 10^{-7} \text{ poise}$$

which can be compared with the following values:

1953×10^{-7} poise, NBS-NACA Tables, empirical equation (1)
1953×10^{-7} poise, Vasilesco, corrected (27)
1953×10^{-7} poise, Johnston and Grilly, measured (18)
1975×10^{-7} poise, van Itterbeek and Keesom, measured (4)
1958×10^{-7} poise, Keyes' empirical formula (35)
1934×10^{-7} poise, Hirschfelder, et al., calculated (25)

The agreement with the majority of the data is well within the accuracy of Macwood's formula, and the accuracy of the calibrated instrument constant is again amply corroborated.

No data concerning the pressure effect have been traced for a comparison to be made. As expected, the influence of pressure on the viscosity of helium is comparatively small.

LIMITING VALUES

It will be recalled that Macwood's formulas, Equations [1], [2], [4], and [5], are valid only if $D\sqrt{\pi\rho/\tau\eta} < 0.3$ and only if the flow between the disks is laminar, which circumstance depends on the Reynolds number $\text{Re} = \omega R^2/\nu$, where ω is the maximum angular velocity. Von Kármán and Cochran have found for an infinite plane, rotating with constant angular velocity about an axis perpendicular to the plane, that transition does not take place if $\text{Re} < 5 \times 10^5$. However, this value seems too high for the oscillating type of motion. Foch and Barriol (41) indicated $\text{Re} < 60$ and noted that above that value centrifuging becomes observable. Table 1 gives these values for each gas. The Reynolds number was calculated with $\omega = 0.0317$ 1/sec in each case. This corresponds to the maximum measurable angle of deflection and was approximately equal for all gases.

TABLE 1   RANGE OF LIMITING FACTORS IN EXPERIMENTS

Gas	Pressure, psi	$D\sqrt{\pi\rho/\tau\eta}$	Re
Air	14.07	0.077	2.603
	225.8	0.299	...
	1007.1	0.613	162.6
Hydrogen	14.78	0.029	0.373
	1003.8	0.236	24.3
Helium	16.65	0.029	0.376
	749.1	0.193	16.35
Nitrogen	15.39	0.077	2.73
	224.0	0.298	...
	1009.4	0.614	162.5
Argon	15.6	0.084	3.09
	200.9	0.301	...
	1009.7	0.659	187.5

It can be seen from Table 1 that for hydrogen and helium the two conditions were well satisfied. In the case of air, hydrogen, and nitrogen, the value of $D\sqrt{\pi\rho/\tau\eta}$ reached 0.3 at about 225 psia and double that value at 1000 psia.

A similar trend is observed as regards the Reynolds number. In this connection, however, it must be borne in mind that maximum angular velocity, corresponding to maximum angle of deflection prevailed for a very short period only, so that at about the fifth oscillation the Reynolds number was less than 60, even for the extreme end of the pressure range.

REMARKS ON ASSUMPTIONS IN THEORY OF OSCILLATING-DISK VISCOMETER

At present there are two derivations of formulas for the oscillating-disk viscometer. One is credited to Macwood (5) and relates to the cases of small and large separations. The two cases are covered by two different formulas corresponding to two different expansions of the hyperbolic tangent which appear in the final expression for damping. This leaves a range of values $0.3 < D\sqrt{\pi\rho/\tau\eta} < 4.0$ out of consideration. The second derivation relates to infinite disk separation only. The current formula was first published, without an indication of its actual derivation, by Andronikashvili (2), and later by Hollis-Hallett (3).[7] Both these authors make use of Meyer's (7) differential equation as well as of his method of specifying the boundary conditions and of solving the differential equation. A similar approach was used by Houston (28) for the rotating-cylinder viscometer.

Whereas Macwood assumed an infinitely thin disk and deduced a separate correction factor for the effect of finite thickness, Andronikashvili and Hollis-Hallett, following Meyer, introduced a finite disk thickness from the outset. De Troyer, van Itterbeek, and van den Berg (21) also published a formula for infinite separation and alluded to an error in Macwood's second paper without, however, specifying its nature.

In both derivations it is *assumed* that the motion of the disk is linear and satisfies the standard equation

$$\ddot{\alpha} + \frac{L}{I}\dot{\alpha} + \frac{K}{I}\alpha = 0 \dots\dots\dots\dots [14]$$

where α is the angle of deflection, I is the moment of inertia of the oscillating system, L the damping factor, and K the elastic constant. It is assumed that both L and K are constant during one experiment, and the derivation seeks to determine the relationship between the damping constant L and the viscosity of the gas η, which is to be measured. Any damping which might exist in the suspension wire, and which, in any case, has been found by all experimenters to be very small compared with viscous damping, is included in the value of L. This relation, or, what amounts to the same, the relation between the logarithmic decrement λ and viscosity, is obtained by solving a simplified

[7] The authors are indebted to Dr. Hollis-Hallett for his private communication which cleared up a point related to his paper.

version of the Navier-Stokes equations with assumed cylindrical symmetry and imposing a damped harmonic (i.e., linear) oscillation of the disk as a boundary condition. The simplifications in the Navier-Stokes equations consist in neglecting compressibility, as well as in the assumption of negligible radial pressure gradients. Finally it is assumed that fluid particles move in planes which are perpendicular to the axis of oscillation, and their paths lie on concentric circles; i.e., that their velocities are purely tangential, the axial and radial components being negligible. These assumptions are sufficient to justify assumption [14].

This last set of assumptions requires accurate verification. In particular, the problem appears to be mathematically over-determined, as the Navier-Stokes equations, together with the actual initial conditions expressed by the initial amplitude and the condition of no slip on solid surfaces, fully determine the motion of a given disk on its suspension, and it cannot, a priori, be assumed that it performs a linear damped oscillation.

In order to verify experimentally how far the assumption of a linear oscillation is justified, it would be necessary to analyze the motion in great detail. The standard method of verification, based on a direct comparison of the value of the logarithmic decrement during several successive beats, must be questioned on two grounds: (a) The accuracy of measurement of the logarithmic decrement from a single cycle is very poor. (b) It is known from the approximate theory of equivalent linearization of the differential equation of nonlinear vibrations due to Kryloff and Bogoliuboff (37) that, for a first approximation, the solution of the nonlinear equation

$$\ddot{x} + \omega_0^2 x = \mu f(x, \dot{x}) \dots\dots\dots\dots [15]$$

where μ is small, is a pseudoharmonic oscillation with a period $2\pi/\omega_0$ and a slowly varying logarithmic decrement

$$\lambda = \frac{\mu}{\pi a \omega_0} \int_0^{2\pi} f(a\cos\phi, -a\omega_0\sin\phi)\sin\phi\,d\phi$$

where a is the amplitude, and ϕ is the phase angle. Thus deviation from linearity is difficult to detect experimentally in a direct manner. The salient point is that the value of the logarithmic decrement is influenced more strongly than that of the period of vibration.

If the problem were only to describe the motion of the disk, Equation [14] might be sufficiently good an approximation, but the converse process need not necessarily lead to an accurate formula for viscosity, because the effect of this assumption on the solution of the Navier-Stokes equations cannot be estimated. For this reason, what is considered a more precise test of the oscillation was devised.

From elementary considerations it is possible to deduce two relations between the constants L/I and K/I in Equation [14], and the two measured quantities, the logarithmic decrement λ, and the period of oscillation, τ

$$\tau = \frac{2\pi}{\sqrt{(K/I) - \frac{1}{4}(L/I)^2}}$$

and

$$\lambda = \frac{\pi L/I}{\sqrt{(K/I) - \frac{1}{4}(L/I)^2}} \Bigg\} \dots\dots\dots [16]$$

If the constant L/I is now eliminated from these two equations, a relationship is obtained, which is independent of the damping. It must be satisfied at all experimental points, if the assumption of linear damping is accurate. In this way we obtain

$$\frac{I}{K} = \frac{\tau^2}{4\pi^2 + \lambda^2} = \left(\frac{\tau}{2\pi}\right)^2 \frac{1}{1 + \Delta^2}$$

where

$$\Delta = \lambda/2\pi \qquad \Bigg\} \quad \dots \dots [17]$$

We now propose to calculate these quantities for the present and for Iwasaki's results. Unfortunately, neither Johnston and Grilly (18) nor Johnston and McCloskey (17) published their experimental readings to enable us to make that comparison.

In normal experimental practice Δ is a very small quantity. It ranged from about 0.01 to about 0.03 in the present series, and from about 0.003 to 0.01 in Iwasaki's experiments.

The values on the right-hand side of Equation [17] are shown plotted as a function of the period τ, in Fig. 13 for the present series of five gases with the values of density shown against some of the experimental points. It is seen that the value of the "constant" I/K from Equation [17] ranges from 28.0 sec^2 for low densities to about 29.0 sec^2 for higher densities, varying by about 3.5 per cent.

This is a measure of the deviation of the motion of the disk from a linear oscillation. Moreover, the deviation seems to increase with increasing gas density or, for a given gas and temperature, with increasing pressure.

In Iwasaki's case (22) the values of λ are so small that Δ^2 in Equation [17] can be neglected with respect to unity. Hence constancy of I/K implies a constant period of oscillation, as it becomes nearly proportional to $(\tau/2\pi)^2$. In actual fact the period varied as follows:

From 7.515 sec to 7.590 sec for Iwasaki's assembly A
From 7.229 sec to 7.265 sec for Iwasaki's assembly B
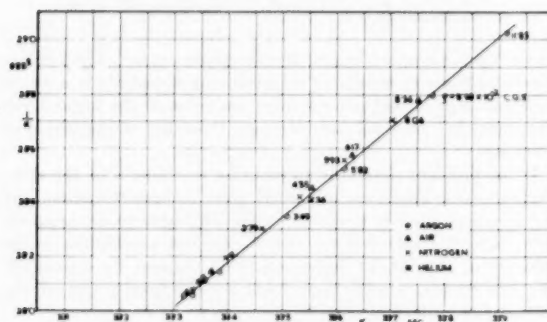From 9.515 sec to 9.571 sec for Iwasaki's assembly C

FIG. 13   VALUES OF I/K FROM EQUATION [17] PLOTTED AGAINST PERIOD OF OSCILLATION, τ
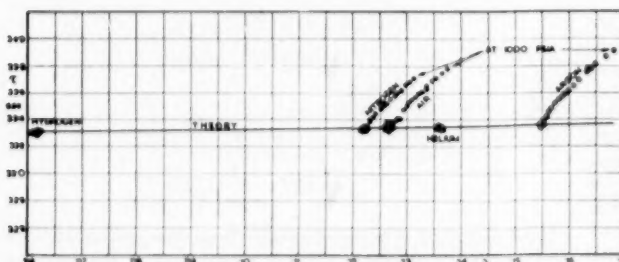(Figures against experimental points denote density in g/cm^3 × 100.)

FIG. 14   VARIATION OF PERIOD τ, WITH LOGARITHMIC DECREMENT λ, FOR PRESENT EXPERIMENTS

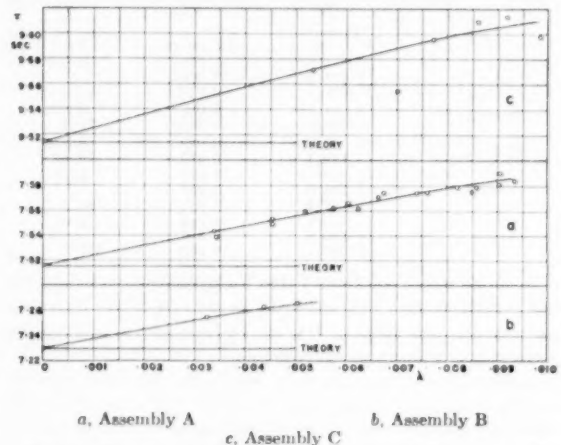a, Assembly A   b, Assembly B
c, Assembly C

FIG. 15   VARIATION OF τ WITH λ FOR IWASAKI'S EXPERIMENTS

giving respective variations in I/K of 0.2, 1.0, and 1.3 per cent for air only, as against the five gases in the present experiments.

A slightly different representation of the same data is given in Figs. 14 and 15. If the period and the logarithmic decrement are selected as variables, then Equation [17] represents the curve

$$\frac{\tau^2}{4\pi^2(I/K)} - \frac{\lambda^2}{4\pi^2} = 1$$

or

$$\frac{\tau^2}{4\pi^2 I/K} - \Delta^2 = 1 \qquad \Bigg\} \quad \dots \dots [18]$$

The curves marked "theory" in Fig. 14 were drawn for a value $K/I = 0.18967$, which fitted the averaged results for hydrogen. In this way excellent agreement was also obtained for helium. In the case of the three heavier gases, air, nitrogen, and argon, agreement is obtained only for the lower range of pressures. In Fig. 15, the lines marked "theory" are nearly horizontal, as Δ was very small in Iwasaki's experiments. They were drawn through the in vacuo values of τ and λ.

Figs. 14 and 15 bring out clearly the deviation from linear motion in the case of denser gases at higher pressure.

CONCLUSION

From the preceding argument it may be concluded that the accuracy of Macwood's equations decreases for higher densities. It is not, however, possible to indicate the degree of approximation, without developing a theory which would be free of the assumption of linear oscillations. The full precision of 1 per cent certainly can be claimed for hydrogen and helium and for the lower pressure range of the three remaining gases. It must, however, be admitted that in the higher density ranges, in the present, as well as in other published data, the uncertainty increases.

This conclusion is not surprising if we consider the known accurate solutions of the Navier-Stokes equations for similar configurations. Von Kármán (38) and Cochran (39) investigated the flow caused by an infinitely large plane revolving steadily around an axis perpendicular to it and found that at all points in the fluid there existed a radial and axial component in addition to the tangential component of velocity. The centrifuging action, disregarded in Macwood's as well as in Meyer's

theory, is particularly pronounced in the neighborhood of the revolving plane. Similar conclusions were reached by Batchelor (40),[a] who investigated qualitatively the motion in a fluid contained between two infinitely large parallel planes, at a fixed distance from each other, of which one revolves steadily about a perpendicular axis. It appears that the momentum imparted to the gas as a result of centrifuging is reflected in increased damping, as the energy can be derived only from the oscillating disk. Therefore, if this phenomenon is neglected, a corresponding increase in the measured value of viscosity will result. Calibration with a gas of known viscosity will, to a certain extent, eliminate the error by leading to a reduced value of the instrument constant, as observed.

Considering the mathematical difficulties which Batchelor encountered in his much simpler problem it must be concluded that the derivation of a more exact equation for the oscillating-disk viscometer is a major undertaking. For that reason Macwood's available formulas were retained for the present, but it should be emphasized again that the inherently great accuracy of an oscillating-disk viscometer is limited by the absence of an accurate theory.

BIBLIOGRAPHY

1   NBS-NACA Tables of Thermal Properties of Gases, U. S. Department of Commerce, Washington, D. C., 1950–1951.
2   "A Direct Observation of Two Kinds of Motion of Helium, II," by E. L. Andronikashvili, *Journal of Technical Physics*, USSR, vol. 10, 1946, p. 201.
3   "Experiments With Oscillating Disk Systems in Liquid Helium, II," by A. C. Hollis-Hallett, Proceedings of the Royal Society of London, England, series A, vol. 210, 1952, p. 404.
4   "Measurements on the Viscosity of Helium Gas Between 293° and 1.6° K," by A. van Itterbeek and W. H. Keesom, *Physica*, vol. 5, 1938, p. 257.
5   "The Theory of the Measurement of Viscosity and Slip of Fluids by the Oscillating Disk Method," by G. E. Macwood, *Physica*, vol. 5, 1938, pp. 374 and 763.
6   "On the Viscosity or Internal Friction of Air and Other Gases," by J. C. Maxwell, Philosophical Transactions of the Royal Society of London, England, vol. 156, 1866, p. 249.
7   "Über die Bestimmung der inneren Reibung nach Coulomb's Verfahren," by O. E. Meyer, *Annalen der Physik*, Wiedemann Series, vol. 32, 1887, p. 642.
8   "The Coefficient of Viscosity of Air," by H. Tomlinson, Proceedings of the Royal Society of London, England, series A, vol. 40, 1886, p. 40.
9   "Über die Viskosität einiger Gase und ihre Abhängigkeit bei tiefen Temperaturen," by H. Vogel, *Annalen der Physik*, Series 4, vol. 43, 1914, p. 1235.
10   "Über die innere Reibung der Gase bei tiefen Temperaturen," by P. Günther, *Zeitschrift für Physik und Chemie*, vol. 110, 1924, p. 626.
11   "Measurement of the Viscosity of Gases Over a Large Temperature Range," by P. Sutherland and O. Maas, *Canadian Journal of Research*, vol. 6B, 1932, p. 428.
12   "Measurements on the Viscosity of Argon Gas at Room Temperature and Between 90 and 55° K," by A. van Itterbeek and O. van Paemel, *Physica*, vol. 5, 1938, p. 1009.
13   "Measurements on the Viscosity of Neon, Hydrogen, Deuterium, and Helium as a Function of Temperature," by A. van Itterbeek and O. van Paemel, *Physica*, vol. 7, 1940, p. 265.
14   "The Viscosity of Liquid Helium," by W. H. Keesom and G. E. Macwood, *Physica*, vol. 5, 1938, p. 737.
15   "The Viscosity of Liquid Hydrogen," by W. H. Keesom and G. E. Macwood, *Physica*, vol. 5, 1938, p. 745.
16   "The Viscosity of Hydrogen Vapour," by W. H. Keesom and G. E. Macwood, *Physica*, vol. 5, 1938, p. 749.
17   "Viscosities of Several Common Gases Between 90° K and Room Temperature," by H. L. Johnston and K. E. McCloskey, *Journal of Physical Chemistry*, vol. 44, 1940, p. 1038.
18   "Viscosities of CO, He, Ne and A Between 80° K and 300° K," by H. L. Johnston and E. R. Grilly, *Journal of Physical Chemistry*, vol. 46, 1942, p. 948.
19   "Measurement of Viscosity in the Critical Region: Ethylene," by S. G. Mason and O. Maas, *Canadian Journal of Research*, vol. 18B, 1940, p. 128.
20   "Some Further Experiments With an Oscillating Disk in Liquid Helium," by P. L. Smith, *Physica*, vol. 16, 1950, p. 808.
21   "Measurements on the Viscosity of Liquid Helium by Means of the Oscillating Disk Method," by A. de Troyer, A. van Itterbeek, and G. J. van den Berg, *Physica*, vol. 17, 1951, p. 50.
22   "Measurement of Viscosities of Gases at High Pressure—I. Viscosity of Air at 50°, 100° and 150° C," by H. Iwasaki, *Scientific Reports*, Tohoku University, Japan, series A, vol. 3, 1951, p. 247.
23   "Compilation of Thermal Properties of Hydrogen in Its Various Isotopic and Ortho-Para-Modifications," by W. H. Woolley, B. R. Scott, and F. G. Brickwedde, National Bureau of Standards, *Journal of Research*, vol. 41, 1948, p. 379.
24   "The Transport Properties of Non-Polar Gases," by J. O. Hirschfelder, R. B. Bird, and E. L. Spotz, *Journal of Chemical Physics*, vol. 16, 1948, p. 968.
25   "Viscosity and Other Physical Properties of Gases and Gas Mixtures," by J. O. Hirschfelder, R. B. Bird, and E. L. Spotz, Trans. ASME, vol. 71, 1949, p. 921.
26   "Viscosity of Air, Oxygen and Nitrogen," by P. J. Rigden, *Philosophical Magazine*, vol. 25, 1938, p. 961.
27   "Recherches Expérimentales sur la Viscosité des Gaz aux Températures Élevées," by V. Vasilesco, *Annales de Physique*, vol. 20, 1945, p. 137 and p. 292.
28   "The Viscosity of Air," by W. V. Houston, *Physical Review*, vol. 52, 1937, p. 751.
29   "Die innere Reibung von Luft im Druckgebiet 1–30 kg/cm²," by G. Kellström, *Arkiv för Matematik, Astronomi och Fysik*, vol. 27A, 1941, p. 1.
30   "The Viscosity of Gases and Gaseous Mixtures at High Pressure," by I. F. Golubev, *Journal of Technical Physics*, USSR, vol. 8, 1938, p. 1932.
31   "Viscosità dell'aria sino a 200 atm," by A. G. Nasini and G. Pastonesi, *Gazzetta Chimica Italiana*, vol. 63, 1933, p. 821.
32   "The Measurement of the Viscosity of Gases at High Pressures. The Viscosity of Nitrogen to 1000 atm," by A. Michels and R. O. Gibson, Proceedings of the Royal Society of London, England, series A, vol. 134, 1932, p. 288.
33   "The Dynamic Viscosity of Nitrogen," by W. L. Sibbitt, G. A. Hawkins, and H. L. Solberg, Trans. ASME, vol. 65, 1943, p. 401.
34   "The Viscosity of Compressed Gases," by H. J. Boyd, *Physical Review*, vol. 35, 1930, p. 1284.
35   "A Summary of Viscosity and Heat Conduction Data for He, A, H_2, O_2, N_2, CO, CO_2, H_2O, and Air," by F. G. Keyes, Trans. ASME, vol. 73, 1951, p. 589.
36   Dissertation, by R. O. Gibson, Amsterdam, 1933 (inaccessible).
37   "Introduction to Non-Linear Mechanics," by N. Kryloff and N. Bogoliuboff, translation by S. Lefschetz, Princeton University Press, Princeton, N. J., 1943.
38   "Hauptaufsätze über laminare und turbulente Reibung," by Th. von Kármán, *Zeitschrift für Angewandte Mathematik und Mechanik*, vol. 1, 1921, p. 233.
39   "The Flow Due to a Rotating Disk," by W. G. Cochran, Proceedings of the Cambridge Philosophical Society, vol. 30, 1934, p. 365.
40   "Note on a Class of Solutions of the Navier-Stokes Equations Representing Steady Rotationally Symmetric Flow," by G. K. Batchelor, *Quarterly Journal of Mechanics and Applied Mathematics*, vol. 4, 1951, p. 29.
41   "Sur le mouvement d'un fluide visqueux au voisinage d'un disque oscillant autour de son axe," by A. Foch and J. Barriol, Comptes Rendus de l'Academie des Sciences, Paris, France, vol. 193, 1931, p. 835.

[a] The authors wish to thank Prof. A. D. Young, Cranfield, for drawing their attention to this publication.

Discussion

C. F. BONILLA.[9] The authors are to be commended on an extremely precise experimental study, permitting, as it does, a re-evaluation of the theory. In computing the logarithmic decrement, the writer wonders, however, whether a linear (or parabolic, if desired) least-squares correlation of the logarithm of each full swing versus the number of the swing (starting at zero for simplicity) would have had advantages.

The following comment does not bear on the pressure coefficient of viscosity, but seems pertinent in view of the atmospheric-pressure viscosities suggested as absolute values:

Vasilesco's viscosity data at and above 0 deg C have been analyzed statistically by the writer and P. L. Walker, H. W. Hoffman, and W. J. Angulo.[10] In addition, the trend with temperature of Vasilesco's viscosity results for nitrogen from 0 to 1100 C was closely matched experimentally. This was considered to corroborate strongly his results on other gases as well. Accordingly, the difference between his and other temperature-coefficient values for air and for nitrogen was surprising. As a check, the following temperature coefficients were computed by differentiating the Sutherland Equations [1] obtained by linear regression of Vasilesco's computed approximate values of Sutherland constant against temperature. These equations agree consistently with his data and of course avoid the large errors possible in a slope computed from two nearby points. These values are all based on Bearden's viscosity for air at 20 C, 181.920 micropoise,[11] which seems the most accurate absolute value available:

Gas	Temperature, deg C	Micropoise/- deg C	Micropoise
Air	21	0.4797	182.3
Nitrogen	21	0.4592	176.2
Argon	20	0.6237	223.2

It is seen that these viscosities are 0.3 to 0.4 per cent higher than those adopted by the authors, the relative agreement, however, thus being within 0.1 per cent. The slopes check well.

A. S. FRIEDMAN.[12] In connection with the results of this excellent piece of research, the writer would like to make a few comments concerning some of the particular molecules and the applicability of the Enskog equations.

Botzen[13,14] at Professor Michels' laboratory in Amsterdam, has evaluated the thermal conductivity and the viscosity of nitrogen as a function of pressure on the basis of the Chapman-Enskog model. The agreement with the experimental viscosity data of Michels and Gibson,[15] and with his own experimental thermal-conductivity data, is very good up to pressures of a few hundred atmospheres, but at higher pressures the computed values are significantly lower than experimental. At 25 C and 1000 atm,

for example, the Enskog model gives values of viscosity about 9 per cent low.

In the range of the authors' experiments, the agreement of the Enskog theory with the Michels and Gibson experimental viscosity data is within a few tenths of one per cent. Hence it is about 2 per cent lower than the authors' values at about 70 atm. The Enskog equation really gives only the ratio of the viscosity to the viscosity at 1 atm. However, since for nitrogen the 1-atm value of Michels agrees with the value given in the paper, the difference in slope between the authors' curve and theirs is still unexplained.

Michels, Schipper, and Rintoul[16] recently measured the viscosity of hydrogen and deuterium from 25 to 125 C at pressures up to 2000 atm with their capillary viscometer. Extrapolation of their results for hydrogen to 21 C shows their measurements to be in excellent agreement with those of the authors. Michels' value of the viscosity at 1 atm, corrected to 21 C, is 885×10^{-7} poise. The Enskog theory here too agrees up to a couple of hundred atmospheres pressure.

As the authors have indicated, there are no high-pressure data on the viscosity of argon at room temperature available at the present time. Michels, Botzen, and the writer[17] have determined at the van der Waals Laboratory recently, the thermal conductivity of argon at pressures up to 2500 atm. In this case, the limitations of the Enskog theory are more apparent.

The assumptions of the Enskog model—hard elastic spheres, no multiple collisions, and so on—are definitely unrealistic at the higher pressures, and even the agreement at the moderately lower pressures is surprising.

F. G. KEYES.[18] This paper provides the most effective and complete discussion of the use of the oscillating disk as applied to viscosity measurements that the writer has read. The method is particularly suitable for measurements at high temperatures in view of the complications inherent in the capillary-flow method, as has been proved by considerable experience.

The determinations of the pressure coefficient of viscosity for gases are relatively few, and it is in this aspect that the oscillating disk offers great promise of providing really accurate data. Such data are important not alone for their practical utility, but they have a broad bearing on the perfection of our knowledge of intermolecular forces. Therefore the authors are to be commended for having carried out measurements to considerable pressures for two monatomic and two diatomic gases, as well as the very important reference gas, air.

The writer learned through a colleague that the authors have contemplated the use of the oscillating disk for the measurement of densities. Densities at high temperatures are extremely difficult to make, and if the oscillating disk could be used it would be a great boon, since for practical purposes we will continue increasingly to be in need of high-temperature–density data at known pressures and temperatures above 800 F.

The writer would be grateful if the authors will describe the use of the oscillating disk for obtaining density data.

AUTHORS' CLOSURE

The authors wish to express their thanks to Prof. C. F. Bonilla, Dr. A. S. Friedman, and to Prof. F. G. Keyes for their kind re-

[9] Columbia University, New York, N. Y.

[10] "The Viscosity of Steam and of Nitrogen at Atmospheric Pressure and High Temperatures," by C. F. Bonilla, R. D. Brooks, and P. L. Walker, Jr., Proceedings of the General Discussions on Heat Transfer, The Institution of Mechanical Engineers, London, England, 1951.

[11] "A Precision Determination of the Viscosity of Air," by J. A. Bearden, *Physical Review*, vol. 56, 1939, pp. 1023–1040.

[12] Thermodynamics Section, National Bureau of Standards, Washington, D. C.

[13] "The Thermal Conductivity of Gases at High Pressure," by A. Botzen, Dissertation, University of Amsterdam, Holland, 1952.

[14] "The Thermal Conductivity of Nitrogen at Pressures Up to 2500 Atmospheres," by A. Michels and A. Botzen, *Physica*, vol. 19, 1953, p. 585.

[15] The Measurement of the Viscosity of Gases at High Pressures— The Viscosity of Nitrogen to 1000 Atms," by A. Michels and R. O. Gibson, Proceedings of the Royal Society of London, England, series A, vol. 134, 1931, pp. 288–307.

[16] "The Viscosity of Hydrogen and Deuterium at Pressures Up to 2000 Atmospheres," by A. Michels, A. Schipper, and R. H. Rintoul, *Physica*, vol. 19, 1953, p. 1011.

[17] "The Thermal Conductivity of Argon at Pressures Up to 2500 Atmospheres," by A. Michels, A. Botzen, and A. S. Friedman, in preparation, 1953.

[18] Professor, Physical Chemistry, Massachusetts Institute of Technology, Cambridge, Mass. Mem. ASME.

marks and for their useful comments. Taking these in turn as they appear, the following remarks may be made:

From a more detailed examination of accuracy it appears that when the logarithmic decrement is measured with the aid of an optical leverage system and a linear scale the accuracy of the logarithmic decrement deduced from two successive amplitudes is poor and it is doubtful whether a least-square correlation of the logarithm of each full swing versus the number of the swing can do very much to improve it. A method which reduces the measurement of the decrement to that of time seems to offer good hope of increasing the intrinsic accuracy of measurement. The authors are now working along these lines and hope to be able to perform more precise determinations of the logarithmic decrement in the future.

It is gratifying to find that the absolute values of viscosity adopted in the paper do not differ by more than 0.3 to 0.4 per cent from those evaluated by Professor Bonilla. The reason for adopting the simplest possible temperature corrections lies in the fact that the corrections themselves were very small. The largest variation in temperature for any single gas did not exceed about 4 deg C and the actual correction was at most of the order of 0.35 per cent. This is well within an over-all accuracy of 1 per cent claimed in the paper.

Regarding the difference in the slope of the viscosity of nitrogen versus pressure referred to by Dr. A. S. Friedman, the authors agree that measurements with the oscillating-disk viscometer show a tendency of giving results which are somewhat too large, the deviation increasing with pressure. It is suggested that this is due to the imperfections in the theory of the instrument used and, in particular, to the fact that the edge correction computed by Macwood does not seem to be precise enough. Analytical work performed since the presentation of the paper shows that the existence of an edge on a disk tends to increase the velocity gradient near the edge as compared with an infinite disk. Thus

the viscous torque computed by Macwood seems to be too low as borne out by the discrepancy between the absolute and calibrated instrument constant C reported. It seems that this discrepancy increases primarily with viscosity and since a uniform correction was applied, the results at higher pressure are likely to be too high. However, it is believed that the result is still good within the 1 per cent claimed.

The oscillating disk has been used to determine densities and an account of such measurements may be found in the paper by Hollis-Hallett (3) quoted in the paper. It is easy to prove by dimensional analysis that the damping torque on an oscillating (or rotating) disk in a viscous fluid of infinite extent is a function of the similarity parameter

$$m = \frac{\rho}{\rho_0} \frac{\delta}{d_0}$$

Here ρ is the density of the fluid, ρ_0 is the density of the disk, δ is the boundary-layer thickness, and d_0 is the thickness of the disk. Since

$$\delta \sim \sqrt{\nu/\omega_0}$$

where ω_0 is the circular frequency in vacuo, ν is the kinematic viscosity $\nu = \eta/\rho$. Hence

$$m \sim \sqrt{\eta\rho}$$

so that the period of oscillation and the logarithmic decrement depend on $\sqrt{\eta\rho}$ and not on the viscosity alone. These remarks are borne out by the equations given by Hollis-Hallett (3).

One of the authors (J. Kestin) is now engaged on analytical work on the subject under consideration under the sponsorship of the Air Research and Development Command (Contract No. AF 18 [600] — 891) and the first report is due to be published by Brown University in June, 1954.

Compressibility of Gases—VIII

Krypton in the Temperature Range 0 to 600 C and Pressure Range 10 to 80 Atm[1]

By E. WHALLEY[2] AND W. G. SCHNEIDER,[2] OTTAWA, CANADA

The compressibility of krypton has been measured in the temperature and pressure range described.

INTRODUCTION

A PROGRAM of measurement of the compressibility of a number of gases over a wide temperature range was undertaken in this laboratory several years ago (1).[3] The main object of the measurements has been to obtain information on intermolecular forces. For this purpose the second and third virial coefficients of the equation

$$\frac{PV}{RT} = 1 + \frac{B_v}{V} + \frac{C_v}{V^2} + \ldots\ldots\ldots\ldots [1]$$

are used; these are related to the potential energy of interaction of a pair of molecules $E(r)$ by the equations

$$B_v = 2\pi N \int_0^\infty (1 - \exp\text{-}E(r)/kT) \, r^2 dr \ldots\ldots\ldots [2]$$

$$C_v = 8\pi^2 N^2 \iiint f_{12}f_{13}f_{23}r_{12}r_{13}r_{23}dr_{12}dr_{13}dr_{13} \ldots [3]$$

where

$$f_{ij} = [1 - \exp\text{-}E(r_{ij})/kT]$$

r_{ij} is the distance between molecules i and j, N is Avogadro's number, and k is the Stefan-Boltzmann constant. The procedure is to assume plausible forms for the intermolecular potential $E(r)$ and choose values of the potential parameters to obtain the best fit to the experimental values of B_v and C_v.

One of the best potentials for spherically symmetrical molecules which has been suggested to date is the Lennard-Jones 12:6 potential

$$E(r) = 4\epsilon \left\{ \left(\frac{r_0}{r} \right)^{12} - \left(\frac{r_0}{r} \right)^6 \right\} \ldots\ldots\ldots\ldots [4]$$

where ϵ and r_0 are, respectively, the depth of the minimum of the potential-energy curve and the low-velocity-collision diameter. This model has met with considerable success in correlating the properties of gases (2). Powers other than 12 and exponential functions have been used for the repulsive potential. Over a short temperature range most potentials with two or more adjustable constants can be fitted to experimental data satisfactorily. Only when a large temperature range, preferably extending both

above and below the Boyle point, is considered, is it possible to decide which potential gives the best fit.

To this end measurements of the virial coefficients have been carried out for several gases over the temperature range 0 to 600 C and for helium the measurements were extended to 1200 C. For carbon tetrafluoride and sulphur hexafluoride, measurements could not be extended to 600 C because of reaction with the vessel. Since the second virial coefficient is the most important for our purposes, the third is of lesser importance and the higher ones of no importance, the pressure range chosen was such as to permit maximum accuracy in the second virial coefficient and yet take full advantage of the high accuracy of pressure measurements by a free-piston gage at high pressures compared with a mercury column at low pressures. The pressure range used has usually been 10 to 50 or 80 atm.

TABLE 1 SUMMARY OF COMPRESSIBILITY MEASUREMENTS TO DATE

Gas	Temp range, deg C	Pressure range, atm	Reference
He	0–1200	10–70	8, 14
A	0–600	10–80	10
CF₄	0–400	10–50	6
SF₆	0–250	10–50	6
CO₂	0–600	10–50	15

Table 1 gives a summary of the compressibility measurements completed to date. With the exception of carbon dioxide, the gases were chosen because of the spherical symmetry of their molecules. A central force field such as that represented by Equation [4] might be expected to apply approximately. For helium (3) a rather more complicated potential than Equation [4] had to be used involving an exponential term in place of r^{-12} and an additional term in r^{-8}. For carbon tetrafluoride, sulphur hexafluoride (4), and argon (5) a potential of type (6) was moderately good and the potential constants obtained for argon could be used to calculate the heat of sublimation and the lattice spacing at 0 deg K quite accurately (5). The carbon-dioxide molecule has strong directional forces (4) and it is not surprising that a central force law cannot be made to fit the virial data satisfactorily. The value of the heat of sublimation of carbon dioxide at 0 deg K, calculated using the best constants in Equation [4] which can be derived from the virial data, is less than half the experimentally measured value.

Compressibility measurements for krypton together with an evaluation of the virial coefficients in the temperature range 0 to 600 C are described in the present paper. It is planned to carry out similar measurements for the remaining inert gases, neon and xenon, and to examine binary mixtures of the inert gases to obtain information on the nature of the force field between unlike molecules.

METHOD OF MEASUREMENT

The method of measurement is based on the expansion method described by Burnett (7). An unknown quantity of gas is confined in a pipette of unknown volume and its pressure P_1 measured. The gas is expanded into another unknown volume and its

---

pressure P_2 measured. If the equation of state of 1 mole of gas can be written

$$PV = A + BP + CP^2 + \ldots \ldots \ldots \ldots [5]$$

where P is the pressure, V the volume and A, B, and C the pressure virial coefficients, and the pipettes are at the same temperature, P_1 and P_2 are related by the equation

$$\frac{P_1}{P_2} = N + (N-1)\frac{B}{A}P_1 + \left\{N - \frac{P_2}{P_1}\right\}\frac{C}{A}P_1^2 + \ldots [6]$$

where N is the ratio of the volume after expansion to that before. By fitting the results of several expansions at different values of P_1 to this equation by the method of least mean squares, the values of N, B/A, and C/A can be evaluated. If the virial coefficients are expressed in amagat units, then by definition at 0 C

$$A_0 + B_0 + C_0 = 1 \ldots \ldots \ldots \ldots \ldots [7]$$

From a knowledge of B_0/A_0 and C_0/A_0, the virial coefficients can be obtained. At temperature T from the definition of the thermodynamic temperature scale, the value of A is

$$A = A_0\frac{T}{T_0} \ldots \ldots \ldots \ldots \ldots \ldots [8]$$

so that A, B, and C can be evaluated at any temperature.

For very high and very low temperatures, it is more convenient to have only one pipette at the required temperature and to maintain the second one at some more convenient temperature such as 0 C (8). Equation [2] is then replaced by

$$\frac{P_1}{P_2} + \frac{B_0}{A_0}(P_1 - P_2) = M + (M-1)\frac{B}{A}(P_1 + P_2)$$

$$+ (M-1)\left\{\frac{B}{A}\right\}^2 P_1 P_2 + \ldots \ldots [9]$$

where $M = 1 + (TV_0)/(T_0 V_T)$, T and V_T are the temperature and volume of the first pipette, T_0 and V_0 are the temperature and volume of the second pipette. A_0 and B_0 are the virial coefficients at the temperature T_0. If A_0 and B_0 are known, B/A can be evaluated by least mean squares.

Knowing A, B, and C, PV can be calculated from Equation [5]. For examination of the intermolecular potentials, the B_v and C_v of Equation [1] can be calculated from the relations

$$B_v = BV_N$$

$$C_v = V_N^2(AC + B^2)$$

where V_N is the normal volume.

APPARATUS

The apparatus has been described previously in some detail (1). A number of modifications have been made and the following is mainly a description of these:

(a) *Pressure Measurements.* The pressure is measured by a free-piston gage as described by Keyes (9) and calibrated against the vapor pressure of very pure carbon dioxide at 0 deg C. The piston is oscillated through about 60 deg to prevent sticking. The frequency of oscillation of the piston must be quite different from the natural swinging frequency of the scale pan to damp oscillations in the pan. Balance of the loading of the piston was indicated by a mercury U-tube having electrical contacts in each arm.

(b) *Temperature Measurement.* A platinum-resistance thermometer of conventional design with mica cross was used in the earlier work. After prolonged exposure to 600 C the ice-

point resistance shifted considerably. Later, thermometers with a quartz cross were used and had a much more stable ice-point resistance.

(c) *The Thermostat.* The thermostat for 0 to 600 C consists of a well-insulated stainless-steel can, equipped with a cover and two high-speed stirrers. Oil is used as the bath liquid below 200 C; from 200 to 600 C a eutectic mixture of lithium, sodium, and potassium nitrates is used. Temperature control is obtained by means of a stainless-steel-jacketed platinum resistance thermometer connected to a Mueller bridge. The bridge unbalance caused movement of a sensitive mirror galvanometer having a 20-ft optical lever which actuated a photorelay circuit. By working in a temperature-controlled room, insulating the part of the control thermometer outside the bath with asbestos ribbon, protecting the part above the bath liquid from splashing, using the minimum number of contacts and making these copper-copper wherever possible, and carefully shielding all contacts from drafts, the mean temperature of the bath could be maintained to ±0.001 deg for days at the lower temperatures, and hours at the higher without manual adjustment. The variations in temperature due to the intermittent heater switching on and off as measured by the quartz thermometer is ±0.002 deg or less. The temperature of the gas inside the pipette is probably constant to better than 0.001 deg.

(d) *Gas-Pipette Assembly.* The gas-pipette assembly is described in reference (1), and shown in Fig. 1, which is self-

A, Gas pipettes
B, Pressure vessels surrounding gas pipettes
C, Gas connections for B
D, Expansion-valve block
E, Vacuum line
F, Line to compressor and gas supply
G, Mercury U-tube
H, Glass capillaries
I, Mercury injector
J, Pressure gage connection
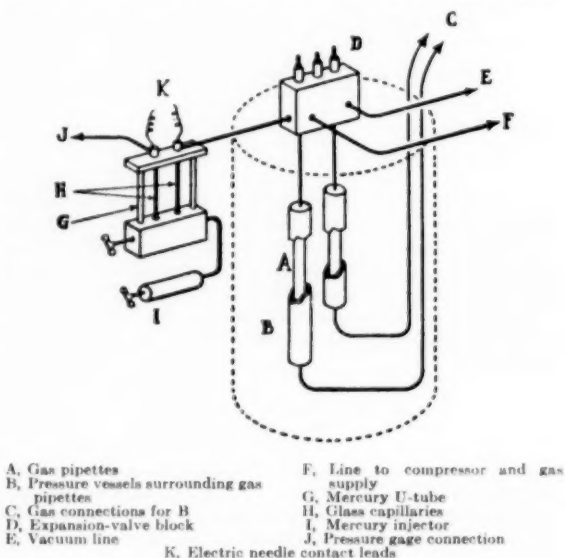K, Electric needle contact leads

FIG. 1   GAS-PIPETTE ASSEMBLY

explanatory. The pipettes are double-walled to enable the pressure inside and outside to be adjusted to the same value, and all joints were welded. They were annealed for several days at temperatures higher than the maximum to which they were to be used to minimize volume changes. The temperature of the valve block and U-tube and the connecting line between them is controlled by water circulation.

PROCEDURE

The gas to be measured is compressed into the large pipette to a pressure of about 80 atm either by condensation into a small pressure bomb and evaporation, or by a mercury piston. At the

same time, the pressure is built up in the pressure vessel surrounding the pipette and thereafter the pressures inside and outside the pipette are kept balanced to within 1 atm. When temperature and pressure equilibrium is obtained, the pressure is recorded and the gas expanded into the second pipette. After the pressure is measured again the expansion valve is closed and the gas in the small pipette is allowed to expand into a gasometer, or condensed. After evacuating the small pipette, the foregoing cycle is repeated. In this manner, about nine pressure ratios are obtained. The isotherm is then repeated starting at a lower initial pressure so as to stagger the points on the pressure ratio-pressure plot.

CORRECTIONS AND TREATMENT OF DATA

The pressures measured by the piston gage are corrected for barometric pressure, temperature variation of the piston, oil head between the bottom of the piston and the top of the mercury in the U-tube, difference in levels of the electrical contacts in the U-tube, air buoyancy of the weights and the scale pan, and so on, and the effects of barometric pressure on the buoyancy, the "dead space" in the valve block, U-tube, and connecting line, and the part of the connections from the valve block to the pipettes which is outside the bath. The method of estimating dead-space factors is similar to that in reference (1).

The corrected values of P_1 and P_2 are fitted to Equation [6] or [9] by the method of least mean squares (10, 11).

COMPARISON WITH OTHER METHODS

The main advantages of the Burnett method of measuring the compressibility of gases are as follows:

1 No volume measurement is needed. This is particularly advantageous at higher temperatures where accurate volume measurements are rather difficult. The ratio of two volumes N is required, but this is determined from each isotherm; if any change in N occurs, e.g., by annealing or overstraining, this is detected immediately.

2 The temperature need not be exactly the thermodynamic temperature since the quantities measured are B and C, and dB/dT and dC/dT are small. If PV is measured directly, a difference of 0.1 deg from the thermodynamic temperature is serious and is very difficult to attain at high temperatures.

Hence all errors, except for a few quite negligible ones, are random and one can state precisely the accuracy of the virial coefficients.

The main disadvantages of the method are that values of PV are not measured directly, and the analysis and working up of the primary data are somewhat more complicated. However, if one takes sufficient terms so that the sum of squares is not reduced significantly by the addition of higher terms and the deviations are distributed randomly, this is not very serious.

MEASUREMENTS FOR KRYPTON

The compressibility of krypton has been measured over the temperature range 0 to 600 C and pressure range 10 to 80 atm by the method described. The krypton used was the highest purity gas supplied by the Linde Company. Mass spectrometer analyses of the gas carried out periodically during the course of the work indicated less than 0.1 per cent nitrogen and less than 0.01 per cent of other inert gases. The results of a typical run are given in Table 2. Values of A, B, and C are given in Table 3. At 0 C the measurements to 80 atm could not be fitted satisfactorily to even a cubic equation in P_1, so the results to 40 atm only were used and gave a good fit to a quadratic equation in P_1. The normal volume is 22.3513 ± 0.0022 l mole^{-1} or $22,351.9 \pm 2.2$ cc mole^{-1}. Beattie, Brierley, and Barriault (12, 13) at M.I.T. recently have published values of the virial coefficients in the equation

$$PV = RT + \frac{B_v}{V} + \frac{C_v}{V^2} + \frac{D_v}{V^3}$$

from measurements of the pressure at densities of from 1 to 10 moles per liter over the temperature range 0 to 300 C. These were converted to the quantities of Equation [5] by the relations

$$A = RT/V_N, \; B = B_V/V_N RT$$

$$C = \frac{C_V - B_V^2/RT}{V_N R^2 T^2}$$

and are compared with our values in Table 3. The reliability of Beattie's values is not certain since the deviations of the experimental and calculated values of $V(PV - RT)$ are not random either for constant temperature or for constant density. There seem to be some errors in the measurements as the graph of $V(PV - RT)$ is slightly S-shaped where, from experience with other gases, one would expect a smoother curve.

TABLE 2 RESULTS OF A TYPICAL RUN FOR KRYPTON, 150 C. RUN NO. 25

P_1 atm	P_1/P_2
73.35857	1.250652
58.65825	1.251482
46.87216	1.252331
37.43294	1.253026
29.87402	1.253656
23.83092	1.254397
18.99802	1.254857
15.13968	1.255311
12.06063	1.255621

TABLE 3 VIRIAL COEFFICIENTS OF KRYPTON

(Units of B, Amagat; of C, Amagat atm^{-1})

T deg C	A	$10^3 B$	$10^6 C$	$10^3 B$	$10^6 C$
		NRC measurements		M.I.T. measurements	
0	1.002807	-2.805 ± 0.022	1.60 ± 0.25	-2.817	-2.41
25	1.094585			-2.342	-0.24
50	1.186364	-1.914 ± 0.012	$+1.97 \pm 0.19$	-1.914	$+0.72$
75	1.278142			-1.575	1.32
100	1.369920	-1.310 ± 0.016	2.50 ± 0.13	-1.291	1.62
125	1.461699			-1.050	1.77
150	1.553477	-0.811 ± 0.016	2.10 ± 0.11	-0.842	1.81
175	1.645255			-0.659	1.77
200	1.737034	-0.481 ± 0.016	1.89 ± 0.09	-0.497	1.68
225	1.828812			-0.376	1.72
250	1.920591			-0.255	1.66
275	2.012369			-0.142	1.54
300	2.104147	0.019 ± 0.017	1.29 ± 0.09	-0.057	1.53
400	2.471261	0.324 ± 0.025	0.98 ± 0.12		
500	2.838374	0.568 ± 0.020	0.63 ± 0.11		
600	3.205487	0.769 ± 0.019	0.29 ± 0.10		

BIBLIOGRAPHY

1 "Compressibility of Gases at High Temperatures—I Methods of Measurement and Apparatus," by W. G. Schneider, *Canadian Journal of Research*, vol. B27, 1949, pp. 339–352.

2 "Viscosity and Other Physical Properties of Gases and Gas Mixtures," by J. O. Hirschfelder, R. B. Bird, and E. L. Spotz, Trans. ASME, vol. 71, 1949, pp. 921–937.

3 "On the Intermolecular Potential of Helium," by J. L. Yntema and W. G. Schneider, *Journal of Chemical Physics*, vol. 18, 1950, pp. 646–650.

4 "Intermolecular Potentials—I Carbon Tetrafluoride and Sulphur Hexafluoride—II Carbon Dioxide," by K. E. MacCormack and W. G. Schneider, *Journal of Chemical Physics*, vol. 19, 1951, pp. 849–855.

5 E. Whalley and W. G. Schneider, to be published.

6 "Compressibility of Gases at High Temperatures—V Carbon Tetrafluoride in the Temperature Range 0–400 C.—VI Sulfur Hexafluoride in the Temperature Range 0–250 C," by K. E. Mac-Cormack and W. G. Schneider, *Journal of Chemical Physics*, vol. 19, 1951, pp. 845–848.

7 "Compressibility Determinations Without Volume Measurements," by E. S. Burnett, *Journal of Applied Mechanics*, Trans. ASME, vol. 58, 1936, pp. A-136–A-140.

8 "Compressibility of Gases at High Temperatures—III The Second Virial Coefficient of Helium in the Temperature Range 600–1200 C," by J. L. Yntema and W. G. Schneider, *Journal of Chemical Physics*, vol. 18, 1950, pp. 641–646.

9 "High Pressure Technic," by F. G. Keyes, *Industrial and Engineering Chemistry*, vol. 23, 1931, pp. 1375–1379.

10 "Compressibility of Gases at High Temperature—VII Argon in the Temperature Range 0–600 C and Pressure Range 10–80 Atmospheres," by E. Whalley, Y. Lupien, and W. G. Schneider, *Canadian Journal of Chemistry*, vol. 31, 1953, pp. 722–733.

11 "Statistical Adjustment of Data," by W. E. Deming, John Wiley & Sons, Inc., New York, N. Y., 1943.

12 "Compressibility of Krypton—I An Equation of State for Krypton and the Weight of a Liter of Krypton," by J. A. Beattie, J. S. Brierley, and R. J. Barriault, *Journal of Chemical Physics*, vol. 20, 1952, pp. 1613–1615.

13 "Compressibility of Gaseous Krypton—II The Virial Coefficients and Potential Parameters of Krypton," by J. A. Beattie, J. S. Brierley, and R. J. Barriault, *Journal of Chemical Physics*, vol. 20, 1952, pp. 1615–1618.

14 "Compressibility of Gases at High Temperatures—II The Second Virial Coefficient of Helium in the Temperature Range 0–600 C," by W. G. Schneider and J. A. H. Duffie, *Journal of Chemical Physics*, vol. 17, 1949, pp. 751–754.

15 "Compressibility of Gases at High Temperatures—IV Carbon Dioxide in the Temperature Range 0–600 C and Pressures Up to 50 Atmospheres," by K. E. MacCormack and W. G. Schneider, *Journal of Chemical Physics*, vol. 18, 1950, pp. 1269–1272.

Discussion

F. G. KEYES.[4] The measurements that Dr. W. G. Schneider and his associates have been carrying out for a number of years at the National Research Council Laboratory at Ottawa on the monatomic gases are important because of the relative simplicity of the interatomic field for these gases. The work is also especially important for its high accuracy. As we have come to know, the spherically symmetrical potential field is the exception, and an accurate knowledge of the properties of the monatomic gases which corresponds so closely to the simple classical field concept becomes of fundamental value as a basis for reference. The work reported by the authors on helium carried up to the extraordinarily high temperature of 1200 C has brought out sharply the complicated character of the positive or repulsive aspect of the potential function.

The results reported on argon indicate that a simpler expression, relative to helium, for the positive potential is serviceable to describe the results. For this rare gas the attractive or negative potential is very large relative to helium which diminishes the amount of information that can be deduced regarding the argon positive potential from p-v-T measurements, because the measured properties can be described more fully in terms of the attractive aspect of the potential than in the case of helium. It may be noted that 1200 C in the case of helium is a reduced temperature of 280. The similar reduced temperature in the case of argon would require astronomical temperatures.

My colleague at M.I.T., Professor Amdur, has completed atomic-beam scattering of argon. The velocity of the beam is so high that the interpenetration of the field is very high, in fact corresponding to enormous temperatures in the case of the argon gas at equilibrium. The measurements show as in the case of helium that the positive potential is, in fact, a complicated exponential form, however, represented in some detail by a Slater-type expression. The results of the scattering experiments together with the remarkably accurate results obtained by the authors will provide much detailed insight into the interatomic field of the rare gases, and thus provide the necessary empirical knowledge for guiding theoretical development.

[4] Professor Emeritus, Physical Chemistry, Massachusetts Institute of Technology, Cambridge, Mass. Mem. ASME.

AN ASME PAPER

Its Preparation,
Submission and Publication,
and Presentation

To a large degree the papers prepared and presented under the ASME sponsorship are evidence by which its professional standing and leadership are judged. It follows, therefore, that to qualify for ASME sponsorship, a paper must not only present suitable subject matter, but it must be well written and conform to recognized standards of good English and literary style.

The pamphlet on "AN ASME PAPER" is designed to aid authors in meeting these requirements and to acquaint them with rules of the Society relating to the preparation and submission of manuscripts and accompanying illustrations. It also includes suggestions for the presentation of papers before Society meetings.

CONTENTS

Price 40¢. No discount allowed. *A remittance must accompany all orders for $5.00 or less. U. S. Postage Stamps are acceptable.*

THE AMERICAN SOCIETY OF MECHANICAL ENGINEERS

29 West 39th Street, New York 18, N. Y.